INVESTIGATIONS ON THE PERFORMANCE ENHANCEMENT TECHNIQUES FOR FREE SPACE OPTICAL COMMUNICATION SYSTEMS

Ph.D. Thesis

by

NARENDRA VISHWAKARMA

DEPARTMENT OF ELECTRICAL ENGINEERING

INDIAN INSTITUTE OF TECHNOLOGY INDORE

November, 2023

INVESTIGATIONS ON THE PERFORMANCE ENHANCEMENT TECHNIQUES FOR FREE SPACE OPTICAL COMMUNICATION SYSTEMS

A THESIS

Submitted in partial fulfillment of the

requirements for the award of the degree

of

DOCTOR OF PHILOSOPHY

by

NARENDRA VISHWAKARMA

DEPARTMENT OF ELECTRICAL ENGINEERING

INDIAN INSTITUTE OF TECHNOLOGY INDORE

November, 2023

INDIAN INSTITUTE OF TECHNOLOGY INDORE

CANDIDATE'S DECLARATION

I hereby certify that the work which is being presented in the thesis entitled "**INVESTIGATIONS ON THE PERFORMANCE ENHANCEMENT TECHNIQUES FOR FREE SPACE OPTICAL COMMUNICATION SYSTEMS**" in the partial fulfillment of the requirements for the award of the degree of **DOCTOR OF PHILOSOPHY** and submitted in the **DEPARTMENT OF ELECTRICAL ENGINEERING, Indian Institute of Technology Indore**, is an authentic record of my own work carried out during the time period from July 2019 to November 2023 under the supervision of Dr. Swaminathan R, Associate Professor, Indian Institute of Technology Indore, India.

The matter presented in this thesis has not been submitted by me for the award of any other degree of this or any other institute.

Narendra
10/11/2023
Signature of the student with date
(NARENDRA VISHWAKARMA)

This is to certify that the above statement made by the candidate is correct to the best of our knowledge.

10/11/2023
Signature of Thesis Supervisor with date
(Dr. SWAMINATHAN R)

NARENDRA VISHWAKARMA has successfully given his Ph.D. Oral Examination held on November 07, 2023.

ACKNOWLEDGEMENTS

I would like to express my sincere gratitude to all those who have supported me throughout my Ph.D. journey. First and foremost, I would like to thank my supervisor, Dr. Swaminathan R., for his invaluable guidance, encouragement, and support. His expertise, wisdom, and constructive criticism have been instrumental in shaping my research and refining my writing. He has been a constant source of inspiration and motivation, pushing me to reach my full potential as a researcher. I would also like to extend my sincere thanks to the members of PSPC committee, Prof. Prabhat Kumar Upadhyay and Prof. Surya Prakash, for their constructive feedback, insightful comments, and expert guidance. Their expertise have contributed immensely to the quality of my research and its presentation. I also want to express my appreciation to Dr. Panagiotis D. Diamantoulakis, Prof. George K. Karagiannidis, and Dr. A. S. Madhukumar for their insights and contributions, which helped us to shape and refine our research work. I am grateful for the time and effort they have invested in reviewing my work and helping me to improve it.

Furthermore, I would like to thank my colleagues and friends, Ankit Jain and Deepshikha Singh, for their unwavering support, encouragement, and camaraderie. Further, I would like to extend my appreciation to my Future Generation Communication Systems Research lab members, Ms Smriti Uniyal, Naveen, Manojkumar Kokare, Nayim Ahamed, and Sandesh Sharma for their unconditional support and collaborative spirit that has made my research journey enjoyable and fulfilling. I have been fortunate to have such an amazing group of people to share this experience with. I would like to express my appreciation to the faculty and staff of the Department of Electrical Engineering for their support and encouragement. Their commitment to academic excellence has provided me with a stimulating and challenging environment in which to learn and grow as a researcher.

Finally, I would like to thank my family, my Daughter, Wife, Mother, Father, and Brother. Their love, support, and understanding have been a constant source of strength and inspiration. I am grateful for their unwavering belief in me and my abilities, even during the most challenging times of my Ph.D. journey. Last but not the least, I would like to thank again my partner Rakhi Vishwakarma, whose unwavering support and countless sacrifices were instrumental in helping me complete this thesis. Without her love and understanding, I believe the journey would have been much more challenging and I will always cherish the memories of our shared journey.

NARENDRA VISHWAKARMA

Dedicated

to

My family

ABSTRACT

Free Space Optics (FSO) is a promising technology for high-speed wireless communication systems. Unlike traditional radio frequency (RF) wireless communication systems, FSO uses optical signals to transmit information through the atmosphere, making it an attractive alternative for high-speed and secure communication links. It is also envisioned that FSO can support seamless ubiquitous high-speed broadband connectivity, which is a significant requirement for sixth-generation (6G) backhaul networks. FSO technology offers several advantages, including high data rates, license-free spectrum, low power consumption, and immunity to electromagnetic interference. However, it also has some limitations such as susceptibility to atmospheric turbulence, misalignment (pointing) errors, and attenuation due to fog, which can cause signal degradation and affect the FSO system performance. In this thesis, various performance enhancement techniques, including hybrid FSO/RF systems, optical reflecting surface (ORS), and optical space shift keying (OSSK) scheme, are discussed to overcome the limitations of the FSO communication.

Firstly, a comprehensive performance analysis of the hybrid FSO/RF system has been carried out in terms of outage probability, average symbol error rate (SER) and ergodic capacity considering a single-threshold-based hard-switching scheme for both terrestrial and satellite communication scenarios. Further, maximal-ratio combining (MRC) and adaptive combining schemes for hybrid FSO/RF system have been proposed to overcome the limitations of the FSO systems. Here, the exact closed-form expressions for the probability density function (PDF) and cumulative distribution function (CDF) of the MRC of FSO and RF links are derived. With the help of the derived MRC channel statistics, unified closed-form expressions for outage probability and average SER are obtained. The FSO channel turbulence for the hard-switching, MRC, and adaptive combining schemes is modeled using the generalized Malaga distribution with pointing errors. The RF channel fading is modeled using the generalized α-η-κ-μ distribution. In addition, the closed-form expression for the ergodic capacity of the adaptive-combining-based hybrid FSO/RF system

is also derived over Malaga (FSO) and κ-μ (RF) fading distributions. The simpler asymptotic expressions are derived to obtain the diversity gain and signal-to-noise ratio (SNR) gain of the above-discussed hybrid systems. The theoretical results unveil that under strong turbulence, high pointing errors, and adverse weather conditions, the performance of the hybrid FSO/RF system over single-link FSO system is improved significantly due to RF backup link.

The deployment of ORS in FSO communication systems has recently garnered much attention due to its ability to reduce line-of-sight (LOS) blockages by providing an alternate propagation path, thereby improving the link reliability. In this work, an ORS-assisted FSO communication system is proposed, which is based on the OSSK technique. Specifically, an upper bound expression for the average bit error rate (BER) and a lower bound for the ergodic capacity are derived. It is observed from the numerical results that the atmospheric turbulence and pointing errors have a negligible effect on the performance of the proposed system. Further, the performance analysis of multiple ORSs-assisted FSO system is carried out based on the selection of the best ORS from the multiple available ORSs. Using the PDF statistics of maximum instantaneous SNR, the outage and average SER expressions are derived for both perfect and imperfect channel state information (CSI) cases. Additionally, the asymptotic expressions, which are mathematically more tractable are presented with the diversity gain analysis. Finally, the numerical results show that imperfect CSI significantly affects the proposed system performance and increasing the number of ORS considerably improves the system performance.

All the derived performance metric expressions are extensively validated using the Monte-Carlo simulations. In conclusion, this thesis provides a comprehensive analysis of various performance enhancement techniques, which are capable of improving the performance of FSO systems.

LIST OF PUBLICATIONS

(A) Publications from PhD thesis work

A.1 In Journals

1. N. Vishwakarma and Swaminathan R., "Performance analysis of hybrid FSO/RF communication over generalized fading models," *Elsevier Optics Communication*, vol. 487, Article 126796, pp. 1-18, 2021. doi: 10.1016/j.optcom.2021.126796, Impact factor: 2.4.
2. N. Vishwakarma and Swaminathan R., "On the capacity performance of hybrid FSO/RF system with adaptive combining over generalized distributions," *IEEE Photonics Journal*, vol. 14, no. 1, pp. 1-12, Feb. 2022, doi: 10.1109/JPHOT.2021.3135115, Impact factor: 2.4.
3. N. Vishwakarma and Swaminathan R., "On the maximal-ratio combining of FSO and RF links over generalized distributions and its applications in hybrid FSO/RF systems,"*Elsevier Optics Communication*, vol. 520, pp. 128542, 2022, doi: 10.1016/j.optcom.2022.128542, Impact factor: 2.4.
4. N. Vishwakarma, Swaminathan R, Panagiotis D. Diamantoulakis, and George K. Karagiannidis, "Performance analysis of RIS-assisted optical space shift keying-based MIMO-FSO system," *IEEE Transactions on Communications*, vol. 71, no. 8, pp. 4751-4763, Aug. 2023, doi: 10.1109/TCOMM.2023.3278312, Impact factor: 8.3.

A.2 In Conferences

1. N. Vishwakarma and Swaminathan R., "On the performance of hybrid FSO/RF system over generalized fading channels," in *proc. 2020 IEEE International Conference on Advanced Networks and Telecommunication Systems (ANTS)*, IIIT Delhi, 2020, pp. 1-6 (Online), doi: 10.1109/ANTS50601.2020.9342806.

2. N. Vishwakarma and Swaminathan R., "Capacity Analysis of Adaptive Combining for Hybrid FSO/RF Satellite Communication System," in *proc. 2021 National Conference on Communications (NCC)*, IIT Kanpur, 2021, pp. 1-6 (Online), doi: 10.1109/NCC52529.2021.9530144.

3. N. Vishwakarma and Swaminathan R., "Performance Analysis of Multiple Optical Reflecting Surfaces Assisted FSO Communication," in *proc. 2023 IEEE Wireless Communications and Networking Conference (WCNC)*, Glasgow, U.K., 2023, pp. 1-6, doi: 10.1109/WCNC55385.2023.10118738.

(B) Other publications during PhD

B.1 In Journals

1. M. Siddharth, S. Shah, N. Vishwakarma, and Swaminathan R, "Performance analysis of adaptive combining based hybrid FSO/RF terrestrial communication," *IET Communications*, vol. 14, no. 12, pp. 4057 - 4068, Dec. 2020, doi: https://doi.org/10.1049/iet-com.2020.0598, Impact factor: 1.6.

2. Swaminathan R, S. Sharma, N. Vishwakarma, and AS Madhukumar, "HAPS-based relaying for integrated space-air-ground networks with hybrid FSO/RF communication: A performance analysis," *IEEE Transactions on Aerospace and Electronic Systems*, vol. 57, no. 3, pp. 1581 - 1599, June 2021, doi: 10.1109/TAES.2021.3050663, Impact factor: 4.4.

3. S. Shah, M. Siddharth, N. Vishwakarma, R. Swaminathan and A. S. Madhukumar, "Adaptive-combining-based hybrid FSO/RF satellite communication with and without HAPS," *IEEE Access*, vol. 9, pp. 81492-81511, 2021, doi: 10.1109/ACCESS.2021.3086024, Impact factor: 3.9.

4. S. Uniyal, N. Vishwakarma, and Swaminathan R., "Multihop IRS-assisted free space optics communication with DF relaying: a performance analysis," *Applied Optics*, vol. 62, pp. 4716-4726, 2023, doi: 10.1364/AO.487194,

Impact factor: 1.905.

(B.2) **In Conferences**

1. S. Sharma, N. Vishwakarma, and Swaminathan R., "Performance analysis of IRS-assisted hybrid FSO/RF communication system," in *proc. IEEE National Conference on Communications (NCC)*, IIT Bombay, 2022, pp. 1-6 (Online), doi: 10.1109/NCC55593.2022.9806764.

2. S. Uniyal, N. Vishwakarma, S. Sharma, and Swaminathan R., "Intelligent reflecting surfaces-aided mixed FSO/RF communication system," in *proc. IEEE Wireless Communications and Networking Conference (WCNC)*, Glasgow, U.K., 2023, pp. 1-6, doi: 10.1109/WCNC55385.2023.10118874.

3. S. Uniyal, N. Vishwakarma, D. Singh, and Swaminathan R., "Reconfigurable intelligent surfaces-aided mixed THz/FSO communication system," in *proc. 2023 IEEE GLOBECOM*, 2023 [accepted].

4. S. Uniyal, N. Vishwakarma, D. Singh, and Swaminathan R., "IRS-aided hybrid FSO/RF communication system with selection combining," *submitted to NCC 2024*.

Contents

ABSTRACT **i**

LIST OF PUBLICATIONS **iii**

LIST OF FIGURES **xiv**

LIST OF TABLES **xix**

LIST OF ABBREVIATIONS **xxii**

LIST OF SYMBOLS **xxiv**

1 Introduction **1**

1.1 Background 1

1.2 Motivations 3

1.3 Contributions 5

1.4 Thesis Organization 8

1.5 Chapter Summary 8

2 Literature Review **11**

2.1 FSO Channel Modeling 14

2.1.1 Atmospheric turbulence 14

2.1.2 Pointing errors 16

2.1.3 Atmospheric attenuation 17

2.1.4 Channel Estimation Errors 17

2.2 Techniques to Improve FSO performance 18
2.2.1 MIMO Schemes 19
2.2.2 Relaying techniques 21
2.2.3 Hybrid FSO/RF system 25
2.2.4 Reconfigurable Intelligent Surface (RIS) 31
2.3 Chapter Summary 35

3 Performance Analysis of Hybrid FSO/RF Communication Over Generalized Fading Models 37

3.1 Introduction 37
3.2 Organization of the chapter 39
3.3 System and Channel Models 39
3.3.1 FSO Channel Model 42
3.3.2 RF channel Model 45
3.4 Outage Analysis 47
3.5 Average SER Analysis 47
3.6 Ergodic Capacity Analysis 50
3.7 Asymptotic Analysis 51
3.7.1 Outage Probability 52
3.7.2 SER Analysis 52
3.7.3 Capacity Analysis 56
3.8 Numerical Results and Discussion 57
3.8.1 Optimum Values of Beam Width and Switching Threshold SNR 58
3.8.2 Outage and Average SER Performances 60
3.8.3 Ergodic Capacity Performance 74
3.8.4 Results For Satellite Communication Scenario 79
3.9 Chapter Summary 82

4 On the Maximal-Ratio Combining of FSO and RF Links Over Generalized Distributions and its Applications in Hybrid FSO/RF Sys-

tems **85**

4.1 Introduction 85
4.2 Organization of the chapter 87
4.3 System and Channel Models 87
4.3.1 FSO Channel Model 91
4.3.2 Combined FSO Channel Statistics 93
4.3.3 RF Channel Model 94
4.4 Outage Probability Analysis 95
4.4.1 Hybrid FSO/RF with MRC Scheme 95
4.4.2 Hybrid FSO/RF with Adaptive Combining Scheme 96
4.5 Average SER Analysis 98
4.5.1 Hybrid FSO/RF with MRC Scheme 99
4.5.2 Hybrid FSO/RF with Adaptive Combining Scheme 100
4.6 Asymptotic Analysis and Optimization 101
4.6.1 Outage Probability 102
4.6.1.1 Hybrid FSO/RF with MRC Scheme 102
4.6.1.2 Hybrid FSO/RF with Adaptive Combining Scheme . 103
4.6.2 Average SER 103
4.6.2.1 Hybrid FSO/RF with MRC Scheme 104
4.6.2.2 Hybrid FSO/RF with Adaptive Combining Scheme . 104
4.6.3 Diversity Gain Analysis 105
4.6.3.1 Hybrid FSO/RF with MRC Scheme 105
4.6.3.2 Hybrid FSO/RF with Adaptive Combining Scheme . 106
4.6.4 beam width Optimization 109
4.7 Numerical Results and discussion 110
4.8 Chapter Summary 124

5 On the Capacity Analysis of Hybrid FSO/RF System with Adaptive Combining over Generalized Distributions **126**

5.1 Introduction 126

5.2 Organization of the Chapter 127
5.3 System and Channel Models 128
5.3.1 FSO Channel Statistics 128
5.3.2 RF Channel Model 129
5.3.3 SNR Statistics of Adaptive Combining Scheme 130
5.4 Ergodic Capacity Analysis 131
5.5 Asymptotic Ergodic Capacity Analysis 134
5.6 Numerical Results and Discussions 136
5.7 Chapter Summary 146

6 Performance Analysis of Optical Reflecting Surface-Assisted Optical Space Shift Keying-based MIMO-FSO system 148
6.1 Introduction 148
6.2 Organization of the Chapter 149
6.3 System and Channel Models 150
6.3.1 System Model 150
6.3.2 Channel Model 151
6.3.2.1 Pointing Errors Model 152
6.3.2.2 Atmospheric Turbulence Model 153
6.3.2.3 PDF of End-to-End FSO Channel 154
6.4 Performance Analysis 155
6.4.1 Average Bit Error Rate 155
6.4.2 Ergodic Capacity Analysis 158
6.4.3 High Average SNR Analysis and Diversity Gain 160
6.4.4 Convergence Test 161
6.5 Numerical and Simulation Results 162
6.6 Chapter Summary 171

7 Performance Analysis of Multiple Optical Reflecting Surfaces Assisted FSO Communication 174

7.1 Introduction 174
7.2 Organization of the Chapter 175
7.3 System and Channel Models 176
7.3.1 System Model 176
7.3.2 Channel Model 177
7.3.2.1 Atmospheric Turbulence Model 177
7.3.2.2 Pointing Errors Model 178
7.3.2.3 PDF of End-to-End FSO Channel 178
7.3.2.4 PDF of Imperfect Channel 179
7.3.3 SNR Statistics 180
7.3.3.1 With Perfect CSI 180
7.3.3.2 With Imperfect CSI 181
7.4 Performance Analysis 182
7.4.1 Outage Probability 182
7.4.1.1 Outage Probability for Perfect CSI 182
7.4.1.2 Outage Probability for Imperfect CSI 183
7.4.2 Average Symbol Error Rate 183
7.4.2.1 Average Symbol Error Rate for Perfect CSI 183
7.4.2.2 Average Symbol Error Rate for Imperfect CSI 185
7.5 Asymptotic Analysis and Diversity Gain 185
7.5.1 Asymptotic Outage Probability 186
7.5.1.1 Asymptotic Outage Probability for Perfect CSI . . . 186
7.5.1.2 Asymptotic Outage Probability for Imperfect CSI . . 186
7.5.2 Asymptotic Average SER 187
7.5.2.1 For Perfect CSI 187
7.5.2.2 For Imperfect CSI 188
7.6 Numerical and Simulation Results 188
7.7 Chapter Summary 196

8 Conclusions and Future Work **197**

8.1 Concluding Remarks 197

8.2 Future Research Scope 201

Appendices **205**

A Expressions for α and β **206**

B **209**

B.1 Convergence Test for $f_{\gamma_{RF}}(\gamma)$ 209

B.2 Convergence Test for $f_{\gamma_{MRC}}(\gamma)$ 210

C **212**

C.1 Proof of Theorem 6.1 212

C.2 Proof of Theorem 6.2 213

D Proof of Theorem 7.1 **215**

Bibliography **217**

List of Figures

2.1 Application of FSO in various scenarios 12

2.2 Block diagram of direct detection and heterodyne detection techniques 13

2.3 Impact of different atmospheric and weather conditions on the FSO link 14

2.4 System block for a mixed FSO/RF system 22

2.5 Hybrid FSO/RF system and its applications 26

2.6 Depiction of a RIS-assisted wireless communication system 32

3.1 Hybrid FSO/RF system model 40

3.2 Average SER versus switching threshold SNR γ_{th} and beam width w_0 60

3.3 Ergodic capacity versus switching threshold SNR γ_{th} and beam width w_0 61

3.4 Outage probability and average SER versus average SNR of FSO link for different distributions 62

3.5 Asymptotic and average SER performance plots for different values of switching threshold SNR and RF average SNR 63

3.6 Average SER performance of hybrid FSO/RF system for different modulation schemes 65

3.7 Performance comparison of hybrid FSO/RF and single-link FSO systems for both the detection schemes 66

3.8 Average SER performance of hybrid FSO/RF and FSO systems for different pointing error coefficient values 67

3.9 Average SER and probability of usage of FSO/RF link versus average SNR of FSO link for different turbulence conditions 69
3.10 Outage probability and average SER versus transmit power of FSO link for different weather conditions 71
3.11 Switching probability versus average SNR of FSO link under different weather conditions 72
3.12 Outage and average SER performance of hybrid FSO/RF system for different values of link distance and average SNR of RF link 73
3.13 Normalized ergodic capacity versus average SNR of FSO link for different distributions 74
3.14 Normalized ergodic capacity versus average SNR of FSO link for different detection techniques 75
3.15 Normalized ergodic capacity versus average SNR of FSO link for different pointing errors conditions 76
3.16 Ergodic capacity versus average SNR of FSO link for different turbulence conditions 77
3.17 Normalized ergodic capacity versus average SNR of FSO link for different values of $\overline{\gamma}_{RF}$ 78
3.18 Normalized ergodic capacity versus average SNR of FSO link for different values of link distance 78
3.19 Average SER versus average SNR of FSO link for different values of zenith angle and wind speed 80
3.20 Normalized ergodic capacity performance of FSO and hybrid FSO/RF systems for different zenith angle and wind speed values 82

4.1 System model based on the Adaptive combining scheme 89
4.2 Flowchart for computing average SER using Monte-Carlo simulations 111
4.3 Convergence test for CDF expressions in (4.22) and (4.26) 111
4.4 Average SER versus switching threshold SNR γ_T and beam width w_0 114
4.5 Average SER of adaptive combining for various distributions 115

4.6 Average SER comparison for different hybrid FSO/RF schemes . . . 116
4.7 Outage performance for strong and weak turbulence conditions 118
4.8 Asymptotic SER performance of MRC and adaptive combining schemes 119
4.9 Average SER of single-link FSO and MRC systems under varying link distance and pointing errors 121
4.10 Average SER of single-link FSO and adaptive combining for different weather conditions 122
4.11 Average SER for heavy fog and different background noise conditions 123

5.1 Normalized ergodic capacity versus switching threshold SNR γ_T and beamwidth w_0 138
5.2 Normalized ergodic capacity performance of the adaptive combining system with and without γ_T^{opt} under different $\overline{\gamma}_{RF}$ 140
5.3 Normalized ergodic capacity performance of the adaptive combining system for various distributions 140
5.4 Normalized ergodic capacity performance for different pointing errors and turbulence conditions 142
5.5 Normalized ergodic capacity performance under various weather conditions 143
5.6 Comparison of ergodic capacity (in Gbps) for different system models 145

6.1 The ORS-assisted OSSK-based MIMO-FSO system model 151
6.2 Convergence test for average BER and ergodic capacity expressions . 163
6.3 Average BER under different turbulence conditions 164
6.4 Average BER for different pointing errors 164
6.5 Average BER performance for different N_t and N_r 165
6.6 Average BER performance for different weather conditions 167
6.7 Performance comparison of different FSO systems 167
6.8 Capacity performance for different turbulence and pointing errors conditions 169

6.9 Capacity performance for different N_t 169
6.10 Capacity performance for different N_r 169
6.11 Capacity performance comparison of various MIMO systems 170

7.1 The selection-based multiple ORSs-assisted FSO system model 177
7.2 Outage probability under perfect CSI for different number of ORSs . 189
7.3 Average SER performance under perfect CSI for different number of ORSs 190
7.4 Average SER performance under perfect CSI for different modulation techniques 191
7.5 Average SER performance under perfect CSI for various turbulence conditions 191
7.6 Average SER for perfect CSI under clear air and foggy conditions . . 192
7.7 Outage probability under perfect CSI for different pointing errors conditions 193
7.8 Outage probability under imperfect CSI for various ORSs and different pointing errors 193
7.9 Average SER performance under imperfect CSI for different number of ORSs 194
7.10 Average SER performance under imperfect CSI for various correlation coefficients 195
7.11 Average SER performance under imperfect CSI for different detection techniques 195

8.1 Multiple ORSs-assisted FSO system model 201
8.2 RIS-assisted Mixed FSO/THz system 202

List of Tables

2.1 Literature summary on relay-assisted FSO system and mixed FSO/RF systems . . . 24
2.2 Literature summary on hybrid FSO/RF system models . . . 30
2.3 Literature summary on RIS-assisted RF and FSO system models . . . 34

3.1 Parameters involved in the PDF of Malaga distribution . . . 43
3.2 Parameters involved in the PDF of α-η-κ-μ distribution . . . 46
3.3 Simulation parameters of FSO and RF links . . . 57
3.4 Truncation Accuracy of Summation Limits . . . 58
3.5 List of FSO and RF distributions and their parameters . . . 61
3.6 List of channel models and parameters assumed to obtain Fig. 3.4 . . 63
3.7 List of channel models and parameters assumed to obtain Fig. 3.13 . 74
3.8 Simulation parameters for satellite communication scenario . . . 79

4.1 List of notations . . . 95
4.2 FSO/RF parameters used in the simulations . . . 112
4.3 Truncation accuracy of summation limits . . . 113
4.4 The optimum values of w_0 and γ_T . . . 115
4.5 List of channel models and parameters assumed to obtain Fig. 4.6 . . 116

5.1 List of notations . . . 131
5.2 Execution time for exact and asymptotic expressions . . . 136
5.3 Weather parameters used in the simulations . . . 137
5.4 Truncation accuracy of summation limits . . . 137

5.5 The optimum values of γ_T and w_0 139
5.6 Example of FSO and RF distributions which are derived as special cases of Malaga and κ–μ distributions 141
5.7 List of distribution models with their parameters values to plot Fig. 5.3 141

6.1 List of major parameters and notations 154
6.2 Truncation accuracy of summation limits for BER 163
6.3 Truncation accuracy of summation limits for capacity 164

7.1 List of notations 180
7.2 Truncation accuracy for the infinite summation in (7.27) 189
7.3 SNR gain comparison in Fig. 7.7 194

List of Abbreviations

5G	Fifth Generation
6G	Sixth Generation
AWGN	Additive White Gaussian Noise
AF	Amplify-and-Forward
BPSK	Binary Phase-Shift Keying
BER	Bit Error Rate
CSI	Channel State Information
CDF	Cumulative Distribution Function
DF	Decode-and-Forward
DH	Dual-Hop
FSO	Free space optics
Gbps	Gigabits per second
HD	Heterodyne Detection
IR	Infrared
IRS	Intelligent Reflecting Surface
IM/DD	Intensity Modulation/Direct Detection
LOS	Line-of-Sight
MPSK	M-ary Phase-Shift-Keying
MRC	Maximal-Ratio Combining
MIMO	Multiple-Input Multiple-Output
MISO	Multiple-Input Single-Output
ORS	Optical Reflecting Surface

OSM	Optical Spatial Modulation
OSSK	Optical Space Shift Keying
OWC	Optical Wireless Communication
PDF	Probability Density Function
RF	Radio frequency
RIS	Reconfigurable Intelligent Surface
SATCOM	Satellite Communication
SC	Selection combining
SNR	Signal-to-Noise Ratio
SIMO	Single-Input Multiple-Output
SM	Spatial Modulation
SSK	Space Shift Keying
SER	Symbol Error Rate

List of Symbols

$\mathbb{E}[\cdot]$	Expectation operator
$\mathrm{Ei}(\cdot)$	Exponential integral function
$\mathrm{erf}(\cdot)$	Error function, $\mathrm{erf}(z) = \frac{2}{\sqrt{\pi}} \int_0^z e^{-t^2} dt$
$\mathrm{erfc}(\cdot)$	Complementary error function, $\mathrm{erfc}(z) = 1 - \mathrm{erf}(z)$
$\exp(\cdot)$	Exponential function
$f_\gamma(\cdot)$	Probability Density Function of γ
$F_\gamma(\cdot)$	Cumulative Distribution Function of γ
$G\,{}_{p}^{m}\,{}_{q}^{n}(\cdot)$	Meijer G-function
$G\,{}^{0,n:m_1,n_1;m_2,n_2}_{p,q:p_1,q_1;p_2,q_2}\,[\,\cdot,\cdot]$	Extended generalized bivariate Meijer G-function
$H\,{}_{p}^{m}\,{}_{q}^{n}(\cdot)$	Fox's H function
$H\,{}^{0,n:m_1,n_1;m_2,n_2}_{p,q:p_1,q_1;p_2,q_2}\,[\cdot,\cdot]$	Bivariate Fox's H function
$H\,{}^{0,n:\,m_1,n_1;\,\cdots\,;\,m_r,n_r}_{p,q:\,p_1,q_1;\,\cdots\,;\,p_r,q_r}\,[\cdot,\cdots,\cdot]$	Multivariate Fox's H-function
$I_v(\cdot)$	Modified Bessel function of first kind of order v
$K_v(\cdot)$	Modified Bessel function of second kind of order v
$L_n(\cdot)$	Laguerre polynomial, $L_n(x) = \sum\limits_{r=0}^{n} \frac{(-1)^r}{r!}\binom{n}{r} x^r$
$\Pr(\cdot)$	Probability of an event
$\mathrm{Q}(\cdot)$	Gaussian Q-function, $\mathrm{Q}(x) = \frac{1}{\sqrt{2\pi}} \int_x^\infty e^{-t^2/2} dt$
$(x)_n$	Pochhammer symbol, $(x)_n = \Gamma(x+n)/\Gamma(x)$
$\binom{A}{B}$	Combination between A and B
$\Gamma(\cdot)$	Gamma function, $\Gamma(x) = \int_0^\infty t^{x-1} e^{-t} dt$
$\gamma(:,:)$	Lower incomplete gamma function, $\gamma(a,x) = \int_0^x t^{a-1} e^{-t} dt$

Chapter 1

Introduction

1.1 Background

Free space optics (FSO) communication technology has attracted the domain of wireless communications remarkably over the last few decades [1, 2, 3, 4]. The FSO communication refers to an optical wireless communication (OWC) technique to transmit data in the form of modulated light beams through atmosphere [5]. It is a wireless communication technology that utilizes laser beams to establish optical links between transmitter and receiver without the need for physical cables or optical fibers [6, 7]. Further, the FSO communication offers several advantages such as huge bandwidth, high data rates upto several gigabits per second (Gbps), high security due to narrow laser beam transmission, unlicensed spectrum (i.e. frequencies above 3 terahertz) and immunity to electromagnetic interference [8, 9, 10]. Due to these advantages, the FSO communication technology finds its application in terrestrial communications, wireless backhaul networks, satellite communications, underwater wireless communications, secure military communications, etc [11, 12, 13, 14].

As data-driven applications are growing and expanding day-by-day, the spectrum used for radio frequency (RF) technology is becoming scarce, congested, and expensive to acquire [15, 16]. In this context, the FSO technology has emerged as a promising alternative to the current RF-based wireless communication systems, as the FSO communication operates in near infrared (IR) region, which is an unlicensed spectrum. [17, 4].

Despite the aforementioned benefits, the FSO communication is susceptible to atmospheric turbulence, scintillation, pointing errors due to misalignment between transmitter and receivers apertures, and atmospheric attenuation or pathloss due to weather conditions like fog, snow, and haze [18, 19, 20, 21]. These channel distortions can severely affect the performance of the FSO communication and limits the FSO communication to shorter distances up to few kilometers. To overcome these limitations, various techniques and schemes are employed to improve the performance of FSO communication such as multiple-input multiple-output (MIMO) schemes, hybrid FSO/RF communication, intelligent reflecting surfaces, etc [22, 23, 24, 25, 26, 27].

MIMO plays a crucial role in mitigating the adverse atmospheric effects on FSO communication using various techniques, including receive diversity, transmit diversity, optical spatial modulation (OSM), etc [28, 29, 30, 31, 32, 33, 34]. These schemes aim to improve the link reliability and spectral efficiency of the FSO systems by combating the FSO channel impairments. Cooperative relaying technique is another way to achieve distributed spatial diversity to overcome the effects of FSO channel fading [35, 36]. In addition, relaying techniques are also useful to enhance the coverage area of FSO communication [37, 38]. To improve the reliability of the FSO system, a hybrid FSO/RF system integrates the FSO subsystem with a more reliable RF subsystem as a backup [25, 39]. The RF communication system uses electromagnetic waves to transmit data, which are less susceptible to atmospheric turbulence, fog, and pointing errors, but have limited bandwidth and suffer from interference due to other RF sources. On the other hand, the FSO communication system, which is more prone to atmospheric attenuation and weather conditions like fog, snow, etc., provides huge bandwidth and high data rates [40]. Since rain and fog rarely occur at the same time, the FSO and RF links can complement each other in bad weather conditions. By combining these two technologies, the hybrid FSO/RF systems can achieve high-speed data transmission with improved link reliability [41].

Recently, the use of reconfigurable intelligent surface (RIS) or intelligent reflecting surface (IRS) has gained popularity and is emerging as a promising technique to provide improved link reliability and enhanced coverage area [42, 43, 44, 45, 46]. IRS consists of planar surfaces, typically made of metallic or dielectric materials, with a large number of passive reflecting elements that can be controlled electronically to modify the propagation of radio waves [47]. By intelligently manipulating the reflection properties of these surfaces, IRS can enhance the signal quality and efficiency of wireless communications, especially in scenarios with limited coverage and capacity.

1.2 Motivations

The main motivations of the thesis are as follows:

- In the maximal-ratio combining (MRC)-based hybrid FSO/RF system models [48, 49], the RF link stays active irrespective of the channel conditions of FSO link, which will lead to wastage of RF power. Moreover, the data rate of FSO link should be reduced to the data rate of RF link for efficient diversity combining. These problems can be addressed using the hard-switching-based hybrid FSO/RF system model, where only one of the FSO or RF link will be active at a given time.

- No prior works on the performance analysis of the hybrid FSO/RF system for terrestrial and satellite (SATCOM) scenarios over generalized RF and FSO fading distributions, namely Malaga and α-η-κ-μ distributions, are available in the literature to the best of our knowledge.

- Adaptive combining scheme for hybrid FSO/RF system, which is a variant of the MRC scheme, can provide both switching and diversity combining benefits. In addition, conservation of RF link power is possible using this scheme, when the RF subsystem is in standby mode. Thus, the adaptive combining scheme circumvents all the drawbacks of the diversity combining schemes and the hard-switching scheme of the hybrid FSO/RF system. Specifically, the performance of hybrid FSO/RF systems based on MRC and adaptive combining schemes over the generalized Malaga and α-η-κ-μ fading distributions is unavailable in the literature.

- In the existing works on hybrid FSO/RF systems, the non-zero boresight pointing errors and background noise, which have a significant impact on the system performance, have not been included in the modeling of FSO system. In addition, the effect of erroneous feedback link on the system performance has not been considered.

- In FSO communication, there are different obstacles in the line-of-sight (LOS) path, which are unsuitable for transmitting optical signals. In such situations, the use of optical RIS can provide an alternate path for data transmission [50, 51, 52]. In addition, an optical space shift keying (OSSK) is a low complexity spatial modulation scheme proposed for the MIMO-FSO system to achieve high spectral efficiency, where the index of the transmitting aperture is used to transfer the data.

- OSSK-based FSO system is also prone to the shortcomings of the FSO systems [53, 54, 55]. In the existing works on optical RIS [50, 51, 52], a single RIS or cascaded multiple RISs were considered for the FSO systems with a single transmitting and receiving apertures without any diversity combining techniques.

- To overcome the limitations of the FSO-based systems, an optical reflecting surface (ORS)-assisted OSSK-based FSO system is proposed in our current work. An ORS is a special case of optical IRS, when it operates as a perfect mirror. Further, the performance of the ORS-assisted OSSK-based FSO system has not been analyzed in the literature to the best of our knowledge.

- To improve the FSO system performance assisted by a single ORS in a backhaul network scenario, it is mandatory to consider multiple ORSs between source and destination. However, none of the works are available in the literature to the best of our knowledge on the modelling and performance analysis of multiple ORSs-assisted FSO system.

- Since the wireless channel varies rapidly due to fading and atmospheric attenuation, it is nearly impossible to acquire the perfect channel state information (CSI) at the receiver without errors [56, 57]. Therefore, it is crucial to study the impact of imperfect CSI errors on the performance of the multiple ORSs-assisted FSO system.

- The exact closed-form expressions for average symbol error rate (SER) and ergodic capacity involve complicated Meijer G-function, bivariate Fox's H-function, and multivariate Fox's H-function, which are not easily tractable. The asymptotic expressions are relatively simpler and useful to give more insights into the system behaviour and vital parameters such as diversity gain and signal-to-noise ratio (SNR) gain of the system can be obtained from the asymptotic expressions. Hence, asymptotic analysis needs to be carried out for the above-mentioned system models.

1.3 Contributions

The major contributions of this thesis are as follows:

- The exact closed-form expressions for outage probability, average SER, and ergodic capacity are obtained for hard-switching-based hybrid FSO/RF system over generalized distributions (i.e. Malaga and α-η-κ-μ distributions). The performance of the hybrid FSO/RF system over different combinations of FSO and RF channel models has been obtained as special cases without carrying out the analysis separately for terrestrial and SATCOM scenarios.

- The expressions for the probability density function (PDF) and cumulative distribution function (CDF) of MRC of the FSO and RF links are derived in closed-form, where the FSO link follows the Malaga distribution with the non-zero boresight pointing errors and the RF link is modeled using the α-η-κ-μ distribution. Using the obtained statistical functions (i.e. PDF and CDF), the closed-form expressions for outage probability and average SER of MRC and adaptive-combining-based hybrid FSO/RF systems are obtained.

- Simpler asymptotic expressions for outage probability, average SER, and ergodic capacity are derived for hard-switching-based, MRC-based, and adaptive-combining-based hybrid FSO/RF systems. In addition, the diversity gains of the above-mentioned hybrid systems are obtained for different scenarios.

- The optimum switching threshold SNR value γ_{th}^{opt} and optimum beam waist value w_0^{opt} are determined, which are required for the optimal performance of the hard-switching-based and adaptive-combining-based hybrid FSO/RF systems.

- Performance comparison of the single-link FSO, hard-switching, MRC, and adaptive-combining-based hybrid FSO/RF systems has been carried out. Furthermore, the SNR gains of hard-switching, MRC and adaptive combining schemes have been reported over the single-link FSO system under various scenarios.

- All the derived expressions for hard-switching, MRC, and adaptive-combining-based hybrid FSO/RF systems are unified under intensity modulation/direct detection (IM/DD) and heterodyne detection (HD) techniques and are verified using Monte-Carlo simulations.

- The closed-form expressions are derived for the PDF of cascaded FSO channel with ORS and the PDF of absolute difference between two cascaded FSO channels. The FSO channel turbulence from source to ORS and from ORS to destination is modeled using the generalized Malaga distribution, including pointing errors. With the aid of the above-obtained expressions, the PDF and MGF of the instantaneous SNR are derived for the proposed ORS-assisted OSSK-based MIMO-FSO system.

- Further, from the derived channel statistics, a tight upper bound on the average BER and a lower bound on the ergodic capacity are determined and useful insights from the derived analytical expressions are provided. In addition, the diversity gain of the ORS-assisted OSSK-based MIMO-FSO system is also determined from the asymptotic BER expressions.

- The performance of the proposed ORS-assisted OSSK-based MIMO-FSO system is compared with the various existing conventional FSO systems such as single-link FSO system, OSSK-based MIMO-FSO system without ORS, and OSSK-based dual-hop (DH) decode-and-forward (DF) relaying system and detailed insights on the performance comparison are included in the numerical results.

- A multiple ORSs-aided FSO system considering a selection scheme to select the best ORS is proposed. Specifically, the exact expression for PDF of the cascaded FSO channel by including turbulence, pointing errors, and atmospheric attenuation is derived for perfect and imperfect CSI cases.

- The closed-form expression for the end-to-end PDF of the maximum instantaneous SNR among multiple ORSs-aided FSO links is derived over Gamma-Gamma turbulence distribution with pointing errors. Using the above PDF expression, the unified PDF and CDF statistics of overall instantaneous SNR are obtained

- Furthermore, the closed-form expressions for the outage probability and average SER of multiple ORSs-aided FSO system are determined. Simpler asymptotic expressions, which give more useful insights into the multiple ORSs system, are also obtained along with performing diversity gain analysis.

- Finally, the convergence tests are performed on the infinite series of various expressions that are used to evaluate outage, average SER, and ergodic capacity. The tests confirmed that all the derived expressions are absolutely convergent.

1.4 Thesis Organization

The subsequent chapters of this thesis are structured as follows: Chapter 2 comprises a comprehensive exploration of the state-of-the-art in FSO communication and its applications. It delves into various techniques aimed at improving the FSO communication system, such as relay-assisted transmission, spatial diversity, hybrid FSO/RF systems, and IRS. Chapter 3 introduces the hybrid FSO/RF system based on hard-switching scheme. It presents analyses of exact and asymptotic outage probability, average SER, and ergodic capacity. Chapter 4 extends the analysis of the hybrid FSO/RF system to MRC and adaptive combining schemes. This chapter provides exact and asymptotic outage probability and average SER analyses. Further, the ergodic capacity analysis of the adaptive-combining system is presented in Chapter 5. In Chapter 6, the performance of the ORS-assisted OSSK-based MIMO-FSO system is examined in terms of bounds on average BER and ergodic capacity. Chapter 7 focuses on the performance evaluation, i.e. outage probability and average SER, of multiple ORSs-assisted FSO system under perfect and imperfect CSI cases. Lastly, Chapter 8 concludes the thesis by summarizing the findings and exploring potential future directions for further research.

1.5 Chapter Summary

In this chapter, the advantages and limitations of FSO technology were explored and compared it with RF wireless communication systems demonstrating the potential of FSO as a revolutionary next-generation wireless communication solution. The current and future applications of FSO technology were highlighted, including wireless backhaul for cellular networks, disaster recovery communication, and SAT-

COM. Additionally, various techniques aimed at enhancing the performance of FSO communication were discussed. Further, the motivations behind the thesis were explained and the major contributions of the thesis were highlighted. Finally, the organization of the thesis is outlined.

Chapter 2

Literature Review

The 5^{th} generation (5G) wireless networks have now been deployed in most countries and will be expected to reach all over the world by 2023. Exponentially increasing wireless multimedia devices during the last decade require a high volume of data, ultra-high bandwidth, and high data rate connectivity. Within this context, now the researchers are interested in the development of 6^{th} generation (6G) and beyond wireless technologies, which offer ultra-high bandwidth, extremely high data rates, low latency, substantial throughput, and ultra-reliable links [58, 59, 60, 61, 62]. However, it is indeed a great challenge to fulfil the very high data rate requirement of 6G and beyond wireless communication systems. Moreover, the RF wireless communication is currently facing sparse spectrum resources and the demand for RF spectrum is also increasing with the growing popularity of new wireless devices and new applications such as smart city, high-speed backhaul networks, etc [63]. Thus, the time has come to consider other possible options for 6G and beyond wireless systems, which can cater the needs of data heavy wireless devices.

FSO is an emerging technology which fulfils the ever-growing demands of ultra-high data rate and massive bandwidth requirements [11, 64, 65]. FSO refers to unguided transmission in free space using optical carriers and it utilizes the unlicensed near IR band, which operates at frequencies above 300 GHz [66]. It offers a huge amount of optical bandwidth, allowing the data rates upto 10 Gbps

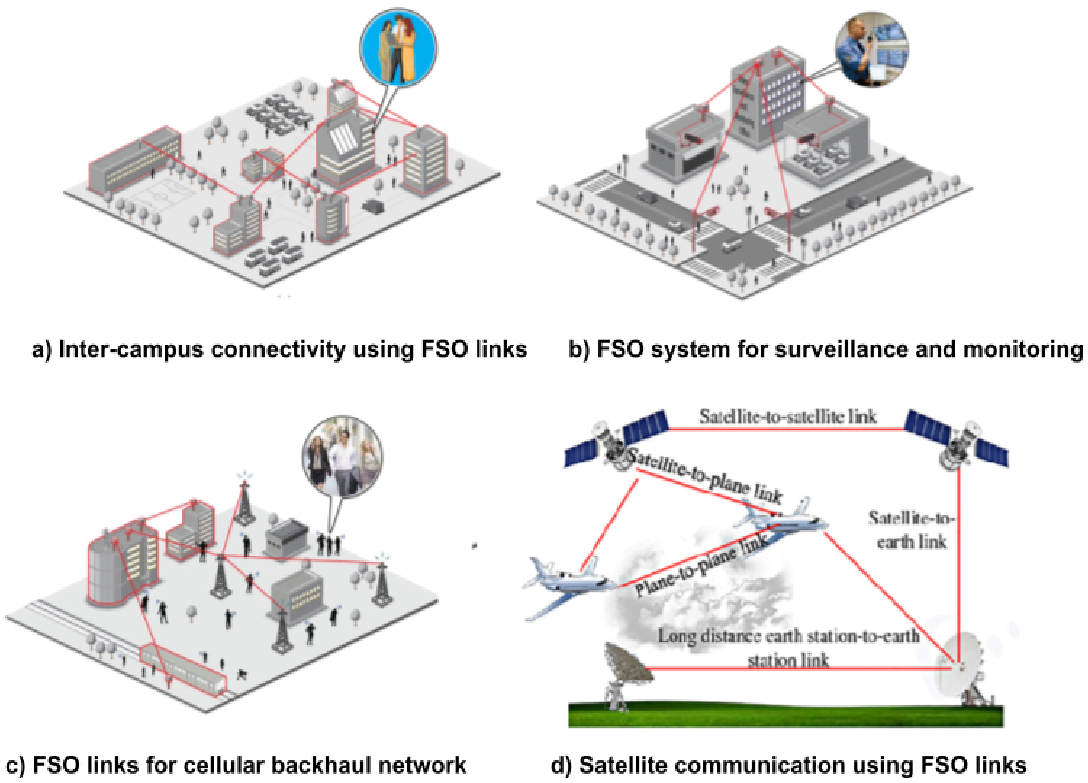

Fig. 2.1: Application of FSO in various scenarios

[67, 68, 69]. The significant advantages of the FSO communication include the low latency, high security, ease of deployment without optical fibre installation, etc. The FSO links can be employed for a variety of applications such as enterprise/campus area connectivity, extending metropolitan area network, wireless video surveillance, live video broadcasting, backhaul connectivity for wireless cellular networks, disaster recovery communication, and military communication as illustrated in Fig. 2.1 [14, 70, 71, 72]. The FSO communication can also be employed in satellite communication (SATCOM) systems for performance improvement in terms of data rate [73, 74, 75]. The uplink performance of a SATCOM system assuming FSO link between ground-station and satellite was investigated in [76].

The key components of a FSO communication system includes the transmitter, receiver, and modulator. In general, the sub-carrier intensity modulation (SIM) scheme is used to modulate the FSO signals [11]. In SIM, the RF sub-carrier signal undergoes pre-modulation using the information signal. The RF sub-carrier can be modulated using different modulation techniques such as binary phase-shift key-

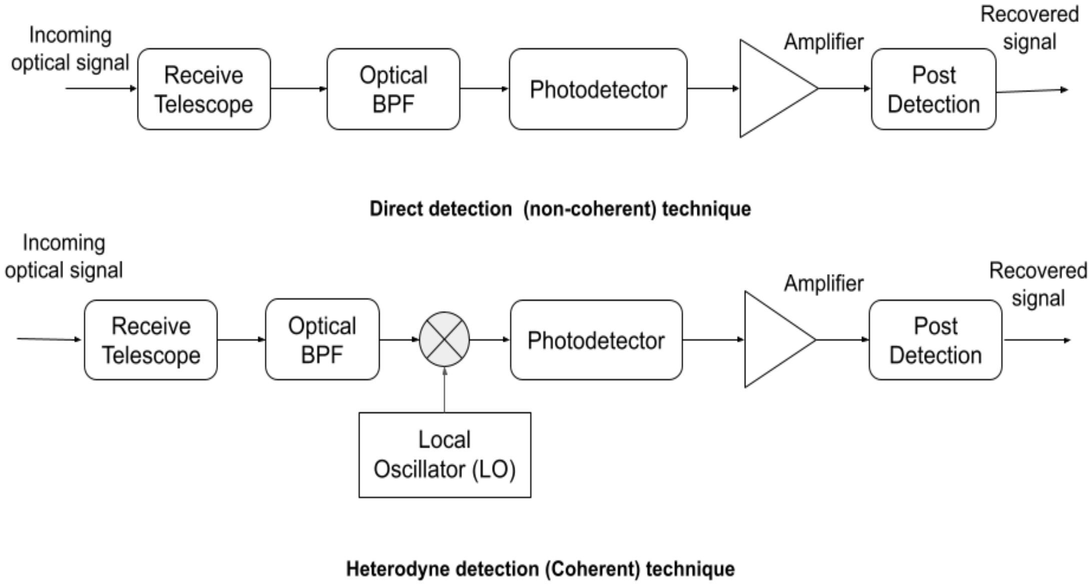

Fig. 2.2: Block diagram of direct detection and heterodyne detection techniques

ing (BPSK), frequency modulation (FM), amplitude modulation (AM), quadrature phase-shift keying (QPSK), quadrature amplitude modulation (QAM), and others [77, 78, 79]. Further, the intensity of the optical carrier is modulated by this pre-modulated signal. For the demodulation of these optical signals, two types of detection techniques can be used at the receiver, i.e. direct detection and heterodyne detection [80].

Heterodyne detection is a type of coherent detection technique [81, 82], which requires a local oscillator (LO) at the receiver. The incoming optical signal is mixed with a coherent carrier signal, which is generated from the LO, then it is converted into the electrical signal as shown in Fig. 2.2. Due to this spatial mixing, the weak incoming signal is amplified and the coherent receiver is sensitive to the signal. This will improve the performance of the coherent detection technique. The direct detection is a non-coherent technique [83] in which the received optical signals are passed through a bandpass filter to limit the background noise. The optical signals are then directed onto a photo-detector to produce an output electrical signal as illustrated in Fig. 2.2. This electrical signal is proportional to the instantaneous intensity of the received optical signal. After that the low-pass filter is used to receive the information signal effectively.

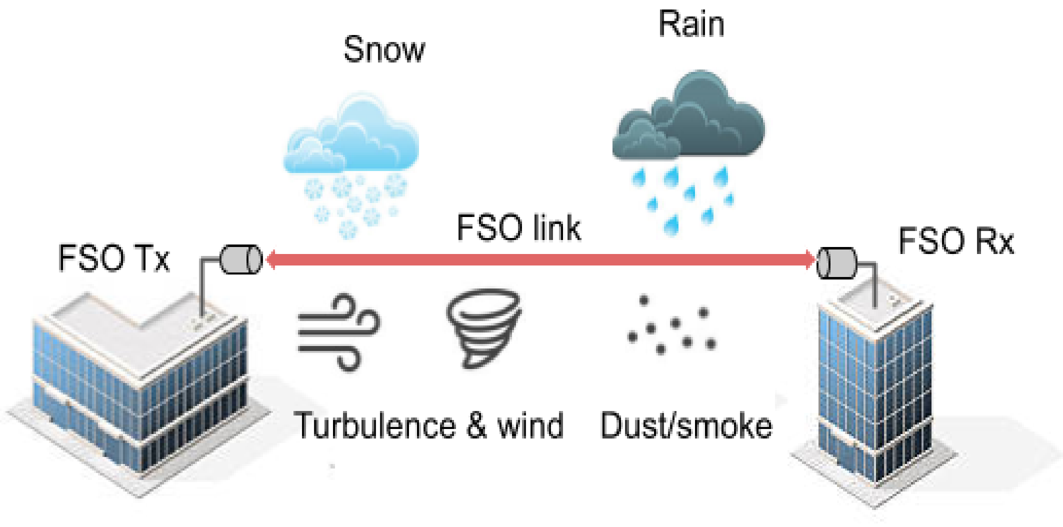

Fig. 2.3: Impact of different atmospheric and weather conditions on the FSO link

2.1 FSO Channel Modeling

Despite of many advantages offered by FSO communication, there are certain limitations which affect the performance and reliability of FSO communication systems. During transmission, the FSO link encounters various losses such as atmospheric turbulence-induced fading, pointing errors due to beam divergence, and atmospheric attenuation. The weather conditions such as fog, snow, and smog also affect the FSO link performance and restrict FSO communication to shorter distances upto few kilometres (km) as shown in Fig. 2.3.

2.1.1 Atmospheric turbulence

The primary source of turbulence in FSO communication is the earth's atmosphere. Due to the variations in the temperature, pressure, and wind movement, the refractive index of the air changes, causing the light beams to scatter [84, 85]. This phenomenon of rapid and random intensity fluctuations of the received light signal is known as atmospheric turbulence or scintillation [86, 87]. It leads to fluctuations in the intensity, phase, and angle of the light, resulting in signal degradation. As the laser beam propagates through the atmosphere, it encounters varying refractive indices. These irregularities can cause the light to undergo interference, leading to scintillation effects. Scintillation can cause signal fading, degradation in the received SNR, and errors in the received data [88]. Atmospheric turbulence can also cause the transmitted laser beam to wander or deviate from its intended path. Beam wander can result in misalignment between the transmitting and receiving terminals, leading to signal loss or degradation in signal quality [86].

Atmospheric turbulence can be characterized by the index of refraction structure parameter C_n^2, which represents the turbulence strength [88]. The index C_n^2 is dependent on both altitude and link distance and the typical values of C_n^2 can vary from 10^{-17} to 10^{-13} [89]. Furthermore, the magnitude of intensity fluctuations caused by atmospheric turbulence can be quantified using the scintillation index and it is expressed as $\sigma_I = E[I^2]/E[I]^2 - 1$ [90], where $E[I^2]/E[I]^2$ is the ratio of the standard deviation of intensity fluctuations to the average intensity. The scintillation index provides a measure of the severity of turbulence, with higher values indicating stronger turbulence and increased signal variability.

To study the complete statistical characteristics of the turbulence of FSO channel, various statistical channel models were proposed in the literature. The most widely accepted distribution model for characterizing the weak turbulence is log-normal distribution [88, 90]. However, the log-normal distribution is not suitable for modeling the moderate-to-strong turbulence of the FSO channel [87, 91]. In the literature, the Gamma-Gamma distribution is extensively used to model the moderate-to-strong turbulence due to its excellent fit with experimental data [91, 92, 93, 94]. Furthermore, several other distributions are available such as exponential distribution, K-distribution, Weibull, I-K distribution, etc., to model the turbulence. Recently, the generalized Malaga distribution was proposed to characterize the atmospheric turbulence-induced fading of the FSO link [95]. The physical model of the Malaga distribution consists of three parts: 1) the line-of-sight (LOS) component, 2) coupled-to-LOS component, which is scattered due to propagation axis eddies, and 3) statistically independent component that is scattered due to off-axis eddies. Further, the generalized Malaga distribution incorporates the known distributions like Gamma-Gamma, log-normal, K-distribution, etc., as special cases [57], [95], [96].

2.1.2 Pointing errors

Pointing errors occur due to misalignment between the transmitting and receiving terminals of the FSO system. These errors can occur due to various factors and can significantly impact the performance of the communication link. Mechanical vibrations caused by environmental factors and building sway can introduce pointing errors in FSO systems [94, 97, 98]. The vibrations can cause the slight movement in the aperture of the transmitter or receiver, leading to misalignment. Thermal effects is also one of the causes for pointing errors in FSO communication. Temperature changes can induce thermal expansion or contraction in the FSO system components, affecting the alignment between the transmitter and receiver apertures [18, 82]. Additionally, atmospheric conditions such as strong winds or turbulence can introduce pointing errors in FSO systems. The movement of the air can affect the direction of the transmitted laser beam, causing misalignment at the receiving terminal [21, 98].

Several recent works have explored the statistical modeling of pointing errors and their effects on the system performance [21, 94, 99, 100]. Assuming that the statistical properties of pointing errors follow independent Gaussian distributions in both the horizontal and vertical directions, the radial displacement due to pointing errors is modeled using a Rayleigh distribution [94, 100]. Moreover, in [94, 100], the performance of the single-link FSO system was investigated by considering the effects of turbulence, pointing errors, and attenuation in the FSO channel model. The turbulence-induced fading was modeled using Gamma-Gamma distribution and Malaga distribution in [94] and [100], respectively.

2.1.3 Atmospheric attenuation

Atmospheric attenuation, also known as path loss, occurs in FSO communication due to the absorption and scattering of light by the atmosphere and it leads to degradation in the signal strength [9]. The atmosphere contains various aerosols, dust particles, and water vapour, which can scatter and absorb light [9, 101, 102]. Scattering occurs when light interacts with small particles or molecules in the atmosphere such as dust, smoke, fog, rain, snow, etc., causing the light beam to spread out and reducing the power density at the receiver [103, 104]. Absorption, on the other hand, leads to loss of energy in the signal. Both scattering and absorption contribute to signal attenuation and decrease the effective range of FSO communication [105, 106]. In case of rain, the particle sizes are significantly larger than the wavelength of the optical signal, resulting in relatively minimal impact on FSO transmission [101, 104]. When the diameter of the particles is comparable to the wavelength, the scattering coefficient increases significantly. Hence, fog and haze are considered as the most detrimental environmental conditions for FSO transmission [9, 103].

Mathematically, the atmospheric attenuation or path loss encountered by the FSO link is defined using Beers-Lambert law as

$$I_l = \exp\left(-L\omega_l\right),$$

where ω_l (in dB/km) denotes the attenuation coefficient [73, eq. (8.70)] and L (in km) is total distance of the propagation path.

2.1.4 Channel Estimation Errors

In wireless communication systems, channel estimation is the process of estimating the characteristic of the channel, such as its gain, phase, frequency response, or impulse response. These estimations are essential for reliable signal detection and decoding. However, due to various factors like interference, multipath propagation, channel fading, time-varying channels, etc., the estimated channel characteristics may deviate from the actual channel, leading to channel estimation errors [107, 108, 109].

Due to channel estimation errors, it is often challenging to acquire a complete channel state information (CSI) in practice. Since the wireless channel varies rapidly due to fading and atmospheric attenuation, it is nearly impossible to acquire the perfect CSI at the receiver without any error [56, 110]. Therefore, it is crucial to study the impact of channel estimation errors on the performance of the system. In [108] and [57], the performance of the FSO communication was investigated over imprecise channel by assuming turbulence model as Gamma-Gamma and Malaga distributions, respectively. In [109], performance analysis of the FSO system was carried out by including the impact of turbulence, pointing error and imperfect CSI over the Fisher-Snedecor ($\mathcal{F}$) turbulence channel model. Further, the authors in [111] investigated the FSO system empowered by a single IRS assuming imperfect CSI over the $\mathcal{F}$-distribution model. In [56, 110], the effect of imperfect CSI on the performance of the mixed FSO/RF system was analyzed.

2.2 Techniques to Improve FSO performance

To mitigate the effects of turbulence, pointing errors, and pathloss due to atmospheric attenuation in FSO channel, several enhancement techniques are employed, including multiple-input multiple-output (MIMO), cooperative relaying, hybrid FSO/RF communication, intelligent reflecting surfaces (IRS), etc. The above-mentioned techniques aim to compensate for signal fluctuations and improve the overall performance of the FSO systems in the presence of channel impairments.

2.2.1 MIMO Schemes

In literature, various MIMO schemes, which offer spatial diversity, were proposed to mitigate the aforementioned drawbacks of the FSO communication. In spatial diversity techniques, multiple apertures at the transmitter [28, 112] or receiver [29, 113] or combination of both [114, 115, 116] can be employed to obtain the diversity benefit. Authors in [117] exploited the multiple-input single-output (MISO) for the FSO system by utilizing a transmit laser selection scheme to extract the full diversity and obtained better performance. In [22], the asymptotic bit error rate (BER) was derived for a single-input multiple-output (SIMO) system with MRC scheme at the destination and the SIMO system was compared with the single-link FSO system over Malaga distribution. In [31], MIMO techniques were studied to enhance the performance of the FSO system under the effects of both turbulence and pointing errors over Gamma-Gamma fading distribution. Furthermore, in [23], the performance of a MIMO-FSO system was presented in which Alamouti space-time block-coding was employed at the transmitter and switch-and-examine combining scheme was employed at the receiver. Additionally, in [23], the atmospheric turbulence of the FSO link was modeled using Malaga distribution without considering the effect of pointing errors.

The severity of turbulence-induced fading can also be mitigated using a larger aperture at the receiver, which averages the intensity fluctuations, and this technique is known as aperture averaging [118, 119]. In [120], the effect of aperture averaging on the turbulence fluctuations was studied over Gamma-Gamma and lognormal distributions under different turbulence conditions. In [121], the aperture averaging technique was proposed for terrestrial as well as SATCOM scenarios to counteract the shortcomings of FSO communication. Furthermore, the performance of FSO communication was analyzed over Gamma-Gamma turbulence-induced fading with beam-wander-induced pointing errors.

Additionally, various diversity combining schemes can be utilized at the receiver for multiple beams. These include selection combining (SC), maximal-ratio combining (MRC), switch-and-stay combining (SSC), etc., to achieve maximum system diversity. In a SC scheme [122, 123], the receiver compare the signals from the multiple antennas and the signal with the highest instantaneous SNR will be selected. By utilizing the SC scheme, the impact of fading can be reduced and the overall performance of the system is improved. In [124, 125], authors employed the MRC technique to improve the performance of the FSO system, in which the receiver combined the signals from the multiple antennas in such a way that the output SNR of the overall system is maximized. Unlike the SC scheme, which selects only one signal with the highest SNR, MRC combines all the received signals based on their instantaneous SNRs. In [126], FSO system with multiple photodetectors was proposed and in [23], $2 \times L$ MIMO FSO system model was considered. Further, switch-and-examine combining (SEC) and MRC techniques were used for performance improvement of the FSO system in [126] and [23], respectively. FSO-based SSC system with a single transmit aperture and two receive apertures for improving the reliability of a single-link FSO system was presented in [127]. In case of the SSC scheme, if the instantaneous SNR of the first operating FSO link drops below a particular threshold value, then the data is transmitted through the secondary backup FSO link irrespective of its instantaneous SNR.

A low complexity modulation scheme known as optical spatial modulation (OSM) was proposed for the MIMO-FSO system to achieve the higher data rates and high spectral efficiency [33]. Note that spatial modulation is an index modulation scheme in which the data information is transmitted in both antenna and signal spaces [34, 128, 129]. Further, a special case of OSM is termed as optical space shift keying (OSSK), where only one transmitting aperture is active at a given time instant and the data is decoded as the index of the activated transmitting aperture [53, 54]. In [55], the authors evaluated the performance of an FSO system based on the OSSK scheme over Gamma-Gamma distribution. However, in [55], the effect of pointing errors was neglected in the modeling of FSO channel. Moreover, in [130], the performance of a MISO-OSSK system was studied under jamming signals. The authors in [131] have analyzed the ergodic capacity of an OSSK-based FSO system by assuming Gamma-Gamma and negative-exponential distributions. Further, in [132], a mathematical framework was developed for the MIMO-OSSK-based FSO system in which average BER and ergodic capacity (EC) performances were investigated over non-generalized negative-exponential, log-normal, and Gamma-Gamma distributions.

2.2.2 Relaying techniques

Relay-assisted FSO system and cooperative diversity schemes were also proposed to enhance the coverage and to mitigate the limitations of the FSO communication [37, 133, 134, 135]. In [37], the performance of a dual-hop (DH) FSO system was investigated in which source communicates with destination with a relay placed in between. Further, a decode-and-forward (DF) relaying based DH FSO system was analyzed in [133] over Gamma-gamma turbulence. In [134, 135], performance of the multi-hop FSO system was analyzed, where the multiple relays were used to improve the reliability and coverage of the FSO communication system. Furthermore, cooperative diversity is an alternative approach to realize the spatial diversity gain [136]. In cooperative diversity technique [137, 138], the information signal sent from source to destination is also intercepted by other nodes, such as relays. By collectively processing and transmitting their information, the source and relays create a virtual antenna array despite having only one antenna each.

In prior works [139], [140], the relay-assisted mixed FSO/RF system was proposed to improve the performance and to extend the coverage area of FSO communication. In case of a mixed FSO/RF system, usually the message signal from source-to-relay node will be transmitted over the RF link and the decoded or amplified message signal from relay-to-destination node will be transmitted over the FSO link, which can be employed as a last-mile access as illustrated in Fig. 2.4. Further,

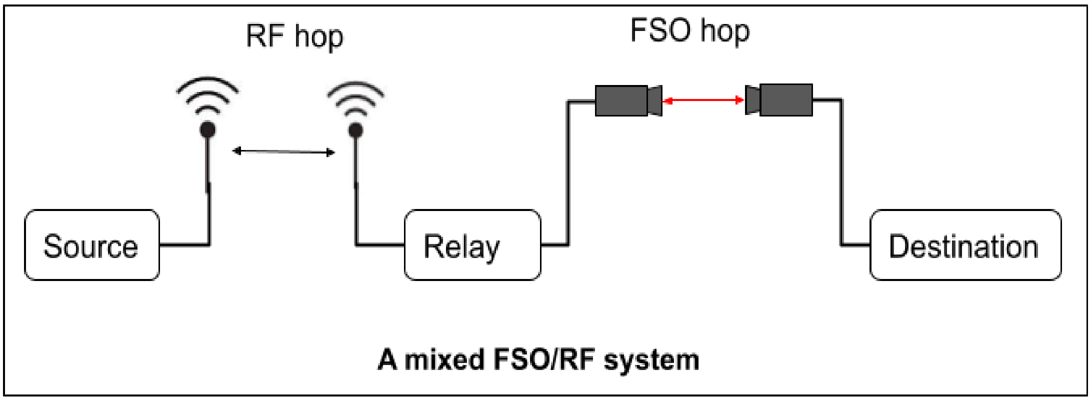

Fig. 2.4: System block for a mixed FSO/RF system

the message will be decoded or amplified at the relay node depending upon the relaying protocols, i.e. DF or amplify-and-forward (AF). The performance analysis of a DF-relaying-based mixed FSO/RF system was carried out in [139] assuming Malaga and Nakagami-m distributions. In [140], the performance of an AF-relaying-based mixed FSO/RF system was investigated in which FSO and millimeter wave RF were deployed for backhauling the cellular network. The performance analysis was carried out over Malaga distribution in case of FSO communication and Rician distribution in case of millimeter wave RF communication.

Relay-assisted mixed FSO/RF systems having the virtue of cooperative diversity were also investigated in [141], [142], [139], [143], and [144] using AF and DF relaying techniques. In [141]-[142], the relay-to-destination FSO link was modeled using Gamma-Gamma turbulence-induced fading distribution and the source-to-relay RF link was characterized by Nakagami-m distribution. Further, in [144], the performance metrics like outage probability (OP), average bit error probability (BEP), and ergodic capacity were studied for a mixed FSO/RF system, where the FSO link was modeled using double generalized Gamma (DGG) distribution with generalized non-zero boresight pointing errors and the RF link was characterized using extended generalized-K (EGK) shadowed fading model. But in [143], a mixed FSO/RF system was studied, where the FSO link was utilized in the first hop followed by RF link in the other hop. Further, AF relaying technique was assumed to amplify the signal at the relay node and the signals were combined using SC technique at the receiver.

The relays in the form of aerial platforms such as unmanned aerial vehicle (UAV), high-altitude platform station (HAPS), low-altitude platform station (LAPS), etc. can also be placed between satellite and ground-station for enhancing the performance of FSO-based SATCOM [145]. A HAPS-based cooperative relay system was analyzed in [146] with satellite-to-HAPS and HAPS-to-terrestrial FSO links were modeled using Gamma-Gamma distribution.

In summary, Table 2.1 presents an overview of the research works conducted on the relay-assisted FSO and mixed FSO/RF systems, including the channel modeling and performance metrics.

Table 2.1: Literature summary on relay-assisted FSO system and mixed FSO/RF systems

Ref.	**System type**	**Relaying technique**	**FSO channel, RF channel**	**Performance metrics**
[37]	DH FSO	AF relay	Gamma-Gamma	OP, BER, EC
[133]	DH FSO	DF relay	Gamma-Gamma	BER
[134]	Multi-hop FSO	AF relay	Gamma-Gamma	BER, EC
[135]	Multi-relay-assisted FSO	DF and AF relay	Lognormal	OP
[138]	Cooperative DH FSO	AF relay	Lognormal	BEP
[137]	Cooperative DH FSO	DF relay	Lognormal	BEP
[139]	Mixed FSO/RF	DH with DF relay	Malaga, Nakagami-m	OP, BER, EC
[140]	Mixed FSO/RF	DH with AF relay	Malaga, Rician	OP, BER, EC
[141]	Mixed FSO/RF	DH with AF relay	Gamma-Gamma, Nakagami-m	OP, BER, EC
[142]	Mixed FSO/RF	DH with DF relay	Gamma-Gamma, Nakagami-m	OP, BER, EC
[143]	Mixed FSO/RF	DH with AF relay	DGG, Nakagami-m	OP, BER
[144]	Mixed FSO/RF	DH with AF and DF relay	DGG, EGK shadowed fading	OP, BEP, EC

2.2.3 Hybrid FSO/RF system

To enhance the reliability and to mitigate the losses, one can backup the FSO link with a more reliable RF link, which is less susceptible to atmospheric turbulence, pointing errors, and weather conditions like fog, haze, and smog. However, the RF link is sensitive to small scale fading and rain [147]. Meanwhile, the FSO link is not much affected by small-scale fading and rain. Thus, the FSO and RF links in parallel will complement each other in all channel conditions to improve the overall performance of both FSO and RF communications. In this context, the hybrid FSO/RF communication is considered as a promising candidate for 5G and beyond wireless communication systems, especially for wireless backhaul connectivity [70]. The hybrid FSO/RF communication can also be employed as backhaul links in applications such as ship connectivity, cellular network, space communication, and remote connectivity as shown in Fig. 2.5.

In a typical hybrid FSO/RF system, the data will be transmitted using FSO or RF link or both and the same depends on the type of switching scheme used, e.g. soft-switching, hard-switching, MRC, and adaptive-combining. The RF link is mainly used as a backup for the FSO link to improve the system performance. In [25], [39], a hard-switching scheme for a hybrid FSO/RF system was proposed and analyzed. In the proposed single-threshold-based hard-switching scheme, when the quality of FSO link is unacceptable, the hybrid system will switch to the RF link and the FSO subsystem will be entering into a standby mode. Moreover, this switching scheme involves frequent hardware switching with sub-optimal performance. In [25], the performance of the hybrid FSO/RF system with hard switching scheme was investigated in which only one link will be active depending upon the quality of the FSO link. The atmospheric turbulence of FSO channel was characterized using a log-normal distribution, which can model only weak turbulence condition and the RF fading channel was modeled using Nakagami-m distribution. Furthermore, in [148], a hard-switching-based MIMO hybrid FSO/RF system was proposed, where both

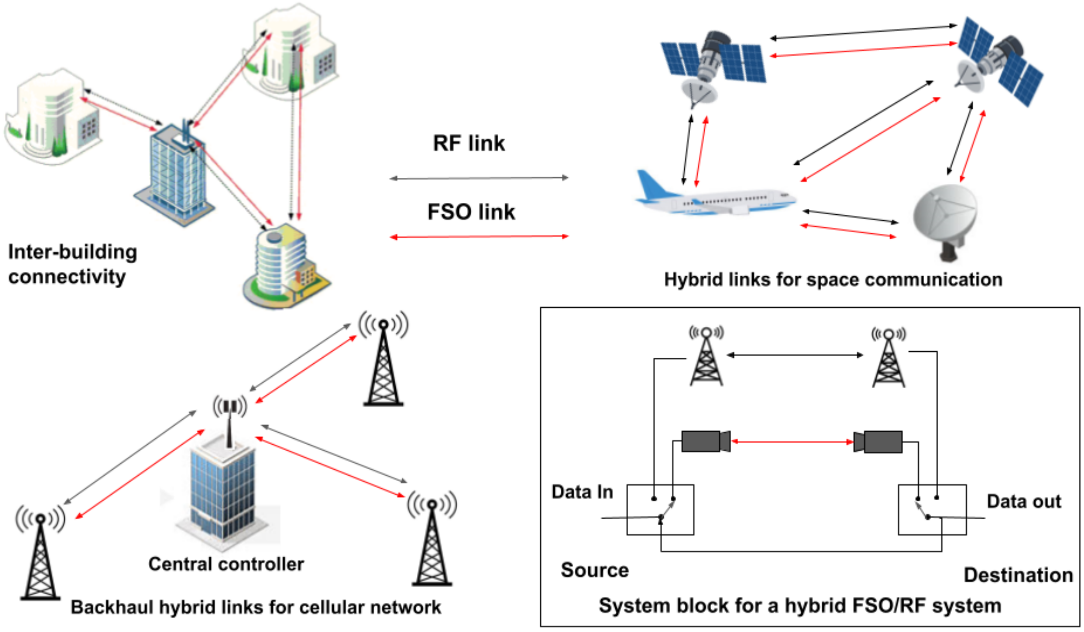

Fig. 2.5: Hybrid FSO/RF system and its applications

FSO and RF subsystems comprise multiple transmit and receive apertures/antennas. Here, the FSO link experiences Malaga fading and the RF link was characterized by κ-μ shadowed fading distribution. In [149], the authors evaluated the performance of a hybrid FSO/RF system using a real experiment test setup considering both FSO and RF links under the effects of atmospheric turbulence and high temperature.

A novel soft switching scheme using a bit-interleaved coding for hybrid FSO/RF system was proposed in [41] and the results were presented under various weather and turbulence conditions. It is to be noted that the atmospheric turbulence-induced fading of the FSO channel in [41] was characterized using Gamma-Gamma distribution, which can model moderate to strong turbulence conditions. In [150], a soft-switching scheme based on Raptor codes was proposed for a hybrid FSO/RF system and the practicality of such scheme was demonstrated by implementing Raptor encoder and decoder in a field programmable gate arrays (FPGAs).

The diversity combining schemes were discussed for the hybrid FSO/RF system in [151], [152], [48], and [49]. In addition, both FSO and RF links were combined at the receiver using various diversity combining techniques such as SC and MRC [153], [154]. In [151], the outage and BER performance of a hybrid FSO/RF system with SC scheme was analyzed over Gamma-Gamma (FSO), Malaga and Nakagami-

m (RF) fading channels. Similarly, in [152], the performance of SC scheme for hybrid system was investigated over the generalized Malaga and $\eta - \mu$ fading models. In [48], SC and MRC of FSO and RF links for hybrid FSO/RF system were studied over Gamma-Gamma (FSO) and Rician (RF) fading distributions without considering the effect of pointing errors. Similarly, the unified performance of hybrid FSO/RF system considering SC and MRC schemes was presented in [49] over Gamma-Gamma-based FSO and $\kappa - \mu$ shadowed-fading-based RF distributions by including the non-generalized zero boresight pointing errors in case of the FSO link. The limitations of the above-discussed diversity combining schemes for hybrid systems [48]$-$[49] are given as follows: (i) The power of RF link is wasted as long as the quality of FSO link is acceptable and (ii) The transmission data rate of the hybrid system is scaled down to the data rate of RF link due to simultaneous transmission of message signal over FSO and RF links.

A novel switching scheme called adaptive combining was proposed for hybrid FSO/RF system in [155], which is a variant of the MRC scheme. In case of the adaptive combining scheme, the FSO link is always active and the RF link will be in a standby mode, if the quality of the FSO link is satisfactory. However, if the FSO link quality is unacceptable, then the RF link will be activated by sending a 1-bit feedback signal to the transmitter and MRC of both FSO and RF links is performed at the receiver. It is to be noted that both switching and diversity combining benefits can be obtained using the adaptive combining scheme and also conservation of RF link power is possible using this scheme, when the RF subsystem is in standby mode. Thus, the adaptive combining scheme circumvents all the drawbacks of the diversity combining schemes and the hard-switching scheme of the hybrid FSO/RF system. The outage and average SER (ASER) performance of the adaptive combining scheme for hybrid FSO/RF system was presented in [156] and a power adaptation strategy was proposed in [157]. In [158] and [159], the performance of the adaptive-combining-based hybrid FSO/RF system was investigated for terrestrial and SATCOM scenarios, respectively.

In the existing works with respect to adaptive combining, the performance analysis was carried out assuming Gamma-Gamma and Nakagami-m or Rician fading distributions for FSO and RF links, respectively. The non-generalized distributions like Rayleigh, Rician, and Nakagami-m cannot model the practical scenarios more accurately. In last few years, the generalized RF fading distributions namely α-η-μ, α-κ-μ, κ-μ, and η-μ have gained much interest among the research community due to their extensive range of applications and their flexibility in modeling various channel scenarios [160]. The performance analysis of wireless communication system over α-κ-μ, κ-μ, and η-μ fading models was presented in [161], [162], [163], and [164]. Recently, α-η-κ-μ, a new and a very comprehensive distribution that models RF channel fading was proposed in [165] and it includes most of the well-known distributions as special cases. In [166] and [167], the exact closed-form expressions were derived for outage probability, average BER, and normalized average capacity considering a digital communication system over α-η-κ-μ distribution.

In [168], [169], and [170] a switching-based DH cooperative diversity scheme for the hybrid FSO/RF system with DF relaying technique was investigated. In [168], a novel switching scheme was proposed for a DH hybrid FSO/RF system using DF relaying technique, where FSO and RF links were combined at the destination using MRC scheme. Moreover, in [169], a DH FSO system with an additional RF backup link to improve reliability of the relay-based FSO system was proposed and its performance was investigated. Furthermore, a multi-hop hybrid FSO/RF system based on the hard-switching scheme assuming DF relay was analyzed in [171]. In [168], [170], and [171], the modeling of the FSO link was restricted to Gamma-Gamma distribution and in [169], the FSO link was modeled using Malaga distribution. Similarly, for modeling the small-scale fading of RF link, the Nakagami-m distribution was assumed in [170], [171]. The authors in [172] have explored the hybrid FSO/RF system for HAPS-assisted SATCOM system with the mobile network supported by an UAV. Additionally, the performance of a HAPS-based SATCOM system was extensively analyzed in [173]. Here, hybrid FSO/RF system with FSO link backed by RF link was considered between ground station and HAPS, which acts as a relay node. However, only FSO link was considered between HAPS and satellite.

In a nutshell, the overall status of the research works carried out in hybrid FSO/RF systems along with the details of channel modeling and pointing errors has been tabulated in Table 2.1.

Table 2.2: Literature summary on hybrid FSO/RF system models

Ref.	**Technique/Scheme**	**FSO channel**	**RF channel**	**Pointing error**	**Metrics**
[41]	Soft-switching	Gamma-Gamma	Rician	Not included	PEP
[25]	Hard-switching	Log-normal	Nakagami-m	Not included	OP, BER, EC
[39]	Hard-switching	Gamma-Gamma	Rician	Zero boresight	OP, BER
[174]	Hard-switching	Malaga	α-η-κ-μ	Zero boresight	SER
[154]	SC	Malaga	Nakagami-m	Zero boresight	OP, BER
[48]	MRC and SC	Gamma-Gamma	Rician	Not included	Average BER
[49]	MRC and SC	Gamma-Gamma	κ-μ	Zero boresight	OP, BER
[148]	MIMO	Malaga	κ-μ	Zero boresight	OP, SER, EC
[155]	Adaptive combining	Gamma-Gamma	Nakagami-m	Not included	OP
[158]	Adaptive combining	Gamma-Gamma	Nakagami-m	Zero boresight	OP, SER
[159]	Adaptive combining	Gamma-Gamma	Rician	Non-zero boresight	OP, SER
[168]	DH cooperative DF relay	Gamma-Gamma	Nakagami-m	Zero boresight	OP, SER
[169]	DH cooperative DF relay	Malaga	Nakagami-m	Zero boresight	OP, SER, average capacity
[171]	Multi-hop DF relay	Gamma-Gamma	Nakagami-m	Zero boresight	OP, EC

2.2.4 Reconfigurable Intelligent Surface (RIS)

The reconfigurable intelligent surface (RIS) or IRS has emerged as a promising solution for addressing the demands of the future wireless communications such as enhanced bandwidth, extended coverage, and improved link reliability [45], [175]. The RIS module is a passive planar surface capable of modifying the properties of incoming electromagnetic waves such as amplitude, phase, and polarization [42, 176]. In [43], authors have proposed a RIS-assisted RF system in which data is transmitted in a dual-hop manner from transmitter to receiver via RIS as shown in Fig. 2.6. Further, the average symbol error probability (ASEP) performance of the RIS-assisted system was investigated over Rayleigh fading distribution based on the central limit theorem. In [177], the authors presented a more accurate performance analysis of the RIS-assisted RF system over Rician fading using the Laguerre series method for different modulation schemes. In [51], multiple RISs were deployed in a smart radio network to realize a cascaded RIS-assisted system and the performance was analyzed in terms of outage probability, ASEP, and ergodic capacity (EC) over conventional binary modulation schemes assuming Nakagami-m distribution. The authors in [178] have investigated the BER performance of a RIS-assisted system considering the index modulation schemes, i.e. spatial modulation (SM) and space shift keying (SSK). In [179], the authors have proposed a new RIS-phase modulation scheme by superimposing the message-bearing phase offsets on the typical RIS phase shifts to transmit the extra information and investigated the outage probability and ASEP of RIS-aided MISO system with the proposed phase modulation scheme.

Recently, the usage of RIS technology has also been extended to FSO scenario to combat the LOS link blockage issue due to buildings, trees, and other obstacles [52]. The optical RIS-based FSO system has the advantage of lower hardware cost as compared to the FSO-based relaying system, since active components, which are essential at the relay nodes such as power amplifiers, encoders, decoders, etc., are not required in case of RIS [180]. The RISs are made up of meta-surfaces that can

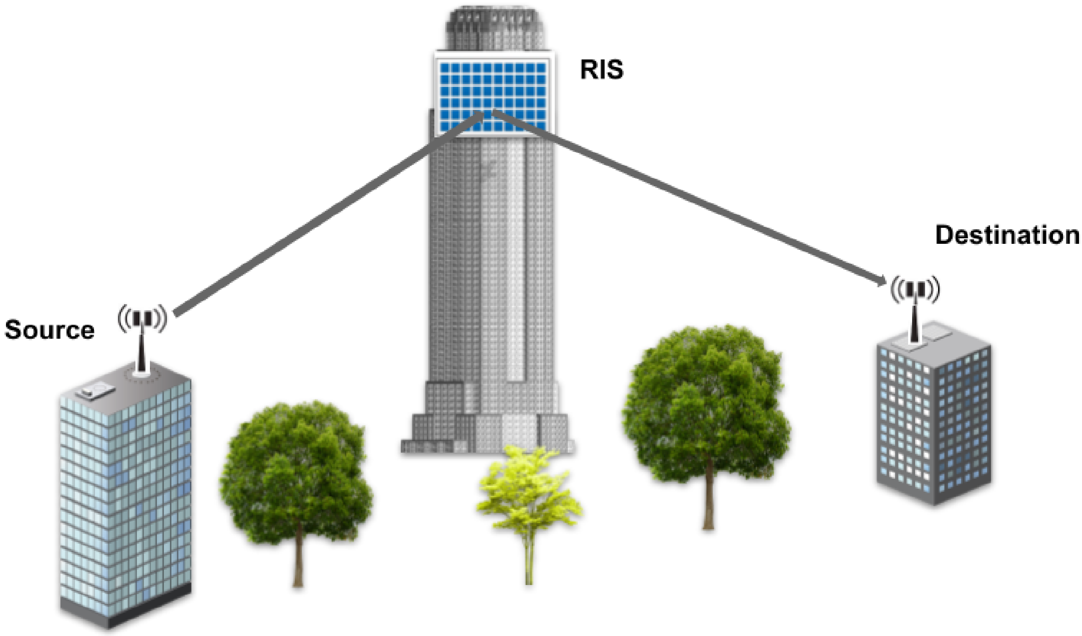

Fig. 2.6: Depiction of a RIS-assisted wireless communication system

be categorized as reconfigurable and non-reconfigurable surfaces depending on their configuration after fabrication [26]. In [50], the authors proposed a solution to the problem of skip-zones in FSO communication by using a RIS module between a source and a destination. Further, the cascaded FSO channel statistics were derived in [50] over the Gamma-Gamma distribution for investigating the performance of the system. In [181], the RIS-assisted FSO system was investigated over a large number of RIS elements to improve the performance and enhance the coverage area. Further, in [181], it was observed that the performance of the RIS-assisted FSO system improves drastically with an increase in the number of RIS elements. In [27], the authors presented a comprehensive performance of the RIS-assisted FSO system by investigating the metrics like OP, EC, and average bit error rate (ABER) over the generalized distributions. In [182], a RIS-aided mixed RF/FSO system is analyzed, where a single RF source is equipped with RIS and a single FSO link is used to connect relay and destination. Authors in [183] proposed a RIS-assisted hybrid FSO/RF system to improve the reliability in which both FSO and RF subsystems are assisted by RIS. Further, in [184], authors have considered the UAV-based RIS system with hybrid FSO/RF communication, where both FSO and RF links are equipped by a single RIS. In [185], a HAPS-based satellite-aerial-ground network was proposed, where RIS-aided UAV acts as a relay between HAPS and ground station. In addition, HAPS-to-UAV link was empowered by a hybrid FSO/RF communication.

In a nutshell, Table 2.3 provides a summary of the current research status of performance analysis of various RIS-based wireless system models.

Table 2.3: Literature summary on RIS-assisted RF and FSO system models

Ref.	**System model**	**Number of RIS**	**Modulation technique**	**FSO/RF channel**	**Performance Metrics**
[43]	RIS-aided RF system	Single	M-ary PSK	Rayleigh	ASEP
[176]	RIS-assisted RF system	Single	Binary modulation schemes	Rayleigh	OP, ABER, average channel capacity
[177]	RIS-assisted RF system	Single	Binary modulation schemes	Rician	OP, ASEP, average channel capacity
[51]	Cascaded RIS-assisted RF system	Multiple	Binary modulation schemes	Nakagami-m	OP, EC, ASEP
[178]	RIS-assisted RF system	Single	SM and SSK	Rayleigh	Average BER
[179]	MISO system with MRT scheme	Single	RIS-phase modulation scheme	Rayleigh	OP, ASEP
[27]	RIS-assisted FSO system	Single	Binary modulation schemes	Gamma–Gamma, $\mathcal{F}$-distribution, Malaga	OP, ABER, EC
[50]	RIS-aided FSO system	Single	Binary modulation schemes	Gamma–Gamma	OP, ABER, EC
[181]	RIS-aided FSO system	Single	Binary modulation schemes	Gamma–Gamma	OP, ABER, EC
[182]	RIS-aided mixed FSO/RF with relay network	Two	Binary PSK	Gamma–Gamma/ Rayleigh	OP, ASEP
[183]	RIS-assisted hybrid FSO/RF system	Two	Binary PSK	Gamma–Gamma/ Rayleigh	OP, ABER, EC
[184]	UAV-based RIS-assisted hybrid FSO/RF system	Single	M-ary PSK	Gamma–Gamma/ Nakagami-m	ASER, channel capacity

2.3 Chapter Summary

This chapter encompasses an in-depth exploration of the state-of-the-art in FSO communication, assessing its advantages, applications, and limitations while comparing it to RF and other wireless communication systems. Additionally, the chapter discusses the impairments encountered in the FSO channel such as atmospheric turbulence, atmospheric attenuation due to fog and rain, pointing errors, and channel estimation errors. To enhance the performance and overcome the impairments in FSO systems, several improvement techniques have been explored. These techniques include MIMO schemes, relaying techniques, hybrid FSO/RF communications, and the usage of IRS between source and destination. Their purpose is to mitigate the atmospheric effects, thereby ensuring reliable and efficient FSO communication. Finally, the chapter concludes by addressing the challenges and open research problems that need to be explored for further improvement of the FSO communication.

Chapter 3

Performance Analysis of Hybrid FSO/RF Communication Over Generalized Fading Models

3.1 Introduction

The upcoming 6^{th} generation (6G) wireless communication standard should be capable enough to satisfy the high data rate, low latency, and substantial throughput requirements. In this regard, FSO communication is an emerging technology which fulfils the ever-growing demands of ultra-high data rate and massive bandwidth requirements. Further, the FSO links can be employed for a variety of applications such as enterprise/campus area connectivity, extending metropolitan area network, live video broadcasting, backhaul connectivity for wireless cellular networks, and satellite communications [70].

Nevertheless, the FSO communication suffers from atmospheric turbulence-induced fading, atmospheric attenuation, and misalignment or pointing errors. The weather conditions such as fog, snow, and smog also affect the FSO link performance and restrict FSO communication to shorter distances upto few kilometres [80]. To enhance the reliability and to mitigate the losses, one can backup the FSO link with a more reliable RF link, which is less susceptible to atmospheric turbulence, pointing errors, and weather conditions like fog, haze, and smog. However, the RF link is sensitive to small scale fading and rain [147]. Meanwhile, the FSO link is not much affected by small-scale fading and rain. Thus, the FSO and RF links in parallel will complement each other in all channel conditions to improve the overall performance of both FSO and RF communications. In this context, a hybrid FSO/RF communication is considered as a promising candidate for 6G and beyond wireless communication systems, especially for wireless backhaul connectivity [70].

In a typical hybrid FSO/RF system, any one of the FSO or RF link or both will be activated depending upon the link quality or the type of switching scheme used [25], [39]. In [25], the performance of the hybrid FSO/RF system with hard switching scheme was investigated in which only one link will be active depending upon the quality of the FSO link. The atmospheric turbulence of FSO channel was characterized using a log-normal distribution, which can model only weak turbulence condition and the RF fading channel was modeled using Nakagami-m distribution. The Malaga distribution is a generalized distribution used to model atmospheric turbulence of FSO channel from which log-normal, Gamma-Gamma, exponential, and other known distributions can be obtained as special cases [95]. In the existing works [25, 41, 39], the performance of hybrid FSO/RF was analyzed over non-generalized distributions like Gamma-Gamma and Nakagami-m.

In this chapter, a unified performance analysis of a single-hop hybrid FSO/RF system is carried out by assuming a single-threshold-based hard-switching scheme. We consider generalized Malaga and α-η-κ-μ fading distributions for modeling FSO and RF links, respectively. The exact closed-form expressions for outage probability, average symbol error rate (SER), and ergodic capacity are derived for the proposed hybrid FSO/RF system considering both atmospheric turbulence and pointing errors in case of FSO link and small scale fading in case of RF link. Additionally, we have also investigated the performance of the hybrid FSO/RF system for both uplink and downlink satellite communication scenarios. Further, the optimum switching threshold SNR value γ_{th}^{opt} and optimum beam width value w_0^{opt} of the hybrid FSO/RF system are also determined to achieve optimal performance.

3.2 Organization of the chapter

The remainder of the chapter is structured as follows. In Section 3.3, the system model and the channel models of both FSO and RF links with statistical characteristics are discussed. The outage analysis and average SER analysis of hybrid FSO/RF system are presented in Sections 3.4 and 3.5, respectively. The ergodic capacity expression for hybrid FSO/RF system is given in Section 3.6. In Section 3.7, the asymptotic analysis for outage, average SER, and ergodic capacity is presented. Section 3.8 presents the numerical results and the concluding remarks of this chapter are given in Section 3.9.

3.3 System and Channel Models

In this work, a single-threshold-based hybrid FSO/RF system is considered, where one of the two links either FSO or RF link will be activated depending upon the instantaneous SNR of FSO link as shown in Fig. 3.1. In this switching strategy, transmission over FSO links is given a greater priority than transmission over RF links. If the instantaneous SNR of an FSO link drops below a predetermined threshold SNR value γ_{th}, then the RF link is used to transmit the message signal. It is important to note that before each transmission phase, the channel states of FSO and RF links are estimated at the receiver. These estimates are used to calculate the instantaneous SNR of the FSO and RF links. Based on these calculated instantaneous SNR values, a one-bit feedback signal will be used to activate the backup RF link at the transmitter, in case if the FSO link is not satisfactory. We assume that the transmitter receives the feedback bit without any errors and the receiver has full channel state information (CSI). It is assumed that the FSO subsystem uses a sub-carrier intensity modulation based M-ary phase-shift-keying (SIM-MPSK) scheme

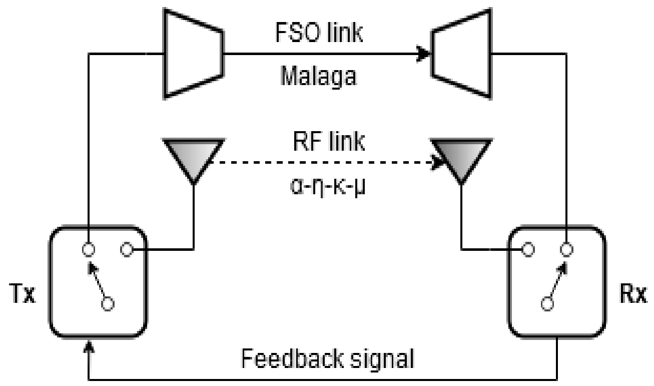

Fig. 3.1: Hybrid FSO/RF system model

at the transmitter, in which the up-converted MPSK signal modulates the intensity of laser beam [80]. Furthermore, the FSO receiver employs both HD and DD methods. Note that HD is a type of coherent detection technique, which requires a local oscillator to generate a carrier signal at the receiver [80]. Moreover, the MPSK signalling technique is used to modulate RF signals.

The generalized Malaga distribution is taken into account for modeling the atmospheric turbulence of the FSO link. It is important to note that majority of the atmospheric turbulence models used for modeling the FSO channel, including the log-normal distribution, Gamma-Gamma distribution, K distribution, etc., are all included in the Malaga distribution [95]. Further, the small-scale fading of RF link is described using the recently proposed α-η-κ-μ distribution [165], which includes wide variety of RF fading models like α-κ-μ, α-η-μ, κ-μ, η-μ, Rice, Nakagami-m, etc. The performance parameter expressions for a wide range of distributions can be obtained as special cases from the generalized distributions, eliminating the need for analyzing each distribution separately.

The FSO channel model considered in this chapter includes atmospheric turbulence, pointing errors and path loss. Moreover, the RF channel model also includes atmospheric fading and path loss components. Let the atmospheric turbulence, pointing errors and pathloss encountered by FSO link be denoted as I_a, I_p, and I_l, respectively. The effective channel irradiance of FSO link is given by $I_{FSO} = I_a I_p I_l$. The output received signals at the receiver corresponding to HD and IM/DD schemes are denoted as $y_{IM/DD}$ and y_{DD}, respectively. Let the transmitted input signal for both the channels be $x_{IM/DD}$ and x_{HD}. The output equations for the received FSO signal under HD and IM/DD techniques are, respectively, given by

$$y_{HD} = \sqrt{\eta_e P_F} \sqrt{I_{FSO}} x_{HD} + n_{HD}, \tag{3.1}$$

$$y_{IM/DD} = \eta_e P_F I_{FSO} x_{IM/DD} + n_{IM/DD}, \tag{3.2}$$

where η_e denotes the optical-to-electrical conversion coefficient, P_F is the optical power at the transmitter, $n_{IM/DD}$ represents the additive white Gaussian noise (AWGN) with zero-mean and variance σ_{HD}^2, and $n_{IM/DD}$ represents the AWGN with zero-mean and variance $\sigma_{IM/DD}^2$. Similarly, the equation for the received baseband RF signal is given by:

$$y_{RF} = \sqrt{P_R g_R} h_{RF} x_{RF} + n_{RF}, \tag{3.3}$$

where h_{RF} is the small-scale fading coefficient of the RF channel, P_R is the transmitted RF power, x_{RF} is the transmitted MPSK symbol, n_{RF} is the AWGN with zero-mean and variance given by σ_{RF}^2 (in dBm) $= B_R + N_0 + N_f$. Here, B_R is the RF bandwidth (in dBMHz), N_0 is the noise power spectral density (in dBm/MHz), and N_f is the noise figure. The average RF channel gain g_R at 60 GHz carrier frequency is given by [41]

$$g_R = G_t + G_r - 20 \log_{10} \left(\frac{4\pi L}{\lambda_r} \right) - (\zeta_{oxy} + \zeta_{rain}) L, \tag{3.4}$$

where G_r and G_t represent the receive and transmit antenna gain values, L is the link distance, λ_r is the wavelength of RF signal, and ζ_{rain} and ζ_{oxy} indicate the attenuation due to rain and oxygen absorption, respectively.

3.3.1 FSO Channel Model

The Malaga distribution statistically accounts for three components of the observed field at the receiver as follows: (a) U_L indicates the LOS component (b) U_C^S denotes the coupled to LOS component that is scattered by the eddies on the propagation axis (c) U_G^S is the third component, which is scattered to the receiver by off-axis eddies [95]. The probability density function (PDF) of irradiance I_a of FSO link modeled using Malaga distribution, is given by [95, eq. (24)]

$$f_{I_a}(I_a) = A_M \sum_{d=1}^{\beta} a_d I_a^{\frac{\alpha+d}{2}} K_{\alpha-d}\left(2\sqrt{\frac{\alpha\beta I_a}{y\beta+\Omega'}}\right), \tag{3.5}$$

where

$$A_M = \frac{2\alpha^{\alpha/2}}{y^{1+\alpha/2}\Gamma(\alpha)}\left(\frac{y\beta}{y\beta+\Omega'}\right)^{\beta+\alpha/2}, \tag{3.6}$$

$$a_d = \binom{\beta-1}{d-1}\frac{(y\beta+\Omega')^{1-d/2}}{(d-1)!}\left(\frac{\Omega'}{y}\right)^{d-1}\left(\frac{\alpha}{\beta}\right)^{d/2}, \tag{3.7}$$

$\alpha > 0$ represents the large-scale irradiance fluctuation, $\beta > 0$ is related to the amount of small-scale irradiance fluctuation and is assumed as a natural number as mentioned in [95], $K_v(\cdot)$ represents the modified Bessel function of second kind of order v [186, eq.(8.432.1)], and $\Gamma(\cdot)$ is the gamma function [186, eq. (8.31.1)]. The major parameters involved in the PDF of I_a are mentioned in Table 3.1. Further, the expressions used to calculate α and β for terrestrial and satellite communication scenarios are given in the Appendix A.

The radial displacement ϱ between the beam centre and detector centre, which induces pointing error, has been modeled using Rayleigh distribution. The amount of the received power collected at the receiver aperture of radius a can be expressed in Gaussian form as [94]

$$I_p \approx A_0 \exp(-2\varrho^2/w_{L_{eq}}), \tag{3.8}$$

where $A_0 = \mathrm{erf}^2(v)$, $v = \frac{\sqrt{\pi}\,a}{\sqrt{2}\,w_L}$, and $w_{L_{eq}} = \frac{w_L^2\sqrt{\pi}\mathrm{erf}(v)}{2v\exp(-v^2)}$. Here, A_0 represents the fraction of the power collected at $\varrho = 0$, w_L is the Gaussian beam width, $w_{L_{eq}}$ is

Table 3.1: Parameters involved in the PDF of Malaga distribution

Symbol	Description/expression
Ω'	$\Omega' = \Omega + 2\,b_0\rho + 2\sqrt{2\,b_0\rho\,\Omega}\cos(\phi_A - \phi_B)$
Ω	Average power of LOS component (U_L)
ϕ_A	Deterministic phase of LOS
ϕ_B	Deterministic phase of coupled-to-LOS scatter component
y	$y = 2\,b_0(1-\rho)$, average power of the scattered component received by off-axis eddies
$2\,b_0$	Average power of the total scatter components U_S^C & U_S^G
$0 < \rho < 1$	Amount of scattering power coupled to LOS component

the equivalent beam width, and erf$(\cdot)$ represents the error function [186, eq. (8.25)]. Further, the Gaussian beam width can be given in terms of link distance L and wavelength λ_f as

$$w_L \approx w_0\sqrt{1+\theta_0(\lambda_f L/\pi w_0^2)^2}, \quad \theta_0 = \quad 1+\frac{2w_0^2}{\rho_0^2(L)}, \quad \rho_0^2(L) = (0.55C_n^2\,k_n^2 L)^{-3/5}, \tag{3.9}$$

where w_0 represents the beam width at $L = 0$, C_n^2 is the refractive index parameter, and $k_n = \frac{2\pi}{\lambda_f}$ is the wave number. It is to be noted that the radial displacement ϱ follows the Rayleigh distribution [94, 100] and using the random variable transformation in (3.8), the PDF of pointing errors I_p can be expressed as [94, eq. (11)]

$$f_{I_p}(I_p) = \frac{g^2}{A_0^{g^2}} I_p^{g^2-1}; \quad 0 \le I_p \le A_0, \tag{3.10}$$

where $g = \frac{w_{L_{eq}}}{2\sigma_s}$ represents the pointing error coefficient and σ_s is the jitter standard deviation. Beers Lambert Law [94] defines the atmospheric path loss of an optical link as $I_l = \exp(-\zeta_w L)$, where ζ_w is the attenuation coefficient which depends on weather conditions.

The combined atmospheric channel state of FSO link includes irradiance, pointing errors and path loss and is written as $I_{FSO} = I_a I_p I_l$. The PDF of composite channel irradiance $I_{FSO} = I_a I_p I_l$ can be derived by using random variable transformation as

$$f_{I_{FSO}}(I) = \frac{g^2 A_M}{2I} \sum_{d=1}^{\beta} b_d \, G_{1\,3}^{3\,0}\left(\frac{\alpha\beta I}{(y\beta+\Omega')I_l A_0} \middle| \begin{matrix} g^2+1 \\ g^2, \alpha, d \end{matrix} \right), \tag{3.11}$$

where $b_d = a_d(\alpha\beta/(y\beta+\Omega^{'}))^{-(\alpha+d)/2}$ and $G_{p\,q}^{m\,n}(\cdot)$ represents Meijer G-function [187, eq.(07.34.02.0001.01)].

The instantaneous SNR and the average SNR of FSO link for HD scheme are, respectively, given by

$$\gamma_{HD} = I_{FSO} \frac{P_F \eta_e}{\sigma_{HD}^2}, \tag{3.12}$$

$$\overline{\gamma}_1 = (y+\Omega^{'})kA_0 I_l \frac{P_F \eta_e}{\sigma_{HD}^2}, \tag{3.13}$$

where $\mathbb{E}[I_{FSO}] = (y+\Omega^{'})kA_0 I_l$, $\mathbb{E}[\cdot]$ denotes the expectation operation, and $k = \frac{g^2}{g^2+1}$. By applying the random variable transformation using $\gamma_{HD} = \overline{\gamma}_1 I_{FSO}/[(y+\Omega^{'})kA_0 I_l]$, the PDF of instantaneous SNR of FSO link is given by

$$f_{\gamma_{HD}}(\gamma) = \frac{g^2 A_M}{2\gamma} \sum_{d=1}^{\beta} b_d \, G_{1\,3}^{3\,0}\left(B_M \frac{\gamma}{\overline{\gamma}_1} \middle| \begin{matrix} g^2+1 \\ g^2, \alpha, d \end{matrix} \right), \tag{3.14}$$

where $B_M = k\,\alpha\,\beta\,(y+\Omega^{'})/(y\beta+\Omega^{'})$. Similarly, for IM/DD technique, the instantaneous SNR and the average electrical SNR of FSO link can be written, respectively, as

$$\gamma_{IM/DD} = I_{FSO}^2 \frac{P_F^2 \eta_e^2}{\sigma_{IM/DD}^2}, \tag{3.15}$$

$$\overline{\gamma}_2 = [(y+\Omega^{'})k\,A_0 I_l]^2 \frac{P_F^2 \eta_e^2}{\sigma_{IM/DD}^2}, \tag{3.16}$$

By applying random variable transformation using $\gamma_{IM/DD} = \overline{\gamma}_2 I_{FSO}^2/[(y+\Omega^{'})\,k\,A_0 I_l]^2$, the PDF of the instantaneous SNR of IM/DD detection scheme is obtained as

$$f_{\gamma_{IM/DD}}(\gamma) = \frac{g^2 A_M}{4\gamma} \sum_{d=1}^{\beta} b_d \, G_{1\,3}^{3\,0}\left(B_M \sqrt{\frac{\gamma}{\overline{\gamma}_2}} \middle| \begin{matrix} g^2+1 \\ g^2, \alpha, d \end{matrix} \right), \tag{3.17}$$

Combining two PDFs in (3.14) and (3.17) result in a single expression that leads to the unification of HD and IM/DD techniques. The unified expression for the PDF of instantaneous SNR of FSO link γ_{FSO} is given by

$$f_{\gamma_{FSO}}(\gamma) = \frac{g^2 A_M}{2^r \gamma} \sum_{d=1}^{\beta} b_d \, G_{1\,3}^{3\,0}\left(B_M \left(\frac{\gamma}{\overline{\gamma}_r}\right)^{\frac{1}{r}} \middle| \begin{matrix} g^2+1 \\ g^2, \alpha, d \end{matrix} \right), \tag{3.18}$$

where the parameter r specifies the type of detection technique. The PDF in (3.18) represents the PDF of HD and IM/DD schemes for $r = 1$ and 2, respectively. The cumulative distribution function (CDF) of instantaneous SNR of FSO link γ_{FSO} can be calculated as

$$F_{\gamma_{FSO}}(\gamma_{th}) = \int_0^{\gamma_{th}} f_{\gamma_{FSO}}(x)\, dx, \tag{3.19}$$

$$F_{\gamma_{FSO}}(\gamma_{th}) = C_1 \sum_{d=1}^{\beta} t_d \, G_{r+1\;3r+1}^{\;3r\;\;\;1}\left(A_1 \middle| \begin{matrix} 1, K_1 \\ K_2, 0 \end{matrix} \right), \tag{3.20}$$

where $A_1 = \frac{B_M^r \gamma_{th}}{r^{2r}\overline{\gamma}_r}$, $K_1 = \frac{g^2+1}{r}...\frac{g^2+r}{r}$, $K_2 = \frac{g^2}{r}...\frac{g^2+r-1}{r}, \frac{\alpha}{r}...\frac{\alpha+r-1}{r}, \frac{d}{r}...\frac{d+r-1}{r}$, $C_1 = \frac{g^2 A_M}{2^{2r-1}\pi^{r-1}}$, and $t_d = b_d\, r^{\alpha+d-1}$.

3.3.2 RF channel Model

The α-η-κ-μ fading model mainly comprises of (a) arbitrary number of multipath clusters in a nonlinear environment (b) arbitrary number of dominant components and (c) arbitrary multipath powers. The envelope h_{RF} of α-η-κ-μ model is defined as [165]

$$h_{RF}^{\alpha_R} = \sum_{i=1}^{\mu_x}(X_i + \lambda_{x_i})^2 + \sum_{i=1}^{\mu_y}(Y_i + \lambda_{y_i})^2, \tag{3.21}$$

where $\alpha_R > 0$ signifies the nonlinearity of the medium, X_i and Y_i are mutually independent Gaussian random processes with zero mean and variances σ_x^2 and σ_y^2, respectively, λ_{x_i} and λ_{y_i} are the mean of in-phase and quadrature components of cluster i, and μ_x and μ_y are the number of in-phase and quadrature components of multipath clusters, respectively. The PDF of envelope h_{RF}, which follows α-η-κ-μ

Table 3.2: Parameters involved in the PDF of α-η-κ-μ distribution

Symbol	Expression	Description
η	$\frac{\mu_x\sigma_x^2}{\mu_y\sigma_y^2}$	Ratio of the power of in-phase to quadrature component
κ	$\frac{\lambda_x^2+\lambda_y^2}{\mu_x\sigma_x^2+\mu_y\sigma_y^2}$	Ratio of the sum of the power of dominant components to scattered waves
μ	$\frac{\mu_x+\mu_y}{2}$	Number of multipath clusters
p	$\frac{\mu_x}{\mu_y}$	Ratio of the number of in-phase and quadrature multi-path components
q	$\frac{\mu_y\sigma_y^2\lambda_x^2}{\mu_x\sigma_x^2\lambda_y^2}$	Product of two ratios: ratio of the power of quadrature to in-phase dominant component and ratio of the power of in-phase to quadrature scattered component

model, can be written as [165]

$$f_{h_{RF}}(h) = \frac{\alpha_R\, h^{\alpha_R\mu-1}\exp\left(-h^{\alpha_R}/2\right)}{2^{\mu}\Gamma(\mu)}\sum_{l=0}^{\infty}\frac{l\,!\,c_l}{(\mu)_l}L_l^{\mu-1}(2\,h^{\alpha_R}), \tag{3.22}$$

where $(\mu)_l$ represents pochhammer symbol, c_0 and c_l are given in [165, eq. (30)] and [165, eq. (15)], respectively, $\Gamma(\cdot)$ is the gamma function [186, eq. (8.31.1)], and $L_\mu^l(\cdot)$ is defined as a Laguerre polynomials [186, eq. (8.970.1)]. The remaining parameters in (3.22) are given in Table 3.2.

The instantaneous SNR of RF link with α-η-κ-μ fading distribution including the path loss is given by

$$\gamma_{RF} = \frac{|h_{RF}|^2\overline{\gamma}_{RF}}{g_R}. \tag{3.23}$$

where $\overline{\gamma}_{RF} = g_R\frac{P_R}{\sigma_{RF}^2}$ is the average SNR of RF link. By utilizing the random variable transformation $\gamma_{RF} = |h_{RF}|^2\overline{\gamma}_{RF}/g_R$ and after some manipulations, the PDF of instantaneous SNR of RF link is given by

$$f_{\gamma_{RF}}(\gamma) = \tilde{\alpha}\sum_{l=0}^{\infty}\sum_{m=0}^{l}\frac{c_l(-l)_m\gamma^{\tilde{\alpha}(\mu+m)-1}\exp\left(-\gamma^{\tilde{\alpha}}/2\overline{\gamma}_{RF}^{\tilde{\alpha}}\right)}{m!\,\Gamma(\mu+m)\,2^{\mu-m}\overline{\gamma}_{RF}^{\tilde{\alpha}(\mu+m)}}, \tag{3.24}$$

where $\tilde{\alpha} = \alpha_R/2$ is used for notational ease. The CDF of instantaneous SNR of RF link can be written as

$$F_{\gamma_{RF}}(\gamma_{th}) = \int_0^{\gamma_{th}} f_{\gamma_{RF}}(t)\,dt = \sum_{l=0}^{\infty}\sum_{m=0}^{l} \frac{c_l\,(-l)_m 4^m}{m!\,\Gamma(\mu+m)}\gamma\left(\mu+m, \frac{\gamma_{th}^{\tilde{\alpha}}}{2\,\overline{\gamma}_{RF}^{\tilde{\alpha}}}\right), \quad (3.25)$$

where $\gamma(:,:)$ represents the lower incomplete gamma function [186, eq. (8.350.1)].

3.4 Outage Analysis

In this section, the outage probability expression in closed-form for the hybrid FSO/RF system is derived. In hybrid FSO/RF system, if the instantaneous SNR of both the FSO and RF links are lesser than a threshold SNR value γ_{th}, then the system will be declared to be in outage. The expression for outage probability of hybrid FSO/RF system is given by

$$P_{out}^{H} = F_{\gamma_{FSO}}(\gamma_{th})\, F_{\gamma_{RF}}(\gamma_{th}), \quad (3.26)$$

where $F_{\gamma_{FSO}}(\gamma_{th})$ and $F_{\gamma_{RF}}(\gamma_{th})$ are the CDFs of FSO and RF links, which are given by (3.20) and (3.25), respectively.

3.5 Average SER Analysis

The average SER of a single-threshold-based switching scheme for hybrid FSO/RF system is given by $P_e^H = B_{FSO}(\gamma_{th}) + F_{\gamma_{FSO}}(\gamma_{th})\, P_e^{RF}$, where $B_{FSO}(\gamma_{th})$ represents the average SER during the non-outage period of FSO link and P_e^{RF} represents the average SER of RF link. The average SER during the non-outage period of FSO link is given by

$$B_{FSO}(\gamma_{th}) = \int_{\gamma_{th}}^{\infty} p(e|x) f_{\gamma_{FSO}}(x) dx, \quad (3.27)$$

where $p(e|x)$ is the conditional SER of MPSK modulation conditioned on the instantaneous SNR x and it is expressed as

$$p(e|x) = \frac{A}{2}\mathrm{erfc}(B\sqrt{x}), \tag{3.28}$$

where $A = 1$ for $M = 2$, $A = 2$ for $M > 2$, $B = \sin(\pi/M)$, and erfc$(\cdot)$ represents the complementary error function. Using [187, eq. (07.34.03.0619.01)], the conditional SER of MPSK can be written in terms of Meijer G-function and is given by

$$p(e|x) = \frac{A}{2\sqrt{\pi}} G_{1\,2}^{2\,0}\left(B^2 x \middle| \begin{matrix} 1 \\ 0, \frac{1}{2} \end{matrix}\right). \tag{3.29}$$

By using the Maclaurin series expansion of erfc$(\cdot)$ function [186, eq. (3.321)], the conditional SER can also be written as

$$p(e|x) = \frac{A}{2}\left[1 - \frac{2}{\sqrt{\pi}}\sum_{n=0}^{\infty}\frac{(-1)^n B^{2n+1} x^{n+\frac{1}{2}}}{n!(2n+1)}\right]. \tag{3.30}$$

Further, by substituting (3.30) and (3.18) in (3.27), $B_{FSO}(\gamma_{th})$ can be written as

$$B_{FSO}(\gamma_{th}) = \underbrace{\int_0^{\infty}\frac{A}{2}\mathrm{erfc}(B\sqrt{x}) f_{\gamma_{FSO}}(x)dx}_{P_e^{FSO}} - \underbrace{\int_0^{\gamma_{th}}\frac{A}{2}\mathrm{erfc}(B\sqrt{x}) f_{\gamma_{FSO}}(x)dx}_{I}, \tag{3.31}$$

where P_e^{FSO} is the average SER of FSO link and after simplification using [187, eq. (07.34.21.0013.01)], the closed form expression is given by

$$P_e^{FSO} = C_2 \sum_{d=1}^{\beta} t_d\, G_{r+2\;3r+1}^{\;3r\;\;\;\;2}\left(A_2 \middle| \begin{matrix} 1, 0.5, K_1 \\ K_2, 0 \end{matrix}\right), \tag{3.32}$$

where $C_2 = \frac{Ag^2 A_M}{2^{2r}\pi^{r-\frac{1}{2}}}$ and $A_2 = \frac{B_M^r}{B^2 r^{2r}\overline{\gamma}_r}$.

The integral I in (3.31) can be evaluated by expanding the erfc$(\cdot)$ function using Maclaurin series [186, eq. (3.321.1)] and after simplification using [187, eq. (07.34.21.0084.01)], the integral I is written as $I = I_1 - I_2$ and the expressions for

I_1 and I_2 are, respectively, given by

$$I_1 = \frac{A}{2} F_{\gamma_{FSO}}(\gamma_{th}),$$
$$I_2 = C_2 \sum_{d=1}^{\beta} t_d \sum_{n=0}^{\infty} D_n G_{r+1\ 3r+1}^{3r\ \ \ 1} \left(A_1 \middle| {}^{-n+0.5, K_1}_{K_2, -n-0.5}\right),$$

where $D_n = \frac{2(-1)^n B^{2n+1}}{n!\,(2n+1)} \gamma_{th}^{n+\frac{1}{2}}$.

The average SER of RF link is given by

$$P_e^{RF} = \int_0^{\infty} p(e|t)\, f_{\gamma_{RF}}(t) dt \tag{3.33}$$

By substituting (3.24) and (3.29) in (3.33) and after substituting the exponential function in its Meijer G-form using [187, eq. (07.34.03.0228.01)], the expression for P_e^{RF} can be written as

$$P_e^{RF} = \frac{A\tilde{\alpha}}{2\sqrt{\pi}} \sum_{l=0}^{\infty} \sum_{m=0}^{l} \frac{c_l(-l)_m}{m!\,\Gamma(\mu+m)\, 2^{\mu-m} \overline{\gamma}_{RF}^{\tilde{\alpha}(\mu+m)}} \int_0^{\infty} t^{\tilde{\alpha}(\mu+m)-1} G_{1\ 2}^{2\ 0} \left(B^2 t \middle| \begin{matrix} 1 \\ 0, 0.5 \end{matrix} \right)$$
$$\times G_{0\ 1}^{1\ 0} \left(\frac{t^{\tilde{\alpha}}}{2\overline{\gamma}_{RF}^{\tilde{\alpha}}} \middle| \begin{matrix} - \\ 0 \end{matrix} \right) dt \tag{3.34}$$

By solving the above expression using [187, eq. (07.34.21.0013.01)], the average SER of RF link is given by

$$P_e^{RF} = \frac{A\tilde{\alpha}}{2\sqrt{\pi}} \sum_{l=0}^{\infty} \sum_{m=0}^{l} \frac{c_l(-l)_m j^{\frac{1}{2}} i^{\delta-1}}{m!\,\Gamma(\mu+m)\, 2^{\mu-m} (2\pi)^{\frac{i+j}{2}-1} (B^2 \overline{\gamma}_{RF})^{\delta}}$$
$$\times G_{2i\ j+i}^{j\ \ 2i} \left(\frac{i^i}{B^{2i}(2j\overline{\gamma}_{RF}^{\tilde{\alpha}})^j} \middle| \begin{matrix} B_1 \\ B_2, B_3 \end{matrix} \right), \tag{3.35}$$

where $\delta = \tilde{\alpha}(\mu+m)$, $\tilde{\alpha} = i/j$, i and j are positive integers, $B_1 = \frac{1-\delta}{i}, ..., \frac{i-\delta}{i}, \frac{0.5-\delta}{i}, ...,$ $\frac{i-0.5-\delta}{i}$, $B_2 = 0, \frac{1}{j}, .., \frac{j-1}{j}$, and $B_3 = \frac{0-\delta}{i}, ..., \frac{i-1-\delta}{i}$.

3.6 Ergodic Capacity Analysis

The best achievable capacity is given in terms of average (or ergodic) capacity. The average capacity of the hybrid FSO/RF system is given by

$$\bar{C}_{hybrid} = \bar{C}_{FSO}(\gamma_{th}) + F_{\gamma_{FSO}}(\gamma_{th})\bar{C}_{RF}, \tag{3.36}$$

where $\bar{C}_{FSO}(\gamma_{th})$ is the average capacity of FSO link during the non-outage period and $\bar{C}_{RF}$ is the average capacity for RF link. The average capacity of FSO link during the non-outage period can be expressed as

$$\begin{aligned} \bar{C}_{FSO}(\gamma_{th}) &= \underbrace{W_F \int_0^{\infty} \log_2(1+\varepsilon_r\, x) f_{\gamma_{FSO}}(x)dx}_{\bar{C}_{FSO}} \\ &- \underbrace{W_F \int_0^{\gamma_{th}} \log_2(1+\varepsilon_r\, x) f_{\gamma_{FSO}}(x)dx,}_{I_C} \end{aligned} \tag{3.37}$$

where ε_r is a constant and for heterodyne detection (i.e. $r=1$), $\varepsilon_1 = 1$ and for IM/DD detection (i.e. $r=2$), $\varepsilon_2 = e/(2\,\pi)$, W_F denotes the bandwidth of FSO signal, and $\bar{C}_{FSO}$ is defined as the average capacity of FSO link. By substituting the Meijer G-form of $\log_2(1+x)$ [187, eq. (07.34.03.0830.01)] in (3.37) and after utilizing [187, eq. (07.34.21.0013.01)], the average capacity of FSO link can be written as

$$\bar{C}_{FSO} = C_4 \sum_{d=1}^{\beta} t_d\, G^{\,3r+2\ \ 1}_{\,r+2\ \ 3r+2}\left(A_3\Big|\,{}^{0,1,K_1}_{K_2,0,0}\right), \tag{3.38}$$

where $C_4 = \frac{g^2 A_M W_F}{2^r(2\pi)^{r-1}\ln(2)}$ and $A_3 = \frac{B_M^r}{\varepsilon_r\, r^{2r}\bar{\gamma}_r}$.

The integral I_C in (3.37) can be evaluated by expanding $\log_2(1+x)$ in its series form [188]. After substituting (3.18) in (3.37), I_C can be written after simplification using [187, eq. (07.34.21.0084.01)] as $I_C = I_1 + I_2$, where I_1 and I_2 are, respectively, given by

$$I_1 = W_F \log_2(z) F_{\gamma_{FSO}}(\gamma_{th}), \tag{3.39}$$

$$I_2 = C_4 \sum_{d=1}^{\beta} t_d \sum_{n=1}^{\infty} \frac{(-1)^{n-1}}{n\, z^n} \sum_{i=0}^{n} \binom{n}{i} (1-z)^{n-i} \varepsilon_r^i \gamma_{th}^i G_{\,r+1\;3r+1}^{\,3r\;\;\;1} \left(A_1 \middle| \begin{matrix} 1-i, K_1 \\ K_2, -i \end{matrix} \right), \tag{3.40}$$

where $z = \frac{\varepsilon_r \gamma_{th}+1}{2}$.

The ergodic channel capacity of RF link is formulated as

$$\bar{C}_{RF} = W_R \int_0^{\infty} \log_2(1+t) f_{\gamma_{RF}}(t) dt, \tag{3.41}$$

where W_R is the bandwidth of RF signal. By substituting Meijer G-form of $\log_2(1+t)$ [187, eq. (07.34.03.0830.01)] and (3.24) in (3.41) and after utilizing [187, eq. (07.34.21.0012.01)], $\bar{C}_{RF}$ is expressed as

$$\begin{aligned} \bar{C}_{RF} =& \frac{W_R \tilde{\alpha}}{\ln 2} \sum_{l=0}^{\infty} \sum_{m=0}^{l} \frac{c_l (-l)_m}{m!\, \Gamma(\mu+m)\, 2^{\mu-m} \overline{\gamma}_{RF}^{\tilde{\alpha}(\mu+m)}} \\ & \times H_{2\;3}^{3\;1} \left(\frac{1}{2\overline{\gamma}_{RF}^{\tilde{\alpha}}} \middle| \begin{matrix} (-\tilde{\alpha}(\mu+m),\tilde{\alpha}),(1-\tilde{\alpha}(\mu+m),\tilde{\alpha}) \\ (0,1),(-\tilde{\alpha}(\mu+m),\tilde{\alpha}),(-\tilde{\alpha}(\mu+m),\tilde{\alpha}) \end{matrix} \right), \end{aligned} \tag{3.42}$$

where $H_{p\;q}^{m\;n}(\cdot)$ represents the Fox's H-function [189]. Using [189, eq. (1.60)], the ergodic capacity of RF link can be further simplified as

$$\bar{C}_{RF} = \frac{W_R \tilde{\alpha}}{\ln 2} \sum_{l=0}^{\infty} \sum_{m=0}^{l} C_5\, H_{2\;3}^{3\;1} \left(\frac{1}{2\overline{\gamma}_{RF}^{\tilde{\alpha}}} \middle| \begin{matrix} (0,\tilde{\alpha}),(1,\tilde{\alpha}) \\ (\mu+m,1),(0,\tilde{\alpha}),(0,\tilde{\alpha}) \end{matrix} \right), \tag{3.43}$$

where $C_5 = \frac{c_l (-l)_m 4^m}{m!\, \Gamma(\mu+m)}$.

3.7 Asymptotic Analysis

The closed-form expressions derived for outage probability, average SER, and ergodic capacity are computationally very complex. To give more insights into the system behaviour, we have carried out the asymptotic analysis at high SNR values. The asymptotic expressions are computationally less complex and are also used to determine the SNR gain G_c and diversity gain G_d of the system.

3.7.1 Outage Probability

The asymptotic expression for the outage probability of hybrid FSO/RF system is calculated by assuming the average SNR of FSO link tending to infinity for a fixed value of RF average SNR and is given by

$$P_{out}^{H\infty} = F_{\gamma_{FSO}}^{\infty}(\gamma_{th})\, F_{\gamma_{RF}}(\gamma_{th})\,, \tag{3.44}$$

where $F_{\gamma_{RF}}(\gamma_{th})$ is given by (3.25) and by employing [187, eq. (07.34.06.0040.01)] in (3.20), $F_{\gamma_{FSO}}^{\infty}(\gamma_{th})$ is calculated as

$$F_{\gamma_{FSO}}^{\infty}(\gamma_{th}) = C_1 \sum_{d=1}^{\beta} t_d \sum_{u=1}^{3r} \left(\frac{B_M^r \gamma_{th}}{r^{2r}\overline{\gamma}_r}\right)^{K_{2,u}} \frac{\Lambda_1}{K_{2,u}}\,, \tag{3.45}$$

where $\Lambda_1 = \frac{\prod_{s=1;\, s\neq u}^{3r} \Gamma(K_{2,s}-K_{2,u})}{\prod_{s=1}^{r} \Gamma(K_{1,s}-K_{2,u})}$ and $K_{i,j}$ represents the j^{th} term of K_i. From (3.44) and (3.45), it is observed that $P_{out}^{H\infty} \propto (\overline{\gamma}_r)^{-G_d}$, where $G_d = \min\left(g^2/r, \alpha/r, 1/r\right)$. Thus, the diversity gain of the proposed hybrid FSO/RF system is given by G_d.

3.7.2 SER Analysis

The asymptotic expression for average SER of hybrid FSO/RF system is given by

$$P_e^{H\infty} = B_{FSO}^{\infty}(\gamma_{th}) + F_{\gamma_{FSO}}^{\infty}(\gamma_{th}) P_e^{RF}, \tag{3.46}$$

where $F_{\gamma_{FSO}}^{\infty}(\gamma_{th})$ is given by (3.45), P_e^{RF} is given by (3.35) and $B_{FSO}^{\infty}(\gamma_{th})$ is the asymptotic SER expression for FSO link during the non-outage period at high SNR. Similar to the asymptotic outage expression, Meijer G-function is expanded by its asymptotic form using [187, eq. (07.34.06.0040.01)] in order to calculate $B_{FSO}^{\infty}(\gamma_{th})$ and the same is given by

$$B_{FSO}^{\infty}(\gamma_{th}) = C_2 \sum_{d=1}^{\beta} t_d \sum_{u=1}^{3r} A_2^{K_{2,u}} \frac{\Gamma\left(K_{2,u}+\frac{1}{2}\right)\Lambda_1}{K_{2,u}} - \frac{A}{2} F_{\gamma_{FSO}}^{\infty}(\gamma_{th}) + C_2 \sum_{n=0}^{\infty} D_n \sum_{d=1}^{\beta} t_d \sum_{u=1}^{3r} \frac{A_1^{K_{2,u}}\Lambda_1}{\left(K_{2,u}+n+\frac{1}{2}\right)}. \tag{3.47}$$

Now the diversity gain and the SNR gain of the hybrid FSO/RF system are obtained for three different cases using the following theorems.

Theorem 3.1. *The diversity and SNR gains of the hybrid FSO/RF system for the case when the average SNR of RF link $\overline{\gamma}_{RF}$ is assumed to be a constant are, respectively, given by*

$$G_d^{(1)} = \min\left(g^2/r, \alpha/r, 1/r\right) \tag{3.48}$$

$$G_c^{(1)} = \left(\frac{r^{2r}}{B_M^r}\right)\left\{\sum_{d=1}^{\beta} t_d \Lambda_1 \left[C_1\left(P_e^{RF} - \frac{A}{2}\right)\frac{\gamma_{th}^{K_{2,u}}}{K_{2,u}} + C_2 \sum_{n=0}^{\infty} \frac{D_n \gamma_{th}^{K_{2,u}}}{K_{2,u}+n+\frac{1}{2}} + C_2 \frac{\Gamma(K_{2,u}+\frac{1}{2})}{(B^2)^{K_{2,u}} K_{2,u}}\right]\right\}^{-\frac{1}{K_{2,u}}} \tag{3.49}$$

Proof. As $\overline{\gamma}_{RF}$ is assumed to be a constant, the average SER of RF link P_e^{RF} will also be a constant. By fixing $\gamma_{th} = \gamma_{th}^{opt}$, where γ_{th}^{opt} is the optimum threshold SNR value, and from (3.45), (3.46) and (3.47), the asymptotic average SER in terms of average SNR of FSO link $\overline{\gamma}_r$ can be expressed as

$$\begin{aligned} P_e^{H\infty} &= \sum_{d=1}^{\beta} t_d \left(\frac{B_M^r}{r^{2r}\overline{\gamma}_r}\right)^{K_{2,u}} \Lambda_1 \left[C_1\left(P_e^{RF} - \frac{A}{2}\right)\frac{\gamma_{th}^{K_{2,u}}}{K_{2,u}}\right. \\ &+ \left. C_2 \sum_{n=0}^{\infty} \frac{D_n \gamma_{th}^{K_{2,u}}}{K_{2,u}+n+\frac{1}{2}} + C_2 \frac{\Gamma(K_{2,u}+\frac{1}{2})}{(B^2)^{K_{2,u}} K_{2,u}}\right], \end{aligned} \tag{3.50}$$

where $K_{2,u} = \min\left(g^2/r, \alpha/r, 1/r\right)$ is the dominating term in the asymptotic expression. Thus, the asymptotic average SER in terms of the coding and diversity gains can be expressed as

$$P_e^{H\infty} \approx (G_c \overline{\gamma}_r)^{-G_d} \tag{3.51}$$

By comparing (3.50) and (3.51), the diversity and SNR gain values of the hybrid FSO/RF system are, respectively, given by (3.48) and (3.49), respectively. Since the average SNR of RF link is assumed to be a constant, the diversity gain of hybrid system obtained in this case is equal to the diversity gain of FSO system. Thus, only SNR gain is achieved due to backup RF link. □

Theorem 3.2. *The diversity and SNR gains of the hybrid FSO/RF system for the case when $\overline{\gamma}_{RF} = \overline{\gamma}_r = \overline{\gamma}$ with constant threshold SNR value γ_{th} are, respectively, given by*

$$G_d^{(2)} = \min\left(g^2/r, \alpha/r, 1/r\right) \tag{3.52}$$

$$\begin{aligned} G_c^{(2)} &= \left(\frac{r^{2r}}{B_M^r}\right)\left\{\sum_{d=1}^{\beta} t_d \Lambda_1 \left[C_2 \frac{\Gamma(K_{2,u}+\frac{1}{2})}{(B^2)^{K_{2,u}} K_{2,u}}\right.\right. \\ &+ \left.\left. C_2 \sum_{n=0}^{\infty} \frac{D_n \gamma_{th}^{K_{2,u}}}{K_{2,u}+n+\frac{1}{2}} - \frac{A}{2} C_1 \frac{\gamma_{th}^{K_{2,u}}}{K_{2,u}}\right]\right\}^{-\frac{1}{K_{2,u}}} \end{aligned} \tag{3.53}$$

Proof. Here, we have assumed that the average SNR of RF link is varying and is equal to the average SNR of FSO link, i.e. $\overline{\gamma}_{RF} = \overline{\gamma}_r = \overline{\gamma}$. We have also fixed the switching threshold SNR value γ_{th} such that the value of γ_{th} is much lower as compared to $\overline{\gamma}$. As $\overline{\gamma}_{RF} \to \infty$, the dominating term in (3.35) is obtained by fixing $m = 0$ in the inner summation and after utilizing [187, eq. (07.34.06.0040.01)], the asymptotic expression for the average SER of RF link is given by

$$P_e^{RF\infty} = C_6 \sum_{l=0}^{\infty} c_l \Lambda_2 \left(\frac{1}{\overline{\gamma}_{RF}}\right)^{\tilde{\alpha}\mu}, \tag{3.54}$$

where $\Lambda_2 = \prod_{s=2}^{j} \Gamma(B_{2,s}) \prod_{s=i+1}^{2i} \Gamma(1-B_{1,s})$, $B_{1,s}$ and $B_{2,s}$ represent the s^{th} terms of B_1 and B_2, respectively, and $C_6 = \frac{A\, i^{\tilde{\alpha}\mu}\sqrt{j}}{2^{\mu+\frac{i+j}{2}} \pi^{\frac{i+j-1}{2}} \mu\Gamma(\mu)}$. In this case, it is highly likely that the hybrid FSO/RF will switch to RF link in the low-SNR region, but in the high-SNR region, it is least likely that the hybrid FSO/RF system will switch to RF link due to lower value of γ_{th} compared to $\overline{\gamma}$. Therefore, $P_e^{RF\infty}$ at high SNR values can be neglected from the asymptotic expression of hybrid FSO/RF system and only the FSO term will be dominating in such case. Thus, the diversity gain obtained here is same as the diversity gain of FSO system, which is given by (3.52). By neglecting P_e^{RF} term in (3.49), the SNR gain is given by (3.53). □

Theorem 3.3. *The diversity and SNR gains of the hybrid FSO/RF system for the case when* $\overline{\gamma}_{RF} = \overline{\gamma}_r = \overline{\gamma}$ *with* $\gamma_{th} = \gamma_{th}^{opt}$ *(i.e. obtaining* γ_{th}^{opt} *value corresponding to each* $\overline{\gamma}_{RF}$ *value) are, respectively, given by*

$$G_d^{(3)} = \min\left(\frac{g^2}{r} + \tilde{\alpha}\mu, \frac{\alpha}{r} + \tilde{\alpha}\mu, \frac{1}{r} + \tilde{\alpha}\mu\right) \tag{3.55}$$

$$G_c^{(3)} = \left(C_1 \sum_{d=1}^{\beta} t_d \frac{\Lambda_1}{K_{2,u}} \left(\frac{B_M^r \gamma_{th}}{r^{2r}}\right)^{K_{2,u}} C_6 \sum_{l=0}^{\infty} c_l \Lambda_2\right)^{-\frac{1}{K_{2,u}+\tilde{\alpha}\mu}} \tag{3.56}$$

Proof. In this case, γ_{th}^{opt} is obtained corresponding to each value of $\overline{\gamma}_{RF}$. Thus, there is a significant chance that the RF link will be activated even in the high-SNR region unlike the previous case. By substituting (3.54) in (3.46) in place of P_e^{RF} and considering the dominant terms, the asymptotic expression for the hybrid FSO/RF in terms of $\overline{\gamma}$ can be expressed as

$$P_e^{H\infty} \approx C_1 \sum_{d=1}^{\beta} t_d \frac{\Lambda_1}{K_{2,u}} \left(\frac{B_M^r \gamma_{th}}{r^{2r}}\right)^{K_{2,u}} C_6 \sum_{l=0}^{\infty} c_l \Lambda_2 \left(\frac{1}{\overline{\gamma}}\right)^{K_{2,u}+\tilde{\alpha}\mu} \tag{3.57}$$

Comparing (3.51) and (3.57), the diversity gain and the SNR gain are determined as (3.55) and (3.56), respectively. It is also to be noted that $G_d^{(3)}$ is the highest/full diversity gain value that can be obtained from the proposed hybrid FSO/RF system, as both FSO and RF links contribute in the diversity gain unlike the previous two cases. □

3.7.3 Capacity Analysis

The asymptotic capacity of the hybrid FSO/RF system is given by

$$\bar{C}^{\infty}_{hybrid} = \bar{C}^{\infty}_{FSO}(\gamma_{th}) + F^{\infty}_{\gamma_{FSO}}(\gamma_{th})\, \bar{C}_{RF} \tag{3.58}$$

where $\bar{C}_{RF}$ is given by (3.43), $F^{\infty}_{\gamma_{FSO}}(\gamma_{th})$ is given by (3.45), and $\bar{C}^{\infty}_{FSO}(\gamma_{th})$ represents the asymptotic capacity of FSO link during the non-outage period. By utilizing the method of moments, the asymptotic analysis for the average capacity of a certain transmission link can be carried out by calculating the first-order derivative of n^{th} order moment of the PDF of instantaneous SNR of a transmission link at $n = 0$. Firstly, the n^{th} order moment of the FSO link is given by

$$\mathbb{E}[\gamma^n] = \int_0^{\infty} \gamma^n f_{\gamma_{FSO}}(\gamma) d\gamma = \frac{r\, g^2 A_M \Gamma(\alpha + r\, n)}{2^r (g^2 + r\, n)} \left(\frac{\varepsilon_r\, \overline{\gamma}_r}{B_M^r}\right)^n \sum_{d=1}^{\beta} b_d \Gamma(d + r\, n) \tag{3.59}$$

Taking the first order derivative of (3.59) at $n = 0$, we get the asymptotic expression for the ergodic capacity of FSO link $\bar{C}^{\infty}_{FSO}$ and the same is given by

$$\begin{aligned} \bar{C}^{\infty}_{FSO} \approx \left.\frac{\partial\, \mathbb{E}[\gamma^n]}{\partial n}\right|_{n=0} &= \frac{r\, \Gamma(\alpha) A_M}{2^r} \sum_{d=1}^{\beta} b_d\, \Gamma(d) \Bigg\{ r \left[\psi(\alpha) + \psi(d) - \frac{1}{g^2}\right] \\ &+ \log_2\left(\frac{\varepsilon_r\, \overline{\gamma}_r}{B_M^r}\right) \Bigg\}, \end{aligned} \tag{3.60}$$

where $\psi(\cdot)$ denotes the psi function [186, eq. (8.360)]. The asymptotic capacity of FSO link during the non-outage period assuming constant RF average SNR by applying [187, eq. (07.34.06.0040.01)] in (3.40) is given by

$$\begin{aligned} \bar{C}^{\infty}_{FSO}(\gamma_{th}) = \bar{C}^{\infty}_{FSO} - \log_2(z) F^{\infty}_{\gamma_{FSO}}(\gamma_{th}) - \Bigg[C_4 \sum_{d=1}^{\beta} t_d \sum_{n=1}^{\infty} \frac{(-1)^{n-1}}{n\, z^n} \\ \times \sum_{i=0}^{n} \binom{n}{i} (1-z)^{n-i} \varepsilon_r^i \gamma_{th}^i \sum_{u=1}^{3r} \frac{\Lambda_1 A_1^{K_{2,u}}}{(K_{2,u} + i)} \Bigg]. \end{aligned} \tag{3.61}$$

Table 3.3: Simulation parameters of FSO and RF links

FSO/RF Parameter	**Symbol**	**Value**	
Wavelength FSO	λ_f	1550 nm	
FSO transmit Power	P_F	40 mW	
RF transmit Power	P_R	10 mW	
Responsivity	η_f	0.5 A/W	
Noise variance FSO	σ	10^{-14}	
Jitter standard deviation	σ_s	30 cm	
Phase difference	$\phi_A - \phi_B$	$\pi/2$	
Weather dependent parameters of FSO and RF links			
Weather condition	$\boldsymbol{\zeta_w}$ **(dB/km)**	$\boldsymbol{\zeta_{rain}}$ **(dB/km)**	$\boldsymbol{C_n^2 (m^{-2/3})}$
Clear air	0.43	0	5×10^{-14}
Light fog	4.2	0	1.7×10^{-14}
Moderate rain	5.8	5.6	5×10^{-15}

3.8 Numerical Results and Discussion

In this section, the analytical and simulation results of the performance metrics are presented for the proposed hybrid FSO/RF system under different system configurations. In our simulations, it is assumed that $\rho = 0.596$, $\Omega = 1.3265$, $b_0 = 0.1079$, and $\overline{\gamma}_{RF} = 5$ dB, unless and otherwise stated. The list of FSO and RF parameters considered in the simulations are given in Table 3.3. The truncation accuracy of the summation limits n and l are listed in Table 3.4 along with the corresponding values of the average SER and the ergodic capacity for $\overline{\gamma}_r = 5$ dB and 15 dB. From the Table 3.4, it is inferred that the maximum value of the infinite summation limits of average SER P_e^H can be truncated to $n = 20$ and $l = 30$, as $n > 20$ and $l > 30$ do not have an impact on the fifth decimal figure of the SEP values. Similarly, the maximum value of the infinite summation limits of ergodic capacity $\overline{C}_{hybrid}$ can be truncated to $n = 24$ and $l = 24$, as $n > 24$ and $l > 24$ do not have an impact on the fourth decimal figure of the capacity values.

Table 3.4: Truncation Accuracy of Summation Limits

Expressions	**Truncation values**		**Final values of expressions**	
	n	l	$\overline{\gamma}_r = 5$ dB	$\overline{\gamma}_r = 15$ dB
P_e^H	10	10	0.006929	0.007646
	15	20	0.000072	0.000011
	20	30	0.000127	0.000079
	25	35	0.000126	0.000079
	30	40	0.000127	0.000079
$\overline{C}_{hybrid}$	10	10	2.80901	3.69061
	15	15	2.82002	3.69641
	24	24	2.81845	3.69641
	28	28	2.81848	3.69642
	30	30	2.81848	3.69641

3.8.1 Optimum Values of Beam Width and Switching Threshold SNR

The optimum values of beam width and switching threshold SNR of hybrid FSO/RF system are obtained using numerical optimization method. In Fig. 3.2(a), to obtain the optimum value of threshold SNR γ_{th}^{opt}, the average SER of hybrid FSO/RF system is plotted against the threshold SNR. The optimum value of threshold SNR γ_{th}^{opt} is chosen corresponding to the value for which the average SER is minimum. In Fig. 3.2(a), we assume that the FSO link is modeled as Malaga distribution and RF link is modeled as α-η-κ-μ distribution in which the optimum threshold value is obtained as $\gamma_{th}^{opt} = 1$ dB. In addition, the optimum threshold values are obtained for other cases also using the same method. It is observed that the optimum switching threshold SNR γ_{th}^{opt} varies with the parameters of RF link and it remains same irrespective of the variations in the FSO link parameters. The main reason is given as follows: When the quality of available RF link is good, then to achieve minimum SEP, the optimum threshold value should increase. This is due to the fact that when γ_{th}^{opt} increases, the FSO system will be in outage frequently and hence, RF link will be used with higher probability. This will improve the overall performance by nullifying the FSO channel distortions.

In Fig. 3.2(b), the average SER is plotted against the beam width for different values of aperture radius a to obtain the optimum values of beam width w_0^{opt}. The FSO link parameters taken into consideration are as follows: $C_n^2 = 1 \times 10^{-13}$, $L = 3000$ m, and average SNR $\overline{\gamma}_r = 40$ dB. Similarly, the RF parameters assumed here are as follows: $\alpha_R = 1$, $\eta = 2$, $\kappa = 0.5$, $\mu = 2.5$, $p = 1$, $q = 1$, $\overline{\gamma}_{RF} = 5$ dB and $\gamma_{th}^{opt} = 2$ dB. From Fig. 1(b), it is observed that the minimum value of SER occurs at $w_0 = 4$ cm for $a = 35, 40, 45, 50$ cm. Hence, the optimum beam width value remains same irrespective of the variation in the receive aperture radius. In a similar way, w_0^{opt} values are obtained for other cases.

Fig. 3.3(a), shows the ergodic capacity of hybrid FSO/RF system versus switching threshold SNR γ_{th}. The threshold SNR for which the capacity reaches the maximum value is chosen as the capacity optimal switching threshold SNR γ_{th}^{opt}. The FSO link parameters are assumed as $C_n^2 = 2 \times 10^{-13}$, $L = 1000$ m, $a = 13$ cm, $w_0 = 2$ cm and $\overline{\gamma}_r = 10$ dB. Similarly, the RF links parameters assumed here are as follows: $\alpha_R = 1$, $\eta = 1.5$, $\kappa = 0.25$, $\mu = 0.5$, $p = 1$, $q = 1$. Here, we have taken different values of average SNR of RF link and the corresponding values of the optimum switching threshold SNR γ_{th}^{opt} are obtained as $3, 7, 10,$ and 13 dB for $\overline{\gamma}_{RF} = 0, 5, 10,$ and 15 dB, respectively. The ergodic capacity is plotted against the beam width in Fig. 3.3(b) for different values of receive aperture radius a to obtain the optimum values of beam width w_0^{opt} for $L = 3000$ m. Here, the FSO links parameters assumed are $C_n^2 = 1 \times 10^{-13}$ and $\overline{\gamma}_r = 40$ dB. Similarly, the RF link parameters assumed are $\alpha_R = 1$, $\eta = 2$, $\kappa = 0.5$, $\mu = 2.5$, $p = 1$, $q = 1$, $\overline{\gamma}_{RF} = 5$ dB and $\gamma_{th}^{opt} = 2$ dB. From Fig. 3.3(b), it is observed that the maximum value of capacity occurs at $w_0 = 4$ cm for receive aperture radius values $a = 35, 40, 45, 50$ cm, which is exactly the same optimum value of w_0 obtained in Fig 3.2(b).

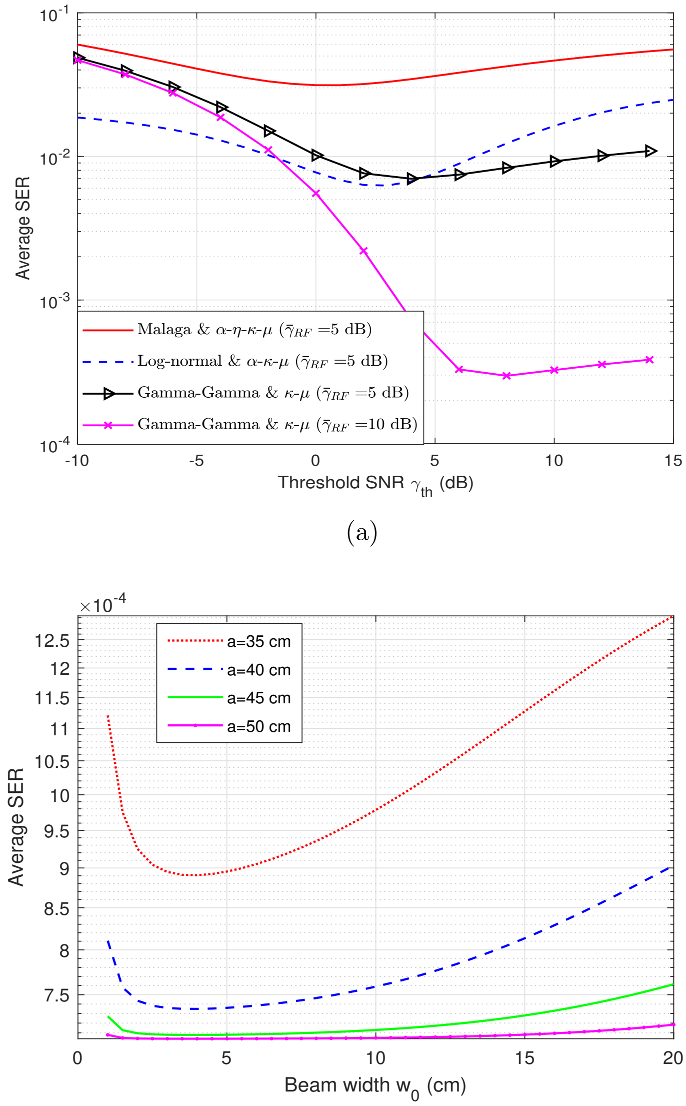

(a)

(b)

Fig. 3.2: Average SER versus switching threshold SNR γ_{th} and beam width w_0

3.8.2 Outage and Average SER Performances

Remark 3.1. *It is to be noted that the performances of hybrid FSO/RF system over different distributions assumed in Fig. 3.2 and Fig. 3.4 are not meant for comparison. In particular, the performance curves in Fig. 3.5 illustrate various distributions that can be obtained as special cases using the generalized Malaga and* α-η-κ-μ *distributions. Thus, it is inferred that the performance analysis of the hybrid FSO/RF system assuming generalized distributions for modeling FSO and RF channels will*

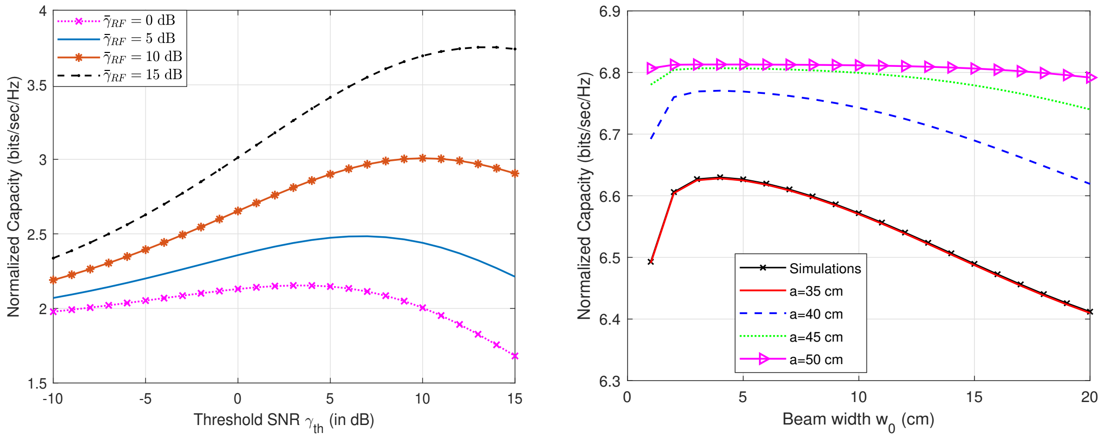

(a) (b)

Fig. 3.3: Ergodic capacity versus switching threshold SNR γ_{th} and beam width w_0

Table 3.5: List of FSO and RF distributions and their parameters

FSO distribution	**Parameter value**
Log-normal	$\rho = 0,\ y \to 0$
Gamma–Gamma	$\rho = 1,\ \Omega' = 1,\ y = 0$
K distribution	$\rho = 0,\ \Omega = 0$

RF distribution	$\boldsymbol{\alpha_R}$	$\boldsymbol{\eta}$	$\boldsymbol{\kappa}$	$\boldsymbol{\mu}$
α-κ-μ	α_R	p	κ	μ
κ-μ	2	p	κ	μ
Rice	2	p	k	1
Nakagami-m	2	p	0	m

be very much useful to analyze the system performance over numerous terrestrial and satellite communication scenarios, where the individual channel models such as Gamma–Gamma, lognormal, K, Nakagami-m distributions, etc. up to now cannot offer. It is also to be noted that the performance of hybrid FSO/RF system over different distributions mainly depends on turbulence or fading conditions and the related parameters are given in Table 3.6.

Fig. 3.4(a) and 3.4(b) show the outage probability and average SER of hybrid FSO/RF system for different distributions that can be derived as special cases of Malaga distribution and α-η-κ-μ distribution. The values of the parameters used to obtain other distributions from the generalized Malaga and α-η-κ-μ distributions are given in the Table 3.5. We assume BPSK modulation scheme and IM/DD technique. From the plots, it is observed that all the analytical results are matching with the Monte-Carlo simulation results, which justify the correctness of our theoretical analysis. Moreover, it is also observed that at high-SNR region, the asymptotic SER

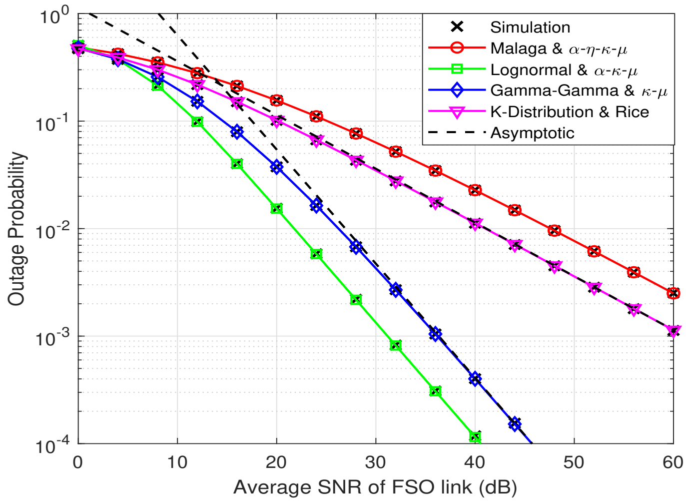

(a)

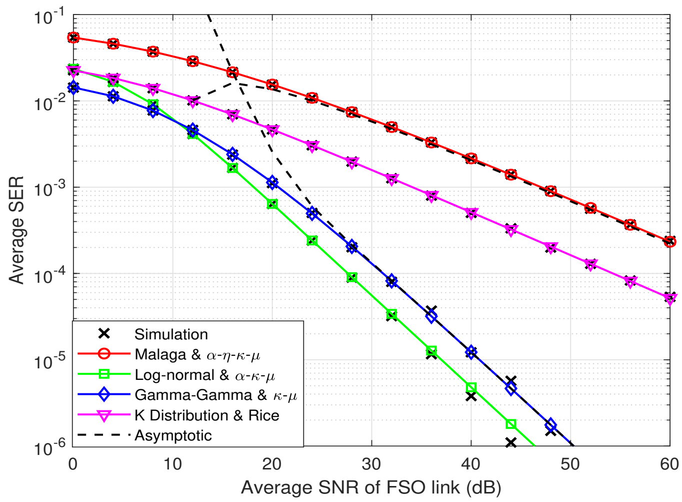

(b)

Fig. 3.4: Outage probability and average SER versus average SNR of FSO link for different distributions

and outage curves are tight enough to match the exact performance curves. Further, there are bends in the asymptotic curves shown in Fig. 3.4 and 3.7 particularly in the low-SNR region. This is due to the fact which is explained as follows : The asymptotic outage and SER expressions depend on the powers of $1/\overline{\gamma}_r$. Therefore, in the high-SNR region, the asymptotic curves will converge and tend to match the exact analytical results as observed in Fig. 3.4 and 3.7. However, in the low-SNR region, the asymptotic performance parameter values are generally unpredictable and they depend on the number of dominant terms taken into consideration in the

Table 3.6: List of channel models and parameters assumed to obtain Fig. 3.4

FSO models	$\mathbf{C_n^2(m^{-2/3})}$	$\boldsymbol{\rho}$	$\boldsymbol{\Omega}$	$\mathbf{b_0}$	**a (cm)**	$\mathbf{w_0^{opt}}$ **(cm)**	$\boldsymbol{\gamma_{th}^{opt}}$ **(dB)**
Malaga	1×10^{-13}	0.596	1.3265	0.1079	35	4	1
Log-normal	4×10^{-15}	0	1.3265	0	16	2	3
Gamma–Gamma	1×10^{-14}	1	1	0	18	2	4
K distribution	4×10^{-12}	0	0	0.1079	20	2	3

RF models	$\boldsymbol{\alpha_R}$	$\boldsymbol{\eta}$	$\boldsymbol{\kappa}$	$\boldsymbol{\mu}$	**p**	**q**
α-η-κ-μ	1	1	0.75	2	1	1
α-κ-μ	2	1	2	1.5	1	1
κ-μ	2	1	1.5	3	1	1
Rice	2	1	4	1	1	1

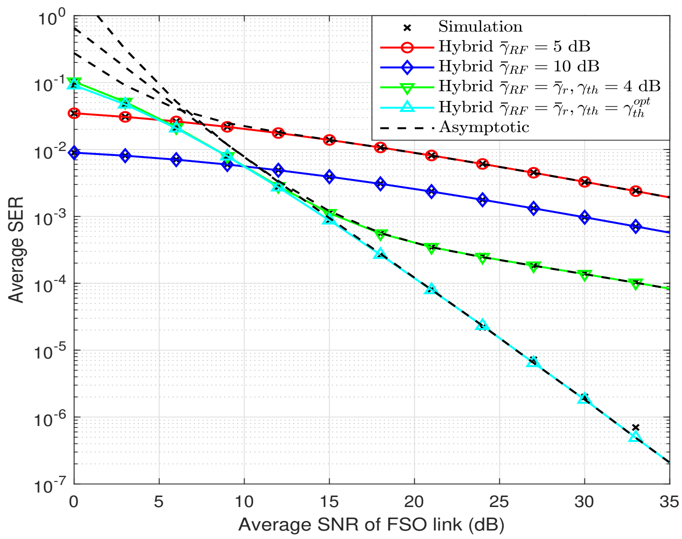

Fig. 3.5: Asymptotic and average SER performance plots for different values of switching threshold SNR and RF average SNR

asymptotic expressions. This will sometime result in bending of the asymptotic curves near the low-SNR region in some scenarios. The values of the parameters used to obtain the plots in Fig. 3.4 are given in Table 3.6.

Fig. 3.5 shows the average and asymptotic SER performances of hybrid FSO/RF system considering different $\overline{\gamma}_{RF}$ values. We assume four different cases, which are given as follows: 1) $\overline{\gamma}_{RF} = 5$ dB and $\gamma_{th} = \gamma_{th}^{opt}$, 2) $\overline{\gamma}_{RF} = 10$ dB and $\gamma_{th} = \gamma_{th}^{opt}$, 3) $\overline{\gamma}_{RF} = \overline{\gamma}_r$ and $\gamma_{th} = 4$ dB, and 4) $\overline{\gamma}_{RF} = \overline{\gamma}_r$ and $\gamma_{th} = \gamma_{th}^{opt}$. From Fig. 3.5, it is observed that the hybrid FSO/RF system with $\overline{\gamma}_{RF} = 10$ dB (i.e. case 2) performs better than the system with $\overline{\gamma}_{RF} = 5$ dB (i.e. case 1) due to the availability of better quality RF link. It is also observed that the performance of the hybrid system for the case when $\overline{\gamma}_{RF} = \overline{\gamma}_r$ and $\gamma_{th} = 4$ dB (i.e. case 3) is better as compared to case 1 and 2, especially in the high-SNR region, and degradation in the performance is noticed with respect to case 3 in the low-SNR region. This is because, when the average SNR of RF link also varies with the average SNR of FSO link (i.e. $\overline{\gamma}_{RF} = \overline{\gamma}_r$), the performance deteriorates till $\overline{\gamma}_{RF} = 5$ dB and 10 dB compared to case 1 and case 2, respectively, due to degradation in the quality of RF link. It is also observed that the slope of the asymptotic SER curve for case 3 in the high-SNR region is similar to the slope of the curves for case 1 and 2. Consequently, the diversity gains of the hybrid FSO/RF system for case 1, 2 and 3 are equal and is equal to the diversity gain of FSO system, which is given by $\min(g^2/2, \alpha/2, 1/2)$ as mentioned Theorem 1 and 2 assuming IM/DD scheme.

Therefore, if $\overline{\gamma}_{RF}$ is a constant (i.e. case 1 and 2), then the backup RF link in the hybrid system will contribute only to the SNR gain and the diversity gain obtained will be equal to the diversity gain of FSO system. This is due to the fact that when $\overline{\gamma}_{RF}$ is a constant, the optimum switching threshold SNR value γ_{th}^{opt} is also fixed. Thus, the probability that the instantaneous SNR of FSO link γ_{FSO} falls below fixed γ_{th}^{opt} is very less in the high-SNR region, as $\overline{\gamma}_r >> \gamma_{th}^{opt}$ and the FSO link will remain active for most of the occasion. Hence, only FSO link contributes to the diversity gain of the hybrid FSO/RF system. The above inference is also applicable to case 3, since only the FSO link contributes to the diversity gain of hybrid system even with varying $\overline{\gamma}_{RF}$. This is mainly due to fixed γ_{th} and hence, there is a very less chance that the hybrid FSO/RF system will switch to RF link in the high-SNR region.

It is noted that the best SER performance is obtained for the case when $\overline{\gamma}_{RF} = \overline{\gamma}_r$ and $\gamma_{th} = \gamma_{th}^{opt}$ (i.e. case 4) especially in the high-SNR region compared to all other cases. It is also noticed that the system exploits the full diversity gain as mentioned in Theorem 3. This is due to the fact that when $\overline{\gamma}_{RF}$ varies with $\overline{\gamma}_r$ and if $\gamma_{th} = \gamma_{th}^{opt}$

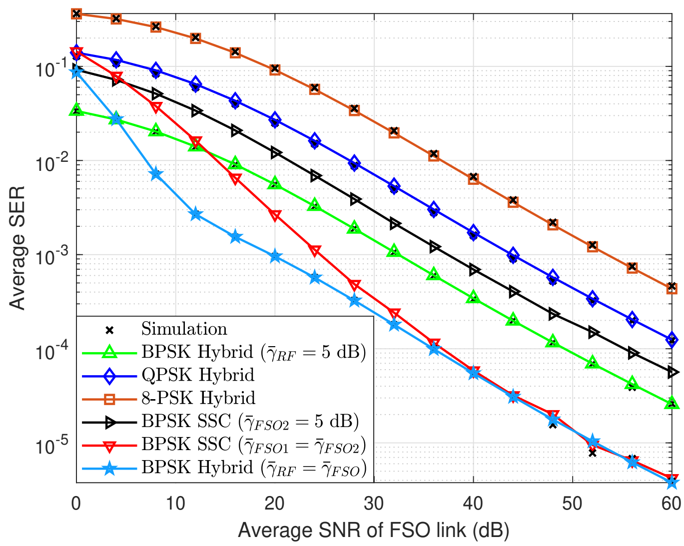

Fig. 3.6: Average SER performance of hybrid FSO/RF system for different modulation schemes

unlike case 3, then the optimum switching threshold SNR also increases with $\overline{\gamma}_{RF}$ as noticed in Fig. 3.2(a). So the probability that $\gamma_{FSO} < \gamma_{th}^{opt}$ or the probability that the hybrid system will switch to RF link is higher compared to case 3 especially in the high-SNR region. Therefore, both FSO and RF links will contribute to the diversity gain of the hybrid FSO/RF system due to which full diversity gain, which is equal to $\min\left(\frac{g^2}{r} + \tilde{\alpha}\mu, \frac{\alpha}{r} + \tilde{\alpha}\mu, \frac{1}{r} + \tilde{\alpha}\mu\right)$, is obtained from case 4. Finally, the obtained diversity gain values from Theorem 1, 2, and 3 are validated using the asymptotic SEP curves, as they are tight enough to match the exact curves at the high-SNR region.

In Fig. 3.6, the average SER performance is given for different modulation schemes for the hybrid FSO/RF system considering the IM/DD technique. Also, we have compared the proposed hybrid FSO/RF system with the FSO-based switch-and-stay combining (SSC) scheme [127] assuming two receive apertures and one transmit aperture. In case of SSC, if the instantaneous SNR of first FSO link (i.e. active link) drops below a particular threshold SNR value, then the transmission switches to the second FSO link regardless of its instantaneous SNR. Here, the second FSO link is used as a backup for the first FSO link. The performance plots for hybrid FSO/RF and SSC systems are obtained for two different scenarios, i.e. fixed average SNR scenario with $\overline{\gamma}_{RF} = \overline{\gamma}_{FSO2} = 5$ dB and varying average SNR

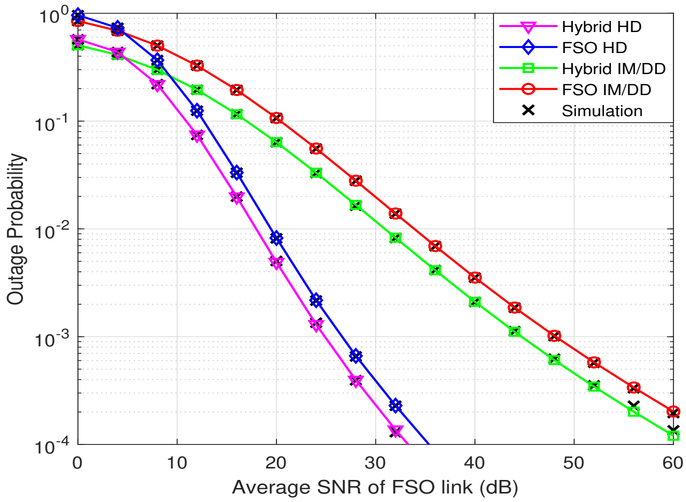

(a)

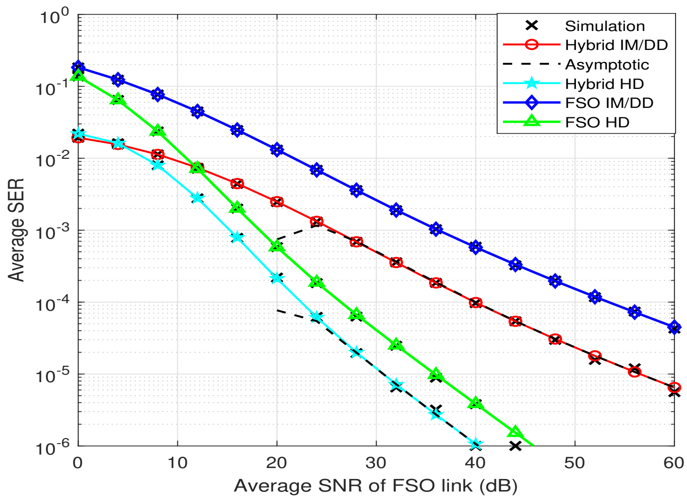

(b)

Fig. 3.7: Performance comparison of hybrid FSO/RF and single-link FSO systems for both the detection schemes

scenario with $\overline{\gamma}_{RF} = \overline{\gamma}_r$ and $\overline{\gamma}_{FSO1} = \overline{\gamma}_{FSO2} = \overline{\gamma}_r$, where $\overline{\gamma}_{FSO1}$ and $\overline{\gamma}_{FSO2}$ are the average SNRs of first and second FSO links of SSC scheme, respectively. From the performance curves, it can be clearly seen that the performance of the hybrid system decreases with increase in modulation order M, as expected. From Fig. 3.6, it is also inferred that the hybrid FSO/RF system outperforms the FSO-based SSC scheme in both the scenarios. Further, this performance improvement is mainly due to the usage of reliable RF backup in case of hybrid system, which performs better than FSO backup link in case of SSC scheme.

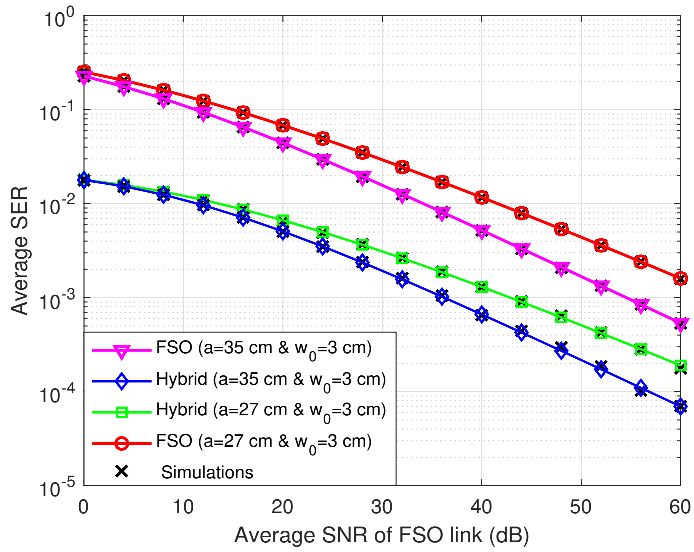

Fig. 3.8: Average SER performance of hybrid FSO/RF and FSO systems for different pointing error coefficient values

Fig. 3.7 shows the performance comparison of FSO, hybrid FSO/RF systems considering both IM/DD and HD schemes with asymptotic curves. We assume $C_n^2 = 1 \times 10^{-13}$ (i.e. the strong turbulence condition), $L = 1000$ m, $a = 11$ cm, $w_0^{opt} = 2$ cm. The parameters of RF link are assumed as $\alpha_R = 1.5$, $\eta = 2$, $\kappa = 0.75$, $\mu = 2$, $p = 5$, $q = 1$, $\overline{\gamma}_{RF} = 5$ dB, and $\gamma_{th}^{opt} = 2$ dB. In Fig. 3.7(a), the outage performance of hybrid FSO/RF system is compared with FSO system. The SNR gain values obtained from hybrid FSO/RF system over FSO system due to the RF backup link to achieve an outage probability of 10^{-3} for IM/DD and HD schemes are 3 dB and 2 dB, respectively. Similar trends can be seen from the average SER plots shown in Fig. 3.7(b). The performance of HD technique is significantly greater as compared to IM/DD technique, especially in high-SNR region, due to its coherent detection nature. From Fig. 3.7(b), it is observed that the hybrid FSO/RF system offers SNR gain values of about 7 dB and 3 dB over single-link FSO system to achieve an average SER of 10^{-2} for IM/DD and HD techniques, respectively. From Fig. 3.7(b), it is also observed that at the high-SNR region, the asymptotic SER curves are tight enough to match the exact SER curves. Thus, hybrid FSO/RF system with IM/DD scheme provides better SNR gain as compared to HD scheme over single-link FSO system.

Fig. 3.8 shows the effect of pointing errors on the performance of hybrid FSO/RF system by varying pointing error coefficient. It is to be noted that the pointing error coefficient indirectly depends on aperture radius a and beam width w_0 as given in (3.10). The detection technique assumed is IM/DD and the FSO and RF parameters assumed are $C_n^2 = 2 \times 10^{-13}$, $L = 2000$ m, $\alpha_R = 1$, $\eta = 1.5$, $\kappa = 5$, $\mu = 3.25$, $p = 1$, $q = 1$, $\overline{\gamma}_{RF} = 5$ dB, and $\gamma_{th}^{opt} = 3$ dB. The performance of hybrid FSO/RF system is shown for two cases, which are given as follows: (1) $a = 27$ cm, $w_0^{opt} = 3$ cm, and $g = 1.03$ (2) $a = 35$ cm, $w_0^{opt} = 3$ cm, and $g = 2.5$. Note that the severity of pointing errors is high for low values of g and hence, for both FSO and hybrid systems degradation in the performance is noticed for $g = 1.03$ compared to $g = 2.5$. From Fig. 3.8, it is also observed that to achieve the average SER of 10^{-2}, the SNR gain values obtained using hybrid FSO/RF system over FSO system are 5 dB and 2 dB for $g = 1.03$ and $g = 2.5$, respectively. The hybrid system provides better system performance over FSO system in both the cases and it is also noticed that better SNR gain is achieved for the case when the severity of pointing errors is high.

Fig. 3.9(a) shows the average SER versus average SNR of FSO link for strong and weak turbulence conditions. For strong turbulence condition, we assume $C_n^2 = 1 \times 10^{-13}$, $\alpha = 2.18$, $\beta = 1$, $a = 45$ cm, and $w_0^{opt} = 4$ cm and for weak turbulence condition, we assume $C_n^2 = 4 \times 10^{-15}$, $\alpha = 8.9$, $\beta = 8$, $a = 15$ cm, and $w_0^{opt} = 4$ cm. The other parameters assumed are given as follows: $L = 3000$ m, $\alpha_R = 2$, $\eta = 2$, $\kappa = 2$, $\mu = 3$, $p = 1$, $q = 1$, and $\overline{\gamma}_{RF} = 5$ dB. We have obtained the same optimum threshold value, which is given by $\gamma_{th}^{opt} = 4$ dB, for both the turbulence conditions. From the plots, it is observed that the hybrid FSO/RF system outperforms the single-link FSO system under both the turbulence conditions. In Fig. 3.9(a), the SNR gains obtained from hybrid FSO/RF system due to RF backup link compared to FSO system to achieve the average SER of 10^{-3} are 21 dB and 5 dB for strong and weak turbulence conditions, respectively. It can be assessed that the hybrid FSO/RF system provides much better SNR gain under strong turbulence condition compared to weak turbulence condition.

The reason behind achieving higher SNR gain under strong turbulence condition

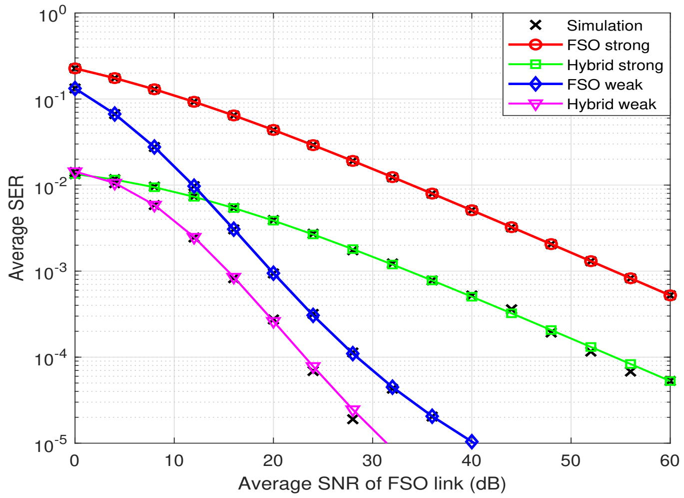

(a)

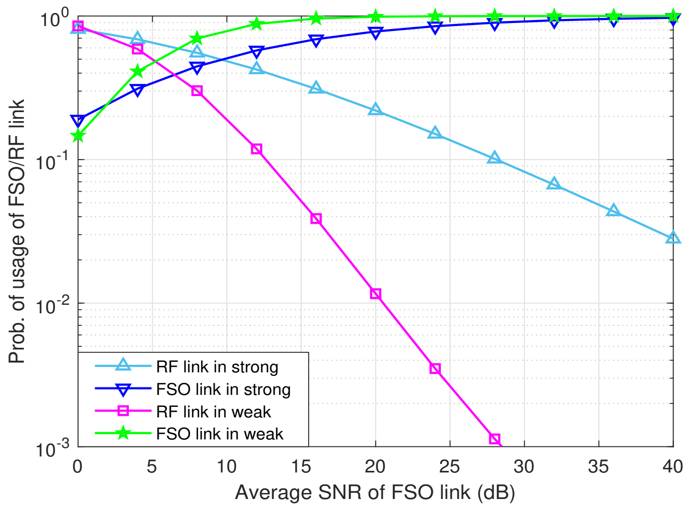

(b)

Fig. 3.9: Average SER and probability of usage of FSO/RF link versus average SNR of FSO link for different turbulence conditions

has been explained using Fig. 3.9(b). Here, the probability of usage of FSO/RF link versus average SNR of FSO link under strong and weak turbulence conditions is shown. It is clearly observed that the probability of usage of FSO link is higher under weak turbulence condition compared to strong turbulence condition. As the FSO link is less prone to channel distortions under weak turbulence condition, the probability that the FSO system switches to RF link in case of hybrid system is less as evident from Fig. 3.9(b). Moreover, it is also noticed from Fig. 3.9(b) that the probability of usage of FSO link is less under strong turbulence condition. This is due to the fact that when the FSO link is more prone to atmospheric channel distortions, then the probability that the FSO system switches to RF link in case of hybrid system is high. Since the hybrid FSO/RF system switches to RF link with higher probability under strong turbulence condition compared to weak turbulence, high SNR gain due to backup RF link is achieved. This is also exactly the same reason behind achieving better SNR gain for the case when the severity of pointing errors is high as inferred in Fig. 3.8. Note that the probability of usage of RF and FSO links is evaluated from the outage and non-outage probabilities of FSO link, respectively. Moreover, considerable improvement in the performance of hybrid FSO/RF system is observed in the low-SNR region compared to FSO system as shown in Fig. 3.9(a). This is because, the probability of usage of RF link is very high compared to FSO link in the low-SNR region as noticed in Fig. 3.9(b).

In Fig. 3.10(a) and 3.10(b), the outage probability and average SER plots versus the FSO transmit power are shown for various weather conditions as given in Table 3.3. Here, we assume two scenarios of weather condition (i.e. moderate fog and rain) for both single-link FSO and hybrid FSO/RF systems. It is observed from Fig. 3.10 that the single-link FSO system performs better under rainy condition compared to moderate foggy condition in terms of both outage and average SER, as expected. This is because, the FSO link is more prone to foggy scenario compared to rainy scenario due to high attenuation values. It is also noticed that the hybrid FSO/RF system outperforms the single-link FSO system in both the weather conditions. From Fig. 3.10(a), it is also observed that the outage performance of hybrid FSO/RF system under moderate foggy condition is better than rainy condition when the transmit power is less than -15 dBm and vice-a-versa when the transmit power is more than -15 dBm. Similarly, in Fig. 3.10(b), when the transmit power is below -18 dBm, it is observed that the average SER of hybrid system under moderate foggy condition is less than the hybrid system under rainy condition and the observation is vice-a-versa when the transmit power is above -18 dBm. This is because, when the transmit power is high, then the FSO link will be used with higher probability compared to the RF link as shown in Fig. 3.11. Since the FSO

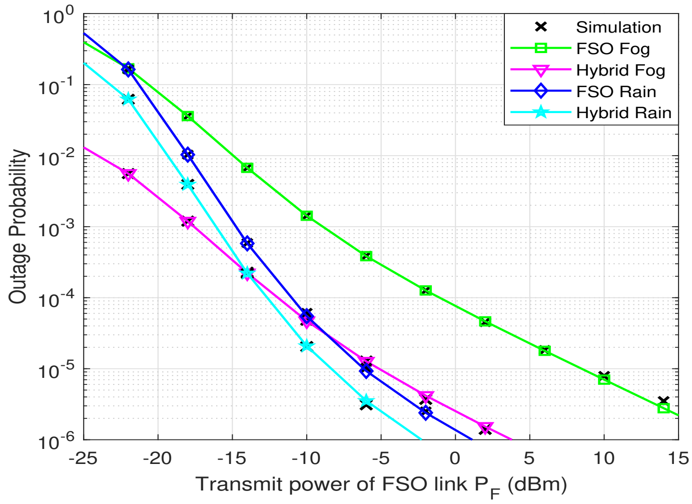

(a)

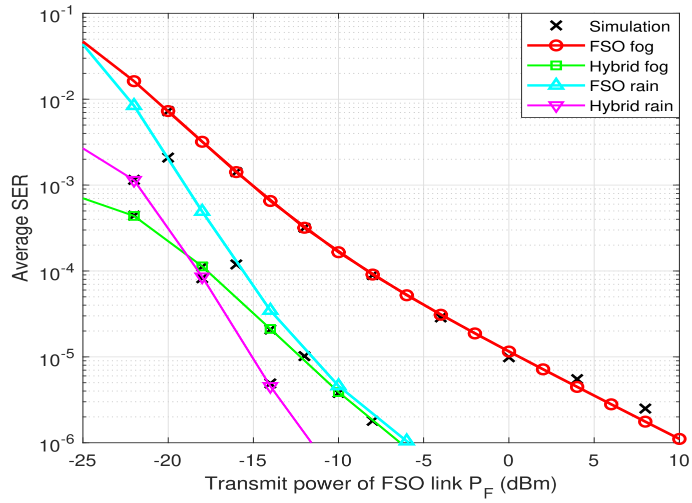

(b)

Fig. 3.10: Outage probability and average SER versus transmit power of FSO link for different weather conditions

link performance deteriorates under foggy condition compared to rainy condition, improvement in the performance is noticed for hybrid FSO/RF system under rainy condition. Similarly, when the transmit power is less, then the RF link will be used with higher probability, which is also observed in Fig. 3.11. Since the RF link is more prone to rainy condition compared to foggy condition, improvement in the performance of the hybrid system is noticed for foggy condition compared to rainy condition. From Fig. 3.10(a), the SNR gain values obtained using hybrid FSO/RF system over FSO system to achieve the outage probability of 10^{-3} under moderate foggy and rainy conditions are 9 dBm and 2 dBm, respectively. Similarly in Fig.

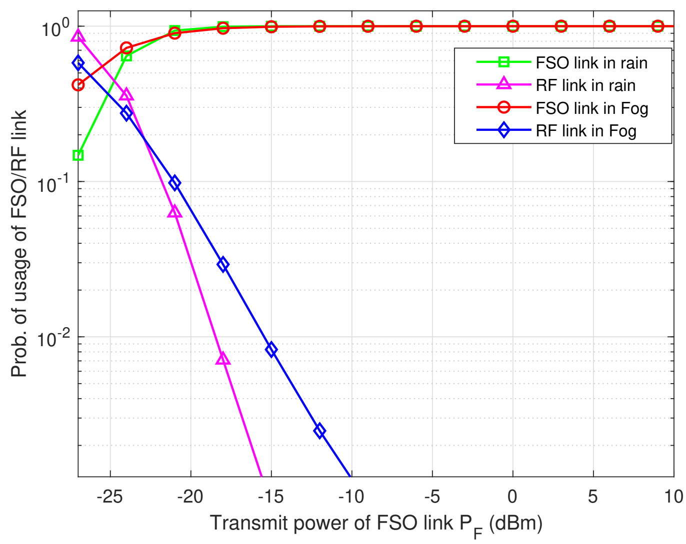

Fig. 3.11: Switching probability versus average SNR of FSO link under different weather conditions

3.10(b), the hybrid FSO/RF system offers the SNR gains of around 9 dBm and 3 dBm over FSO system to achieve the average SER of 10^{-4} under moderate foggy and rainy conditions, respectively. Hence, the backup RF link in hybrid FSO/RF system offers more SNR gain under moderate foggy condition compared to rainy condition.

Fig. 3.11 shows the probability of usage of FSO/RF link versus the transmit power of FSO link for different weather conditions. As evident from the figure, the probability of usage of RF link under moderate foggy condition is higher compared to rainy condition especially for the case when the transmit power is more than -22 dBm. This is due to the fact that the FSO link is more prone to atmospheric attenuation due to fog. Therefore, the probability that the FSO system switches to RF link is high. Since RF link is less sensitive to attenuation due to fog, high SNR gain is achieved due to backup RF link as mentioned in previous paragraph.

Fig. 3.12 shows the performance of hybrid FSO/RF system for different link distance values L under moderate turbulence condition with $C_n^2 = 4\times10^{-14}$ assuming two different values of average SNR of RF link (i.e. $\overline{\gamma}_{RF} = 5$ dB and 10 dB). The RF link parameters are assumed as $\alpha_R = 0.75$, $\eta = 2$, $\kappa = 0.5$, $\mu = 2.5$, $p = 1$, and $q = 1$. The optimum threshold values are obtained as $\gamma_{th}^{opt} = 0$ dB and $\gamma_{th}^{opt} = 2$ dB, respectively, for $\overline{\gamma}_{RF} = 5$ dB and 10 dB. It is observed that for shorter link distance

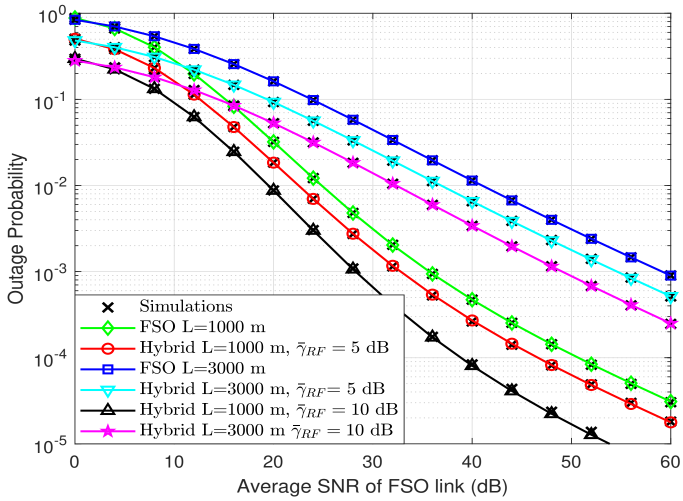

(a)

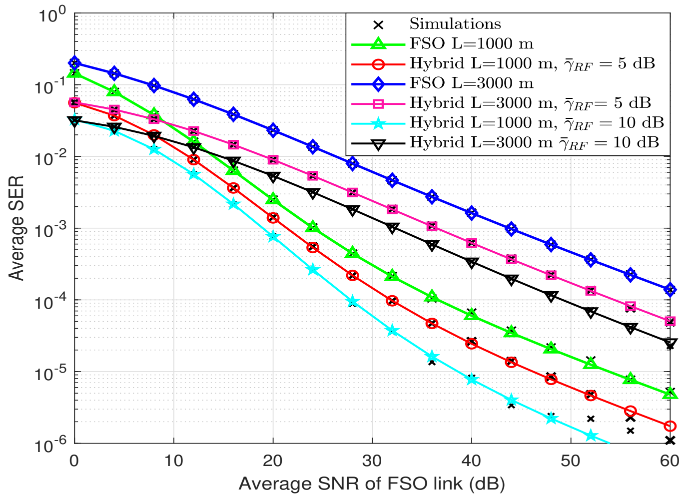

(b)

Fig. 3.12: Outage and average SER performance of hybrid FSO/RF system for different values of link distance and average SNR of RF link

values, the hybrid FSO/RF system provides better performance as compared to longer distance values. This is due to the fact that if the link distance increases, then the values of scattering parameters α and β will decrease, which will make the system sensitive to strong turbulence condition and thus affects the performance of the hybrid system to a greater extent. It is also noticed that higher SNR gain is obtained from the hybrid FSO/RF system compared to the single-link FSO system for large values of link distance L. The reason behind this phenomenon is the same as explained using Fig. 3.9(b). When the link distance is large, the FSO link is more prone to channel distortions and hence, the probability of usage of RF link is

Table 3.7: List of channel models and parameters assumed to obtain Fig. 3.13

FSO models	**a (cm)**	$\mathbf{w_0^{opt}}$ **(cm)**	γ_{th}^{opt} **(dB)**	**RF models**	α_R	η	κ	μ	**p**	**q**
Malaga	45	4	6	α-η-κ-μ	1	2	0.5	0.5	1	1
Log-normal	16	4	7	α-κ-μ	3	1	0	0.75	1	1
Gamma–Gamma	18	4	7	κ-μ	2	1	1	0.5	1	1
K-distribution	35	4	7	Rice	2	1	0.25	1	1	1

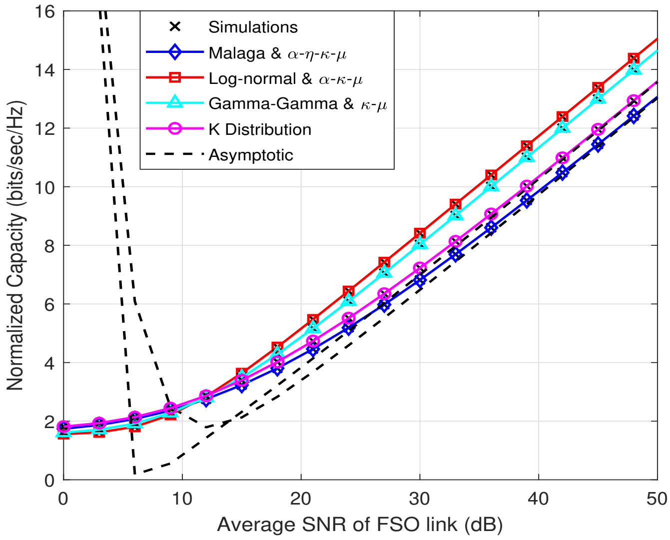

Fig. 3.13: Normalized ergodic capacity versus average SNR of FSO link for different distributions

high due to which high SNR gain is obtained. It can be noticed from Fig. 3.12(a) and 3.12(b) that the performance in terms of both outage probability and average SER of the hybrid FSO/RF system is improved with increase in the average SNR of RF link.

3.8.3 Ergodic Capacity Performance

Fig. 3.13 shows the normalized ergodic capacity in bits/second/hertz (bits/sec/Hz) of hybrid FSO/RF system for different distributions, which are derived as special cases of Malaga and α-η-κ-μ distributions along with asymptotic curves. The values of the parameters used for FSO and RF links to obtain different distributions are given in Table 3.7. Here, we assume IM/DD technique for all cases. From Fig. 3.13, it is observed that the asymptotic curves match the exact capacity curves at high SNR region. All the analytical results are matched with the Monte-Carlo sim-

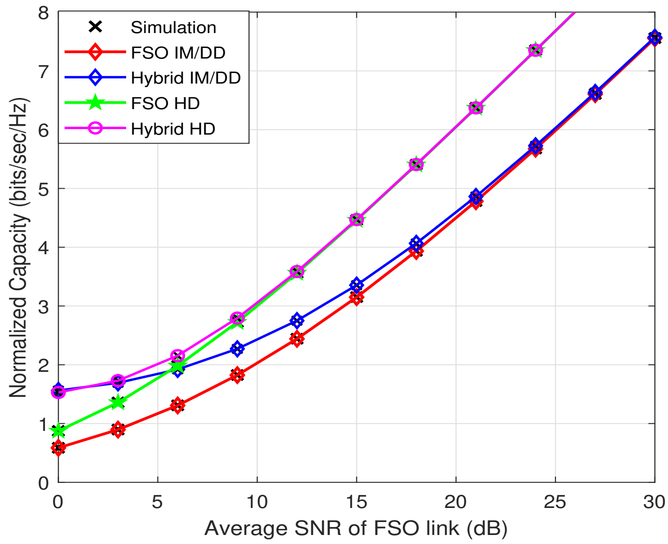

Fig. 3.14: Normalized ergodic capacity versus average SNR of FSO link for different detection techniques

ulations, which justify the correctness of our analysis. Please note that normalized ergodic capacity (in bit/sec/Hz) is depicted in Fig. 3.13, 3.14, 3.15, 3.17, and 3.18, with the assumption that $W_F = 1$ Hz and $W_R = 1$ Hz. In addition, Fig. 3.16 shows the ergodic capacity in Gbps, by assuming $W_F = 1$ GHz and $W_R = 250$ MHz. It is worth noting that the normalized ergodic capacity (in bits/sec/Hz) is required to calculate the spectral efficiency of the hybrid FSO/RF systems.

Fig. 3.14 presents the normalized ergodic capacity of hybrid FSO/RF for both the detection techniques i.e IM/DD and HD for $L = 1000$ m. The parameters of FSO link are assumed as $C_n^2 = 1 \times 10^{-13}$, $a = 11$ cm, $w_0^{opt} = 2$ cm, and the parameters of RF link are assumed as $\alpha_R = 2$, $\eta = 2.5$, $\kappa = 0.25$, $\mu = 0.5$, $p = 1$, $q = 1$, and $\overline{\gamma}_{RF} = 5$ dB. Note that the switching threshold values obtained for IM/DD and HD schemes are, respectively, given by $\gamma_{th}^{opt} = 6$ and 2 dB. From Fig. 3.14, it is observed that the normalized ergodic capacity performance of HD is better than IM/DD technique similar to the outage and average SER performances. The SNR gain values obtained in case of the hybrid FSO/RF system over single-link FSO system to achieve the normalized capacity of 2 bits/sec/Hz for IM/DD and HD schemes are 4 dB and 1 dB, respectively. Therefore, the hybrid FSO/RF system with IM/DD technique provides better SNR gain over single-link FSO system as

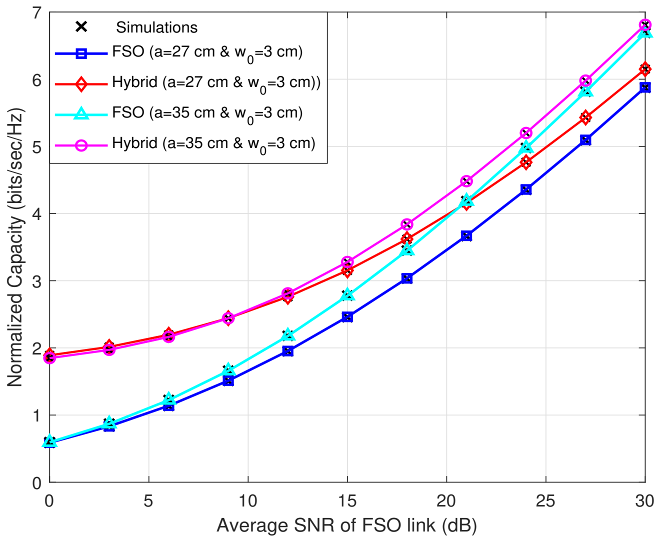

Fig. 3.15: Normalized ergodic capacity versus average SNR of FSO link for different pointing errors conditions

compared to HD technique. This is again due to the fact that the probability of usage of RF link is higher under IM/DD scheme compared to HD scheme.

In Fig. 3.15, the effect of pointing errors on the normalized capacity of FSO and hybrid FSO/RF systems is presented by varying the pointing error coefficient g. The parameters assumed in our simulations are $C_n^2 = 2 \times 10^{-13}$, $L = 2000$ m, $\alpha_R = 1$, $\eta = 1$, $\kappa = 0.5$, $\mu = 0.75$, $p = 1$, $q = 1$, $\overline{\gamma}_{RF} = 5$ dB, and $\gamma_{th}^{opt} = 7$ dB. The normalized ergodic capacity of hybrid FSO/RF system is shown for two cases: (1) $a = 25$ cm, $w_0^{opt} = 3$ cm, and $g = 0.86$ (significant pointing errors case), (2) $a = 35$ cm, $w_0^{opt} = 3$ cm corresponding value of $g = 2.5$ (less significant pointing errors case). It is observed that the effect of pointing errors is high for lower values of g as mentioned before and hence, the capacity performance deteriorates for $g = 0.86$ compared to $g = 2.5$. It is also noticed in Fig. 3.15 that the hybrid system provides better performance over single-link FSO system in both the cases, especially in the low-SNR region. Since the RF average SNR is fixed, the optimum switching threshold SNR will be a constant. Thus, at high-SNR region (i.e. for the case when $\overline{\gamma}_r >> \gamma_{th}^{opt}$), the FSO link will be used with higher probability compared to RF link and the capacity of hybrid system will be almost equal to the capacity of FSO system as shown in Fig. 3.15.

Fig. 3.16 shows the ergodic capacity in gigabits/second/hertz (Gbps) versus

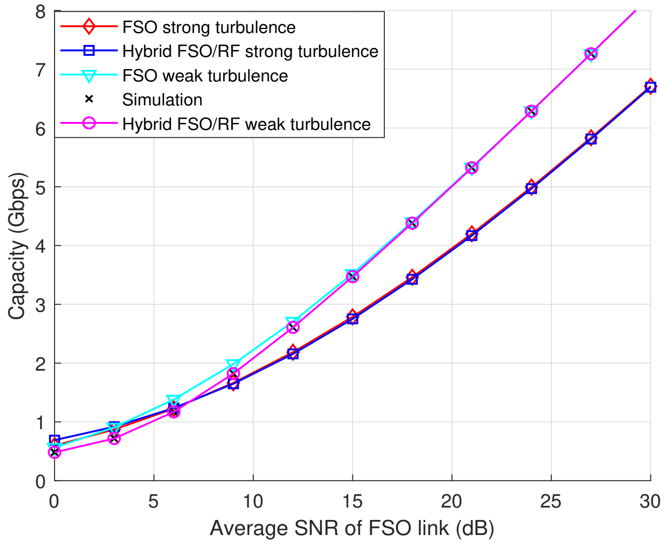

Fig. 3.16: Ergodic capacity versus average SNR of FSO link for different turbulence conditions

the average SNR of FSO link under different turbulence conditions. We consider $C_n^2 = 1\times10^{-13}$, $a = 45$ cm, and $w_0^{opt} = 4$ cm for strong turbulence and $C_n^2 = 4\times10^{-15}$, $a = 15$ cm, and $w_0^{opt} = 4$ cm for weak turbulence. In addition, other parameters assumed are $L = 3000$ m, $W_F = 1$ GHz, $W_R = 250$ MHz, $\alpha_R = 2$, $\eta = 2.5$, $\kappa = 0$, $\mu = 0.6$, $p = 1$, $q = 1$, $\overline{\gamma}_{RF} = 5$ dB and $\gamma_{th}^{opt} = 6$ dB for both the turbulence conditions. Firstly, it is observed that both FSO and hybrid systems achieve higher capacity under weak turbulence condition compared to strong turbulence condition. From the plots, it is also noticed that the ergodic capacity of hybrid FSO/RF system is nearly equal to the single-link FSO system in both the turbulence conditions. However, in weak turbulence condition, especially in the low-SNR region, the ergodic capacity of single-link FSO system is slightly higher than the hybrid FSO/RF system. This is mainly due to the fact that the bandwidth of the FSO signal is much higher than the bandwidth of the RF signal. Thus, it can be concluded that the RF backup link helps in improving the reliability of FSO communication to a larger extent as shown in Fig. 3.7, 3.8, 3.9, 3.10, and 3.12 by compromising on the ergodic capacity in the low-SNR region to a smaller extent.

In Fig. 3.17, the effect of backup RF link on the normalized capacity of hybrid FSO/RF system is shown by varying the average SNR of RF link. We assume $C_n^2 = 2 \times 10^{-13}$, $L = 1000$ m, $a = 13$ cm, and $w_0^{opt} = 2$ cm. Here, we consider

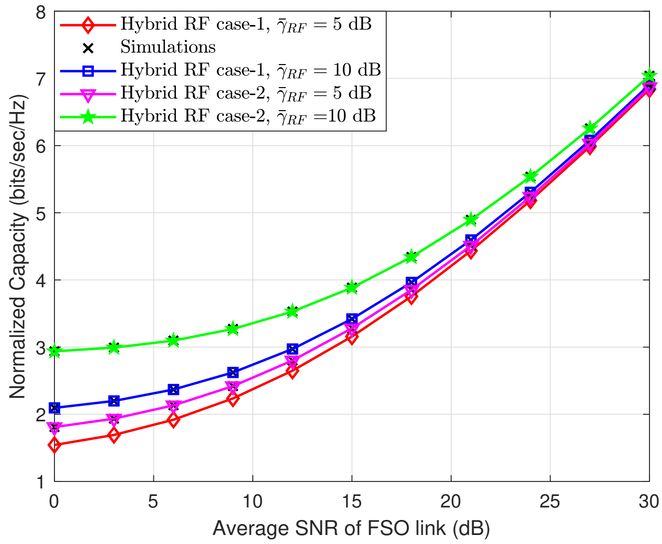

Fig. 3.17: Normalized ergodic capacity versus average SNR of FSO link for different values of $\overline{\gamma}_{RF}$

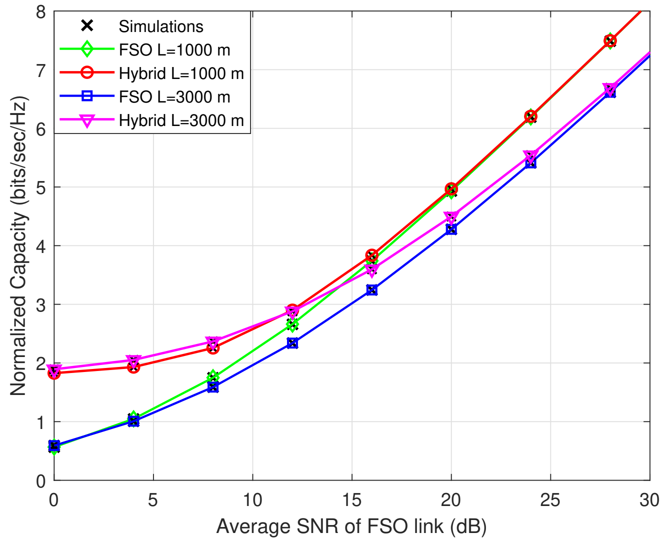

Fig. 3.18: Normalized ergodic capacity versus average SNR of FSO link for different values of link distance

two different cases of RF link parameters. For case 1, we assume $\alpha_R = 1$, $\eta = 1.5$, $\kappa = 0.1$, $\mu = 0.25$, $p = 1$, $q = 1$, and $\gamma_{th}^{opt} = 6$ dB and 8 dB for $\overline{\gamma}_{RF} = 5$ dB and 10 dB, respectively. Similarly, for case 2, we assume $\alpha_R = 2$, $\eta = 1$, $\kappa = 5$, $\mu = 3$, $p = 1$, $q = 1$, and $\gamma_{th}^{opt} = 7$ dB and 12 dB for $\overline{\gamma}_{RF} = 5$ dB and 10 dB, respectively. It is observed that for both the cases, the normalized capacity of hybrid FSO/RF system improves with increase in the average SNR of RF link.

Fig. 3.18 shows the normalized ergodic capacity versus the average SNR of FSO link for different values of link distance L. The FSO link parameters are assumed

Table 3.8: Simulation parameters for satellite communication scenario

Parameter	**Values**
Satellite altitude H	620 Km
Ground station aperture height h_0	1 m
Beam radius at transmitter W_0	2 cm
Front phase curvature radius F_0	∞
Zenith angle θ_Z	(a) 30° (b) 60° (c) 80°
RMS wind speed v_s	(a) 11 m/s (b) 21 m/s (c) 31 m/s
Average SNR of RF link $\overline{\gamma}_{RF}$	5 dB

as $C_n^2 = 4 \times 10^{-14}$, $\rho = 0.95$, and $b_0 = 0.25$. Similarly, the RF link parameters are assumed as $\alpha_R = 0.75$, $\eta = 2$, $\kappa = 0$, $\mu = 0.8$, $p = 1$, $q = 10$, and $\gamma_{th}^{opt} = 8$ dB. It is observed that the normalized capacity performance degrades as L increases and for longer link distance (i.e. $L = 3000$ m), the hybrid FSO/RF system provides higher SNR gain compared to shorter link distance (i.e. $L = 1000$ m).

3.8.4 Results For Satellite Communication Scenario

In this section, we present the average SER and ergodic capacity performances of satellite communication scenario for different values of wind speed and zenith angle. We consider a single-hop communication scenario between ground station and low earth orbit (LEO) satellite. Here, zenith angle indicates the angle between the zenith and the propagation orientation between ground station and satellite. We have assumed Malaga distribution to model the atmospheric turbulence of FSO link and κ-μ distribution for modeling the small scale fading of RF link [164]. The hybrid FSO/RF satellite communication system is compared with FSO-based satellite system and the SNR gain values obtained due to backup RF link in case of hybrid system over FSO system have been reported similar to terrestrial communication scenario. The values of FSO and RF parameters considered for satellite communication scenario are given in Table 3.8.

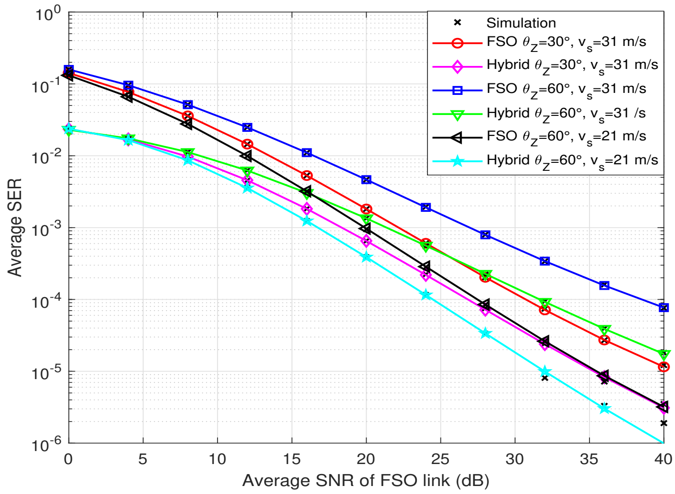

(a) Uplink scenario

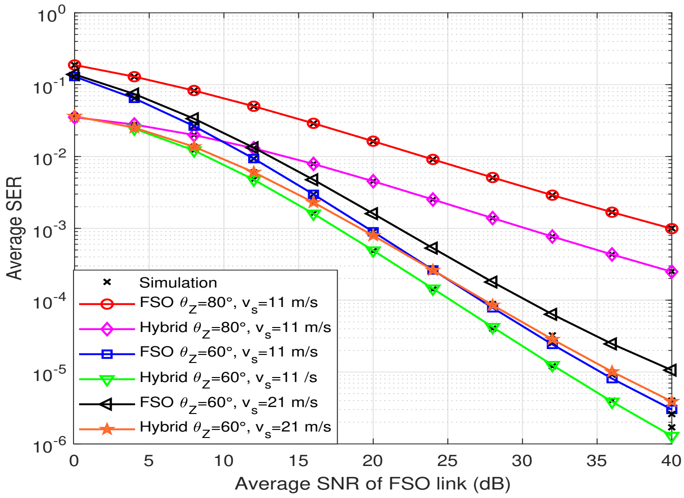

(b) Downlink scenario

Fig. 3.19: Average SER versus average SNR of FSO link for different values of zenith angle and wind speed

Fig. 3.19 presents the average SER performance comparison of FSO and hybrid FSO/RF systems considering both uplink and downlink scenarios for two different values of zenith angle θ_Z and wind speed v_s. The RF link parameters are assumed as $\alpha_R = 2$, $\eta = 1$, $\kappa = 2$, $\mu = 1.5$, $p = 1$, $q = 1$, and $\gamma_{th}^{opt} = 3$. In Fig. 3.19(a), the FSO-based satellite link parameters for uplink scenario are assumed as $v_s = 21$, 31 m/s, $\theta_Z = 30°, 60°$, and $g = 1.7$. It is observed that the performances of both FSO and hybrid FSO/RF systems deteriorate with increase in the values of zenith angle and wind speed. Moreover, the hybrid FSO/RF system outperforms the FSO system in all three cases as shown in Fig. 3.19(a). It is to be noted that when zenith angle or wind velocity decreases, the Rytov variance parameter, given by (A.5) and (A.8), also decreases and the small and large scale turbulence parameters (i.e. α and β) increase. Since the diversity gain depends on α and β, considerable improvement in the SER performance is observed in terms of diversity gain with decrease in wind velocity and zenith angle.

Otherwise, the propagation distance of FSO beam increases with increase in zenith angle, leaving it more vulnerable to atmospheric channel distortions compared to the scenario with low zenith angle value. Therefore, considerable degradation in the performance is noticed with increase in zenith angle value. Further, as the wind velocity increases, the formation of vortexes in air also increases, which will effectively change the refractive index of the medium. This will cause beam wander induced pointing errors and lead to loss of signal-to-noise ratio (SNR) at the receiver, which in turn degrades the performance as observed from the uplink performance trends. For satellite communication scenario, the SNR gains offered by hybrid system over FSO system to achieve the average SER of 10^{-4} are given by 4 dB, 7 dB and 2 dB, respectively, for three cases, which are give as follows: 1) $\theta_Z = 30^\circ, v_s = 31$ m/s, 2) $\theta_Z = 60^\circ, v_s = 31$ m/s, and 3) $\theta_Z = 60^\circ, v_s = 21$ m/s.

In Fig. 3.19(b), the downlink average SER performance of FSO and hybrid FSO/RF systems are compared assuming $v_s = 11$, 21 m/s, $\theta_Z = 60^\circ, 80^\circ$, and $g = 1.7$. The downlink performance trends shown in Fig. 3.19(b) are similar to uplink performance trends shown Fig. 3.19(a). Moreover, it is noticed that as the wind speed and zenith angle increases, higher SNR gain is obtained using hybrid FSO/RF system compared to FSO system. Thus, backup RF link helps in enhancing the reliability of FSO communication to a larger extent for the worst case scenarios (i.e. the scenarios with high wind velocity and zenith angle), which is mainly due to high probability of usage of RF link in all these scenarios especially in the low-SNR region.

Fig. 3.20 shows the normalized ergodic capacity versus the average SNR of FSO link for different values of zenith angle and wind speed for uplink scenario. The FSO

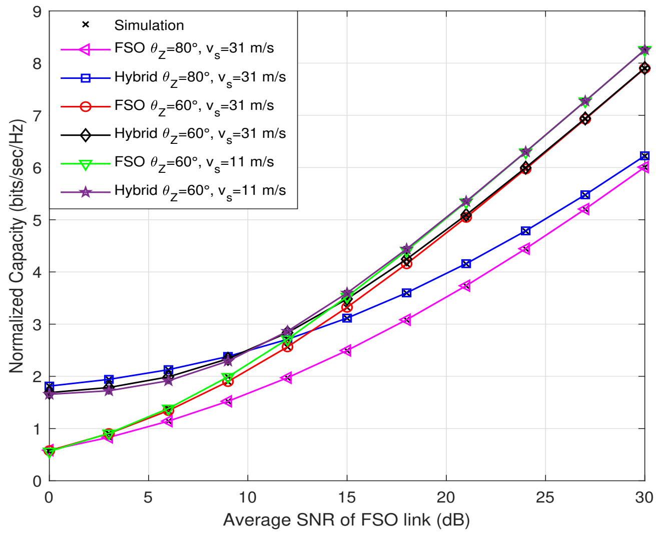

Fig. 3.20: Normalized ergodic capacity performance of FSO and hybrid FSO/RF systems for different zenith angle and wind speed values

link parameters are assumed as $v_s = 11$, 31 m/s, $\theta_Z = 60°, 80°$, and $g = 1.5$ and the RF link parameters are assumed as $\alpha_R = 2$, $\eta = 1$, $\kappa = 0.25$, $\mu = 0.75$, $p = 1$, $q = 1$, and $\gamma_{th}^{opt} = 7$. The normalized ergodic capacity of single-link FSO and hybrid FSO/RF systems are compared for three different cases, which are given as follows: 1) $\theta_Z = 80°, v_s = 31$ m/s, 2) $\theta_Z = 60°, v_s = 31$ m/s, and 3) $\theta_Z = 60°, v_s = 11$ m/s. It is observed that the normalized capacity of both single-link FSO and hybrid FSO/RF systems improve with decrease in zenith angle and wind speed values. In addition, improvement in the normalized capacity performance of hybrid FSO/RF system is observed compared to FSO system in all three cases especially in the low-SNR region. Since the probability of usage of RF link is less at the high-SNR region, the normalized capacity of hybrid FSO/RF system almost matches with the normalized capacity of FSO system.

3.9 Chapter Summary

The chapter presents the performance analysis of a hybrid FSO/RF system using a single-threshold-based switching scheme over generalized fading channel models for terrestrial and satellite communication scenarios. The closed-form expressions for outage, average SER, and ergodic capacity are derived assuming generalized

Malaga distribution for FSO link and α-η-κ-μ distribution for RF link. In addition, asymptotic expressions are also derived, and diversity and SNR gains are determined for three different scenarios. Using numerical optimization technique, the optimal switching threshold SNR and beam width values were determined that minimize the average SER and outage probability, while maximizing the ergodic capacity. The study shows that the hybrid FSO/RF system performs better than the FSO-based SSC and single-link FSO systems. The impact of various channel conditions and the effect of atmospheric turbulence and weather conditions are also studied. Finally, it is concluded that the RF backup link in hybrid FSO/RF communication helps in improving the reliability of FSO communication to a larger extent by compromising on the ergodic capacity in the low-SNR region to a smaller extent.

Chapter 4

On the Maximal-Ratio Combining of FSO and RF Links Over Generalized Distributions and its Applications in Hybrid FSO/RF Systems

4.1 Introduction

The performance of the FSO communication is significantly improved by the use of backup RF link in hybrid FSO/RF system as seen in Chapter 3. However, in case of hard-switching-based hybrid FSO/RF system discussed in Chapter 3, there is a problem of frequent hardware switching between FSO and RF sub-systems. It is a major bottleneck in the case of a hard-switching scheme and for efficient switching between FSO and RF links, the CSI is also required at the transmitter. To alleviate these issues, the FSO and RF links of the hybrid FSO/RF system were combined using SC and MRC in [48]-[49], where transmission of feedback bits to the transmitter as well as the requirement of CSI at the transmitter are not mandatory.

In case of a hybrid FSO/RF system based on MRC scheme, the message signals are transmitted simultaneously over both FSO and RF links and are combined at the receiver based on their instantaneous SNRs. The output SNR of the system after MRC will be equal to the sum of the instantaneous SNR of FSO and RF links. However, the RF link is active throughout even if the FSO link has better transmission quality. This results in wastage of RF power. Further, to enable efficient diversity combining, the transmission rate of the FSO link should be reduced to the transmission rate of the RF link. These issues can be addressed using adaptive combining, which is a variant of the MRC scheme. In [155], the adaptive combining scheme for the hybrid FSO/RF system was proposed in which the FSO link is always active and the RF link is activated only when the instantaneous SNR of the FSO link drops below a predefined threshold SNR value. Further, FSO and RF links are combined using the MRC technique at the destination.

The performance analysis of the adaptive-combining-based hybrid FSO/RF system in terms of outage probability and average SER was presented in [158, 159, 156]. It is to be noted that both switching and diversity combining benefits can be obtained using the adaptive combining scheme. Therefore, the adaptive combining scheme can be considered as an excellent solution to counteract the limitations of hard-switching and diversity combining schemes for hybrid FSO/RF systems as well as nullifying the effects of atmospheric channel distortions encountered by FSO signal. In earlier works on adaptive combining system [155, 157, 158, 159, 156], modeling of the FSO link and the RF link was restricted to Gamma-Gamma and Nakagami-m distributions, respectively. Moreover, in [155, 157, 158, 159, 156], the effect of non-zero bore-sight pointing errors, background noise, and erroneous feedback link on the performance of adaptive combining system was not considered.

In this chapter, the exact closed-form expressions for the PDF and CDF of MRC of the FSO and RF links are derived, where the FSO link follows the generalized Malaga distribution with the non-zero boresight pointing errors and the RF link is modeled using the generalized α-η-κ-μ distribution. Using the obtained statistical functions (i.e. PDF and CDF), the unified closed-form expressions for outage probability and average SER of MRC and adaptive-combining-based hybrid FSO/RF systems are derived. Further, the optimum switching threshold SNR and optimum beam width values for the adaptive combining scheme are obtained. The effects of background noise and erroneous feedback link on the performance of adaptive combining system are presented in the numerical results. Using the less-complex asymptotic expressions, the diversity gains of MRC and adaptive combining schemes are obtained for various cases. Additionally, the conditions to achieve full diversity gain are also given.

4.2 Organization of the chapter

The rest of the chapter is organized as follows: Section 4.3 discusses the system model and channel models of FSO and RF links. Section 4.4 presents the statistical characteristics like PDF and CDF of MRC and the outage probability of MRC and adaptive combining schemes is also investigated. The average SER expressions for MRC and adaptive combining schemes are derived in Section 4.5. In Section 4.6, the asymptotic analysis of outage and average SER are presented, along with diversity gain calculation and beam width optimization. Section 4.7 discusses the numerical results and related inferences followed by concluding remarks in Section 4.8.

4.3 System and Channel Models

In this chapter, we consider a hybrid FSO/RF system with MRC of FSO and RF links. In addition, we also consider the adaptive-combining-based switching scheme, which is a variant of the MRC scheme, for hybrid FSO/RF system. The sub-carrier IM is assumed, where laser beam intensity is modulated by up-converted MPSK scheme at the transmitter [147]. For detecting the received FSO symbols at the receiver, DD and HD techniques are assumed. The received FSO baseband signals for HD and IM/DD techniques are, respectively, given by [190, eq. (1), (2)]

$$y_1 = \sqrt{\eta_f \, P_F} \, \sqrt{I_F} \, x_1 + n_1, \tag{4.1}$$

$$y_2 = \eta_f \, P_F \, I_F \, x_2 + n_2, \tag{4.2}$$

where y_p is the output baseband signals at the receiver, $p = 1$ indicates HD technique, $p = 2$ indicates IM/DD technique, x_p is the transmitted input MPSK symbols, I_F denotes the combined FSO channel fading due to atmospheric turbulence, path loss, and pointing errors, η_f is the responsivity of a photo-detector, P_F denotes the FSO transmit power, and n_p is the FSO channel noise, which is given as the sum of two zero-mean Gaussian processes, i.e. thermal noise n_{th} and background noise n_{bk}, with variances denoted as σ_{th}^2 and σ_{bk}^2, respectively. Further, the background noise variance can be written in terms of thermal noise variance σ_{th}^2 as $\sigma_{bk}^2 = K_b \sigma_{th}^2$, where the parameter K_b signifies the amount of background noise power with respect to thermal noise power [191]. The overall noise variance of the FSO link is given as $\sigma_p^2 = \sigma_{th}^2(1 + K_b)$. Similarly, the received baseband MPSK modulated RF signal is given by [41, eq. (6)]

$$y_3 = \sqrt{P_R \, G_R} \, h_R \, x_3 + n_3, \tag{4.3}$$

where P_R is the RF transmit power, h_R is the RF fading channel coefficient, x_3 is the transmitted input symbol, and n_3 is the AWGN with zero-mean and variance σ_{RF}^2. Here, $\sigma_{RF}^2\,(\text{dB}) = B_R N_0 + NF$, where B_R denotes the RF bandwidth, N_0 is the noise spectral density (in dBm/MHz), and NF is the noise figure (in dB). Further, G_R is defined as the average RF channel gain and is given by [41, eq. (7)]

$$G_R(\text{dB}) = G_t + G_r - 20 \log_{10}\left(\frac{4\pi L}{\lambda_R}\right) - (\zeta_{ox} + \zeta_{rn} + \zeta_{fog})\, L, \tag{4.4}$$

where G_t and G_r denote the gain values (in dB) of receive and transmit antennas, respectively, L is the link distance, λ_R is the RF wavelength, ζ_{ox} and ζ_{rn} are the attenuation factors due to oxygen absorption and rain, respectively, and ζ_{fog} is the

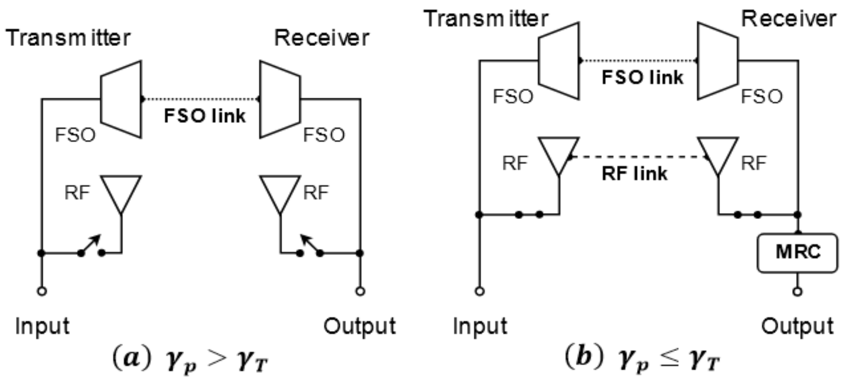

Fig. 4.1: System model based on the Adaptive combining scheme

attenuation factor due to fog [192].

In case of a hybrid FSO/RF system based on a simple MRC scheme, the message signals are simultaneously transmitted over both FSO and RF links and are combined at the receiver using the MRC scheme such that the output SNR of the system is maximized. The output SNR of the system after MRC will be equal to the sum of the instantaneous SNR of FSO and RF links [48]−[49]. This is based on the fact that the output instantaneous SNR of MRC scheme after combining the message signals received from multiple links is equal to the sum of the instantaneous SNR of the individual link [48]. Further, the transmission data rate of the FSO link should be reduced to the data rate of the RF link to enable efficient diversity combining. The output signal after MRC is given as [158, eq. (2)]

$$y_C = \sqrt{\gamma_p}\frac{y_p}{\sigma_p} + \sqrt{\gamma_{RF}}\frac{y_3}{\sigma_3}, \tag{4.5}$$

where γ_p is the unified instantaneous SNR of the FSO link and γ_{RF} is the instantaneous SNR of the RF link. The instantaneous SNR of the hybrid FSO/RF system based on the MRC scheme is given by [48, eq. (31)]

$$\gamma_{MRC} = \gamma_p + \gamma_{RF} \tag{4.6}$$

In case of a hybrid FSO/RF system based on the adaptive combining scheme, which is a variant of MRC, the FSO link is always active and the RF link will be in a standby mode, if the instantaneous SNR of the FSO link is greater than the predefined switching threshold SNR γ_T. So the message signals will be first transmitted only over FSO link. However, if the instantaneous SNR of the FSO link is lesser than the predefined threshold SNR, then the RF link will be activated by sending a 1-bit feedback signal to the transmitter. After that the message signals will be transmitted over both FSO and RF links and MRC will be performed at the receiver as shown in Fig. 4.1. The instantaneous SNR of the hybrid FSO/RF system based on the adaptive combining scheme can be written as [158, eq. (3)]

$$\gamma_c = \begin{cases} \gamma_p, & \gamma_p > \gamma_T \\ \gamma_{MRC} = \gamma_p + \gamma_{RF}, & \gamma_p \leq \gamma_T. \end{cases} \tag{4.7}$$

It is important to note that prior to each symbol-by-symbol transmission phase, the receiver estimates channel states of both the FSO and RF links. These estimates are utilized to calculate the instantaneous SNR of both the links. Using these calculated instantaneous SNR values, feedback bits will be sent to the transmitter to activate the RF link, if the FSO link is not satisfactory. The atmospheric turbulence affecting FSO links is well-known for its slow fading characteristics. This is due to the relatively long coherence time of the FSO channel, typically in the range of 1-100 milliseconds (1-100 ms) [94]. As a result, the effects of turbulence-induced fading persist over a large number of transmitted bits/symbols. Furthermore, we have considered the inclusion of pointing errors in our analysis, which introduce rapid signal fluctuations. Thus, the coherence time of the combined FSO channel (i.e. atmospheric turbulence and pointing errors) will not be very long. Therefore, we assume that the FSO channel remains constant for atleast a few hundred symbols and the CSI is estimated periodically at every few hundred symbol interval through channel estimation techniques at the receiver.

The main assumptions considered in this chapter are given as follows:

- Both FSO and RF channels transmit identical information in a symbol-by-symbol manner under MRC and adaptive combining schemes.

- Both channels are assumed to be slowly varying nature, where RF channel remains constant for atleast one symbol duration and FSO channel remains constant for a few hundred symbol duration.
- Both FSO and RF links operate at the same data rate when combined at the receiver using MRC for enabling efficient diversity combining.
- Furthermore, CSI of both FSO and RF links is assumed to be perfectly available at the receiver
- It is also assumed in our theoretical analysis that 1-bit feedback signal at the transmitter is received successfully without error for switching to MRC mode of operation in adaptive combining scheme. However, the impact of erroneous feedback link on the performance of adaptive-combining system is shown using Monte-Carlo simulations.

4.3.1 FSO Channel Model

The FSO signal during transmission experiences various losses such as atmospheric turbulence, pointing errors, and atmospheric attenuation or path loss due to weather conditions. In this chapter, it is assumed that atmospheric turbulence-induced fading I_a encountered by the FSO link follows the generalized Malaga distribution and the PDF of Malaga distribution is given in Chapter 3, Section 3.3.1, eq. (3.5). Further, the atmospheric attenuation or path loss of the FSO link is defined using Beers-Lambert law [168] as $I_l = \exp(\zeta_w L)$, where ζ_w denotes the attenuation factor due to atmospheric weather conditions, as given in Chapter 3, Section 3.3.1. The pointing error model is assumed as nonzero boresight, which is described in the following paragraph.

The misalignment between the beam and the detector center due to building sway or mechanical vibration of the receiver gives rise to the pointing errors. For the non-zero boresight pointing errors, the radial displacement between the beam center and the center of detector is given by $\hat{r} = \sqrt{X^2 + Y^2}$, where X denotes the displacement along the horizontal axis and modeled as Gaussian random variable with mean and variance as m_x and δ_x^2, respectively. Further, Y represents the displacement along the elevation axis and is independently modeled as Gaussian random variable with mean and variance as m_y and δ_y^2, respectively. Thus, $\hat{r} > 0$ follows the Beckmann distribution [193, eq. (3)] and since its PDF is not in closed-form, an approximate closed-form expression for the PDF of Beckmann distribution using modified Rayleigh distribution has been utilized and the same is given by [144, eq. (6)]

$$f_{\hat{r}}(z) \approx \frac{z}{\delta_{eq}^2} \exp\left(-\frac{z^2}{2\delta_{eq}^2}\right), \tag{4.8}$$

where $\delta_{eq}^2 = \left(\left(3m_x^2\delta_x^4 + 3m_y^2\delta_y^4 + \delta_x^6 + \delta_y^6\right)/2\right)^{1/3}$. Further, the fraction of received power at the detector $I_e(\hat{r})$ is given by [94]

$$I_e(\hat{r}) \approx S_0 \exp\left(-\frac{2\hat{r}^2}{w_{L_{eq}}^2}\right), \tag{4.9}$$

where S_0 is the amount of the power received at detector $\hat{r} = 0$ and $w_{L_{eq}}$ is the equivalent beam width. By using the random variable transformations, the PDF of non-zero boresight pointing errors I_e can be written as [144, eq. (8)]

$$f_{I_e}(I_e) = \frac{g_{eq}^2}{S_{eq}^{g_{eq}^2}} I_e^{g_{eq}^2 - 1}; \quad 0 \leq I_e \leq S_{eq}, \tag{4.10}$$

where $g_{eq} = \frac{w_{Leq}}{2\delta_{eq}}$ denotes the pointing error coefficient and $S_{eq} = \varepsilon S_0$. Here, ε is given by

$$\varepsilon = \exp\left(\frac{1}{g_{eq}^2} - \frac{1}{2g_x^2} - \frac{1}{2g_y^2} - \frac{m_x^2}{2g_x^2\delta_x^2} - \frac{m_y^2}{2g_y^2\delta_y^2}\right) \tag{4.11}$$

where $g_x = \frac{w_{Leq}}{2\delta_x}$ and $g_y = \frac{w_{Leq}}{2\delta_y}$. Further, the expressions for S_0 and $w_{L_{eq}}$ are given by

$$S_0 = \operatorname{erf}^2(v), \;\; v = \frac{\sqrt{\pi}\, r_0}{\sqrt{2}\, w_L}, \;\; w_{L_{eq}}^2 = \frac{w_L^2 \sqrt{\pi} \operatorname{erf}(v)}{2v \exp(-v^2)}, \tag{4.12}$$

where r_0 represents the receiver aperture radius and and w_L is called as Gaussian beam width, which is given by [94]

$$w_L \approx w_0\sqrt{1+\Theta_0(\lambda_F L/\pi w_0^2)^2}, \quad \Theta_0 = 1+\frac{2w_0^2}{\varrho_0^2(L)}, \quad \varrho_0(L) = (0.55C_n^2\, k_f^2 L)^{-3/5}, \tag{4.13}$$

where λ_F is the FSO wavelength, w_0 is the beam width at $L = 0$, k_f is the wave number, and C_n^2 represents the refractive index structure parameter of the FSO link. It is to be noted that the special case of zero boresight pointing errors can be obtained by substituting $m_x = m_y = 0$ and $\delta_x = \delta_y = \delta$. Further, we get $\varepsilon = 1$, $S_{eq} = S_0$, and $\delta_{eq} = \delta$ as well as (4.10) comes in agreement with the PDF of zero boresight pointing errors in Chapter 3, eq. (3.10).

4.3.2 Combined FSO Channel Statistics

Considering the effects of atmospheric turbulence, pointing errors, and path loss, the combined FSO channel state can be written as $I_F = I_a\, I_e\, I_l$. The unified expressions for instantaneous SNR and the average electrical SNR of the combined FSO link, which account for both HD and IM/DD techniques, are obtained, respectively, as

$$\gamma_p = |I_F|^p \frac{(P_F\eta_f)^p}{\sigma_p^2}, \tag{4.14}$$

$$\overline{\gamma}_p = [(y+\Omega^{'})\xi\, S_{eq} I_l]^p \frac{(P_F\eta_f)^p}{\sigma_p^2}, \tag{4.15}$$

where $\xi = g_{eq}^2/(g_{eq}^2+1)$ and p is the parameter for unifying HD and IM/DD techniques. Further, by applying power transformation using (4.14) and (4.15), we get $\gamma_p = \frac{\overline{\gamma}_p |I|^p}{[(y+\Omega^{'})\,\xi\, S_{eq} I_l]^p}$. Thus, the unified PDF of instantaneous SNR of the FSO link can be written as [174, eq. (1)]

$$f_{\gamma_p}(\gamma) = \frac{g_{eq}^2 D}{2^p \gamma}\sum_{d=1}^{\beta} b_d\, G_{1\,3}^{3\,0}\left(B_1 \left(\frac{\gamma}{\overline{\gamma}_p}\right)^{\frac{1}{p}} \middle| \begin{matrix} g_{eq}^2+1 \\ g_{eq}^2, \alpha, d \end{matrix} \right), \tag{4.16}$$

where

$$D = \frac{2\alpha^{\alpha/2}}{y^{1+\alpha/2}\Gamma(\alpha)} \left(\frac{y\beta}{y\beta + \Omega'}\right)^{\beta+\alpha/2}, \tag{4.17}$$

$$b_d = \binom{\beta - 1}{d - 1} \frac{(y\beta + \Omega')^{1-\alpha/2}}{(d-1)!} \left(\frac{\Omega'}{y}\right)^{d-1} \alpha^{-(\alpha/2)}\beta^{-d}, \tag{4.18}$$

$G_{p\ q}^{m\ n}(\cdot)$ denotes Meijer G function [187, eq. (07.34.02.0001.01)], B_1 is given in Table 4.1 and the remaining parameters in (4.16) are defined in Chapter 3, Table 3.1. Further, the unified expression for CDF of instantaneous SNR of the FSO link γ_p is obtained as [174, eq. (2)]

$$F_{\gamma_p}(x) = \int_0^x f_{\gamma_p}(\gamma)\, d\gamma = C_1 \sum_{d=1}^{\beta} t_d G_{p+1\ 3p+1}^{3p\ \ 1}\left(B_2 x \middle| \begin{matrix} 1, \mathcal{K}_1 \\ \mathcal{K}_2, 0 \end{matrix}\right), \tag{4.19}$$

where $\mathcal{K}_1 = \frac{g_{eq}^2+1}{p} \ldots \frac{g_{eq}^2+p}{p}$ having p terms, $\mathcal{K}_2 = \frac{g_{eq}^2}{p} \ldots \frac{g_{eq}^2+p-1}{p}, \frac{\alpha}{p} \ldots \frac{\alpha+p-1}{p}, \frac{d}{p} \ldots \frac{d+p-1}{p}$ having $3p$ terms, C_1, t_d, and B_2 are defined in Table 4.1.

4.3.3 RF Channel Model

The RF fading channel h_R follows the α-η-κ-μ distribution for which the modeling and PDF is given in Chapter 3, Section 3.3.2. The instantaneous SNR of the RF link considering the atmospheric path loss component is given by

$$\gamma_{RF} = \frac{|h_R|^2 \overline{\gamma}_{RF}}{G_R}, \tag{4.20}$$

where $\overline{\gamma}_{RF} = G_R \frac{P_R}{\sigma_{RF}^2}$ denotes the average SNR of RF link. Further, by applying the power transformation of random variable, the PDF of γ_{RF} is given by [174, eq. (3)]

$$f_{\gamma_{RF}}(\gamma) = \tilde{\alpha} \sum_{l=0}^{\infty} \sum_{m=0}^{l} \frac{c_l (-l)_m \gamma^{\tilde{\alpha}(\mu+m)-1} \exp\left(-\frac{\gamma^{\tilde{\alpha}}}{2\overline{\gamma}_{RF}^{\tilde{\alpha}}}\right)}{m!\Gamma(\mu+m) 2^{\mu-m} \overline{\gamma}_{RF}^{\tilde{\alpha}(\mu+m)}}, \tag{4.21}$$

Table 4.1: List of notations

$C_1 = \frac{g_{eq}^2 D}{2^{2p-1}\pi^{p-1}}$	$C_2 = \frac{\tilde{\alpha} g_{eq}^2 D}{2^{2p-1}\pi^{p-1}}$	$C_3 = \frac{A\tilde{\alpha} g_{eq}^2 D}{2^{2p}\pi^{p-\frac{1}{2}}}$	$t_d = b_d\, p^{\alpha+d-1}$
$M_{1,m} = \frac{(-l)_m c_l}{m!\Gamma(\mu+m)2^{\mu-m}}$	$M_{2,m} = \frac{(-l)_m c_l 4^m}{m!\Gamma(\mu+m)}$	$M_{3,n} = \frac{2(-1)^n B^{2n+1}}{n!(2n+1)}$	$B_2 = \frac{B_1^p}{p^{2p}\overline{\gamma}_p}$
$Q_{1,i} = \frac{(-1)^i \Gamma(\tau_1)}{i! 2^i \overline{\gamma}_{RF}^{\tau_1}}$	$Q_{2,n} = \frac{(-1)^n}{n! \tau_2 2^{(\tau_2/\tilde{\alpha})} \overline{\gamma}_{RF}^{\tau_2}}$	$Q_{3,i} = \frac{(-1)^i}{i! 2^i \overline{\gamma}_{RF}^{\tau_1}}$	$\tau_1 = \tilde{\alpha}(\mu + m + i)$
$B_1 = \frac{\alpha\, \beta\, \xi (y+\Omega')}{y\beta+\Omega'}$	$B_3 = \frac{B_1^p}{K^2 p^{2p} \overline{\gamma}_p}$	$\xi = g_{eq}^2/(g_{eq}^2+1)$	$\tau_2 = \tilde{\alpha}(\mu + m + n)$

where $\tilde{\alpha}$, η, κ, μ, and other parameters are given in Chapter 3, Section 3.3.2, Table 3.2. Further, the CDF of γ_{RF} is determined as [174, eq. (4)]

$$F_{\gamma_{RF}}(x) = \int_0^x f_{\gamma_{RF}}(t) dt = \sum_{l=0}^{\infty} \sum_{m=0}^{l} \frac{M_{1,m}}{2^{-\mu-m}} \gamma\left(\mu+m, \frac{x^{\tilde{\alpha}}}{2\overline{\gamma}_{RF}^{\tilde{\alpha}}}\right), \tag{4.22}$$

where $\gamma(:,:)$ denotes the lower incomplete gamma function [186, eq.(8.350.1)] and $M_{1,m}$ is given in Table 4.1. It is to be noted that the PDF and CDF expressions in (4.21) and (4.22) consist of an infinite series. Hence, a convergence test for (4.21) is presented in Appendix (sub-section A) and convergence of (4.22) is shown in Fig. 4.3 (a), which confirm that (4.21) and (4.22) are absolutely convergent.

4.4 Outage Probability Analysis

This section investigates the outage probability of MRC and adaptive combining schemes individually over the generalized fading channels.

4.4.1 Hybrid FSO/RF with MRC Scheme

The MRC scheme is said to be in an outage when the instantaneous SNR γ_{MRC} is below a threshold value γ_{OT} and the outage probability of the MRC scheme for hybrid FSO/RF system can be expressed as

$$P_{MRC}^{out} = F_{\gamma_{MRC}}(\gamma_{OT}) = \int_0^{\gamma_{OT}} f_{\gamma_{MRC}}(\gamma) d\gamma\,, \tag{4.23}$$

where $F_{\gamma_{MRC}}(\cdot)$ and $f_{\gamma_{MRC}}(\cdot)$ represent the CDF and the PDF of the γ_{MRC}, respectively. Since the FSO and RF links are statistically independent, the integral to evaluate the PDF of $\gamma_{MRC} = \gamma_p + \gamma_{RF}$ can be written as

$$f_{\gamma_{MRC}}(\gamma) = \int_0^{\gamma} f_{\gamma_p}(t) f_{\gamma_{RF}}(\gamma - t) dt \tag{4.24}$$

By substituting (4.16) and (4.21) in (4.24), we obtain $f_{\gamma_{MRC}}(\gamma)$ by expanding $\exp\left(-\frac{(\gamma-t)^{\tilde{\alpha}}}{2\bar{\gamma}_{RF}^{\tilde{\alpha}}}\right)$ term and using [187, eq.(07.34.21.0084.01)] as

$$f_{\gamma_{MRC}}(\gamma) = C_2 \sum_{d=1}^{\beta} t_d \sum_{l=0}^{\infty} \sum_{m=0}^{l} M_{1,m} \sum_{i=0}^{\infty} Q_{1,i} \gamma^{\tau_1 - 1} G_{p+1\ 3p+1}^{3p\ \ \ 1} \left(B_2 \gamma \middle| \begin{matrix} 1, \mathcal{K}_1 \\ \mathcal{K}_2, 1-\tau_1 \end{matrix} \right), \tag{4.25}$$

where C_2, τ_1, $M_{1,m}$, and $Q_{1,i}$ are defined in Table 4.1. Further, by substituting (4.25) in (4.23) and by using [187, eq. (07.34.21.0084.01)], the CDF of γ_{MRC} is derived as

$$F_{\gamma_{MRC}}(x) = C_2 \sum_{d=1}^{\beta} t_d \sum_{l=0}^{\infty} \sum_{m=0}^{l} M_{1,m} \sum_{i=0}^{\infty} Q_{1,i} x^{\tau_1} G_{p+2\ 3p+2}^{3p\ \ \ 2} \left(B_2 x \middle| \begin{matrix} 1-\tau_1, 1, \mathcal{K}_1 \\ \mathcal{K}_2, 1-\tau_1, -\tau_1 \end{matrix} \right) \tag{4.26}$$

Thus, the outage probability for a given threshold SNR value γ_{OT} can be calculated by replacing x with γ_{OT} in (4.26).

It is to be noted that the PDF and CDF expressions in (4.25) and (4.26) consist of two infinite series. Thus, a convergence test for (4.25) is presented in Appendix B.2 and convergence of (4.26) is shown in Fig. 4.3 (b). From these convergence tests, it is evident that (4.25) and (4.26) are absolutely convergent.

4.4.2 Hybrid FSO/RF with Adaptive Combining Scheme

In case of hybrid FSO/RF system based on the adaptive combining scheme, if the instantaneous SNR γ_c, which is given by (4.7), is lesser than the outage threshold

γ_{OT}, then the system will be declared to be in the outage. The outage probability for the same can be expressed as [155]

$$P_{AC}^{out} = F_{\gamma_c}(\gamma_{OT}) \tag{4.27}$$

where $F_{\gamma_c}(x)$ is the CDF of γ_c and is given by [155, eq. (7)]

$$F_{\gamma_c}(x) = P(\gamma_p > \gamma_T, \gamma_p < x) + P(\gamma_p \leq \gamma_T, \gamma_{MRC} < x) \tag{4.28}$$

In the adaptive-combining-based hybrid system, for the case when $\gamma_{OT} \leq \gamma_T$, the instantaneous SNR of the FSO link should be lesser than the outage threshold SNR (i.e. $\gamma_p < \gamma_{OT}$), as instantaneous SNR of the MRC of both FSO and RF links is below the outage threshold SNR (i.e. $\gamma_{MRC} = \gamma_p + \gamma_{RF} < \gamma_{OT}$). Thus, the outage probability is obtained as the probability that γ_{MRC} is lesser than the outage threshold SNR (i.e. $\Pr(\gamma_{MRC} < \gamma_{OT})$). For the second case, when $\gamma_{OT} > \gamma_T$, the outage probability is calculated as the sum of two probabilities. In first part, the probability is calculated for FSO link under the conditions $\gamma_p > \gamma_T$ and $\gamma_p < \gamma_{OT}$. Further, in the second part, the probability is determined such that $\gamma_{MRC} = \gamma_p + \gamma_{RF} < \gamma_{OT}$, provided the instantaneous SNR of FSO is below the threshold SNR, i.e. $\gamma_p < \gamma_T$. Therefore, the CDF expression given in (4.28) can be re-written as

$$F_{\gamma_c}(x) = \begin{cases} F_{\gamma_{MRC}}(x), & x \leq \gamma_T. \\ F_1(x) + F_{\gamma_p}(x) - F_{\gamma_p}(\gamma_T), & x > \gamma_T. \end{cases} \tag{4.29}$$

where

$$F_1(x) = \int_0^{\gamma_T} f_{\gamma_p}(\gamma) F_{\gamma_{RF}}(x-\gamma) d\gamma \tag{4.30}$$

By substituting (4.16) and (4.22) in (4.30), then expanding $\gamma\left(\mu+m, \frac{x^{\tilde{\alpha}}}{2\bar{\gamma}_{RF}^{\tilde{\alpha}}}\right)$ by using [186, eq. (8.354.1)], and after applying [187, eq. (07.34.21.0084.01)], $F_1(x)$ is given by

$$F_1(x) = C_2 \sum_{d=1}^{\beta} t_d \sum_{l=0}^{\infty} \sum_{m=0}^{l} M_{2,m} \sum_{n=0}^{\infty} Q_{2,n} \sum_{j=0}^{\tau_2} \binom{\tau_2}{j} (-\gamma_T)^j x^{\tau_2 - j}$$
$$\times G_{p+1\ 3p+1}^{3p\ \ 1} \left(B_2 \gamma_T \middle| \begin{matrix} 1-j, \mathcal{K}_1 \\ \mathcal{K}_2, -j \end{matrix} \right), \tag{4.31}$$

where τ_2, $Q_{2,n}$, and $M_{2,m}$ are mentioned in Table 4.1. Now in order to derive the PDF of γ_c, we differentiate (4.29) to get

$$f_{\gamma_c}(\gamma) = \begin{cases} f_{\gamma_{MRC}}(\gamma), & \gamma \leq \gamma_T. \\ f_{\gamma_p}(\gamma) + g_c(\gamma), & \gamma > \gamma_T. \end{cases} \tag{4.32}$$

where

$$g_c(\gamma) = \int_0^{\gamma_T} f_{\gamma_p}(x) f_{\gamma_{RF}}(\gamma - x) dx \tag{4.33}$$

By substituting (4.16) and (4.21) in (4.33), then using the series expansion of $\exp\left(-\frac{(\gamma-x)^{\tilde{\alpha}}}{2\bar{\gamma}_{RF}^{\tilde{\alpha}}}\right)$ term, and after utilizing [187, eq. (07.34.21.0084.01)], the above integral is evaluated as

$$g_c(\gamma) = C_2 \sum_{d=1}^{\beta} t_d \sum_{l=0}^{\infty} \sum_{m=0}^{l} M_{1,m} \sum_{i=0}^{\infty} Q_{3,i} \sum_{j=0}^{\tau_1 - 1} \binom{\tau_1 - 1}{j} (-\gamma_T)^j \gamma^{\tau_1 - j - 1}$$
$$\times G_{p+1\ 3p+1}^{3p\ \ 1} \left(B_2 \gamma_T \middle| \begin{matrix} 1-j, \mathcal{K}_1 \\ \mathcal{K}_2, -j \end{matrix} \right), \tag{4.34}$$

where $Q_{3,i}$ is given in Table 4.1.

4.5 Average SER Analysis

The average SER for an MPSK modulated system is calculated by averaging the conditional SER over the PDF of the instantaneous SNR of the given scheme (i.e. MRC or adaptive combining) [147]. In this section, the average SER of the hybrid

FSO/RF system is derived for both MRC and adaptive combining schemes.

4.5.1 Hybrid FSO/RF with MRC Scheme

The average SER of the MRC scheme can be obtained as

$$\overline{P}_e^{MRC} = \int_0^\infty p(e|\gamma) f_{\gamma_{MRC}}(\gamma) d\gamma \,, \tag{4.35}$$

where $p(e|\gamma)$ is the conditional SER and for MPSK signalling, it is expressed as

$$p(e|\gamma) = \frac{A}{2}\mathrm{erfc}(K\sqrt{\gamma}), \tag{4.36}$$

where $A = 1$ for $M = 2$, $A = 2$ for $M > 2$, $K = \sin(\pi/M)$, M represents the modulation order, and erfc$(\cdot)$ denotes the complementary error function. Additionally, erfc$(\cdot)$ can be expressed in the form of Meijer G-function by using [187, eq. (07.34.03.0619.01)] and $p(e|\gamma)$ can be re-written as

$$p(e|\gamma) = \frac{A}{2\sqrt{\pi}} G_{1\,2}^{2\,0}\left(K^2\gamma \middle| \begin{matrix} 1 \\ 0, \frac{1}{2} \end{matrix}\right). \tag{4.37}$$

Substituting (4.25) and (4.37) in (4.35) and applying [187, eq. (07.34.21.0013.01)], the average SER of the MRC scheme is given by

$$\overline{P}_e^{MRC} = C_3 \sum_{d=1}^{\beta} t_d \sum_{l=0}^{\infty} \sum_{m=0}^{l} M_{1,m} \sum_{i=0}^{\infty} \frac{Q_{1,i}}{K^{2\tau_1}} G_{p+3\;3p+2}^{3p\;\;\;3}\left(B_3 \middle| \begin{matrix} 1, 1-\tau_1, 0.5-\tau_1, \mathcal{K}_1 \\ \mathcal{K}_2, -\tau_1, 1-\tau_1 \end{matrix}\right), \tag{4.38}$$

where B_3 is given in Table 4.1.

4.5.2 Hybrid FSO/RF with Adaptive Combining Scheme

The average SER of adaptive combining scheme is given by

$$\overline{P}_e^{AC} = \int_0^\infty p(e|\gamma) f_{\gamma_c}(\gamma) d\gamma, \tag{4.39}$$

where $f_{\gamma_c}(\gamma)$ is replaced by (4.32) and $\overline{P}_e^{AC}$ can be rewritten as

$$\overline{P}_e^{AC} = \underbrace{\int_0^{\gamma_T} p(e|\gamma) f_{\gamma_{MRC}}(\gamma) d\gamma}_{I_1} + \underbrace{\int_{\gamma_T}^\infty p(e|\gamma) f_{\gamma_p}(\gamma) d\gamma}_{I_2} + \underbrace{\int_{\gamma_T}^\infty p(e|\gamma) g_c(\gamma) d\gamma}_{I_3} \tag{4.40}$$

To evaluate I_1, the conditional SER $p(e|\gamma)$ is expanded using Maclaurin series [186, eq. (3.321.1)] and is given by

$$p(e|\gamma) = \frac{A}{2}\left[1 - \frac{2}{\sqrt{\pi}} \sum_{n=0}^{\infty} \frac{(-1)^n K^{2n+1} \gamma^{n+\frac{1}{2}}}{n!(2n+1)}\right]. \tag{4.41}$$

By substituting (4.41) in I_1 and after utilizing [187, eq. (07.34.21.0084.01)], the term I_1 is given by

$$I_1 = I_{11} - I_{12}\,, \tag{4.42}$$

where

$$I_{11} = \frac{A}{2} F_{\gamma_{MRC}}(\gamma_T), \tag{4.43}$$

$$\begin{aligned} I_{12} = {} & C_3 \sum_{d=1}^{\beta} t_d \sum_{l=0}^{\infty} \sum_{m=0}^{l} M_{1,m} \sum_{n=0}^{\infty} M_{3,n} \sum_{i=0}^{\infty} Q_{1,i} \gamma_T^{\tau_1+n+\frac{1}{2}} \\ & \times G^{\,3p\;\;2}_{\,p+2\;3p+2}\left(B_2\gamma_T \middle| \begin{matrix} 0.5-\tau_1-n, 1, \mathcal{K}_1 \\ \mathcal{K}_2, 1-\tau_1, -\tau_1-n-0.5 \end{matrix}\right), \end{aligned} \tag{4.44}$$

C_3 and $M_{3,n}$ are given in Table 4.1. Since direct evaluation of I_2 by using [187, eq. (07.34.21.0085.01)] results in the divergence issue, we derive I_2 by splitting into two parts (i.e. I_{21} and I_{22}) and is given as

$$I_2 = \underbrace{\int_0^\infty p(e|\gamma) f_{\gamma_p}(\gamma) d\gamma}_{I_{21}} - \underbrace{\int_0^{\gamma_T} p(e|\gamma) f_{\gamma_p}(\gamma) d\gamma}_{I_{22}} . \tag{4.45}$$

To evaluate I_{21}, we replace $f_{\gamma_p}(\gamma)$ and $p(e|\gamma)$ by (4.16) and (4.37), respectively, and then by utilizing [187, eq. (07.34.21.0013.01)], we obtain as

$$I_{21} = \frac{C_3}{\tilde{\alpha}} \sum_{d=1}^{\beta} t_d \, G_{p+2\ 3p+1}^{3p\ \ 2} \left(B_3 \middle| \begin{matrix} 1, 0.5, \mathcal{K}_1 \\ \mathcal{K}_2, 0 \end{matrix} \right). \tag{4.46}$$

By substituting (4.16) and (4.41) in I_{22} and with the aid of [187, eq. (07.34.21.0084.01)], I_{22} is calculated as

$$\begin{aligned} I_{22} = \frac{A}{2} C_1 \sum_{d=1}^{\beta} t_d G_{p+1\ 3p+1}^{3p\ \ 1} \left(B_2 \gamma_T \middle| {}^{1, \mathcal{K}_1}_{\mathcal{K}_2, 0} \right) - \frac{C_3}{\tilde{\alpha}} \sum_{d=1}^{\beta} t_d \sum_{n=0}^{\infty} M_{3,n} \gamma_T^{n+\frac{1}{2}} \\ \times G_{p+1\ 3p+1}^{3p\ \ 1} \left(B_2 \gamma_T \middle| {}^{-n+0.5, \mathcal{K}_1}_{\mathcal{K}_2, -n-0.5} \right). \end{aligned} \tag{4.47}$$

Similarly, by substituting (4.37) and (4.34) in I_3 and using [187, eq. (07.34.21.0085.01)], the integral I_3 is evaluated as

$$\begin{aligned} I_3 = C_3 \sum_{d=1}^{\beta} t_d \sum_{l=0}^{\infty} \sum_{m=0}^{l} M_{1,m} \sum_{i=0}^{\infty} Q_{3,i} \sum_{j=0}^{\tau_1 - 1} \binom{\tau_1 - 1}{j} (-1)^j \gamma_T^{\tau_1} G_{2\ 3}^{3\ 0} \left(K^2 \gamma_T \middle| {}^{1, 1-\tau_1+j}_{-\tau_1+j, 0, 0.5} \right) \\ \times G_{p+1\ 3p+1}^{3p\ \ 1} \left(B_2 \gamma_T \middle| {}^{1-j, \mathcal{K}_1}_{\mathcal{K}_2, -j} \right). \end{aligned} \tag{4.48}$$

4.6 Asymptotic Analysis and Optimization

Since the exact closed-form expressions for outage and average SER are very complex to comprehend, computationally efficient asymptotic expressions need to be derived for the performance parameters by assuming average SNR values tending to infinity. Further, the asymptotic expressions can be used to derive the diversity gain of the system.

4.6.1 Outage Probability

In this section, the asymptotic expression for the outage probability is derived under the condition that the average SNR of the FSO link tends to infinity and the average SNR of the RF link is considered as a constant. Since $\overline{\gamma}_p \to \infty$, the input argument of the Meijer G-function will tend to zero. By using [187, eq. (07.34.06.0040.01)], Meijer G-function can be expanded into the Taylor series form as $\sum_{i=0}^{\infty} T_i(\overline{\gamma}_p)^{-i}$, where the minimum value of i is given as the diversity gain of the system for non-zero values of T_i.

4.6.1.1 Hybrid FSO/RF with MRC Scheme

The asymptotic outage expression for the MRC scheme is derived by assuming $\overline{\gamma}_p \to \infty$, which leads to $B_2 \to 0$ in (4.26), and by using [187, eq. (07.34.06.0040.01)], the asymptotic outage expression is written as

$$F^{\infty}_{\gamma_{MRC}}(x) = C_2 \sum_{d=1}^{\beta} t_d \sum_{l=0}^{\infty} \sum_{m=0}^{l} M_{1,m} \sum_{i=0}^{\infty} Q_{1,i} x^{\tau_1} \sum_{u=1}^{3p} \frac{\Lambda_1 \Gamma(\mathcal{K}_{2,u})\, B_4}{\Gamma(1+\tau_1+\mathcal{K}_{2,u})} \left(\frac{x}{\overline{\gamma}_p}\right)^{\mathcal{K}_{2,u}}, \tag{4.49}$$

where $\Lambda_1 = \frac{\prod_{s=1;\, s\neq u}^{3p} \Gamma(\mathcal{K}_{2,s}-\mathcal{K}_{2,u})}{\prod_{s=1}^{p} \Gamma(\mathcal{K}_{1,s}-\mathcal{K}_{2,u})}$, $B_4 = \left(\frac{B_1^p}{p^{2p}}\right)^{\mathcal{K}_{2,u}}$, and $\mathcal{K}_{i,j}$ represents the j^{th} term of $\mathcal{K}_i$.

4.6.1.2 Hybrid FSO/RF with Adaptive Combining Scheme

Similar to the MRC scheme, the asymptotic outage probability expression for the adaptive combining scheme is expressed as

$$F_{\gamma_c}^{\infty}(x) = \begin{cases} F_{\gamma_{MRC}}^{\infty}(x), & x \leq \gamma_T. \\ F_1^{\infty}(x) + F_{\gamma_p}^{\infty}(x) - F_{\gamma_p}^{\infty}(\gamma_T), & x > \gamma_T. \end{cases} \tag{4.50}$$

The asymptotic outage expression when $\gamma_{OT} \leq \gamma_T$ is given by (4.49). Further, the asymptotic expressions for the case when $\gamma_{OT} > \gamma_T$ can be obtained by applying [187, eq. (07.34.06.0040.01)] in both (4.31) and (4.19). After simplifying the expressions, $F_1^{\infty}(x)$ and $F_{\gamma_p}^{\infty}(x)$ can be, respectively, obtained as

$$F_1^{\infty}(x) = C_2 \sum_{d=1}^{\beta} t_d \sum_{l=0}^{\infty} \sum_{m=0}^{l} M_{2,m} \sum_{n=0}^{\infty} Q_{2,n} \sum_{j=0}^{\tau_2} \binom{\tau_2}{j} (-\gamma_T)^j x^{\tau_2 - j} \sum_{u=1}^{3p} \frac{\Lambda_1 B_4}{(j + \mathcal{K}_{2,u})} \left(\frac{\gamma_T}{\overline{\gamma}_p}\right)^{\mathcal{K}_{2,u}} \tag{4.51}$$

$$\text{and} \quad F_{\gamma_p}^{\infty}(x) = C_1 \sum_{d=1}^{\beta} t_d \sum_{u=1}^{3p} \frac{\Lambda_1 B_4}{\mathcal{K}_{2,u}} \left(\frac{x}{\overline{\gamma}_p}\right)^{\mathcal{K}_{2,u}} \tag{4.52}$$

4.6.2 Average SER

The asymptotic expressions for average SER of MRC and adaptive combining schemes are derived in the same manner as done for the outage probability in the previous subsections.

4.6.2.1 Hybrid FSO/RF with MRC Scheme

By assuming $B_3 \to 0$ in (4.38) and utilizing [187, eq. (07.34.06.0040.01)], the asymptotic SER expression for the MRC system is obtained as

$$\overline{P}_e^{MRC\infty} = C_3 \sum_{d=1}^{\beta} t_d \sum_{l=0}^{\infty} \sum_{m=0}^{l} M_{1,m} \sum_{i=0}^{\infty} \frac{Q_{1,i}}{K^{2\tau_1}} \sum_{u=1}^{3p} \Lambda_1 B_5 \frac{\Gamma(\mathcal{K}_{2,u})\Gamma(0.5+\tau_1+\mathcal{K}_{2,u})}{\Gamma(1+\tau_1+\mathcal{K}_{2,u})} \left(\frac{1}{\overline{\gamma}_p}\right)^{\mathcal{K}_{2,u}} \tag{4.53}$$

where $B_5 = \left(\frac{B_1^p}{K^2 p^{2p}}\right)^{\mathcal{K}_{2,u}}$.

4.6.2.2 Hybrid FSO/RF with Adaptive Combining Scheme

In case of the adaptive combining scheme, the asymptotic average SER expression is the sum of the individual asymptotic terms, which can be written as

$$\overline{P}_e^{AC\infty} = I_{11}^{\infty} - I_{12}^{\infty} + I_{21}^{\infty} - I_{22}^{\infty} + I_3^{\infty}, \tag{4.54}$$

where the asymptotic expression for each integral can be calculated by using the limiting form of Meijer G-function [187, eq. (07.34.06.0040.01)] in (4.43), (4.44), (4.46), (4.47), and (4.48). After simplification, the following asymptotic expressions for each integral is obtained as

$$I_{11}^{\infty} = \frac{A}{2} F_{\gamma_{MRC}}^{\infty}(\gamma_T), \tag{4.55}$$

$$\begin{aligned} I_{12}^{\infty} = {} & C_3 \sum_{d=1}^{\beta} t_d \sum_{l=0}^{\infty} \sum_{m=0}^{l} M_{1,m} \sum_{n=0}^{\infty} M_{3,n} \sum_{i=0}^{\infty} Q_{1,i} \gamma_T^{\tau_1+n+\frac{1}{2}} \\ & \times \sum_{u=1}^{3p} \frac{\Lambda_1 B_4 \Gamma(\mathcal{K}_{2,u})}{(0.5+\tau_1+n+\mathcal{K}_{2,u})\Gamma(\tau_1+\mathcal{K}_{2,u})} \left(\frac{\gamma_T}{\overline{\gamma}_p}\right)^{\mathcal{K}_{2,u}}, \end{aligned} \tag{4.56}$$

$$I_{21}^{\infty} = \frac{C_3}{\tilde{\alpha}} \sum_{d=1}^{\beta} t_d \sum_{u=1}^{3p} \frac{\Lambda_1 B_5 \Gamma\left(\mathcal{K}_{2,u} + \frac{1}{2}\right)}{\mathcal{K}_{2,u}} \left(\frac{1}{\overline{\gamma}_p}\right)^{\mathcal{K}_{2,u}}, \tag{4.57}$$

$$\begin{aligned} I_{22}^{\infty} &= \frac{A}{2} C_1 \sum_{d=1}^{\beta} t_d \sum_{u=1}^{3p} \frac{\Lambda_1 B_4}{\mathcal{K}_{2,u}} \left(\frac{\gamma_T}{\overline{\gamma}_p}\right)^{\mathcal{K}_{2,u}} - \frac{C_3}{\tilde{\alpha}} \sum_{d=1}^{\beta} t_d \sum_{n=0}^{\infty} M_{3,n} \gamma_T^{n+\frac{1}{2}} \\ &\times \sum_{u=1}^{3p} \frac{\Lambda_1 B_4}{\mathcal{K}_{2,u} + n + \frac{1}{2}} \left(\frac{\gamma_T}{\overline{\gamma}_p}\right)^{\mathcal{K}_{2,u}}, \end{aligned} \tag{4.58}$$

$$\begin{aligned} I_3^{\infty} &= C_3 \sum_{d=1}^{\beta} t_d \sum_{l=0}^{\infty} \sum_{m=0}^{l} M_{1,m} \sum_{i=0}^{\infty} Q_{3,i} \sum_{j=0}^{\tau_1 - 1} \binom{\tau_1 - 1}{j} (-1)^j \gamma_T^{\tau_1} G_{2\,3}^{3\,0}\left(K^2 \gamma_T \middle|\, {}^{1,1-\tau_1+j}_{-\tau_1+j,0,0.5}\right) \\ &\times \sum_{u=1}^{3p} \frac{\Lambda_1 B_4}{(j + \mathcal{K}_{2,u})} \left(\frac{\gamma_T}{\overline{\gamma}_p}\right)^{\mathcal{K}_{2,u}}. \end{aligned} \tag{4.59}$$

4.6.3 Diversity Gain Analysis

In this subsection, the diversity gain for MRC and adaptive combining schemes is presented, which are based on different conditions with respect to $\overline{\gamma}_p$, $\overline{\gamma}_{RF}$, and γ_T. Also, the conditions for obtaining the full diversity gain from both FSO and RF links in case of MRC and adaptive combining schemes are also discussed.

4.6.3.1 Hybrid FSO/RF with MRC Scheme

The diversity gain of the MRC scheme is derived for two cases as given in Theorem 1 and 2. The asymptotic expression for the average SER of a system can be approximated in terms of average SNR $\overline{\gamma}_p$, diversity gain G_d, and coding gain G_c as

$$P_e^{\infty} \approx (G_c \overline{\gamma}_p)^{-G_d} \tag{4.60}$$

Theorem 4.1. *For an MRC scheme assuming $\overline{\gamma}_p \to \infty$ and considering that the average SNR of RF link $\overline{\gamma}_{RF}$ is a constant, the diversity gain of hybrid FSO/RF* *system is given by*

$$G_d^{M^{(1)}} = \min(g_{eq}^2/p, \alpha/p, 1/p) \tag{4.61}$$

Proof. From (4.53), it can be clearly seen that the dominating terms in the asymptotic SER expansion, which depends on $\overline{\gamma}_p$, is given by $\hat{\mathcal{K}}_{2,u} = \min(\mathcal{K}_{2,u}) = \min(g_{eq}^2/p, \alpha/p, 1/p)$. Therefore, the diversity gain of the MRC scheme is given by (4.61), which is also equal to the diversity gain of an FSO system. □

Theorem 4.2. *For an MRC scheme assuming $\overline{\gamma}_p \to \infty$ and considering that the average SNR of RF link is also varying and is equal to the average SNR of FSO link (i.e. $\overline{\gamma}_{RF} = \overline{\gamma}_p = \overline{\gamma}$), the diversity gain of MRC-based hybrid FSO/RF system is given by*

$$G_d^{M^{(2)}} = \min\left(\frac{g_{eq}^2}{p} + \tilde{\alpha}\mu, \frac{\alpha}{p} + \tilde{\alpha}\mu, \frac{1}{p} + \tilde{\alpha}\mu\right) \tag{4.62}$$

Proof. Since it is assumed that $\overline{\gamma}_{RF} = \overline{\gamma}_p \to \infty$, the dominating terms in (4.53) will be obtained by substituting $m = 0$ and $i = 0$ into the inner summations [166]. This is because, $m > 0$ and $i > 0$ contribute for higher powers of $1/\overline{\gamma}$, which can be ignored. After simplifications, the asymptotic SER of MRC scheme can be obtained as

$$\overline{P}_e^{MRC^\infty} = \frac{C_3}{K^{\alpha_r\mu}} \sum_{d=1}^{\beta} t_d \sum_{l=0}^{\infty} \frac{c_l \Gamma(\tilde{\alpha}\mu)}{\Gamma(\mu) 2^\mu} \sum_{u=1}^{3p} \Lambda_1 B_5 \left(\frac{1}{\overline{\gamma}}\right)^{\mathcal{K}_{2,u}+\tilde{\alpha}\mu} \frac{\Gamma(\mathcal{K}_{2,u})\Gamma(0.5+\tilde{\alpha}\mu+\mathcal{K}_{2,u})}{\Gamma(1+\tilde{\alpha}\mu+\mathcal{K}_{2,u})}. \tag{4.63}$$

Further, by comparing the dominant terms in (4.63) with (4.60), the diversity gain is given by (4.62). It is to be noted that in this case, full diversity gain is achieved from both RF and FSO links using the MRC scheme. □

4.6.3.2 Hybrid FSO/RF with Adaptive Combining Scheme

The diversity gain values of adaptive combining scheme for three different cases are obtained using Theorem 4.3, 4.4 and 4.5.

$$
\begin{aligned}
\overline{P}_e^{AC\infty} = & \sum_{d=1}^{\beta} t_d \sum_{u=1}^{3p} \Lambda_1 \left(\frac{1}{\overline{\gamma}_p}\right)^{\mathcal{K}_{2,u}} \Bigg\{ B_4 \gamma_T^{\mathcal{K}_{2,u}} \sum_{l=0}^{\infty} \sum_{m=0}^{l} M_{1,m} \gamma_T^{\tau_1} \Bigg[\frac{A}{2} C_2 \sum_{i=0}^{\infty} Q_{1,i} \frac{\Gamma(\mathcal{K}_{2,u})}{\Gamma(1+\tau_1+\mathcal{K}_{2,u})} \\
& - C_3 \sum_{n=0}^{\infty} M_{3,n} \sum_{i=0}^{\infty} Q_{1,i}\, \gamma_T^{n+\frac{1}{2}} \frac{\Gamma(\mathcal{K}_{2,u})}{(0.5+\tau_1+n+\mathcal{K}_{2,u})\Gamma(\tau_1+\mathcal{K}_{2,u})} + C_3 \sum_{i=0}^{\infty} Q_{3,i} \\
& \times \sum_{j=0}^{\tau_1-1} \binom{\tau_1-1}{j} (-1)^j G_{2\,3}^{3\,0} \left(K^2 \gamma_T \middle| \begin{smallmatrix} 1,1-\tau_1+j \\ -\tau_1+j,0,0.5 \end{smallmatrix} \right) \frac{1}{(j+\mathcal{K}_{2,u})} \Bigg] + \frac{C_3 B_5 \Gamma\left(\mathcal{K}_{2,u}+\frac{1}{2}\right)}{\tilde{\alpha} \mathcal{K}_{2,u}} \\
& - \frac{A}{2} C_1 \frac{B_4 \gamma_T^{\mathcal{K}_{2,u}}}{\mathcal{K}_{2,u}} + \frac{C_3}{\tilde{\alpha}} \sum_{n=0}^{\infty} M_{3,n} \frac{B_4 \gamma_T^{\mathcal{K}_{2,u}+n+\frac{1}{2}}}{\mathcal{K}_{2,u}+n+\frac{1}{2}} \Bigg\}
\end{aligned} \tag{4.65}
$$

Theorem 4.3. *For an adaptive combining scheme assuming $\overline{\gamma}_p \to \infty$, fixing $\gamma_T = \gamma_T^{opt}$, where γ_T^{opt} is the optimum switching threshold SNR value, and considering a constant $\overline{\gamma}_{RF}$, the diversity gain of the system is given by*

$$
G_d^{AC^{(1)}} = \min(g_{eq}^2/p, \alpha/p, 1/p) \tag{4.64}
$$

Proof. By substituting (4.55), (4.56), (4.57), (4.58), and (4.59) in (4.54) and after some manipulations, $\overline{P}_e^{AC\infty}$ can be written in terms of $\overline{\gamma}_p$ as given by (4.65). Assuming $\overline{\gamma}_{RF}$ as a constant, the dominating terms in (4.65) is given by $\hat{\mathcal{K}}_{2,u} = \min(\mathcal{K}_{2,u})$. Therefore, the diversity gain of the adaptive combining scheme turns out to be same as given for the MRC scheme in (4.64). □

Theorem 4.4. *For an adaptive combining scheme assuming $\overline{\gamma}_{RF} = \overline{\gamma}_p = \overline{\gamma} \to \infty$ and a constant switching threshold value γ_T, the diversity gain of such a hybrid system is given by*

$$
G_d^{AC^{(2)}} = \min(g_{eq}^2/p, \alpha/p, 1/p) \tag{4.66}
$$

Proof. From (4.65), which is given on the top of the next page, it is inferred that assuming $\overline{\gamma}_{RF} = \overline{\gamma}_p \to \infty$ and a constant γ_T, the terms involving the powers of $\frac{\gamma_T}{\overline{\gamma}_p \overline{\gamma}_{RF}}$ will be negligible against the terms containing powers of $\frac{1}{\overline{\gamma}_p}$. Thus, the dominating expression will include only the terms with powers of $\frac{1}{\overline{\gamma}_p}$ and by neglecting other terms in (4.65), we obtain

$$
\begin{aligned}
\overline{P}_e^{AC\infty} &= \sum_{d=1}^{\beta} t_d \sum_{u=1}^{3p} \Lambda_1 \left(\frac{1}{\overline{\gamma}_p}\right)^{\mathcal{K}_{2,u}} \left[\frac{C_3 B_5 \Gamma\left(\mathcal{K}_{2,u}+\frac{1}{2}\right)}{\tilde{\alpha}\mathcal{K}_{2,u}} - \frac{A}{2} C_1 \frac{B_4 \gamma_T^{\mathcal{K}_{2,u}}}{\mathcal{K}_{2,u}}\right. \\
&\quad \left. + \frac{C_3}{\tilde{\alpha}} \sum_{n=0}^{\infty} M_{3,n} \frac{B_4 \gamma_T^{\mathcal{K}_{2,u}+n+\frac{1}{2}}}{\mathcal{K}_{2,u}+n+\frac{1}{2}}\right] \qquad (4.67)
\end{aligned}
$$

From (4.60) and (4.67), the diversity gain in this case is obtained as (4.66), which is same as given by (4.64) and is equal to the diversity gain of an FSO system. □

Theorem 4.5. *For an adaptive combining scheme assuming* $\overline{\gamma}_{RF} = \overline{\gamma}_p = \overline{\gamma} \to \infty$ *and fixing* $\gamma_T = \gamma_T^{opt}$*, the diversity gain of the hybrid system is given by*

$$
G_d^{AC(3)} = \min\left(\frac{g_{eq}^2}{p} + \tilde{\alpha}\mu, \frac{\alpha}{p} + \tilde{\alpha}\mu, \frac{1}{p} + \tilde{\alpha}\mu\right) \qquad (4.68)
$$

Proof. As the average SNR of RF link varies, we have obtained different values of optimum threshold SNR γ_T^{opt} corresponding to each value of $\overline{\gamma}_{RF}$. It is to be noted that γ_T^{opt} values are generally non-decreasing. In such scenario, if $\overline{\gamma}_{RF} = \overline{\gamma}_p \to \infty$ and the values of γ_T^{opt} are also varying, then the terms involving the powers of $\frac{\gamma_T}{\overline{\gamma}_p \overline{\gamma}_{RF}}$ will be comparable to the terms containing the powers of $\frac{1}{\overline{\gamma}}$ and cannot be ignored. Further, by substituting $m = 0$ and $i = 0$ in (4.65), as given in Theorem 2, the dominant terms corresponding to $\overline{\gamma}_{RF} \to \infty$ is obtained and by considering the terms having the powers of $\frac{\gamma_T}{\overline{\gamma}}$, $\overline{P}_e^{AC\infty}$ can be simplified as given by (4.69). By comparing the dominating terms in (4.69) with (4.60), the diversity gain is given by (4.68). Thus, in this case, full (or the highest) diversity gain of the adaptive combining scheme is achieved due to the contribution of RF link, unlike the previous two cases. □

$$
\begin{aligned}
\overline{P}_e^{AC\infty} &= \frac{1}{\Gamma(\mu)2^{\mu}}\sum_{d=1}^{\beta} t_d \sum_{u=1}^{3p}\Lambda_1 B_4\left(\frac{\gamma_T}{\overline{\gamma}}\right)^{\mathcal{K}_{2,u}+\tilde{\alpha}\mu}\sum_{l=0}^{\infty} c_l\left[\frac{A}{2}C_2\frac{\Gamma(\tilde{\alpha}\mu)\Gamma(\mathcal{K}_{2,u})}{\Gamma(1+\tilde{\alpha}\mu+\mathcal{K}_{2,u})}\right.\\
&- C_3\sum_{n=0}^{\infty} M_{3,n}\gamma_T^{n+\frac{1}{2}}\frac{\Gamma(\tilde{\alpha}\mu)\Gamma(\mathcal{K}_{2,u})}{(0.5+\tilde{\alpha}\mu+n+\mathcal{K}_{2,u})\Gamma(\tilde{\alpha}\mu+\mathcal{K}_{2,u})}\\
&\left.+ C_3\sum_{j=0}^{\tilde{\alpha}\mu-1}\binom{\tilde{\alpha}\mu-1}{j}(-1)^j G_{2\,3}^{3\,0}\left(K^2\gamma_T\middle|\,{}^{1,1-\tilde{\alpha}\mu+j}_{-\tilde{\alpha}\mu+j,0,0.5}\right)\frac{1}{(j+\mathcal{K}_{2,u})}\right] \qquad (4.69)
\end{aligned}
$$

4.6.4 beam width Optimization

In this subsection, we present the optimization of transmit beam width. It is important to note that the severity of pointing errors decreases with an increase in the coefficient g_{eq}. As the value of g_{eq} increases, the average SER of the system decreases. Further, the parameter g_{eq} depends on the beam width w_0. Therefore, the g_{eq} can be maximized to determine the optimum value of beam width, i.e. w_0^{opt}, which gives the best SER performance. It is also to be noted that the optimum beam width values depend on the pointing error coefficient values. Further, the optimum beam width values are obtained by differentiating the pointing error coefficient g_{eq} and its equation for generalized non-zero boresight case is different compared to zero boresight pointing errors case. From (4.12), (4.13) and after performing some manipulations, we can write g_{eq}^2 in terms of w_0 as

$$
g_{eq}^2 = \frac{1}{4\delta_{eq}^2}\sum_{n=0}^{\infty} a_n r_0^{2n}\left[w_0^2+\frac{\lambda_F^2L^2}{\pi^2w_0^2}+\frac{2\lambda_F^2L^2}{\pi^2\varrho_0^2(L)}\right]^{1-n} \qquad (4.70)
$$

where a_n is a constant. Further, by differentiating g_{eq}^2 in (4.70) with respect to w_0, we obtain

$$
g_{eq}\frac{dg_{eq}}{dw_0} = \frac{1}{4\delta_{eq}^2}\sum_{n=0}^{\infty} a_n r_0^{2n}(1-n)\left[w_0^2+\frac{\lambda_F^2L^2}{\pi^2w_0^2}+\frac{2\lambda_F^2L^2}{\pi^2\varrho_0^2(L)}\right]^{-n}\left(w_0-\frac{\lambda_F^2L^2}{\pi^2w_0^3}\right) \qquad (4.71)
$$

Now, by equating (4.71) to zero, the optimum beam width w_0^{opt} is given by

$$w_0^{opt} = \sqrt{\frac{\lambda_F L}{\pi}} \tag{4.72}$$

4.7 Numerical Results and discussion

In this section, the analytical and simulation results of the performance metrics are presented under different system configurations. The values of the key parameters and weather dependent parameters used in the simulation results are given in Table 4.2 [41], [48], [170], unless and otherwise specified. We generate 10^7 bits to execute the Monte-Carlo simulations for plotting the simulation results. Further, a detailed flowchart describing the approach to compute average SER using the Monte-Carlo simulations is given in Fig. 4.2. The analytical results are matching with the Monte-Carlo simulations, which validates the accuracy of our derived expressions. Unless and otherwise stated, the average SNR of RF link is fixed to $\overline{\gamma}_{RF} = 5$ dB and few other parameters are assumed as $m_x/r_0 = 3$, $m_y/r_0 = 3$, $\delta_x/r_0 = 3.5$, $\delta_y/r_0 = 3.5$, $\Omega = 1.3265$, $\rho = 0.595$, $b_0 = 0.2158/2$, and $\phi_A - \phi_B = \pi/2$.

The accuracy of truncation limits used for the terms involving infinite summations in equations (4.22), (4.26), (4.31), (4.38), (4.44), (4.47), and (4.48) are given in the last column of Table 4.3. Further, it is inferred from the given values of the above-mentioned equations in Table 4.3 that if the values higher than the upper limits are used, then there will be no effect on the fifth decimal figure of the final calculated values. All the given upper limit values are also applicable to their asymptotic counterparts.

Additionally, in Fig. 4.3, the convergence of the CDFs $F_{\gamma_{RF}}(x)$ and $F_{\gamma_{MRC}}(x)$, which are given by (4.22) and (4.26), is verified. The values of the outage threshold and the switching threshold are assumed as $\gamma_{OT} = 6$ dB and $\gamma_T = 8$ dB, respectively. In Fig. 4.3 (a), $F_{\gamma_{RF}}(\gamma_{OT})$ is plotted against the upper limit of the truncation value of summation limit l for different values of $\overline{\gamma}_p$. From the plots, it is observed that

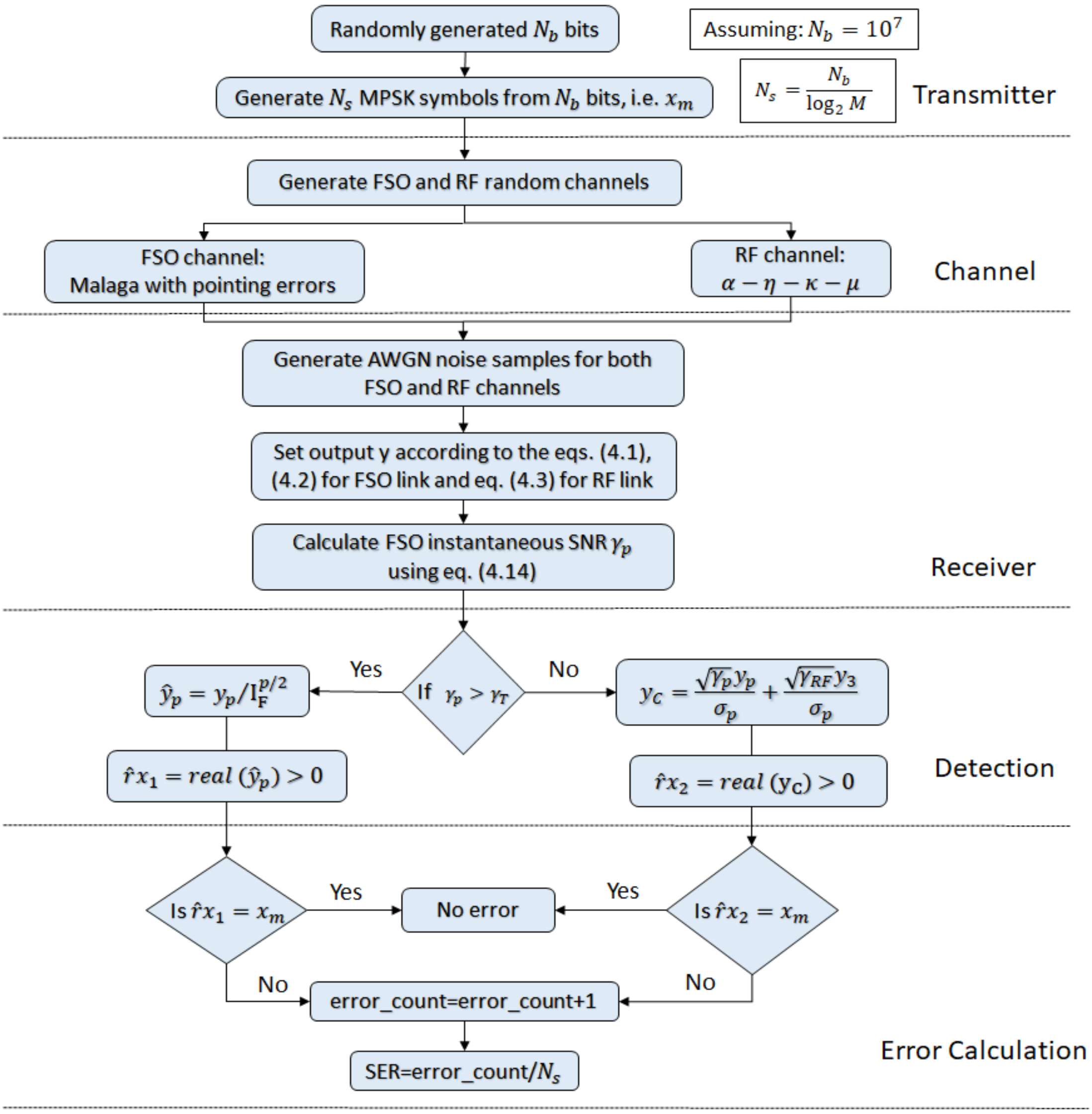

Fig. 4.2: Flowchart for computing average SER using Monte-Carlo simulations

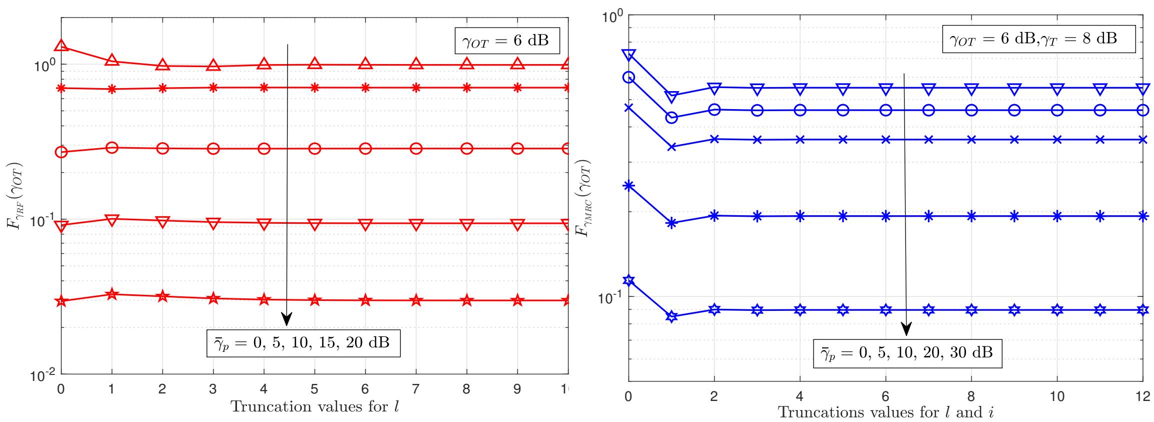

(a) (b)

Fig. 4.3: Convergence test for CDF expressions in (4.22) and (4.26)

Table 4.2: FSO/RF parameters used in the simulations

FSO Parameter	**Symbol**	**Value**
Wavelength FSO	λ_F	1550 nm
Noise variance FSO	σ_p^2	10^{-14}
Responsivity	η_f	0.5 A/W
RF bandwidth	B_R	250 MHz
RF wavelength	λ_R	5 mm
RF transmit power	P_R	10 mW
Transmit antenna gain	G_t	44 dBi
Receive antenna gain	G_r	44 dBi
Attenuation oxygen	ζ_{ox}	15.1 dB/km
Noise power spectral density	N_0	-114 dBm/MHz
Receiver noise figure	NF	5 dB

Weather condition	$\boldsymbol{\zeta_w}$ **(dB/km)**	$\boldsymbol{\zeta_{rn}}$ **(dB/km)**	$\boldsymbol{\zeta_{fog}}$ **(dB/km)**	$\boldsymbol{C_n^2(m^{-2/3})}$
Rain	5.8	5.6	0	5×10^{-15}
Light fog	4.2	0	0	1.7×10^{-14}
Clear air	0.43	0	0	5×10^{-14}
Heavy fog	125	0	3.2	1×10^{-15}

for $l \geq 5$, $F_{\gamma_{RF}}(\gamma_{OT})$ remains almost constant, which is also evident from row-1 of Table 4.3. Similarly, in Fig. 4.3 (b), $F_{\gamma_{MRC}}(\gamma_{OT})$ is plotted against the upper limit of the truncation values of summation limits l and i for different values of $\overline{\gamma}_p$. It is inferred from the Fig. 4.3 (b) that for $l \geq 4$ and $i \geq 4$, $F_{\gamma_{MRC}}(\gamma_{OT})$ remains almost unaltered, which is also confirmed from row-2 of Table 4.3.

In Fig. 4.4(a), we have plotted the average SER against the beam width values to obtain the optimum beam width values. The average SER plots are given for different values of link distance, average SNR of FSO link, and receiver aperture radius. The optimum values of beam width w_0^{opt} obtained using the numerical technique are approximately equal to the values of w_0^{opt} obtained from theoretical optimization as shown in Table 4.4. From (4.72), it is clear that the optimum values of beam width depend only on the link distance and FSO wavelength and it does not depend on other parameters, which is also observed from Fig. 4.4 (a). In Fig. 4.4(b), the

Table 4.3: Truncation accuracy of summation limits

Eq.	Expressions	Truncation values	Final values		Chosen upper limit
			$\overline{\gamma}_p = 10$	$\overline{\gamma}_p = 20$	
(4.22)	$F_{\gamma_{RF}}(x)$	$l = 7$	0.285557	0.029899	$l = 8$
		$l = 8$	0.285601	0.029885	
		$l = 10$	0.285604	0.029880	
(4.26)	$F_{\gamma_{MRC}}(x)$	$l = 7$, $i = 7$	0.361433	0.190509	$l = 8$, $i = 8$
		$l = 8$, $i = 8$	0.361427	0.190506	
		$l = 10$, $i = 10$	0.361425	0.190505	
(4.31)	$F_1(x)$	$l = 5$, $n = 5$	0.349639	0.181830	$l = 6$, $n = 6$
		$l = 6$, $n = 6$	0.349583	0.181804	
		$l = 8$, $n = 8$	0.349585	0.181805	
(4.38)	$\overline{P}_e^{MRC}$	$l = 4$, $i = 4$	0.020838	0.010080	$l = 5$, $i = 5$
		$l = 5$, $i = 5$	0.020834	0.010078	
		$l = 7$, $i = 7$	0.020832	0.010077	
(4.44)	I_{12}	$l = 12$, $n = 12$, $i = 12$	0.160027	0.085264	$l = 13$, $n = 13$, $i = 13$
		$l = 13$, $n = 13$, $i = 13$	0.160018	0.085258	
		$l = 15$, $n = 15$, $i = 15$	0.160018	0.085258	
(4.47)	I_{22}	$n = 13$	0.000061	0.000049	$n = 15$
		$n = 15$	0.000058	0.000046	
		$n = 18$	0.000058	0.000046	
(4.48)	I_3	$l = 3$, $i = 3$	0.000148	0.000073	$l = 5$, $i = 5$
		$l = 5$, $i = 5$	0.000127	0.000074	
		$l = 6$, $i = 6$	0.000127	0.000074	

average SER is plotted with respect to switching threshold SNR values to obtain the optimum threshold SNR for different values of average SNR of RF link $\overline{\gamma}_{RF}$ and FSO link $\overline{\gamma}_p$. It is observed from the plots that the average SER decreases with an increase in switching threshold SNR γ_T and remains approximately constant after a particular value of γ_T. The optimum threshold SNR γ_T^{opt} is achieved when the average SER reaches to a certain level and becomes less sensitive to changes in the threshold SNR value. This particular threshold value is considered as the optimum value of switching threshold SNR. Further, the optimum values of threshold SNR are obtained as γ_T^{opt} = 7 dB, 9 dB, and 10 dB as shown in Table 4.4. Since the average SER decreases with an increase in switching threshold SNR γ_T and remains approximately constant after a particular value of γ_T, a global optimum value does not exist as observed in the figure. It is also inferred from 4.4(b) that the optimum switching threshold is increasing with respect to the average SNR of the RF link and it remains the same irrespective of change in the average SNR of the FSO link. This is mainly due to the fact that an increase in the value of the average

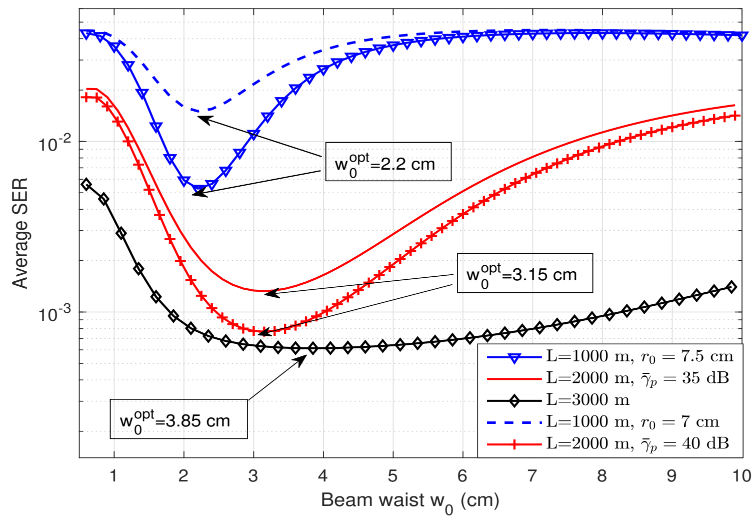

(a)

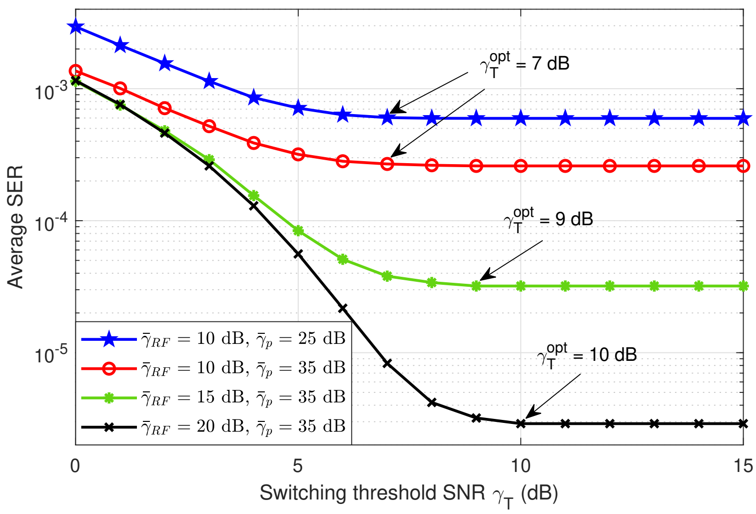

(b)

Fig. 4.4: Average SER versus switching threshold SNR γ_T and beam width w_0

SNR of RF link should increase the optimum switching threshold for achieving the minimum SER value. Further, the FSO subsystem will enter more frequently into outage with an increase in optimum switching threshold SNR value and there will be a higher probability of usage of the RF link. Consequently, the performance of the overall system is improved by counteracting the FSO channel distortions. Hence, the optimum threshold depends on the RF link condition and not on the FSO link condition.

Fig. 4.5 illustrates the average SER of adaptive combining scheme for a variety of distributions which are derived as the special cases of Malaga and α-η-κ-μ

Table 4.4: The optimum values of w_0 and γ_T

Distance L	w_0^{opt} (in cm)	
	Theoretical	Numerical
1000 m	2.22 cm	2.20 cm
2000 m	3.14 cm	3.15 cm
3000 m	3.85 cm	3.85 cm

$\overline{\gamma}_{RF}$ (dB)	$\overline{\gamma}_p$ (dB)	γ_T^{opt} (dB)
10	25	7
10	35	7
15	35	9
20	35	10

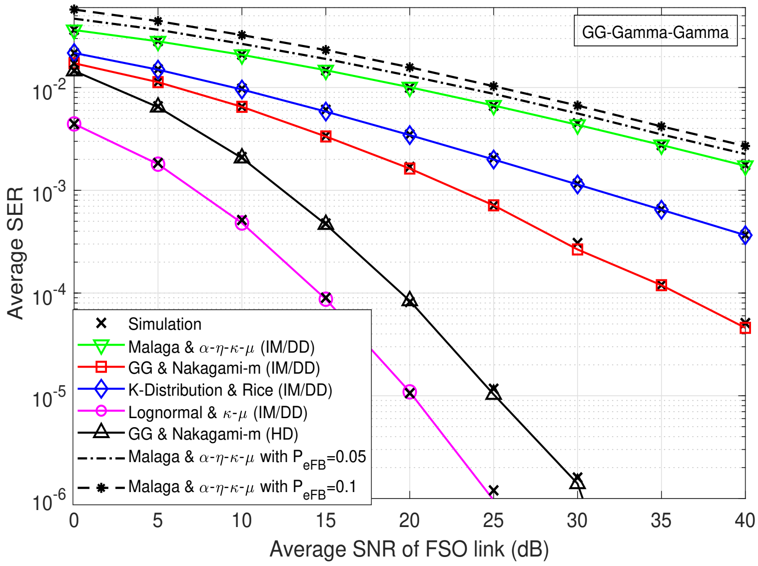

Fig. 4.5: Average SER of adaptive combining for various distributions

distributions. The parameter values of Malaga and α-η-κ-μ distributions required to obtain other distributions as special cases are given in Table 4.5. In addition, the performance comparison of IM/DD and HD techniques is depicted for Gamma-Gamma and Nakagami-m distributions. As expected, it is observed that the HD technique, due to its coherent detection nature, performs better than the IM/DD technique. Additionally, we have shown the impact of erroneous feedback link on the performance of adaptive-combining system assuming the case of Malaga and α-η-κ-μ distributions. Here, the probability that the feedback bits are in error, which is denoted as P_{eFB}, is assumed to be $P_{eFB} = 0.05$ and 0.1. From the plots, it can be noticed that there is a degradation in the performance of the system with erroneous feedback link and the SNR gains obtained by the non-erroneous feedback link over the erroneous link are 3 dB and 5 dB for $P_{eFB} = 0.05$ and 0.1, respectively, to attain the average SER of 10^{-2}.

Table 4.5: List of channel models and parameters assumed to obtain Fig. 4.6

FSO models	$\mathbf{C_n^2(m^{-2/3})}$	$\mathbf{r_0}$ (cm)	$\boldsymbol{\rho}$	$\mathbf{2b_0}$	$\boldsymbol{\Omega}$	$\boldsymbol{\gamma_T^{opt}}$ (dB)
Malaga	2×10^{-13}	35	0.596	0.2185	1.3265	5
Gamma-Gamma	2×10^{-14}	20	1	0	1	6
K distribution	4×10^{-13}	20	0	0.2185	0	6
Log-normal	5×10^{-15}	15	0	0	1.3265	7

RF models	$\boldsymbol{\alpha_R}$	$\boldsymbol{\eta}$	$\boldsymbol{\kappa}$	$\boldsymbol{\mu}$
α-η-κ-μ	2	1.5	0.5	1
Nakagami-m	2	1	0	2
Rice	2	1	2	1
κ-μ	2	1	5	3

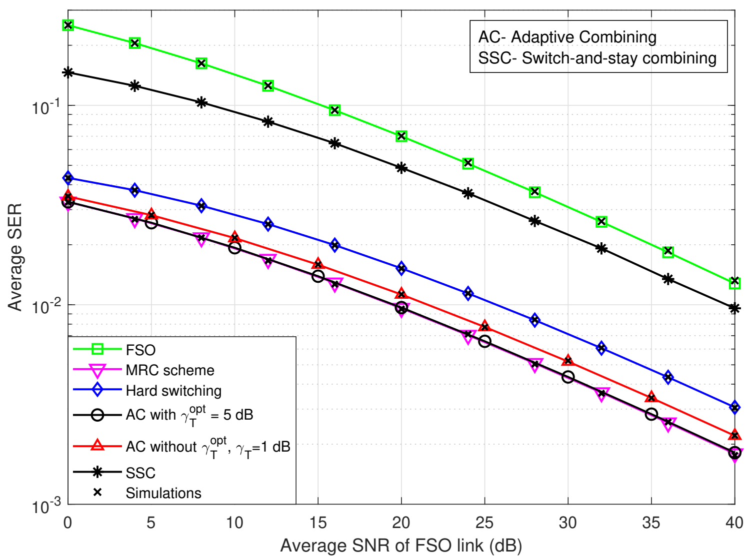

Fig. 4.6: Average SER comparison for different hybrid FSO/RF schemes

Fig. 4.6 shows the performance comparison of single-link FSO system with various hybrid systems based on single-threshold-based hard-switching scheme [190], MRC scheme, and adaptive combining scheme. Additionally, we have compared the FSO-based SSC scheme [127] with the above-mentioned hybrid schemes by assuming two receive apertures and one transmit aperture. The FSO link parameters assumed are given as follows: $C_n^2 = 4 \times 10^{-13}$, $L = 2000$ m, $r_0 = 32$ cm, and $w_0 = 3$ cm. Similarly, the RF link parameters assumed are given as follows: $\alpha_r = 2$, $\eta = 0.4$, $\kappa = 2$, $\mu = 1$, $p = 1$, and $q = 0.1$. The upper limits used for truncating the terms involving infinite summations in order to plot the theoretical average SER curves of MRC and adaptive combining systems are given in the last column of Table 4.3.

It is observed that the MRC-based and adaptive-combining-based hybrid systems outperform the single-link FSO, FSO-based SSC, and hard-switching-based hybrid systems.

Fig. 4.6 also unveils that the adaptive-combining-based hybrid system operating at $\gamma_T^{opt} = 5$ dB achieves the same SER performance as that of the MRC-based hybrid system. It can also be noticed that the SER performance of adaptive-combining-based hybrid system operating at optimum switching threshold SNR value with $\gamma_T^{opt} = 5$ dB performs better than the system operating at non-optimum switching threshold SNR value with $\gamma_T = 1$ dB, as expected. However, still the non-optimal SER performance of the adaptive-combining-based hybrid system is better than the hard-switching-based hybrid system which is operating in its optimal threshold value with $\gamma_{T_{(hard)}}^{opt} = 1$ dB. It is to be noted that in case of the single-threshold-based hard-switching scheme, only FSO or RF link will be active at a given time instant, whereas in case of MRC or adaptive combining scheme both the FSO and RF links can be active simultaneously and the superior performance is mainly due to diversity combining of FSO and RF links. Note that the SNR gain of MRC-based and optimal adaptive-combining-based hybrid systems over the hard-switching-based hybrid system to attain the average SER of 10^{-2} is found to be 5 dB. Further, the non-optimal adaptive-combining-based hybrid system achieves the SNR gain of 4 dB over the hard-switching-based hybrid system to attain the average SER of 10^{-2}. It is also to be noted that even though the adaptive combining and MRC schemes attain the same SER performance, the adaptive combining scheme achieves power saving by effectively utilizing the RF subsystem than the MRC scheme. This is because, the RF link is continuously active in the MRC scheme. However, in the adaptive combining scheme, MRC of FSO and RF links will be employed only when the instantaneous SNR of FSO link drops below a threshold SNR value. Further, the main advantage of MRC over adaptive combining is that the feedback bit from receiver to transmitter for switching between FSO link and MRC of FSO and RF links is not required.

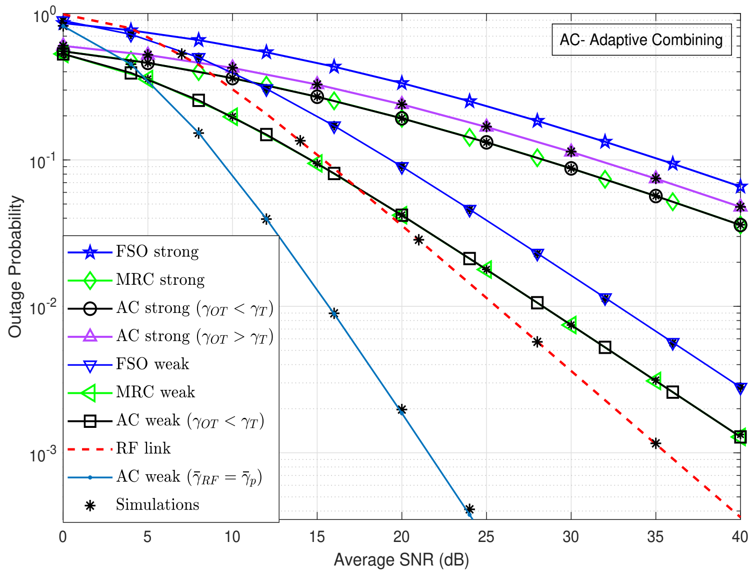

Fig. 4.7: Outage performance for strong and weak turbulence conditions

Fig. 4.7 depicts the outage performance comparison of single-link FSO, single-link RF, MRC-based hybrid, and adaptive-combining-based hybrid systems under strong and weak turbulence conditions assuming $C_n^2 = 1 \times 10^{-13}$ and $C_n^2 = 6 \times 10^{-15}$, respectively, with outage threshold $\gamma_{OT} = 6$ dB and $\gamma_T = 3$ and 8 dB. The upper limits used for truncating the terms involving infinite summations in order to plot the theoretical outage probability curves of MRC system are given in the last column of Table 4.3. It is to be noted that the FSO link is highly susceptible to variations in temperature and pressure in the atmosphere, which causes atmospheric turbulence along the propagation path. This atmospheric turbulence leads to random fluctuations in the received signal strength. As the severity of turbulence increases, the performance of FSO system deteriorates. Hence, strong turbulence condition limits the performance of the FSO system to a greater extent compared to weak turbulence condition. Further, the values of Rytov variance for strong turbulence are generally greater than one and for weak turbulence conditions, it is lesser than one [88]. It is observed from the plots that the adaptive combining scheme while operating at $\gamma_T = 8$ dB, such that $\gamma_{OT} < \gamma_T$, achieves the same performance as that of the MRC scheme, which is also evident from (4.29). Further, the outage performance of the adaptive combining scheme deteriorates while operating at $\gamma_T = 3$ dB (i.e. $\gamma_{OT} > \gamma_T$) compared to the outage performance for the case when $\gamma_{OT} < \gamma_T$.

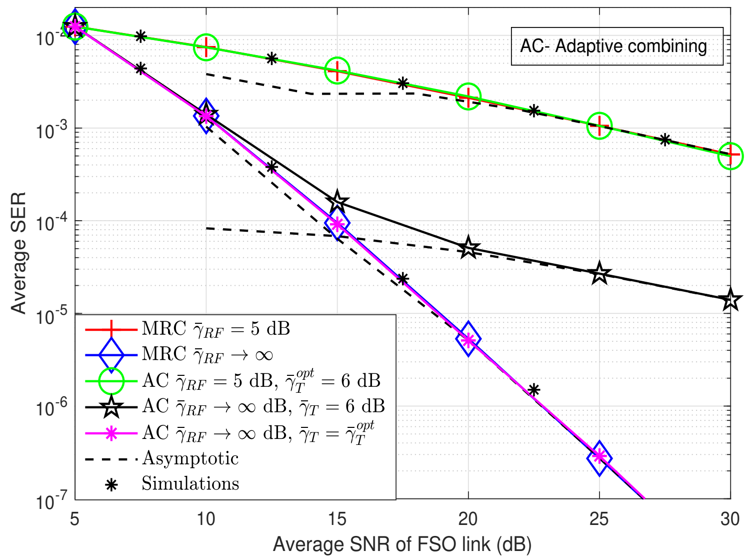

Fig. 4.8: Asymptotic SER performance of MRC and adaptive combining schemes

However, still the adaptive combining scheme achieves better performance than the single-link FSO system. Additionally, the SNR gain values of about 7 dB and 4 dB are obtained using the adaptive combining scheme with $\gamma_{OT} < \gamma_T$ over the single-link FSO system to achieve an outage of 10^{-1} under strong and weak turbulence conditions, respectively. As it can be seen from Fig. 4.7 that the outage performance of both adaptive combining and MRC schemes are better as compared to the single-link FSO system in all conditions due to the back-up RF link and high SNR gains are achieved under strong turbulence condition. In addition, we have given the outage performances of the single-link RF system and the adaptive combining system with $\overline{\gamma}_{RF} = \overline{\gamma}_p$. It can be observed that the single-link RF system performs better than the single-link FSO system, as FSO link suffers from atmospheric turbulence and pointing errors, whereas the RF link experiences only small scale fading. Further, the adaptive combining system with $\overline{\gamma}_{RF} = \overline{\gamma}_p$ under weak turbulence outperforms the other hybrid and RF systems due to the availability of better quality RF link.

In Fig. 4.8, the average SER and asymptotic performances of MRC-based and adaptive-combining-based hybrid FSO/RF systems are illustrated for different cases as discussed in Theorem 1 to 5 in Section V. Firstly, it is observed from the plots that the asymptotic SER curves well agree with the exact SER curves in the high-SNR region, which validates the derived asymptotic SER expressions. When the average SNR of RF link is set to $\overline{\gamma}_{RF} = 5$ dB and $\gamma_T^{opt} = 6$ dB, the diversity gain of MRC and adaptive-combining-based hybrid systems is equal, which is given by $\min(g_{eq}^2/p, \alpha/p, 1/p)$, as mentioned in Theorem 1 and 3. In such a scenario, the diversity gain of the system solely depends on the FSO link and the contribution of the RF link is only with respect to the SNR gain and not with respect to the diversity gain. It is also noticed that the performance of the adaptive combining scheme improves when the average SNR of RF link is varying and is equal to the average SNR of FSO link (i.e. $\overline{\gamma}_{RF} = \overline{\gamma}_p$). The improvement in the performance is due to the availability of better quality RF link with high values of $\overline{\gamma}_{RF}$. From the slope of the SER plot, it can be observed that the diversity gain in this case is also equal to $\min(g_{eq}^2/p, \alpha/p, 1/p)$ as given in Theorem 4. This is because of the fact that the switching threshold SNR value is assumed to be a constant (i.e. $\gamma_T = 6$ dB) irrespective of the average SNR of FSO and RF links. Therefore, as the average SNR of FSO link $\overline{\gamma}_p$ varies and $\overline{\gamma}_p >> \gamma_T$, the probability of the usage of FSO link will be very high compared to the usage of RF link. Thus, the FSO link will only contribute to the diversity gain of the adaptive-combining-based hybrid system under fixed switching threshold SNR condition.

From the asymptotic SER curves under the conditions $\gamma_T = \gamma_T^{opt}$ and $\overline{\gamma}_{RF} = \overline{\gamma}_p$, it is evident that full diversity gain, which is equal to $\min\left(\frac{g_{eq}^2}{p} + \tilde{\alpha}\mu, \frac{\alpha}{p} + \tilde{\alpha}\mu, \frac{1}{p} + \tilde{\alpha}\mu\right)$, can be obtained from both the hybrid systems as given in Theorem 2 and 5. The main reason for the adaptive-combining-based hybrid system to achieve full diversity gain is explained as follows: When the average SNR of RF link varies equally with the average SNR of FSO link, the optimum switching threshold SNR also varies as observed in Fig. 4.4(b). In such a scenario, it is highly likely that the FSO link in the adaptive-combining-based hybrid system will be in outage more frequently and the hybrid system will switch to the MRC of FSO and RF links at high-SNR region with high probability. Since the probability of usage of the backup RF link is higher compared to the fixed switching threshold SNR case, especially in the high-SNR region, full diversity gain due to both FSO and RF links will be obtained.

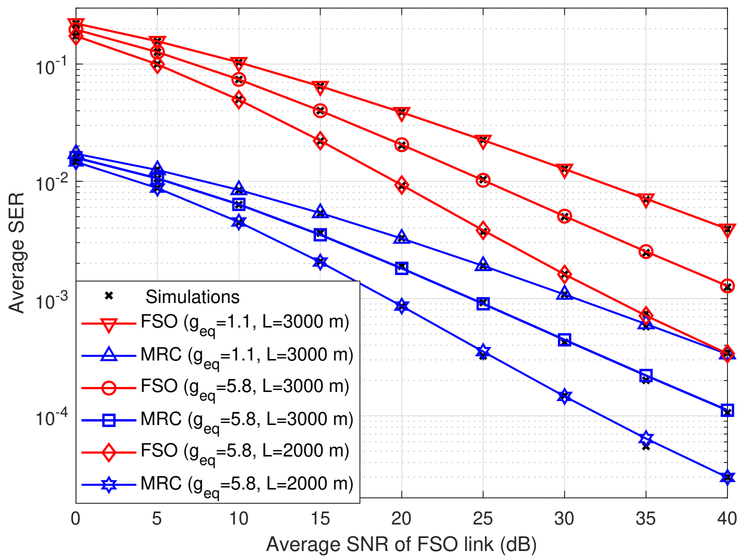

Fig. 4.9: Average SER of single-link FSO and MRC systems under varying link distance and pointing errors

The impact of pointing errors and varying link distance on the average SER performance of the MRC system is depicted in Fig. 4.9. We assume the FSO link parameters as $r_0 = 27$ cm, $w_0 = 4$ cm, $m_x/r_0 = 3$, $m_y/r_0 = 3$, $\delta_x/r_0 = 3.5$, $\delta_y/r_0 = 3.5$, $g_{eq} = 1.1$ for high pointing errors case, and $m_x = 0$, $m_y = 0$, $\delta_x/r_0 = 0.75$, $\delta_y/r_0 = 0.75$, $g_{eq} = 5.8$ for low pointing errors case, where it reduces to zero boresight pointing error case. Further, the link distances are assumed as $L = 2000$ m and $L = 3000$ m. The effect of pointing errors can be seen by varying the pointing error coefficient g_{eq}. It is important to note that the severity of the pointing errors increases with decreasing value of g_{eq} and with an increase in link distance L. As the value of g_{eq} increases, improvement in the performance of single-link FSO and MRC-based hybrid systems has been observed. Further, as the link distance increases, deterioration in the performance of both the systems has been observed. It can also be inferred that the SNR gains of 25 dB and 20 dB are obtained by the MRC-based hybrid system over the single-link FSO system to attain the average SER of 10^{-2} for $g_{eq} = 1.1$ and $g_{eq} = 5.8$ dB, respectively. Moreover, we noticed that the SNR gains achieved by the MRC-based hybrid system over the single-link FSO system to attain the average SER of 10^{-2} for $L = 2000$ m and $L = 3000$ m are 20 dB and 16 dB, respectively. It is clear from the plots that the MRC system achieves high SNR gain for the scenarios with high pointing errors severity and large link distance. This is

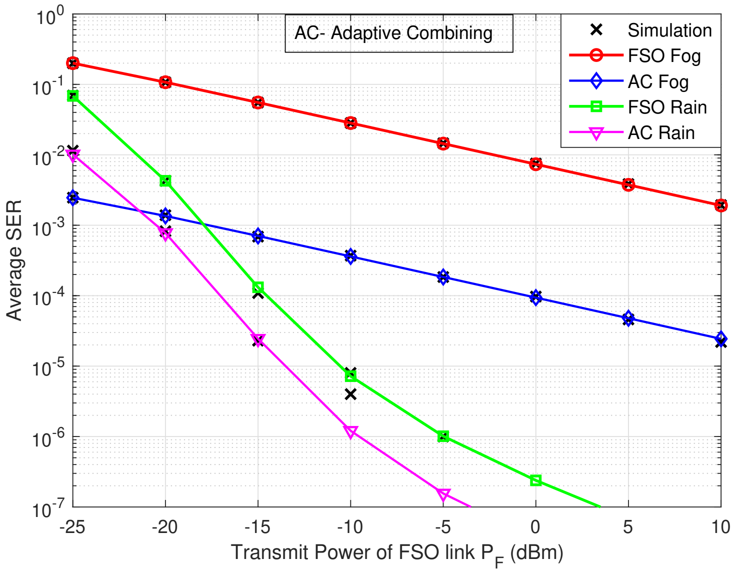

Fig. 4.10: Average SER of single-link FSO and adaptive combining for different weather conditions

due to the fact that high pointing errors, large link distance, and strong turbulence conditions will result in frequent FSO link failure and the contribution from the FSO link in MRC will be less (in terms of instantaneous SNR). Hence, relatively high SNR gains are obtained due to the contribution from the RF link in such cases.

In Fig. 4.10, the average SER against the FSO transmit power is plotted for the adaptive combining scheme under different weather conditions. We have assumed moderate foggy and rainy conditions [41] for comparing the performances of single-link FSO and adaptive-combining-based hybrid systems. The turbulence and weather parameters used in the simulations are given in Table 4.2. From Fig. 4.10, it can be inferred that the performance of single-link FSO system degrades under foggy condition compared to rainy condition, as the FSO link undergoes high attenuation under foggy weather condition. It is noticed that when the transmit power is less than -19 dBm, the SER of adaptive combining scheme is higher under rainy condition compared to foggy condition. This is because, if the FSO transmit power is less, then the RF link will be utilized more frequently to backup the FSO link and since the RF link is more prone to the rainy condition, overall degradation in the system performance of the adaptive combining scheme is observed. Further, the performance improves drastically after -19 dBm under rainy condition and this is due to the fact that at higher values of transmit power, the FSO link is utilized

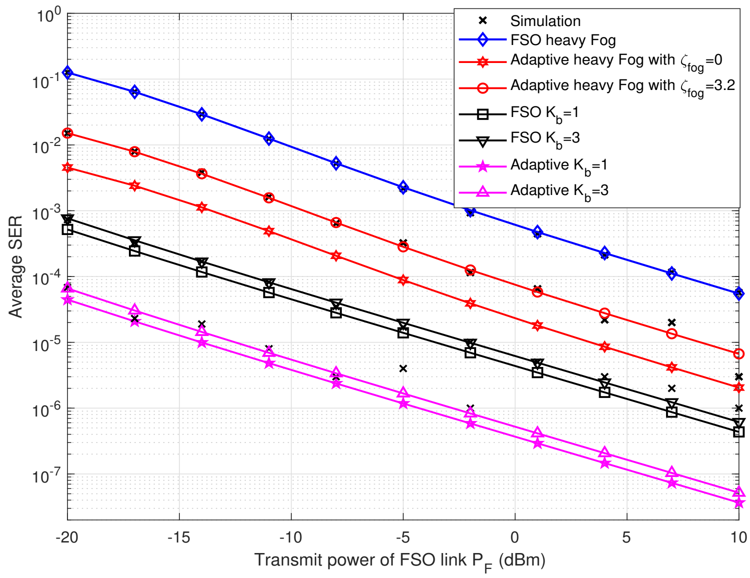

Fig. 4.11: Average SER for heavy fog and different background noise conditions

more frequently with higher probability compared to MRC of FSO and RF links. Since the FSO link is less prone to the rainy condition, improvement in overall performance of the system is observed. From Fig. 4.10, we can also notice that the adaptive-combining-based hybrid system offers more SNR gain over the single-link FSO system under foggy weather condition. This is because, the probability of adaptive combining scheme switching to MRC of FSO and RF links according to (4.7) is very high under foggy condition compared to rainy condition.

In Fig. 4.11, the average SER is plotted with respect to the FSO transmit power under different background noise conditions and heavy fog condition. We have assumed fog attenuation factor values of RF link as $\zeta_{fog} = 0$ and 3.2 dB/km for comparing the performances of single-link FSO and adaptive-combining-based hybrid systems. The turbulence and weather parameters used in the simulations are given in Table 4.2. It is inferred from the plots that the performance of the adaptive combining system degrades with transmit power loss of about 4 dBm for the case when $\zeta_{fog} = 3.2$ dB/Km compared to the case when $\zeta_{fog} = 0$ to achieve an average SER of 10^{-3} due to fog attenuation encountered by RF link. Further, in Fig. 4.11, the effect of background noise on the performance of single-link FSO and adaptive-combining systems has been shown by varying K_b, which signifies the fraction of the background noise. It can be clearly seen from the plots that there is a slight deterioration in the performance of both single-link FSO and adaptive combining systems with an increase in the value of K_b from $K_b = 1$ to 3. Note that increase in K_b indicates that the background noise level is increasing. Further, due to the usage of the backup RF link, the adaptive combining system performs better compared to a single-link FSO system under both heavy fog and background noise conditions.

4.8 Chapter Summary

In this chapter, the novel closed-form expressions for the PDF and CDF of the MRC of FSO and RF links are derived. With the aid of the obtained statistical functions, the unified closed-form expressions for the performance metrics such as outage probability and average SER for MRC-based and adaptive-combining-based hybrid FSO/RF systems were derived considering non-zero boresight pointing errors. From the simpler asymptotic expressions, diversity gains of MRC-based and adaptive-combining-based hybrid systems were determined for various cases and the conditions to obtain full diversity gain from both the hybrid systems were also reported. We also obtained the optimal performance of adaptive combining scheme by determining the optimum switching threshold SNR and beam width values. All the derived expressions were validated using the Monte-Carlo simulations. Further, it was inferred that the average SER of adaptive-combining-based hybrid system operating at the optimum switching threshold SNR value γ_T^{opt} was equal to the average SER of the MRC-based hybrid system. From the numerical analysis, it was also observed that the hybrid system with MRC and adaptive combining schemes perform better than the single-link FSO system and hybrid system with single-threshold-based hard-switching scheme.

Chapter 5

On the Capacity Analysis of Hybrid FSO/RF System with Adaptive Combining over Generalized Distributions

5.1 Introduction

The effects of atmospheric turbulence-induced fading and pointing errors in the FSO channel were minimized by employing cooperative diversity schemes and spatial diversity techniques such as SC and MRC [126, 194, 195]. In addition to spatial diversity techniques, hybrid FSO/RF systems based on switching schemes were also promising solution to counteract FSO channel distortions [25, 41, 39, 171, 190]. However, the hybrid FSO /RF system based on hard-switching scheme suffers from frequent hardware switching between FSO and RF sub-systems and it also requires the CSI at the transmitter. To alleviate these issues, the FSO and RF links of the hybrid FSO/RF system were combined using SC and MRC techniques in [48, 49]. However, to facilitate effective diversity combining, the transmission rate of the FSO link should be decreased to match the transmission rate of the RF link and hence, the achievable capacity decreases in case of hybrid systems based on SC and MRC. To address the capacity degradation issue in diversity combining schemes, the adaptive combining scheme, which is a variant of MRC, has been proposed as explained in the previous chapter.

The earlier works on adaptive combining-based hybrid FSO/RF system were restricted to outage and average SER analysis [155, 158, 159, 157, 156] and the ergodic capacity analysis was unexplored. This chapter investigates the ergodic capacity performance of hybrid FSO/RF system by employing an adaptive-combining-based switching scheme. It is assumed that the FSO link experiences the atmospheric turbulence and non-zero boresight misalignment or pointing errors. In particular, the PDF of the instantaneous SNR of the adaptive combining scheme is derived over the generalized Malaga distribution (FSO link) and κ–μ distribution (RF link). Capitalizing on the SNR statistics, the unified exact closed-form ergodic capacity expressions including their asymptotic form are derived for the adaptive-combining-based hybrid FSO/RF system.

5.2 Organization of the Chapter

This chapter is organized as follows: In Section 5.3, we introduce the system model of the adaptive-combining-based hybrid FSO/RF system as well as the channel models of FSO and RF links. Further, we obtain the PDF of the output instantaneous SNR of the adaptive combining scheme. In Section 5.4, the closed-form expressions for the ergodic capacity are derived. Section 5.5 deals with the asymptotic analysis of ergodic capacity at the high-SNR regime and provides the analytical beamwidth optimization. In Section 5.6, numerical results with detailed discussions are provided followed by concluding remarks in Section 5.7.

5.3 System and Channel Models

We consider a hybrid FSO/RF communication system model based on the adaptive-combining-based switching scheme as discussed in Chapter 4. In the adaptive combining scheme, the FSO link is always active and the RF link is in standby mode provided the instantaneous SNR of the FSO link is above a predefined threshold SNR level, denoted by γ_T. When the instantaneous SNR is below γ_T, then the RF link will be activated and MRC of FSO and RF links will be performed at the receiver.

In this chapter, the generalized Malaga distribution is assumed to characterize the atmospheric turbulence-induced fading of the FSO link, which is denoted as I_a, and its PDF is given in Chapter 3, eq. (3.5). In addition, the non-zero boresight pointing errors I_e and atmospheric path loss I_l are also considered in the FSO channel model, which are already explained in detail in Chapter 4, Section 4.3.1. Furthermore, the combined FSO channel, $I_F = I_a I_e I_l$ and its PDF statistics considered in this chapter are given in Chapter 4, Section 4.3.2.

5.3.1 FSO Channel Statistics

The instantaneous SNR and average electrical SNR of the FSO link are, respectively, given by

$$\gamma_p = |I_F|^p \frac{(P_F \eta_f)^p}{\sigma_p^2}, \tag{5.1}$$

$$\overline{\gamma}_p = \left[\frac{(y+\Omega')g_{eq}^2 S_{eq} I_l}{g_{eq}^2+1}\right]^p \frac{(P_F \eta_f)^p}{\sigma_p^2}, \tag{5.2}$$

From (5.1) and (5.2), the γ_p can be rewritten as

$$\gamma_p = \overline{\gamma}_p \left[\frac{(g_{eq}^2+1)|I_F|}{(y+\Omega')\, g_{eq}^2\, S_{eq} I_l}\right]^p \tag{5.3}$$

Further, by utilizing the random variable transformation technique, the unified PDF of the instantaneous SNR γ_p is obtained as

$$f_{\gamma_p}(\gamma)=\frac{g_{eq}^2 D}{2^p\gamma}\sum_{d=1}^{\beta} b_d\, G_{1\,3}^{3\,0}\left(B_1\left(\frac{\gamma}{\overline{\gamma}_p}\right)^{\frac{1}{p}}\middle|\begin{matrix} g_{eq}^2+1 \\ g_{eq}^2, \alpha, d\end{matrix}\right), \tag{5.4}$$

where the parameters and constants are given in Chapter 4, Section 4.3.2. Note that the expressions for calculating α and β are given in Appendix A.

5.3.2 RF Channel Model

The small-scale fading of the RF channel is modeled using the generalized κ–μ distribution, which includes Nakagami-m, Rice, and Rayleigh distributions as special cases [196]. The PDF of RF fading channel coefficient h_{RF}, which follows the κ–μ distribution, is given by [196, eq. (11)]

$$f_{h_{RF}}(h) = \frac{2\mu(1+\kappa)^{\frac{\mu+1}{2}}h^{\mu}}{\kappa^{\frac{\mu-1}{2}}\exp(\mu\kappa)}\exp\left(-\mu(1+\kappa)h^2\right) I_{\mu-1}\left(2\mu\sqrt{\kappa(1+\kappa)}h\right), \tag{5.5}$$

where $\kappa > 0$ is the ratio of powers of the dominant component to the scattered component and $\mu > 0$ represents the number of multi-path clusters, and $I_v(\cdot)$ is the modified Bessel function of first kind of order v [186, eq. (8.445)]

.

The instantaneous SNR and average SNR of the RF link are, respectively, given by

$$\gamma_{RF} = \frac{|h_{RF}|^2\overline{\gamma}_{RF}}{G_R} \text{ and } \overline{\gamma}_{RF} = G_R\frac{P_R}{\sigma_{RF}^2}, \tag{5.6}$$

where P_R, σ_{RF}^2, and G_R are defined in Chapter 4, Section 4.3. Further, using random variable transformation, the PDF of γ_{RF} is written as

$$f_{\gamma_{RF}}(\gamma) = \frac{\mu(1+\kappa)^{\frac{\mu+1}{2}}\gamma^{\frac{\mu-1}{2}}}{\kappa^{\frac{\mu-1}{2}}\exp(\mu\kappa)\,\overline{\gamma}_{RF}^{\frac{\mu+1}{2}}}\exp\left(-\frac{\mu(1+\kappa)\gamma}{\overline{\gamma}_{RF}}\right) I_{\mu-1}\left(2\mu\sqrt{\frac{\kappa(1+\kappa)\gamma}{\overline{\gamma}_{RF}}}\right). \tag{5.7}$$

By using the series expansion of $I_v(\cdot)$ [186, eq. (8.445)], the PDF of γ_{RF} can be re-written as

$$f_{\gamma_{RF}}(\gamma) = \sum_{j=0}^{\infty} M_{1,j}\gamma^{\mu+j-1}\exp\left(-F\gamma\right), \tag{5.8}$$

where $M_{1,j}$ and F are defined in Table 5.1.

5.3.3 SNR Statistics of Adaptive Combining Scheme

The output SNR of the adaptive-combining-based hybrid FSO/RF system, which is denoted as γ_{AC}, is given by

$$\gamma_{AC} = \begin{cases} \gamma_p, & \gamma_p > \gamma_T \\ \gamma_p + \gamma_{RF}, & \gamma_p \leq \gamma_T, \end{cases} \tag{5.9}$$

where γ_T denotes the predefined switching threshold SNR value. Further, the PDF of γ_{AC} can be defined as [156, eq. (9)]

$$f_{\gamma_{AC}}(\gamma) = \begin{cases} f_{\gamma_p+\gamma_{RF}}(\gamma), & \gamma \leq \gamma_T \\ f_{\gamma_p}(\gamma) + J(\gamma), & \gamma > \gamma_T, \end{cases} \tag{5.10}$$

where

$$f_{\gamma_p+\gamma_{RF}}(\gamma) = \int_0^{\gamma} f_{\gamma_p}(t) f_{\gamma_{RF}}(\gamma - t)dt \tag{5.11}$$

$$\text{and} \qquad J(\gamma) = \int_0^{\gamma_T} f_{\gamma_p}(t) f_{\gamma_{RF}}(\gamma - t)dt. \tag{5.12}$$

By substituting (5.4) and (5.8) in (5.11), followed by the expansion of $\exp(\cdot)$ in terms of its infinite series and after using [187, eq. (07.34.21.0084.01)], the closed-form expression for $f_{\gamma_p+\gamma_{RF}}(\gamma)$ is given by

$$f_{\gamma_p+\gamma_{RF}}(\gamma) = C_1 \sum_{d=1}^{\beta} t_d \sum_{j=0}^{\infty} M_{1,j} \sum_{i=0}^{\infty} M_{2,i}\gamma^{\tau_1-1} G_{p+1\ 3p+1}^{3p\ \ 1}\left(\frac{B_1^p\gamma}{p^{2p}\overline{\gamma}_p}\middle| \begin{matrix} 1, \mathcal{K}_1 \\ \mathcal{K}_2, 1-\tau_1 \end{matrix}\right), \tag{5.13}$$

Table 5.1: List of notations

$M_{1,j} = \frac{F^{\mu+j}(\kappa\mu)^j}{\Gamma(\mu+j)j!\exp(\kappa\mu)}$	$M_{2,i} = \frac{(-F)^i\Gamma(\tau_1)}{i!}$	$F = \frac{\mu(1+\kappa)}{\bar{\gamma}_{RF}}$	$t_d = b_d m^{\alpha+d-1}$
$C_1 = \frac{g_{eq}^2 D}{2^{2p-1}\pi^{p-1}}$	$C_2 = \frac{g_{eq}^2 D\exp\left(\frac{F}{\varepsilon_p}\right)}{2^{2p-1}\pi^{p-1}}$	$\tau_1 = \mu + i + j$	$\tau_2 = \mu + j - 1$
$B_1 = \frac{\alpha\,\beta\, g_{eq}^2(y+\Omega')}{(g_{eq}^2+1)(y\beta+\Omega')}$	$B_2 = \frac{B_1^p\gamma_T}{p^{2p}\bar{\gamma}_p}$	$B_3 = \frac{B_1^p}{p^{2p}\varepsilon_p\bar{\gamma}_p}$	$B_4 = B_1\left(\frac{\gamma_T}{\bar{\gamma}_p}\right)^{\frac{1}{p}}$

where C_1, t_d, $M_{2,i}$, τ_1 are defined in Table 5.1, $\mathcal{K}_1 = \frac{g_{eq}^2+1}{p}, ..., \frac{g_{eq}^2+p}{p}$ has p terms, and $\mathcal{K}_2 = \frac{g_{eq}^2}{p}, ..., \frac{g_{eq}^2+p-1}{p}, \frac{\alpha}{p}, ..., \frac{\alpha+m-1}{p}, \frac{d}{p}, ..., \frac{d+p-1}{p}$ has $3p$ terms. Similarly, the integral in (5.12) is evaluated using [187, eq. (07.34.21.0084.01)] and $J(\gamma)$ is expressed as

$$J(\gamma) = C_1\exp(-F\gamma)\sum_{d=1}^{\beta} t_d \sum_{j=0}^{\infty} M_{1,j} \sum_{i=0}^{\infty}\frac{F^i}{i!}\sum_{l=0}^{\tau_2}\binom{\tau_2}{l}(-1)^l\gamma_T^{i+l}\gamma^{\tau_2-l}$$
$$\times\, G_{p+1\;3p+1}^{3p\;\;1}\left(B_2\left|\begin{matrix}1-(i+l), \mathcal{K}_1\\ \mathcal{K}_2, -(i+l)\end{matrix}\right.\right), \tag{5.14}$$

where τ_2 and B_2 are defined in Table 5.1.

5.4 Ergodic Capacity Analysis

The ergodic capacity of the adaptive-combining-based hybrid FSO/RF system can be written as

$$\bar{C}_{AC} = \frac{1}{\ln(2)}\Bigg\{W_R\underbrace{\int_0^{\gamma_T}\ln(1+\varepsilon_p x)\,f_{\gamma_p+\gamma_{RF}}(x)dx}_{I_1} + W_F\underbrace{\int_{\gamma_T}^{\infty}\ln(1+\varepsilon_p x)f_{\gamma_p}(x)dx}_{I_2}$$
$$+\,W_R\underbrace{\int_{\gamma_T}^{\infty}\ln(1+\varepsilon_p x)J(x)dx}_{I_3}\Bigg\}. \tag{5.15}$$

where ε_p is a constant such that $\varepsilon_1 = 1$ for HD technique (i.e. $p = 1$) and $\varepsilon_2 = e/(2\pi)$ for IM/DD technique (i.e. $p = 2$). Note that the expression in (5.15) is an exact solution for HD, while it is a lower bound for IM/DD [197, eq. (26)]. To evaluate integral I_1, $\ln(1+\varepsilon_p x)$ is re-written by its Meijer G-form using [187, eq.

(07.34.03.0456.01)]. After that by substituting (5.13) and making some changes in variable and limits, the integral I_1 can be written as

$$I_1 = C_1 \sum_{d=1}^{\beta} t_d \sum_{j=0}^{\infty} M_{1,j} \sum_{i=0}^{\infty} M_{2,i} \gamma_T^{\tau_1} \int_0^{\infty} U(z-1) z^{\tau_1 - 1} G_{2\,2}^{1\,2} \left(\gamma_T \varepsilon_p z \middle| \begin{matrix} 1,1 \\ 1,0 \end{matrix} \right)$$
$$\times G_{p+1\;3p+1}^{\;3p\quad 1} \left(B_2 z \middle| \begin{matrix} 1, \mathcal{K}_1 \\ \mathcal{K}_2, 1-\tau_1 \end{matrix} \right) dz, \tag{5.16}$$

where $U(\cdot)$ is the unit step function. By replacing $U(\cdot)$ by its Meijer G-form using [187, eq. (07.34.03.0050.01)] and after utilizing [187, eq. (07.34.21.0081.01)], integral I_1 is given by (5.17).

$$I_1 = C_1 \sum_{d=1}^{\beta} t_d \sum_{j=0}^{\infty} M_{1,j} \sum_{i=0}^{\infty} M_{2,i} \gamma_T^{\tau_1}$$
$$\times G_{1,1:\;2,2:\;p+1,\;3p+1}^{0,1:\;1,2:\;3p,\;\;1} \left[\begin{matrix} 1-\tau_1 \\ -\tau_1 \end{matrix} \middle| \begin{matrix} 1,1 \\ 1,0 \end{matrix} \middle| \begin{matrix} 1, \mathcal{K}_1 \\ \mathcal{K}_2, 1-\tau_1 \end{matrix} \middle| \gamma_T \varepsilon_p, B_2 \right] \tag{5.17}$$

where $G_{\cdot,\cdot:\cdot,\cdot:\cdot,\cdot}^{\cdot,\cdot:\cdot,\cdot:\cdot,\cdot}[\,\cdot,\cdot]$ is the extended generalized bivariate Meijer G-function (EGB-MGF) [198, eq. (1.8)].

The integral I_2, due to divergence issue, cannot be evaluated directly over the limits from γ_T to ∞ by using [187, eq. (07.34.21.0085.01)]. Therefore, I_2 is evaluated by splitting it into two parts as

$$I_2 = \underbrace{\int_0^{\infty} \ln(1+\varepsilon_p x) f_{\gamma_p}(x) dx}_{I_{21}} - \underbrace{\int_0^{\gamma_T} \ln(1+\varepsilon_p x) f_{\gamma_p}(x) dx}_{I_{22}}. \tag{5.18}$$

By substituting $\ln(1+x)$ using its Meijer G-form [187, eq. (07.34.03.0456.01)] and after employing [187, eq. (07.34.21.0013.01)], the integral I_{21} is given by

$$I_{21} = C_1 \sum_{d=1}^{\beta} t_d \, G^{\,3p+2 \;\; 1}_{\,p+2 \;\; 3p+2} \left(B_3 \middle| \begin{matrix} 0, 1, \mathcal{K}_1 \\ \mathcal{K}_2, 0, 0 \end{matrix} \right), \tag{5.19}$$

where B_3 is given in Table 5.1. Similar to I_1, integral I_{22} can be evaluated by using the change of variable followed by modifying the limits and with the aid of [199, eq. (2.3)], I_{22} is given by

$$I_{22} = \frac{g_{eq}^2 D}{2^p} \sum_{d=1}^{\beta} b_d \, H^{\,0,1:\;1,2:\;3,0}_{\,1,1:\;2,2:\;1,3} \left[\begin{matrix} 1;1,\frac{1}{p} \\ 0;1,\frac{1}{p} \end{matrix} \middle| \begin{matrix} (1,1),(1,1) \\ (1,1),(0,1) \end{matrix} \middle| \begin{matrix} (g_{eq}^2+1,1) \\ (g_{eq}^2,1),(\alpha,1),(\beta,1) \end{matrix} \middle| \gamma_T \varepsilon_p, B_4 \right] \tag{5.20}$$

where $H^{\cdot,\cdot:\cdot,\cdot:\cdot,\cdot}_{\cdot,\cdot:\cdot,\cdot:\cdot,\cdot}[\,\cdot,\cdot]$ is the bivariate Fox's H function [199, eq. (1.1)]

Finally, the integral I_3 is solved by using a variable change $z = 1 + \varepsilon_p x$, followed by the binomial expansion of $(z-1)^{\tau_2 - l}$ and after using [186, eq. (2.33.10), (2.33.11)], I_3 is expressed as

$$\begin{aligned} I_3 = {} & C_2 \sum_{d=1}^{\beta} t_d \sum_{j=0}^{\infty} M_{1,j} \sum_{i=0}^{\infty} \frac{F^i}{i!} \sum_{l=0}^{\tau_2} \binom{\tau_2}{l} \gamma_T^{i+l} \sum_{n=0}^{\tau_2 - l} \binom{\tau_2 - l}{n} \frac{(-1)^{\tau_2 - n}}{\varepsilon_p^{\tau_2 - l + 1}} \mathcal{I}(n) \\ & \times G^{\,3p \;\; 1}_{\,p+1 \;\; 3p+1} \left(B_2 \middle| \begin{matrix} 1-(i+l), \mathcal{K}_1 \\ \mathcal{K}_2, -(i+l) \end{matrix} \right), \end{aligned} \tag{5.21}$$

where C_2 is defined in Table 5.1 and $\mathcal{I}(n)$ is given by

$$\mathcal{I}(n) = \frac{\ln(L_t)}{(F/\varepsilon_p)^{n+1}} \Gamma\left(n+1, \frac{F}{\varepsilon_p} L_t\right) + \frac{n!}{(F/\varepsilon_p)^{n+1}} \left[\sum_{p=1}^{n} \frac{\Gamma\left(p, \frac{F}{\varepsilon_p} L_t\right)}{p!} - \mathrm{Ei}\left(-\frac{F}{\varepsilon_p} L_t\right) \right], \tag{5.22}$$

where $L_t = \varepsilon_p \gamma_T + 1$, and $\mathrm{Ei}(\cdot)$ is the exponential integral function [186, eq. (8.21)].

5.5 Asymptotic Ergodic Capacity Analysis

The derived closed-form expressions for the ergodic capacity are very complicated, which are given in terms of extended generalized bivariate Meijer G-function and bivariate Fox's H-function. These functions are quite complex and reveal the limited physical insights of the system. Therefore, we present the less-complicated asymptotic analysis for the ergodic capacity of the adaptive-combining-based hybrid FSO/RF system in the high-SNR region. The asymptotic expression for the ergodic capacity of the adaptive combining system is given by

$$\bar{C}_{AC}^{\infty} = I_1^{\infty} + I_{21}^{\infty} - I_{22}^{\infty} + I_3^{\infty}, \tag{5.23}$$

where I_1^{∞}, I_{21}^{∞}, I_{22}^{∞}, and I_3^{∞} are the asymptotic expressions for the corresponding terms I_1, I_{21}, I_{22}, and I_3, respectively. First, we calculate I_1^{∞} by substituting the definition of EGBMGF [198, eq. (1.8)] in (5.17) and then utilizing Mellin-Barnes type of contour integral [198, eq. (1.3)]. After using the procedure given in [37], I_1 can be written as

$$\begin{aligned} I_1 = {} & C_1 \sum_{d=1}^{\beta} t_d \sum_{j=0}^{\infty} M_{1,j} \sum_{i=0}^{\infty} M_{2,i} \gamma_T^{\tau_1} \Bigg[\frac{1}{2\pi \mathrm{i}} \oint_C \frac{\Gamma(1+s)\,(\Gamma(-s))^2}{\Gamma(1-s)} (\gamma_T \varepsilon_p)^{-s} \\ & \times G_{p+2\;3p+2}^{3p\;\;\;2} \left(B_2 \middle| \begin{matrix} 1-\tau_1+s, 1, \mathcal{K}_1 \\ \mathcal{K}_2, 1-\tau_1, -\tau_1+s \end{matrix} \right) ds \Bigg]. \end{aligned} \tag{5.24}$$

Further, for high values of $\overline{\gamma}_p \gg 1$, the Meijer G-function in (5.24) can be approximated by utilizing [187, eq. (07.34.06.0040.01)]. After applying [198, eq. (1.3)] with some manipulations, we get the asymptotic expression for I_1 as

$$I_1^{\infty} = C_1 \sum_{d=1}^{\beta} t_d \sum_{j=0}^{\infty} M_{1,j} \sum_{i=0}^{\infty} M_{2,i} \gamma_T^{\tau_1} \sum_{u=1}^{3m} \frac{\Lambda_1 B_2^{K_{2,u}} \Gamma(\mathcal{K}_{2,u})}{\Gamma(\tau_1 + \mathcal{K}_{2,u})} G_{3\;3}^{1\;3} \left(\varepsilon_p \gamma_T \middle| \begin{matrix} 1-(\tau_1+\mathcal{K}_{2,u}), 1, 1 \\ 1, 0, -(\tau_1+\mathcal{K}_{2,u}) \end{matrix} \right), \tag{5.25}$$

where $\Lambda_1 = \frac{\prod_{t=1;\, t\neq u}^{3m} \Gamma(\mathcal{K}_{2,t}-\mathcal{K}_{2,u})}{\prod_{t=1}^{p} \Gamma(\mathcal{K}_{1,t}-\mathcal{K}_{2,u})}$.

Using the asymptotic form of Meijer G-function [187, eq. (07.34.06.0040.01)] in (5.19), I_{21}^{∞} is given by

$$I_{21}^{\infty} = C_1 \sum_{d=1}^{\beta} t_d \sum_{u=1}^{3m+2} \frac{\Gamma(1+\mathcal{K}_{3,u})}{\Gamma(1-\mathcal{K}_{3,u})} \Lambda_2 B_3^{\mathcal{K}_{3,u}}, \tag{5.26}$$

where $\Lambda_2 = \frac{\prod_{t=1;\, t\neq u}^{3m+2} \Gamma(\mathcal{K}_{3,t}-\mathcal{K}_{3,u})}{\prod_{t=1}^{p} \Gamma(\mathcal{K}_{1,t}-\mathcal{K}_{3,u})}$ and $\mathcal{K}_3 = [\mathcal{K}_2, 0, 0]$. Now, similar to the evaluation of I_1^{∞}, using [199, eq. (1.1)], [200, eq. (1.1.1)] in (5.20) and after applying the approximation for Fox's H-function [200, eq. (1.8.4)], I_{22}^{∞} can be expressed as

$$I_{22}^{\infty} = \frac{g_{eq}^2 D}{2^p} \sum_{d=1}^{\beta} b_d \sum_{u=1}^{3} B_4^{\mathcal{K}_{4,u}} \frac{\prod_{t=1;t\neq u}^{3} \Gamma(\mathcal{K}_{4,t}-\mathcal{K}_{4,u})}{\Gamma(g_{eq}^2+1-\mathcal{K}_{4,u})} G_{3\,3}^{1\,3}\left(\varepsilon_p \gamma_T \middle| \begin{matrix} 1-\mathcal{K}_{4,u}/m, 1, 1 \\ 1, 0, -\mathcal{K}_{4,u}/m \end{matrix}\right), \tag{5.27}$$

where $\mathcal{K}_4 = \left[g_{eq}^2, \alpha, d\right]$. Finally, by employing [187, eq. (07.34.06.0040.01)] in (5.21), the asymptotic expression for I_3 can be written as

$$I_3^{\infty} = C_2 \sum_{d=1}^{\beta} t_d \sum_{j=0}^{\infty} M_{1,j} \sum_{i=0}^{\infty} \frac{F^i}{i!} \sum_{l=0}^{\tau_2} \binom{\tau_2}{l} \gamma_T^{i+l} \sum_{u=1}^{3m} \frac{\Lambda_1 B_2^{\mathcal{K}_{2,u}}}{i+l+\mathcal{K}_{2,u}} \sum_{n=0}^{\tau_2-l} \binom{\tau_2-l}{n} \frac{(-1)^{\tau_2-n}}{\varepsilon_p^{\tau_2-l+1}} \mathcal{I}(n). \tag{5.28}$$

It is important to note that to obtain the asymptotic expression, we have assumed $\overline{\gamma}_p$ tending to infinity and the value of $\overline{\gamma}_{RF}$ is kept as a constant in (5.25)-(5.28). Further, by assuming both $\overline{\gamma}_p$ and $\overline{\gamma}_{RF}$ tending to infinity, the dominant terms will be obtained by substituting i, $j=0$ in (5.25) and (5.28). Therefore, the asymptotic expressions I_1^{∞} and I_3^{∞}, by assuming both $\overline{\gamma}_p$ and $\overline{\gamma}_{RF}$ tending to infinity, are given by

$$I_1^{\infty} = C_1 \sum_{d=1}^{\beta} t_d \frac{F^{\mu} \gamma_T^{\mu}}{\exp(\kappa\mu)} \sum_{u=1}^{3m} \Lambda_1 B_2^{\mathcal{K}_{2,u}} \frac{\Gamma(\mathcal{K}_{2,u})}{\Gamma(\mu+\mathcal{K}_{2,u})} G_{3\,3}^{1\,3}\left(\varepsilon_p \gamma_T \middle| \begin{matrix} 1-(\mu+\mathcal{K}_{2,u}), 1, 1 \\ 1, 0, -(\mu+\mathcal{K}_{2,u}) \end{matrix}\right) \tag{5.29}$$

Table 5.2: Execution time for exact and asymptotic expressions

Parameters			Execution time (in s)	
α	β	g_{eq}	Exact	Asymptotic
2.1	2	1	118	97
5.1	5	2.6	276	144
10.1	10	6.6	627	216

$$I_3^{\infty} = \frac{C_2 F^{\mu}}{\Gamma(\mu)\exp(\kappa\mu)} \sum_{d=1}^{\beta} t_d \sum_{l=0}^{\mu-1} \binom{\mu-1}{l} \gamma_T^l \sum_{u=1}^{3m} \frac{\Lambda_1 B_2^{\mathcal{K}_{2,u}}}{l+\mathcal{K}_{2,u}} \times \sum_{n=0}^{\mu-1-l} \binom{\mu-1-l}{n} \frac{(-1)^{\mu-1-n}}{\varepsilon_p^{\mu-l}} I(n). \tag{5.30}$$

Further, from (5.26) and (5.27), it is clear that there will be no change in the asymptotic expressions I_{21}^{∞} and I_{22}^{∞}, when $\overline{\gamma}_{RF}$ tends to infinity. The derived asymptotic capacity expressions are computationally very less intensive as compared to the exact capacity expressions. Moreover, we have compared the execution time of the exact and asymptotic expressions under various turbulence parameter values in Table 5.2.

5.6 Numerical Results and Discussions

In this section, the numerical results for ergodic capacity performance are presented. The parameters assumed in our simulations are given in Chapter 4, Table 4.2. In addition, the weather dependent parameter values assumed are given in Table 5.3, unless and otherwise stated. The few other parameters are assumed as $\overline{\gamma}_{RF} = 5$ dB, $\gamma_T = 7$ dB, $m = 2$, $m_x/r_0 = 3$, $m_y/r_0 = 3$, $\delta_x/r_0 = 3.5$, $\delta_y/r_0 = 3.5$, $\Omega = 1.3265$, $b_0 = 0.1092$, $\rho = 0.596$, and $\phi_A - \phi_B = \pi/2$, unless and otherwise stated. It is important to note that normalized ergodic capacity in bits/second/hertz (bits/sec/Hz) is illustrated in Fig. 5.1, 5.2, 5.3, 5.4, and 5.5, under the assumption that $W_F = 1$ Hz and $W_R = 1$ Hz. Additionally, the ergodic capacity in Gigabits/second (Gbps) are plotted in Fig. 5.5, assuming the bandwidths of FSO and RF links as $W_F = 1$ GHz and $W_R = 250$ MHz. It is worth noting that the normalized ergodic capacity (in

Table 5.3: Weather parameters used in the simulations

Weather condition	ζ_w **(dB/km)**	ζ_{rn} **(dB/km)**	$\mathbf{C_n^2}(\mathbf{m^{-2/3}})$
Clear air	0.43	0	5×10^{-14}
Haze	4.2	0	1.7×10^{-14}
Heavy fog	125	0	1×10^{-15}
Moderate rain	5.8	5.6	5×10^{-15}
Heavy rain	9.2	10.2	4×10^{-15}

Table 5.4: Truncation accuracy of summation limits

<table>
<tr><th rowspan="2">Expressions</th><th rowspan="2">Truncation values</th><th colspan="2">Final values</th><th rowspan="2">Upper limit</th></tr>
<tr><th>$\overline{\gamma}_p$=10 dB</th><th>$\overline{\gamma}_p$=20 dB</th></tr>
<tr><td rowspan="3">I_1</td><td>$j = 10$, $i = 10$</td><td>0.373809</td><td>0.290195</td><td rowspan="3">$j = 12$, $i = 12$</td></tr>
<tr><td>$j = 12$, $i = 12$</td><td>0.373781</td><td>0.290189</td></tr>
<tr><td>$j = 14$, $i = 14$</td><td>0.373780</td><td>0.290188</td></tr>
<tr><td rowspan="3">I_3</td><td>$j = 8$, $i = 8$</td><td>0.478791</td><td>0.381022</td><td rowspan="3">$j = 10$, $i = 10$</td></tr>
<tr><td>$j = 10$, $i = 10$</td><td>0.478813</td><td>0.381042</td></tr>
<tr><td>$j = 12$, $i = 12$</td><td>0.478814</td><td>0.381043</td></tr>
</table>

bits/sec/Hz) is required to calculate the spectral efficiency of the hybrid FSO/RF systems.

The truncation accuracy for the infinite summations, which are involved in the ergodic capacity expressions, are given in Table 5.4. Note that if the values greater than the upper limits that are mentioned in the last column of the table are used, then there will be no effect on the fifth decimal figure of the final ergodic capacity values as illustrated in Table 5.4.

Fig. 5.1 shows the normalized ergodic capacity with respect to switching threshold SNR and beamwidth. We assume $C_n^2 = 3 \times 10^{-13}$, $r_0 = 5$ cm, $w_0 = 4$ cm, $\kappa = 2$, and $\mu = 2$. The optimum switching threshold SNR γ_T^{opt} for the adaptive-combining-based hybrid FSO/RF system is determined in Fig. 5.1 (a) by plotting the normalized ergodic capacity against switching threshold SNR for different values of $\overline{\gamma}_p$ and $\overline{\gamma}_{RF}$. From Fig. 5.1 (a), it has been observed that the normalized ergodic

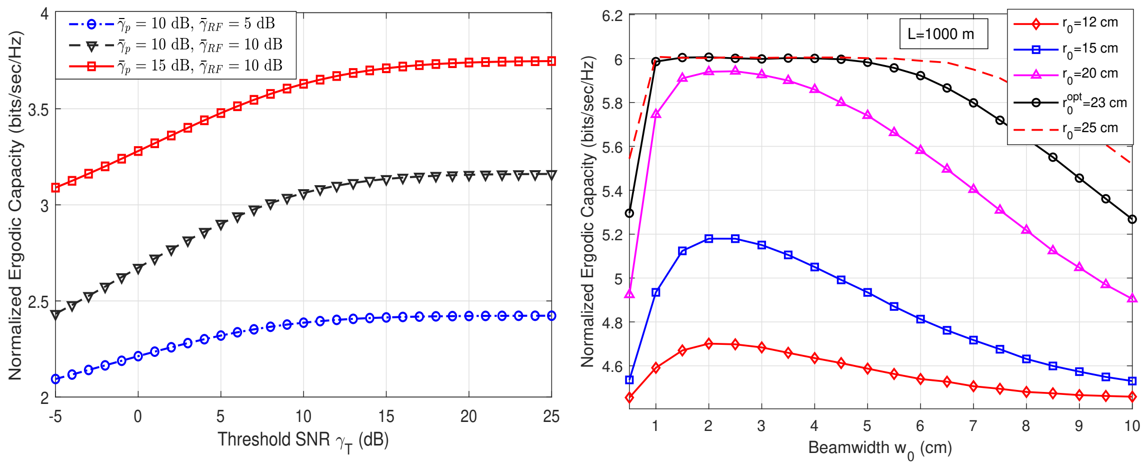

(a) (b)

Fig. 5.1: Normalized ergodic capacity versus switching threshold SNR γ_T and beamwidth w_0

capacity is increasing as the threshold SNR increases, specifically less than 10 dB region. However, beyond this region, capacity begins to saturate without much improvement. The optimum threshold SNR γ_T^{opt} is obtained when the normalized capacity reaches to a certain level and becomes less sensitive to changes in the threshold SNR value. This particular threshold value is considered as the optimum value of switching threshold SNR. It is also noticed that γ_T^{opt} values change by varying $\overline{\gamma}_p$ and $\overline{\gamma}_{RF}$ and the optimum values of γ_T obtained from Fig. 5.1 (a) are given in Table 5.5. Since the normalized capacity increases with increase in switching threshold SNR γ_T and its improvement becomes negligible after a certain value of γ_T, a global maximum value does not exist as seen in Fig. 5.1 (a). Further, we have determined γ_T^{opt} values for Fig. 5.2 using the same numerical optimization technique. In Fig. 5.1 (b), the optimum values of aperture radius r_0^{opt} and beamwidth w_0^{opt} are obtained by plotting the ergodic capacity against w_0 under various r_0 values. The optimum value w_0^{opt} is chosen corresponding to the maximum capacity value for a particular r_0 and the optimum r_0^{opt} is determined when there is no further improvement in the maximum capacity even after increasing the values of $r_0 > r_0^{opt}$.

From (4.70) it can be seen that g_{eq}^2 is directly proportional to $\sum_{k=0}^{\infty} r_0^{2k}$. Therefore, increasing the values of r_0 will result in an exponential rise in the values of g_{eq} and eventually, the capacity will be reaching to a maximum threshold value (i.e. 6

Table 5.5: The optimum values of γ_T and w_0

$\overline{\gamma}_p$ (dB)	$\overline{\gamma}_{RF}$ (dB)	γ_T^{opt} (dB)
10	5	14
10	10	17
15	10	19

Distance L	w_0^{opt} (in cm)	
	Numerical	Theoretical
1000 m	2.0 cm	2.22 cm
2000 m	3.0 cm	3.14 cm
3000 m	3.8 cm	3.85 cm

bits/sec/Hz) for certain values of r_0 and w_0. After that there will be no further improvement in the maximum capacity, which is also evident from Fig. 5.1 (b). This is because, for very high values of g_{eq}, the pointing errors will be negligible and it will not have any effect on the system performance. For the case when $r_0 \geq r_0^{opt}$, there are more than one w_0 values correspond to higher values of g_{eq} (i.e. negligible pointing errors), which eventually lead to the maximum capacity value of 6 bits/sec/Hz. Hence, the curves appear as a horizontal line for the case when $r_0 \geq r_0^{opt}$. However, when $r_0 < r_0^{opt}$, only one value of w_0 corresponds to the maximum value of g_{eq}, which is less than the g_{eq} required to achieve the maximum capacity value. Hence, no horizontal line is obtained for the plots when $r_0 < r_0^{opt}$. It is seen from Fig. 5.1 (b) that the values of w_0^{opt} and r_0^{opt} are obtained as 2 and 23 cm, respectively, for $L = 1000$ m. Further, the values of optimum beamwidth w_0^{opt} obtained using numerical optimization technique are very close to the values of w_0^{opt} determined from theoretical optimization (from Chapter 4, Section 4.6.4) and is shown in Table 5.5. Similarly, we have also determined r_0^{opt} for $L = 2000$ m and 3000 m as 60 cm and 110 cm, respectively.

In Fig. 5.2, the performances of the single-link FSO system, adaptive-combining-based hybrid FSO/RF system with and without optimum switching threshold γ_T^{opt} for different values of $\overline{\gamma}_{RF}$ are compared. The normalized capacity of the adaptive-combining-based hybrid system operating with γ_T^{opt} value is better than the adaptive combining system operating with non-optimum switching threshold SNR value assuming $\gamma_T = 5$ dB. It is also observed that there is a significant improvement in the performance when $\overline{\gamma}_{RF}$ is increased from 5 dB to 10 dB. Further, the adaptive-

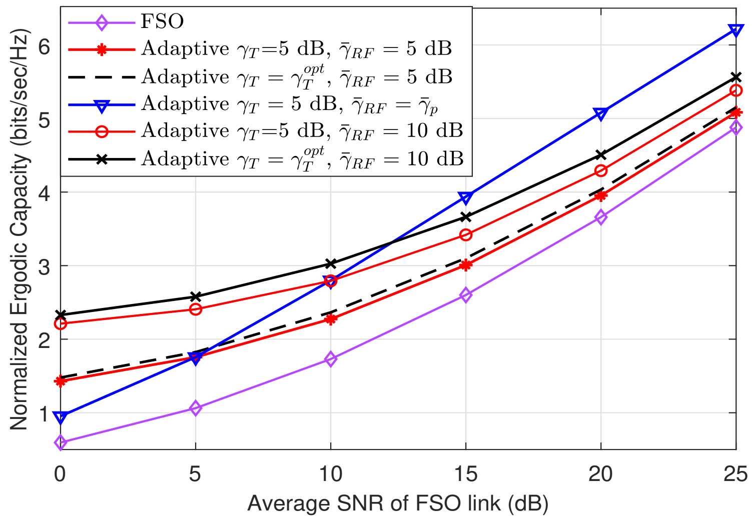

Fig. 5.2: Normalized ergodic capacity performance of the adaptive combining system with and without γ_T^{opt} under different $\overline{\gamma}_{RF}$

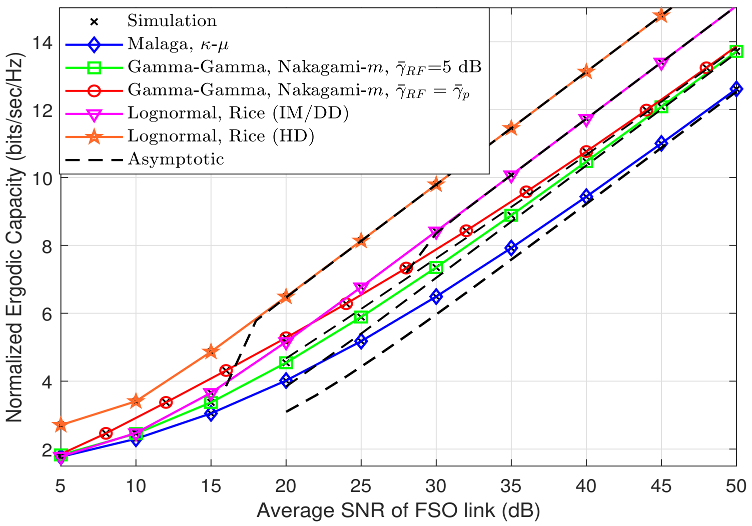

Fig. 5.3: Normalized ergodic capacity performance of the adaptive combining system for various distributions

combining-based hybrid system with $\overline{\gamma}_{RF} = \overline{\gamma}_p$ has superior performance compared to the case with fixed $\overline{\gamma}_{RF}$ due to the availability of better quality RF link. However, it is also noticed that the adaptive-combining-based hybrid system with $\overline{\gamma}_{RF} = \overline{\gamma}_p$ has lesser capacity compared to the case with fixed $\overline{\gamma}_{RF}$ (i.e. $\overline{\gamma}_{RF} = 5$ or 10 dB) when $\overline{\gamma}_p < 5$ or 10 dB. This is because, in these scenarios, the adaptive-combining-based hybrid system operating with fixed RF average SNR values will have higher values of $\overline{\gamma}_{RF}$ compared to the case with $\overline{\gamma}_{RF} = \overline{\gamma}_p$. Moreover, all three configurations of the adaptive-combining-based hybrid system have achieved better normalized ergodic capacity performance than the single-link FSO system due to the backup RF link.

Table 5.6: Example of FSO and RF distributions which are derived as special cases of Malaga and κ–μ distributions

FSO distribution	Parameter value
Log-normal	$\rho = 0$, $y \to 0$
Gamma–Gamma	$\rho = 1$, $\Omega^{'} = 1$, $y = 0$

RF distribution	κ	μ
Rice	K	1
Nakagami-m	0	$\hat{p}$

Table 5.7: List of distribution models with their parameters values to plot Fig. 5.3

FSO models	$C_n^2(m^{-2/3})$	r_0 (cm)	ρ	b_0	Ω	RF models	κ	μ
Malaga	1×10^{-13}	53	0.596	0.1092	1.3265	κ–μ	0.5	1
Gamma–Gamma	7×10^{-15}	15	1	0	1	Nakagami-m	0	2
Log-normal	4×10^{-15}	17.5	0	0	1.5	Rice	2	1

Fig. 5.3 illustrates the normalized ergodic capacity of the adaptive-combining-based hybrid FSO/RF system for different FSO and RF channel distributions, which are obtained as the special cases of the generalized Malaga and κ–μ distributions. The parameters values used to obtain the special cases of Malaga and κ–μ distributions are shown in Table 5.6. Further, the turbulence and other parameter values used in the plots are given in Table 5.7. It can be noticed from the plots that the Monte-Carlo simulation results are tightly matching with the analytical results, which validates the accuracy of our derived capacity expressions. Moreover, in Fig. 5.3, we have also shown the performance of the adaptive-combining-based hybrid system for varying $\overline{\gamma}_{RF}$ along with asymptotic curve assuming Gamma–Gamma and Nakagami-m distributions. It is observed that the asymptotic capacity curves comply with the exact curves at the high-SNR region. Additionally, we have compared the performances of IM/DD and HD techniques for lognormal and Rice distributions. As expected, the HD technique performs better than the IM/DD technique due to its coherent detection nature.

The effects of pointing errors and different turbulence conditions on the ergodic capacity performance are shown in Fig. 5.4. The RF link parameters are assumed as $\kappa = 1$, $\mu = 1$, and $\overline{\gamma}_{RF} = 10$ dB. The FSO link parameters are assumed as $L = 3000$ m, $r_0 = 13$ cm, $w_0 = 4$ cm, $C_n^2 = 1 \times 10^{-13}$ ($\alpha = 2.18$, $\beta = 1$) for strong turbulence, and $C_n^2 = 3.5 \times 10^{-15}$ ($\alpha = 10$, $\beta = 10$) for weak turbulence conditions. The parameter values for high pointing error scenario are assumed as $m_x/r_0 = 3$,

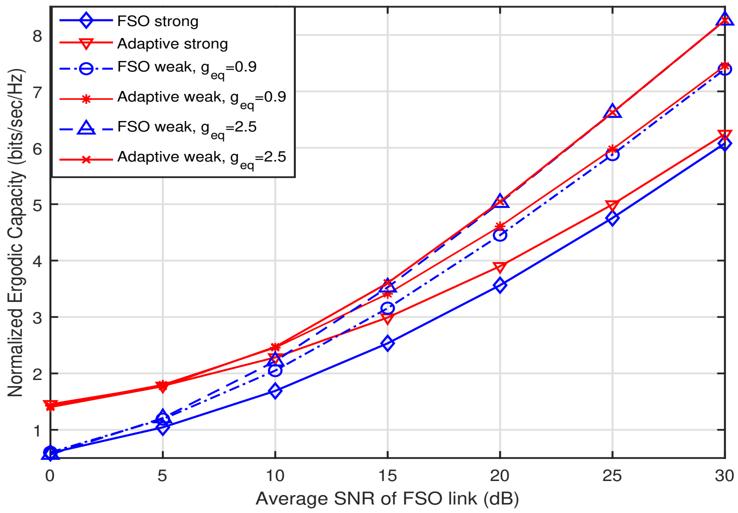

Fig. 5.4: Normalized ergodic capacity performance for different pointing errors and turbulence conditions

$m_y/r_0 = 3$, $\delta_x/r_0 = 3.5$, $\delta_y/r_0 = 3.5$, and $g_{eq} = 0.92$. For low pointing error scenario, we assume $m_x = 0$, $m_y = 0$, $\delta_x/r_0 = 1.5$, $\delta_y/r_0 = 1.5$, and $g_{eq} = 2.66$, where it reduces to zero boresight pointing error case. It can be seen from the plots that as the value of pointing error coefficient g_{eq} increases, the severity of pointing errors decreases and the performances of both single-link FSO and adaptive-combining-based hybrid FSO/RF systems improve significantly. Similarly, the performance of both the systems are better under weak turbulence conditions compared to strong turbulence conditions. From Fig. 5.4, it is also observed that the performance of the adaptive combining system is better than the single-link FSO system in all three scenarios, especially in the low-SNR region. The SNR gain values of the adaptive-combining-based hybrid system over the single-link FSO system to achieve the normalized ergodic capacity of 3 bits/sec/Hz under strong and weak turbulence conditions are observed as 2.5 dB and 1.5 dB, respectively. Similarly, the SNR gain values of 1.5 dB and 0.8 dB are obtained due to adaptive combining scheme for pointing errors cases $g_{eq} = 0.9$ and $g_{eq} = 2.5$, respectively. Thus, it is inferred that the adaptive-combining-based hybrid system achieves high SNR gains over the single-link FSO system under strong turbulence conditions and high pointing errors scenario. It is due to the fact that the adaptive combining system will switch more frequently to the MRC of FSO and RF links with a high probability, when the

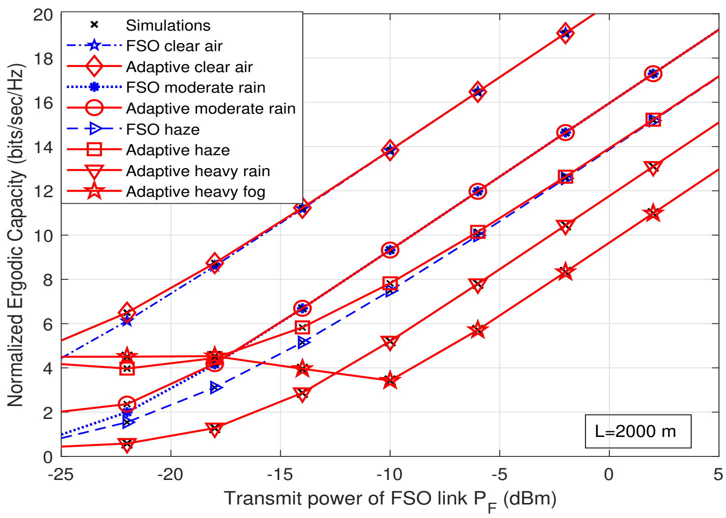

Fig. 5.5: Normalized ergodic capacity performance under various weather conditions

quality of FSO link is not acceptable.

In Fig. 5.5, the normalized ergodic capacity has been plotted with respect to the FSO transmit power under clear air, moderate and heavy rain, haze, and heavy fog conditions. The turbulence and weather parameters assumed in the plots are given in Table 5.3. It is known that the FSO link is more prone to haze weather condition compared to clear air and moderate rain conditions, which is also evident from Fig. 5.5. Therefore, the performance of the single-link FSO system deteriorates in haze weather condition and better performances are obtained in clear air and moderate rain conditions. However, the performance of the adaptive-combining-based hybrid FSO/RF system degrades in moderate rain and heavy rain weather conditions compared to the haze and heavy fog conditions, respectively, especially for lower values of the FSO transmit power (i.e. $P_F < -17$ dBm for moderate rain versus haze and $P_F < -13$ dBm for heavy rain versus heavy fog). This is because, the RF link is utilized more frequently when the FSO transmit power is very low and also the RF link is more sensitive to the rainy condition than hazy and foggy conditions. Further, for very low values of the FSO transmit power, the quality of the FSO link is weak, since the values of the average SNR of the FSO link are very less. In this case, a high quality RF link, which is assumed to have a transmit power of 10 dBm, is utilized more often. Hence, considerable improvement in the ergodic capacity performance of adaptive-combining-based hybrid system is noticed compared to single-link FSO scenario. Now when there is an increase in the FSO transmit power, the usage of RF link decreases and the FSO link is used more frequently, which is weaker than the RF link in terms of transmit power. So there is a slight degradation in performance of the adaptive combining system for low transmit power values, specifically under hazy and foggy conditions. However, when the FSO transmit power increases, the average SNR of the FSO link improves and significant improvement in the performance of the adaptive system is noticed. Further, it can be seen that the performance of the adaptive-combining-based hybrid system degrades when the weather conditions are more severe like heavy rain and heavy fog.

From Fig. 5.5, it is clear that the capacity performance of the adaptive-combining-based hybrid system is better than the single-link FSO system in all the weather conditions. Further, the SNR gains achieved by the adaptive combining scheme over the single-link FSO system are relatively higher in haze condition than the moderate rain and clear air weather conditions due to the usage of the backup RF link with high probability. Moreover, the probability of usage of the backup RF link is very less under clear air and moderate rain weather conditions, even for low values of FSO transmit power. Consequently, the adaptive combining system will not switch more frequently to the MRC mode of operation, since the quality of the FSO link will be acceptable. Thus, the performances of the single-link FSO system and the adaptive-combining-based hybrid system are nearly equal under clear air and moderate rain weather conditions and the curves for both the systems coincide each other.

In Fig. 5.6, the ergodic capacity performance of the single-link FSO, adaptive-combining-based hybrid FSO/RF, hard-switching-based hybrid FSO/RF, and MRC-based hybrid FSO/RF systems are compared in terms of Gbps. The simulation parameters are assumed as $W_F = 1$ GHz, $W_R = 250$ MHz, $C_n^2 = 2 \times 10^{-14}$, $L = 2000$ m, $r_0 = 15$ cm, $w_0 = 4$ cm, $\kappa = 0.5$, $\mu = 1$, and $m = 1$ (i.e. HD technique). It is observed that the single-link FSO system achieves the highest ergodic capacity

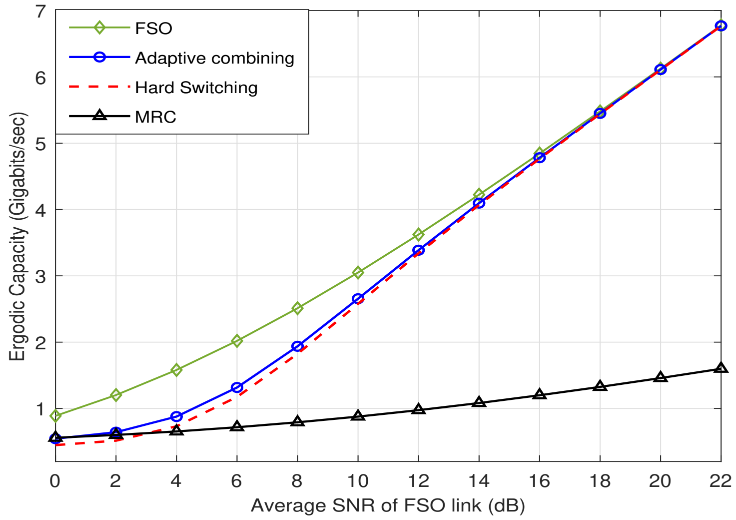

Fig. 5.6: Comparison of ergodic capacity (in Gbps) for different system models

due to its large bandwidth. The capacity performances of the adaptive combining and hard-switching-based hybrid systems are better than the MRC-based hybrid system, but they perform inferior compared to single-link FSO system. Moreover, the capacity performances of both adaptive combining and hard-switching schemes are nearly identical and the capacity values are equal to the single-link FSO system, especially in the high-SNR region. However, both the hybrid systems achieve better reliability in terms of outage and average SER with high SNR gains compared to the single-link FSO system as discussed in Chapter 3 and 4. The reason for the inferior performance of adaptive combining and hard-switching hybrid systems is that the probability of usage of the RF link is high in the low-SNR region and also, the bandwidth of the RF link is lesser than the FSO link.

In addition, the performance of the adaptive combining scheme is slightly better than the hard-switching scheme, especially in the low SNR region. This is because, in adaptive combining scheme, MRC of FSO and RF links is utilized when the quality of FSO link is below the predefined threshold SNR value. However, in case of hard-switching scheme, only single RF backup link is used when the data transmission is not supportive over FSO link. Therefore, due to diversity combining benefit, adaptive combining scheme achieves improved performance compared to hard-switching scheme, especially in the low SNR region. For the same reason, it can also be noticed that the MRC-based hybrid system performs slightly better than the hard-switching-based hybrid system at very low SNR values. It is also to be noted that the MRC-based hybrid system achieves the lowest ergodic capacity among all the systems. This is because, in the MRC-based hybrid system, the overall data rate of the system needs to be scaled down to the data rate of RF link to enable efficient diversity combining. In a nutshell, from the capacity plots, it can be concluded that the ergodic capacity performance (in Gbps) of the adaptive-combining-based hybrid system is far superior compared to the MRC-based hybrid system and is slightly better than the hard-switching-based hybrid system.

5.7 Chapter Summary

In this chapter, the ergodic capacity performance of the hybrid FSO/RF system was analyzed by utilizing the adaptive-combining-based switching scheme over the generalized Malaga and κ–μ distributions. Apart from modeling atmospheric turbulence using the generalized Malaga distribution, the non-zero boresight pointing errors and path loss have been taken into consideration for modeling the combined FSO channel. Further, the optimum switching threshold SNR and beamwidth values, which are required to obtain the best ergodic capacity performance of the adaptive combining system, were determined. From numerical results, it was observed that the ergodic capacity performance (in terms of Gbps) of the adaptive-combining-based hybrid FSO/RF system is better than the MRC-based and hard-switching-based hybrid FSO/RF systems. Thus, it can be concluded that the adaptive combining scheme, a variant of the MRC scheme, can provide higher capacity compared to the hard-switching and MRC schemes for hybrid FSO/RF systems.

Chapter 6

Performance Analysis of Optical Reflecting Surface-Assisted Optical Space Shift Keying-based MIMO-FSO system

6.1 Introduction

Recently, the utilization of reconfigurable intelligent surfaces (RIS) has become increasingly popular as a promising technique to deliver improved SNR, link reliability, and enhanced coverage area. The RIS is also termed as intelligent reflecting surfaces (IRS), large intelligent surfaces (LIS), passive intelligent mirrors, etc. IRS comprises low-cost passive reflecting elements that are made up of meta-surfaces. These elements can adjust the properties like frequency, phase, and polarization of the incident electromagnetic wave. In literature, there is one more low complexity modulation scheme to improve the performance of the wireless communication system in terms of spectral efficiency known as spatial modulation (SM) technique. In SM technique, the information can be conveyed over both antenna and signal spaces [128, 129]. The optical spatial modulation (OSM) is the optical counter-part of SM.

Further, a special case of OSM is termed as optical space shift keying (OSSK), where only one transmitting aperture is active at a given time instant and the data is decoded as the index of the activated transmitting aperture [54]. In [55] and [131], the performance of an FSO system based on the OSSK scheme was analyzed in terms of average BER and ergodic capacity, respectively..

In FSO communication, there are different obstacles in the LOS path, which are unsuitable for transmitting FSO signals and significantly affect the FSO performance [52]. In such situations, the use of optical RIS with the FSO communication can provide an alternate path for its data transmission [26, 50]. Further, the optical RIS, which is nearly passive in nature, has an advantage over the dual-hop relay-assisted systems in terms of lower hardware cost and power requirements [180]. Moreover, in the existing works on optical RIS [50, 181, 27, 183, 184], a single RIS or cascaded multiple RISs were considered for the FSO systems with a single transmitting and receiving apertures without any diversity combining techniques.

To overcome the limitations of the FSO-based systems, an optical reflecting surface (ORS)-assisted OSSK-based FSO system is proposed in this chapter. Further, the closed-form expression for PDF of the ORS-assisted FSO channel is derived over Malaga turbulence model. Moreover, the moment generating function (MGF) of the instantaneous SNR of the overall OSSK-based MIMO-FSO system is obtained. Using the derived channel statistics, an upper bound expression for the average bit error rate (BER) and a lower bound for the ergodic capacity are derived. Additionally, the asymptotic BER is utilized to calculate the diversity gain of the system.

6.2 Organization of the Chapter

The remainder of this Chapter is structured as follows: Section 6.3 outlines the system and channel models for ORS-assisted FSO system with end-to-end channel PDF. In Section 6.4, the average BER and ergodic capacity of the proposed system with the asymptotic analysis are investigated. In addition, a ratio test is also performed to test the convergence of the derived expressions. Section 6.5 presents the numerical results with related inferences and technical insights. Finally, the Chapter is concluded in Section 6.6.

6.3 System and Channel Models

6.3.1 System Model

We consider a $N_t \times N_r$ MIMO-FSO system assisted by an ORS based on the OSSK technique. Here, it is assumed that the ORS is adjusted such that the angle of incidence of the incoming optical signal is equal to the angle of reflection and the phase shift due to ORS is perfectly compensated using the phase-shift profile in [26]. In such a special case, the ORS is equivalent to a simple reflecting mirror, which redirects the incident optical signal to the receiver at the destination. The MIMO-FSO system comprises N_t number of LASER transmitters (i.e. source S) and N_r number of photo-detectors (i.e. destination D), which receives the FSO signals reflected by the ORS element as shown in Fig. 6.1. For simplicity and without the loss of generality, it is assumed that the perfect CSI is available at the receiver. Additionally, it is assumed that there is no direct line-of-sight (LoS) path between the transmitting apertures and the receiving apertures, as the LoS link is blocked due to buildings, trees, and other obstacles in a dense urban environment. At the OSSK encoder, the message bits are split into $\tau_b = \log_2 N_t$ bits. Depending upon the τ_b bits, one of the transmitting aperture is activated by the OSSK encoder and the rest of the optical transmitters will be in an idle state. Therefore, the OSSK-FSO system assists in achieving a spectral efficiency of $\tau_b = \log_2 N_t$. The received signal can be written as

$$\mathbf{Y} = \frac{\eta_f P_t}{N_r}\mathbf{H}\mathbf{X} + \mathbf{E}, \tag{6.1}$$

where $\mathbf{Y} \in \mathbb{R}^{N_r \times 1}$ denotes the received signal vector, η_f denotes the responsivity of the photo-detector, P_t is the FSO transmit power, $\mathbf{X} \in \{\mathbf{x}_i\}$, $1 \leq i \leq N_t$, $\mathbf{x}_i$ is the i^{th}

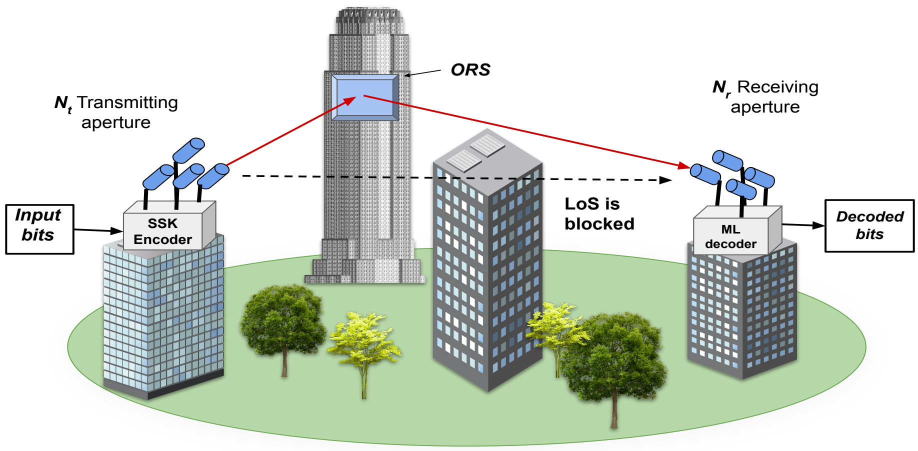

Fig. 6.1: The ORS-assisted OSSK-based MIMO-FSO system model

column of an identity matrix $\mathbf{I}_{N_t}$, and $\mathbf{H} \in \mathbb{R}^{N_r \times N_t}$ represents the combined channel gain matrix. In $\mathbf{H}$ matrix, an element h_{ki} represents the combined channel coefficient between k^{th} receiver and i^{th} transmitter, and $\mathbf{E}$ is the AWGN vector having zero-mean and co-variance matrix $\sigma_n^2 \mathbf{I}_{N_r}$, where σ_n^2 represents the noise variance.

In case of an OSSK-based scheme [54], the maximum likelihood (ML) detector is considered to decode the active transmitting aperture index at the receiver. Therefore, an estimate of the activated transmitting aperture index is given by

$$\hat{i} = \arg\max_i f_{\mathbf{Y}}(\mathbf{Y}|\mathbf{x}_i, \mathbf{H}) = \arg\min_i \sum_{k=1}^{N_r} |Y_k - \eta_f P_t h_{ki}|^2, \tag{6.2}$$

where $\hat{i}$ is the estimated index of the transmitting aperture and $f_{\mathbf{Y}}(\mathbf{Y}|\mathbf{x}_i, \mathbf{H})$ is the PDF of output $\mathbf{Y}$ conditioned on $\mathbf{x}_i$ and $\mathbf{H}$. Further, the estimated aperture index $\hat{i}$ is decoded back into the corresponding τ_b bits.

6.3.2 Channel Model

The FSO channel from S to D is mainly affected by atmospheric turbulence, atmospheric attenuation, and pointing errors. The cascaded FSO channel gain h_{ki} by considering the effects of all the impairments is given by [52], [50]

$$h_{ki} = h_{a_1} h_{a_2} h_\ell h_p, \tag{6.3}$$

where h_{a_1} and h_{a_2} denote the atmospheric turbulence between S to ORS and ORS to D FSO links, respectively, h_p denotes the end-to-end pointing error impairments, and h_ℓ represents the atmospheric attenuation between S and D.

6.3.2.1 Pointing Errors Model

The pointing errors in the ORS-assisted FSO system are mainly due to beam jitter and ORS jitter, which are caused by mechanical vibrations at the transmitter and reflecting surface elements. The fading due to pointing errors in the ORS-assisted FSO system can be expressed as [52]

$$h_p \approx A_0 \exp(-2d^2/W_{z_{eq}}^2), \tag{6.4}$$

where $A_0 = [\text{erf}(v)]^2$, $W_{z_{eq}}^2 = \frac{W_z^2\sqrt{\pi}\text{erf}(v)}{2v\exp(-v^2)}$, and $v = \frac{\sqrt{\pi}r_a}{\sqrt{2}W_z}$. Here, r_a denotes the aperture radius, $W_z = \phi_d L$ represents the beam width, ϕ_d denotes the beam divergence angle, and $L = L_1 + L_2$, where L_1 and L_2 are the distances between S to ORS and ORS to D, respectively. Further, in (6.4), $d = \tan(\theta_s)L_2 \approx \theta_s L_2$ is the instantaneous displacement between the center of the receiver and the actual receiving point of the beam, where θ_s denotes the superimposed pointing error angle, which is formed by the actual incident point at the receiver, reflection point at ORS, and the receiver center [52, Fig. 2]. In addition, θ_s is calculated as $\theta_s = \sqrt{\theta_{sx}^2 + \theta_{sy}^2}$, where $\theta_{sx} \approx \theta_x(1+\frac{L_1}{L_2}) + 2\varphi_x$ is the horizontal component of θ_s and $\theta_{sy} \approx \theta_y(1+\frac{L_1}{L_2}) + 2\varphi_y$ is the vertical component of θ_s. Moreover, θ_x and θ_y are the random variables and they follow Gaussian distribution with zero-mean and variance σ_θ^2. Similarly, φ_x and φ_y are the deflection angles in horizontal and vertical planes, respectively, and are modeled as the Gaussian distribution with zero-mean and variance σ_φ^2. Therefore, the PDF of θ_s can be expressed as [181, eq. (3)]

$$f_{\theta_s}(\theta) = \frac{\theta}{\sigma_\theta^2(1+\frac{L_1}{L_2})^2 + 4\sigma_\varphi^2} e^{-\frac{\theta^2}{2\sigma_\theta^2\left(1+\frac{L_1}{L_2}\right)^2 + 8\sigma_\varphi^2}}. \tag{6.5}$$

Applying the random variable transformation by using (6.4) and (6.5), the PDF of the pointing errors is obtained as

$$f_{h_p}(h) = \frac{\zeta}{A_0^{\zeta}} h^{\zeta-1}, \quad 0 \leq h \leq A_0, \tag{6.6}$$

where $\zeta = \frac{W_{zeq}^2}{4L^2\sigma_\theta^2 + 16L_2^2\sigma_\varphi^2}$.

6.3.2.2 Atmospheric Turbulence Model

The Malaga distribution is assumed to model the atmospheric turbulence. It is a generalized fading distribution, which unifies most of the existing turbulence distribution models in the literature, and provides a great compliance with the published simulation data over all atmospheric turbulence regimes from weak to strong [96]. The unified PDF of h_{a_1} and h_{a_2} following the Malaga distribution is given by [95, eq. (24)]

$$f_{h_{a_l}}(h) = A_l \sum_{p=1}^{\beta_l} a_p^{(l)} h^{\frac{\alpha_l+p}{2}-1} K_{\alpha_l-p}\left(2\sqrt{B_l h}\right), \tag{6.7}$$

where $l = \{1, 2\}$, $B_l = \frac{\alpha_l \beta_l}{y_l \beta_l + \Omega_l'}$, and A_l and $a_p^{(l)}$ are the constants, which are, respectively, given by

$$A_l = \frac{2\alpha_l^{\alpha_l/2}}{y_l^{1+\alpha_l/2}\Gamma(\alpha_l)} \left(\frac{y_l \beta_l}{y_l \beta_l + \Omega_l'}\right)^{\beta_l + \alpha_l/2}, \tag{6.8}$$

$$a_p^{(l)} = \binom{\beta_l - 1}{p - 1} \frac{(y_l \beta_l + \Omega_l')^{1-\frac{p}{2}}}{(p-1)!} \left(\frac{\Omega_l'}{y_l}\right)^{p-1} \left(\frac{\alpha_l}{\beta_l}\right)^{p/2}. \tag{6.9}$$

In (6.7), the modified Bessel function $K_a(\cdot)$ can be written in terms of Meijer G-function [187, eq. (07.34.03.0605.01)] and after some manipulations, we get the PDF of h_{a_l} as

$$f_{h_{a_l}}(h) = \frac{A_l h^{-1}}{2} \sum_{p=1}^{\beta_l} b_p^{(l)} G_{0\,2}^{2\,0}\left(B_l h \,\middle|\, \begin{matrix} - \\ \alpha_l, p \end{matrix}\right), \tag{6.10}$$

Table 6.1: List of major parameters and notations

Parameter	Description
$\alpha_l > 0$	Large-scale atmospheric turbulence parameter [31, eq. (9)]
$\beta_l > 0$	Small-scale atmospheric turbulence parameter [31, eq. (9)]
$\Omega_l^{'}$	$\Omega_l^{'} = \Omega_l + P_l\rho_l + 2\sqrt{P_l\rho_l\Omega_l}\cos\left(\phi_A^{(l)} - \phi_B^{(l)}\right)$
Ω_l	Average power of Line of sight (LOS) component
P_l	Total power of scattered components
$0 < \rho_l < 1$	Factor specifying the amount of scattered power coupled to the LOS component
y_l	$y_l = P_l(1-\rho_l)$, average power of the off-axis scattered component
$\phi_A^{(l)}$	Deterministic phase of LOS component
$\phi_B^{(l)}$	Deterministic phase of coupled-to-LOS scattered component
$\mathrm{erf}(\cdot)$	Error function [201, eq. (3.1.1)]
$K_a(\cdot)$	Modified Bessel function of second kind of order a
$G_{p\ q}^{m\ n}(\cdot)$	Meijer G-function [186, eq. (9.301)]

where $b_p^{(l)} = a_p^{(l)} B_l^{-(\alpha_l+p)/2}$. Note that other key notation and parameters are given in Table 6.1. Additionally, the atmospheric attenuation is modeled using Beers-Lambert law as $h_\ell = \exp(-\alpha_w L)$, where α_w represents the weather dependent attenuation coefficient.

6.3.2.3 PDF of End-to-End FSO Channel

Firstly, the PDF of the end-to-end turbulence of the FSO channel is derived, which is the product of the turbulence of S to ORS and ORS to D links, i.e. $h_a^{eq} = h_{a_1} h_{a_2}$. Using the product of random variables, the PDF of h_a^{eq} can be written as

$$f_{h_a^{eq}}(x) = \int_0^\infty \frac{1}{t} f_{h_{a_1}}(t) f_{h_{a_2}}\left(\frac{x}{t}\right) dt. \tag{6.11}$$

By substituting $f_{h_{a_1}}(t)$ and $f_{h_{a_2}}(x)$ from (6.10) and using [187, eq. (07.34.21.0013.01)], $f_{h_a^{eq}}(x)$ is given by

$$f_{h_a^{eq}}(x) = \frac{A_1 A_2}{4x} \sum_{p=1}^{\beta_1} \sum_{q=1}^{\beta_2} b_p^{(1)} b_q^{(2)} G_{0\,4}^{4\,0} \left(B_1 B_2 x \middle| \begin{matrix} - \\ \mathcal{N}_1 \end{matrix} \right), \tag{6.12}$$

where $\mathcal{N}_1 = [\alpha_2, q, \alpha_1, p]$. Further, the end-to-end FSO channel coefficient is given by the product of turbulence and pointing errors, i.e. $h_{ki} = h_a^{eq} h_p h_\ell$. Similar to h_a^{eq}, the PDF of h_{ki} is expressed as

$$f_{h_{ki}}(x) = \int_{\frac{x}{h_\ell A_0}}^{\infty} \frac{1}{h_\ell t} f_{h_a^{eq}}(t) f_{h_p}\left(\frac{x}{h_\ell t}\right) dt \tag{6.13}$$

By substituting $f_{h_a^{eq}}(\cdot)$ and $f_{h_p}(\cdot)$ from (6.12) and (6.6), respectively, in (6.13) and after applying [187, eq. (07.34.21.0085.01)], $f_{h_{ki}}(x)$ is calculated as

$$f_{h_{ki}}(x) = \frac{A_1 A_2 B_1 B_2 \zeta}{4 A_0 h_\ell} \sum_{p=1}^{\beta_1} \sum_{q=1}^{\beta_2} b_p^{(1)} b_q^{(2)} G_{1\,5}^{5\,0} \left(\frac{B_1 B_2 x}{A_0 h_\ell} \middle| \begin{matrix} \zeta \\ \mathcal{N}_2 \end{matrix} \right), \tag{6.14}$$

where $\mathcal{N}_2 = [\zeta - 1, \alpha_2 - 1, q - 1, \alpha_1 - 1, p - 1]$.

6.4 Performance Analysis

In this section, the upper bound on average BER and lower bound on ergodic capacity of the ORS-assisted OSSK-based MIMO-FSO system are derived. The diversity gain of the system is obtained by applying the high-SNR approximations.

6.4.1 Average Bit Error Rate

A tight upper bound on BER of an OSSK system is given by [132, eq. (10)]

$$\mathrm{BER} \leq \frac{1}{N_t \log_2 N_t} \sum_{i=1}^{N_t} \sum_{j=1}^{N_t} d_H(s_j, s_i) \mathrm{PEP}^{j \to i}, \tag{6.15}$$

where $d_H(s_j, s_i)$ is the Hamming distance between symbols s_j and s_i, $\mathrm{PEP}^{j\to i}$ denotes the pairwise error probability between s_j and s_i and it is expressed as

$$\mathrm{PEP}^{j\to i}{=}\mathrm{Q}\left(\frac{1}{N_r}\sqrt{\frac{\overline{\gamma}_{FSO}\log_2 N_t}{2}\sum_{k=1}^{N_r}|h_{ki}-h_{kj}|^2}\right), \tag{6.16}$$

where $\overline{\gamma}_{FSO} = \frac{\eta_f^2 P_t^2}{\sigma_n^2 \log_2 N_t}$ is the average SNR of the FSO link and $\mathrm{Q}(\cdot)$ is the Gaussian Q-function. In addition, if $i = j$, then $d_H(s_j, s_i)$ is equal to zero, which represents the error-free decoding and its corresponding terms does not contribute to the BER. It is to be noted that the total number of mathematical operations required to calculate the upper bound on average BER for OSSK scheme is $N_t(3N_r-1)$ [132]. In contrast, the computation complexities for calculating the upper bound on average BER of the OSM-based system and repetition coding (RC)-based pulse amplitude modulation (PAM) system are given by $\mathcal{M}N_t(3N_r - 1)$ and $\mathcal{M}(2N_tN_r + N_r - 1)$, respectively, where $\mathcal{M}$ is the modulation order [129]. Therefore, the OSSK-based FSO MIMO system is computationally less expensive in average BER calculations than the above-mentioned OSM and RC-PAM systems.

Theorem 6.1. *The PDF of magnitude of difference between two independent cascaded FSO channels (i.e. $U_{kij} = |h_{ki} - h_{kj}|$), with PDF of each channel following (6.14), is given by*

$$f_{U_{kij}}(u) = \frac{(A_1A_2\zeta)^2B_1B_2}{8A_0h_\ell}\sum_{p=1}^{\beta_1}\sum_{q=1}^{\beta_2}\sum_{r=1}^{\beta_1}\sum_{s=1}^{\beta_2} b_p^{(1)}b_q^{(2)}b_r^{(1)}b_s^{(2)}\sum_{n=0}^{\infty}\left(\frac{-B_1B_2}{A_0h_\ell}\right)^n\frac{u^n}{n!}$$
$$\times\, G_{7\,7}^{5\,6}\left(1\middle|\begin{matrix}\mathcal{N}_3\\ \mathcal{N}_4\end{matrix}\right), \tag{6.17}$$

Proof. See Appendix C.1. □

Theorem 6.2. *The PDF of instantaneous SNR of the ORS-assisted OSSK-based MIMO-FSO system is given by*

$$f_{\gamma_{ij}}(\gamma) = \sum_{n=0}^{\infty} D_n \frac{\gamma^{\frac{n+N_r-2}{2}}}{\Gamma(\frac{N_r+n}{2})} \tag{6.18}$$

Proof. See Appendix C.2. □

It is important to note that the obtained PDF of the instantaneous SNR has a single power series with a power exponent of γ. Now, it is easier to evaluate the integrals based on this power series to calculate the average BER and ergodic capacity expressions for ORS-assisted OSSK-based MIMO FSO system.

Therefore, the average PEP of the MIMO-OSSK is determined by averaging PEP over instantaneous SNR γ_{ij} as

$$\text{APEP}^{j\to i} = \int_0^{\infty} \text{Q}\left(\frac{1}{N_r}\sqrt{\frac{\log_2 N_t}{2}\gamma}\right) f_{\gamma_{ij}}(\gamma) d\gamma. \tag{6.19}$$

Using the relationship $\text{Q}(x) = \frac{1}{2}\text{erfc}\left(\frac{x}{\sqrt{2}}\right)$ and after utilizing [201, eq. 4.1.18], the average PEP is given by

$$\text{APEP}^{j\to i} = \sum_{n=0}^{\infty} \frac{D_n \Gamma\left(\frac{n+N_r+1}{2}\right)}{\sqrt{\pi}(n+N_r)\Gamma\left(\frac{n+N_r}{2}\right)} \left(\frac{2N_r}{\sqrt{\log_2 N_t}}\right)^{N_r+n} \tag{6.20}$$

The upper bound on the average BER of the OSSK-based MIMO-FSO system can be written as

$$\text{ABER} \leq \frac{1}{N_t \log_2 N_t} \sum_{i=1}^{N_t} \sum_{j=1}^{N_t} d_H(s_j, s_i) \times \text{APEP}^{j\to i} \tag{6.21}$$

Since the channel random variables h_{ki} and h_{kj} are independent and identically distributed (i.i.d.), the double summation term $\sum_{i=1}^{N_t}\sum_{j=1}^{N_t} d_H(s_j, s_i)$ in (6.21) can be simplified as $\frac{N_t^2 \log_2 N_t}{2}$ [54, eq. (11)]. Finally, by substituting (6.20) in (6.21), the upper bound expression for the average BER of ORS-assisted MIMO-FSO system is given by

$$\text{ABER} \leq \frac{N_t}{2\sqrt{\pi}} \sum_{n=0}^{\infty} \frac{D_n \Gamma\left(\frac{n+N_r+1}{2}\right)}{(n+N_r)\Gamma\left(\frac{n+N_r}{2}\right)} \left(\frac{2N_r}{\sqrt{\log_2 N_t}}\right)^{N_r+n} \tag{6.22}$$

It can be observed from (6.22) that the derived upper bound will increase by increasing the transmitting apertures N_t, keeping other parameters constant. Consequently, the average BER performance will degrade. However, the spectral efficiency of the OSSK-based FSO system, which is given by $\tau_b = \log_2 N_t$ bits/s/Hz, will improve by increasing N_t. Therefore, a trade-off exists between the average BER and spectral efficiency of the proposed ORS-assisted OSSK-based MIMO FSO system. Further, the upper bound expression in (6.22) is obtained as an infinite summation containing a converging power series, which can be verified by performing a convergence test (i.e. Cauchy ratio test).

Remark 6.1. *The average BER of an ORS-assisted MIMO-FSO system for a special case when $N_t = 2$ and $N_r = 1$ can be reduced as*

$$ABER \leq \frac{1}{\sqrt{\pi}} \sum_{n=0}^{\infty} \frac{D_n \Gamma\left(\frac{n+2}{2}\right)}{\Gamma\left(\frac{n+3}{2}\right)} 2^n \tag{6.23}$$

6.4.2 Ergodic Capacity Analysis

For an OSSK-based MIMO-FSO system, a more practical capacity can be defined in terms of discrete-input continuous-output memoryless channel (DCMC) capacity as [54]

$$C_D \approx 2\log_2 N_t - \log_2\left(N_t + \sum_{i=1}^{N_t} \sum_{\substack{j=1 \\ j \neq i}}^{N_t} \exp\left(-\frac{\overline{\gamma}_{FSO}}{2N_r^2} \times \log_2 N_t \sum_{k=1}^{N_r} (h_{ki} - h_{kj})^2\right)\right). \tag{6.24}$$

Further, by utilizing the Jensen's inequality [132, eq. (21)], a lower bound expression for the DCMC capacity can be determined as

$$C_D^{avg} \geq 2\log_2 N_t - \log_2\left(N_t + \sum_{i=1}^{N_t} \sum_{\substack{j=1 \\ j \neq i}}^{N_t} \mathbb{E}\left[\exp\left(-\frac{\overline{\gamma}_{FSO}}{2N_r^2} \times \log_2 N_t \sum_{k=1}^{N_r} (h_{ki} - h_{kj})^2\right)\right]\right) \tag{6.25}$$

where $\mathbb{E}[\cdot]$ represents the expectation operator. The maximum achievable capacity can be obtained as $\overline{\gamma}_{FSO} \to \infty$ in (6.25). Since $\exp(\cdot)$ function in (6.25) will be equal to zero as $\overline{\gamma}_{FSO} \to \infty$, the maximum achievable capacity is given by

$$C_{D(max)}^{avg} = \log_2 N_t. \tag{6.26}$$

The expectation term on the right hand side of (6.25) can be simplified as

$$\mathbb{E}\left[\exp\left(-\frac{\log_2 N_t}{2N_r^2}\sum_{k=1}^{N_r}\gamma_{kij}\right)\right] = \prod_{k=1}^{N_r}\mathbb{E}\left[\exp\left(-\frac{\gamma_{kij}\log_2 N_t}{2N_r^2}\right)\right] \tag{6.27}$$

where γ_{kij} is given in Appendix C.2. Furthermore, the above expression can be given in terms of MGF as

$$\prod_{k=1}^{N_r}\mathbb{E}\left[\exp\left(-\frac{\gamma_{kij}\log_2 N_t}{2N_r^2}\right)\right] = \prod_{k=1}^{N_r}\Psi_{\gamma_{kij}}\left(-\frac{\log_2 N_t}{2N_r^2}\right) = \Psi_{\gamma_{ij}}\left(-\frac{\log_2 N_t}{2N_r^2}\right) \tag{6.28}$$

where the MGF functions $\Psi_{\gamma_{kij}}(\cdot)$ and $\Psi_{\gamma_{ij}}(\cdot)$ are given by (C.7) and (C.8), respectively. Further, using (6.28), the lower bound on the capacity in (6.25) can be rewritten as

$$C_D^{avg} \geq 2\log_2 N_t - \log_2\left(N_t + \sum_{i=1}^{N_t}\sum_{\substack{j=1 \\ j\neq i}}^{N_t}\Psi_{\gamma_{ij}}\left(-\frac{\log_2 N_t}{2N_r^2}\right)\right) \tag{6.29}$$

Proposition 6.1. *The expression for lower bound on the ergodic capacity of an OSSK-based MIMO-FSO system is given as*

$$C_D^{avg} \geq 2\log_2 N_t - \log_2\left(N_t + (N_t^2 - N_t)\times\sum_{n=0}^{\infty}D_n\left(\frac{2N_r^2}{\log_2 N_t}\right)^{\frac{n+N_r}{2}}\right) \tag{6.30}$$

Proof. By putting $t = \frac{\log_2 N_t}{2N_r^2}$ in (C.8) and substituting its value in (6.29), we get the final expression for C_D^{avg} as (6.30). □

Further, in (6.30), if $\overline{\gamma}_{FSO} \to \infty$, then the maximum value of ergodic capacity is obtained as $C_D^{avg} = \log_2 N_t$, which validates the correctness of the derived ergodic capacity expression. [1]

Remark 6.2. *For a special case, when $N_t = 2$ amd $N_r = 1$, the bound on the ergodic capacity can be simplified as*

$$C_D^{avg} \geq 1 - \log_2 \left(1 + \sum_{n=0}^{\infty} D_n 2^{\frac{n+N_r}{2}} \right) \tag{6.31}$$

6.4.3 High Average SNR Analysis and Diversity Gain

Here, a less complicated expression for the upper bound on average BER is derived using high-SNR approximations. In (6.22), by assuming $\overline{\gamma}_{FSO} \to \infty$, the dominant term will be obtained by taking $n = 0$ and the asymptotic average BER expression is simplified as

$$\begin{aligned} \text{ABER}^{\infty} \leq & \left(\frac{1}{\overline{\gamma}_{FSO}}\right)^{\frac{N_r}{2}} \frac{N_t \Gamma\left(\frac{N_r+1}{2}\right)}{2\sqrt{\pi} N_r \Gamma\left(\frac{N_r}{2}\right)} \left[\frac{N_r (A_1 A_2 \zeta)^2 B_1 B_2}{8 A_0 h_\ell \sqrt{\log_2 N_t}} \sqrt{\pi} \right. \\ & \left. \times \sum_{p=1}^{\beta_1} \sum_{q=1}^{\beta_2} \sum_{r=1}^{\beta_1} \sum_{s=1}^{\beta_2} b_p^{(1)} b_q^{(2)} b_r^{(1)} b_s^{(2)} G_{7\,7}^{5\,6} \left(1 \middle| \begin{matrix} \mathcal{N}_5 \\ \mathcal{N}_6 \end{matrix} \right) \right]^{N_r}, \end{aligned} \tag{6.32}$$

where $\mathcal{N}_5 = [0, 1-\zeta, 1-\alpha_2, 1-q, 1-\alpha_1, 1-p, \zeta]$ and $\mathcal{N}_6 = [\zeta-1, \alpha_2-1, s-1, \alpha_1-1, r-1, -\zeta, 0]$. From the above expression, it can be seen that $\text{ABER}^{\infty} \propto (1/\overline{\gamma}_{FSO})^{\frac{N_r}{2}}$ and the diversity gain is given by $N_r/2$. It is observed that the diversity gain is independent of the factors like turbulence and pointing error parameters unlike the general M-ary modulation-scheme-based FSO system without OSSK scheme [31], [50]. This is because, the pair-wise error probability (PEP), which is used for calculating the average BER of OSSK system, depends on the difference between the channel gains and does not depend on the individual FSO channel gain. In addition, the fluctuations in the atmospheric turbulence or pointing errors do not

[1] It is to be noted that $\overline{\gamma}_{FSO}$ is inside the term D_n, which is given in Appendix C.2.

greatly contribute to the difference in the channel gains. Hence, the diversity gain of the OSSK system is independent of the turbulence and pointing error parameters.

Similarly, the less-complicated asymptotic expression for the given capacity bound can be determined by assuming high value of $\overline{\gamma}_{FSO}$ in (6.30) and the final expression is given as

$$C_D^{\infty} \geq 2\log_2 N_t - \log_2\left[N_t + (N_t^2 - N_t)\left(\frac{2N_r^2 C_0^2}{\log_2 N_t}\right)^{\frac{N_r}{2}}\right], \tag{6.33}$$

where

$$C_0 = \frac{\Gamma\left(\frac{1}{2}\right)}{(\overline{\gamma}_{FSO})^{\frac{1}{2}}}\left[\frac{(A_1A_2\zeta)^2 B_1 B_2}{16A_0 h_\ell}\sum_{p=1}^{\beta_1}\sum_{q=1}^{\beta_2}\sum_{r=1}^{\beta_1}\sum_{s=1}^{\beta_2} \times b_p^{(1)} b_q^{(2)} b_r^{(1)} b_s^{(2)} G_{7\,7}^{5\,6}\left(1\middle|\begin{matrix}\mathcal{N}_7\\ \mathcal{N}_8\end{matrix}\right)\right]. \tag{6.34}$$

It can be seen from (6.33) and (6.34) that by increasing the value of N_r, the factor $C_0^{N_R}$ will decrease significantly with increase in $\overline{\gamma}_{FSO}$. Consequently, there will be an improvement in the ergodic capacity value and the average SNR required to achieve the maximum capacity will be reduced. However, the maximum capacity value will be always equal to $\log_2 N_t$ as given by (6.26), which is independent of N_r.

6.4.4 Convergence Test

To test the convergence of the average BER and capacity expressions in (6.22) and (6.30), respectively, a Cauchy ratio test is performed on the power series of MGF of $\gamma_{kij}(-t)$ in (C.7), which is used to calculate the average BER and ergodic capacity bounds. Further, if the infinite series in $\gamma_{kij}(-t)$ is convergent, then the $\Psi_{\gamma_{ij}}(-t)$ is also convergent and consequently, we can say that the derived average BER and ergodic capacity expressions will be absolutely convergent. For a given series $\sum_{n=0}^{\infty} u_n$, if the following condition is satisfied, i.e.

$$\lim_{n\to\infty} \left| \frac{u_{n+1}}{u_n} \right| < 1, \tag{6.35}$$

then the given series is said to be absolutely convergent. From (C.7), let us assume the series coefficient $u_n = C_n t^{-\frac{n+1}{2}}$ and the ratio of series coefficient is defined as

$$\left| \frac{u_{n+1}}{u_n} \right| = \left| \frac{\left(\frac{-B_1 B_2}{A_0 h_\ell}\right)^{n+1} \frac{t^{-\frac{n+2}{2}} \Gamma\left(\frac{n+2}{2}\right)}{(n+1)! \overline{\gamma}_{FSO}^{\frac{n+2}{2}}} G_{7\,7}^{5\,6}\left(1 \middle| \begin{matrix} \mathcal{N}_7 \\ \mathcal{N}_8 \end{matrix}\right)}{\left(\frac{-B_1 B_2}{A_0 h_\ell}\right)^{n} \frac{t^{-\frac{n+1}{2}} \Gamma\left(\frac{n+1}{2}\right)}{n! \overline{\gamma}_{FSO}^{\frac{n+1}{2}}} G_{7\,7}^{5\,6}\left(1 \middle| \begin{matrix} \mathcal{N}_3 \\ \mathcal{N}_4 \end{matrix}\right)} \right| \tag{6.36}$$

where $\mathcal{N}_7 = 0, n-\zeta+2, n-\alpha_2+2, n-q+2, n-\alpha_1+2, n-p+2, \zeta$ and $\mathcal{N}_8 = \zeta-1, \alpha_2-1, s-1, \alpha_1-1, r-1, n-\zeta+1, n+1$. After simplification, we get

$$\left| \frac{u_{n+1}}{u_n} \right| = \left[\frac{\Gamma\left(\frac{n+2}{2}\right)}{(n+1)\Gamma\left(\frac{n+1}{2}\right)} \right] F \tag{6.37}$$

where $F = \left| \frac{-B_1 B_2 G_{7\,7}^{5\,6}\left(1 \middle| \begin{matrix} \mathcal{N}_7 \\ \mathcal{N}_8 \end{matrix}\right)}{A_0 h_\ell (t \overline{\gamma}_{FSO})^{1/2} G_{7\,7}^{5\,6}\left(1 \middle| \begin{matrix} \mathcal{N}_3 \\ \mathcal{N}_4 \end{matrix}\right)} \right|$. Here, the constant F will always give a positive real number for all n and t. From (6.37), it can be clearly observed that the powers of n in denominator is one higher than numerator and after applying the limit $n \to \infty$, the expression will tend to zero. Therefore, the obtained average BER and ergodic capacity expressions are absolutely convergent.

6.5 Numerical and Simulation Results

This section presents the analytical and simulation results of the proposed system model for average BER and ergodic capacity. The theoretical results are verified by performing the Monte-Carlo simulations for 10^6 data bits. In the proposed ORS-assisted FSO system, the link distances are assumed as $L_1 = L_2 = 250$ m. In addition, the other system parameters are assumed as follows: FSO wavelength

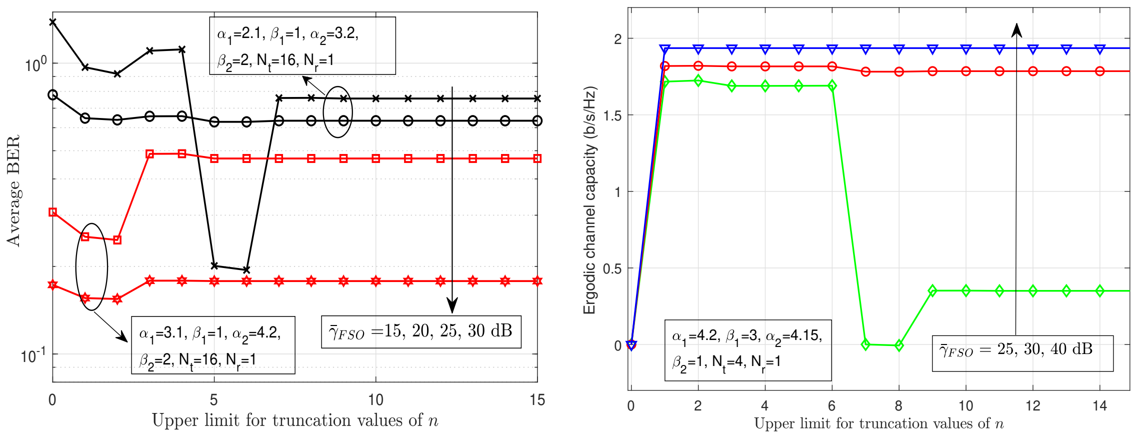

(a) Convergence test of the average BER given by (6.22)

(b) Convergence test of the ergodic capacity given by (6.30)

Fig. 6.2: Convergence test for average BER and ergodic capacity expressions

Table 6.2: Truncation accuracy of summation limits for BER

$\overline{\gamma}_{FSO}$	Final values of BER for truncation limit n				Upper limit
	5	8	11	12	
15	0.200909	0.759853	0.755896	0.755896	$n = 11$
20	0.628429	0.633963	0.633950	0.633950	$n = 11$
25	0.699009	0.699009	0.699009	0.699009	$n = 11$
30	0.298805	0.298805	0.298805	0.298805	$n = 11$

$\lambda_F = 1550$ nm, $\sigma_\theta = 1$ mrad, $\sigma_\varphi = 0.5$ mrad, $r_a = 0.1$ m, $\phi_d = 8$ mrad, $\rho_l = 0.999$, $\phi_A^{(l)} - \phi_B^{(l)} = \pi/2$, $\Omega_l = 1.3265$, and $P_l = 0.2158$, unless and otherwise stated [132], [181]. It is to be noted that the values of turbulence and other parameters for S to ORS and ORS to D links are assumed as $\alpha_1 = \alpha_2 = \alpha$ and $\beta_1 = \beta_2 = \beta$.

The upper limits used for truncating the infinite series in average BER expression, which is given by (6.22), are shown in Table 6.2 and if values higher than the upper limits are used, then the final average BER values will not change up to the sixth decimal place. Further, the upper limits used for truncating the infinite series of ergodic capacity bound in (6.30) are given in Table 6.3, and in the case of values greater than the upper limits, the final capacity values will remain unchanged until the sixth decimal place.

The convergence test of the derived average BER expression given by (6.22),

Table 6.3: Truncation accuracy of summation limits for capacity

$\overline{\gamma}_{FSO}$	Final values of capacity for truncation limit n				Upper limit
	3	5	11	12	
25	1.689138	1.689459	0.350584	0.350584	$n=11$
30	1.816396	1.816400	1.785124	1.785124	$n=11$
40	1.935630	1.935631	1.935627	1.935627	$n=11$

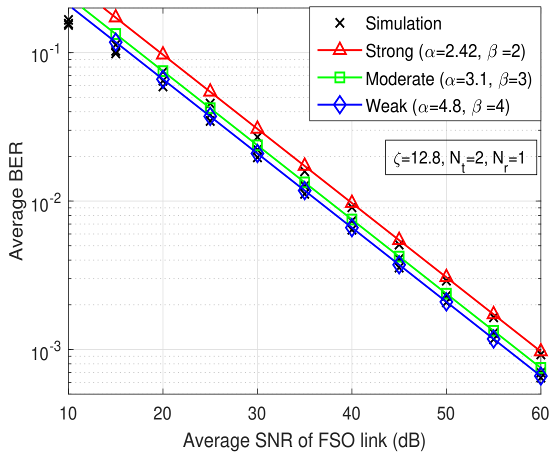

Fig. 6.3: Average BER under different turbulence conditions

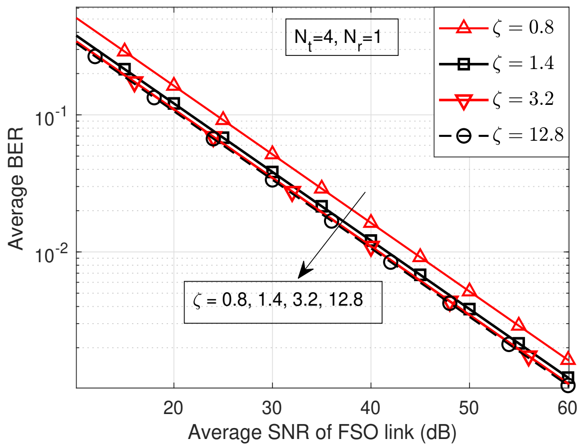

Fig. 6.4: Average BER for different pointing errors

which comprises an infinite series, is performed in Fig. 6.2(a). The average BER is plotted against the upper limit values of n for truncating the infinite series under different turbulence conditions and average SNR values. From the plots, it is clearly noticed that the value of average BER is constant for $n \geq 8$ under different average SNR values, which is also validated from Table 6.2. Therefore, it can be inferred that the infinite series in the average BER expression convergences for $n \geq 8$. Similarly, the convergence test of the ergodic capacity expression given by (6.30) is performed in Fig. 6.2(b). The ergodic capacity bound is plotted against the upper limit values of n for truncating the infinite series under different average SNR values. The plots indicate that the ergodic capacity for $n \geq 10$ remains constant under different average SNR values, which is also evident from Table 6.3.

Fig. 6.3 shows the average BER performance of the proposed system under different turbulence conditions. It can be seen from the plots that the performance improves with a decrease in turbulence severity. However, all the plots for different turbulence conditions have the same slope. This is because, the diversity gain of the

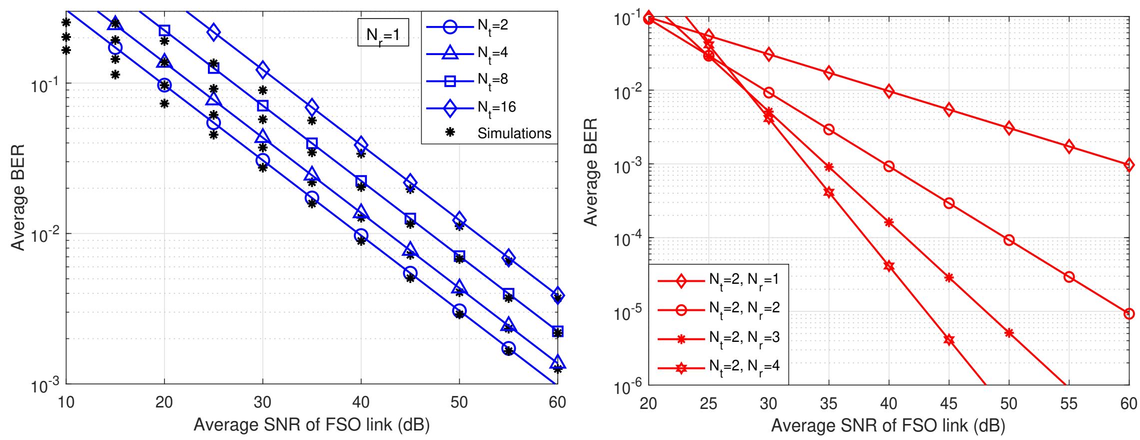

(a) (b)

Fig. 6.5: Average BER performance for different N_t and N_r

OSSK-based MIMO-FSO system does not depend on the atmospheric turbulence conditions, which is also evident from (6.32). On the contrary, this inference is different as compared to the general PSK-based modulation techniques, where the diversity gain of the FSO-based system depends on the turbulence and pointing error parameters [31]–[202]. It is also to be noted that an SNR gain of around 4 dB is achieved to attain a BER of 10^{-2}, as the turbulence strength decreases from strong to weak. Further, the simulation plots almost coincide well with the theoretical upper bounds. This validates the correctness of our theoretical analysis.

In Fig. 6.4, the effect of pointing errors on the performance of the proposed system has been depicted. The turbulence parameters are assumed as $\alpha = 2.95$ and $\beta = 3$ for all pointing error conditions. From the plots, it is inferred that the performance is better for higher values of ζ. Because lower values of ζ imply higher pointing error severity, which deteriorates the system performance. The SNR gain of around 5 dB is achieved to attain the BER of 10^{-2} for high pointing errors scenario (i.e. $\zeta = 0.8$) over low pointing errors scenario (i.e. $\zeta = 12.8$). Here, it can also be seen that the slope is same for all plots and the diversity gain is independent of the channel parameters, as mentioned in Fig. 6.3. It also indicates that the effect of pointing errors is less on the OSSK-based FSO system.

In Fig. 6.5, we investigate the average BER performance of the proposed system model for different values of N_t and N_r by assuming $\alpha = 2.4$, $\beta = 2$, and $\zeta = 12.8$.

It is observed in Fig. 6.5(a) that the performance of $N_t \times 1$ system degrades with increasing N_t. However, the spectral efficiency, which is given by $\log_2 N_t$ bits/s/Hz, increases with increasing N_t. Therefore, there is a trade-off between spectral efficiency and average BER in the case of an OSSK-based FSO system. This is because, the probability of error in detecting the index of the transmitting antenna increases as N_t increases. By substituting $\sum\limits_{i=1}^{N_t}\sum\limits_{j=1}^{N_t} d_H(s_j, s_i) = \frac{N_t^2 \log_2 N_t}{2}$ in (6.15) and assuming low SNR condition (i.e. $\overline{\gamma}_{FSO} \to 0$), the upper bound on BER after simplification can be written as BER $\leq N_t/4$. Since the BER is linearly varying with N_t, the average BER is not significantly tight, especially at low SNR values. However, the upper bound on average BER is tightly matching with the simulation results as the SNR increases, which is observed in Fig. 6.5(a) for $N_t = 8$ and 16.

In Fig. 6.5(b), the average BER is shown for different N_r assuming $N_t = 2$. It can be clearly seen that the average BER of the $N_t \times N_r$ system drastically improves with the increasing number of receiving apertures N_r, especially in the high-SNR regime. It is also evident from Fig. 6.5(b) that the diversity gain of the proposed system depends on the value of N_r, since the slope of the BER curves increases with an increase in N_r. Further, the SNR gain obtained by $N_r = 2$ over $N_r = 1$ is 20 dB to achieve a BER value of 10^{-3}. Similarly, the SNR gain achieved by $N_r = 3$ and $N_r = 4$ over $N_r = 2$ and $N_r = 3$ are 5 dB and 2 dB, respectively. Thus, it can be inferred that the SNR gain decreases with increasing N_r. Note that the diversity gain is calculated in Section 6.4.3 as $N_r/2$ and the same is also justified in Fig. 6.5(b).

In Fig. 6.6, the performance of the proposed system is given for different weather conditions by plotting the average BER against the transmit power. The values of the parameters are assumed as $\alpha = 2.62$, $\beta = 2$, and α_w (in dB/km) = 0.43, 20, and 5.8 for clear air, foggy, and rainy weather conditions, respectively. From the plots, it can be observed that the proposed system performs better in clear air compared to rainy and foggy weather conditions due to less atmospheric attenuation. Since the FSO system is more prone to foggy weather condition compared to rainy condition,

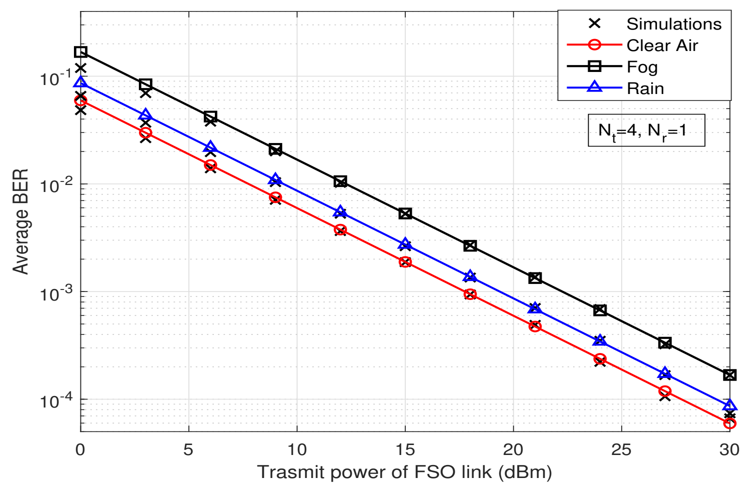

Fig. 6.6: Average BER performance for different weather conditions

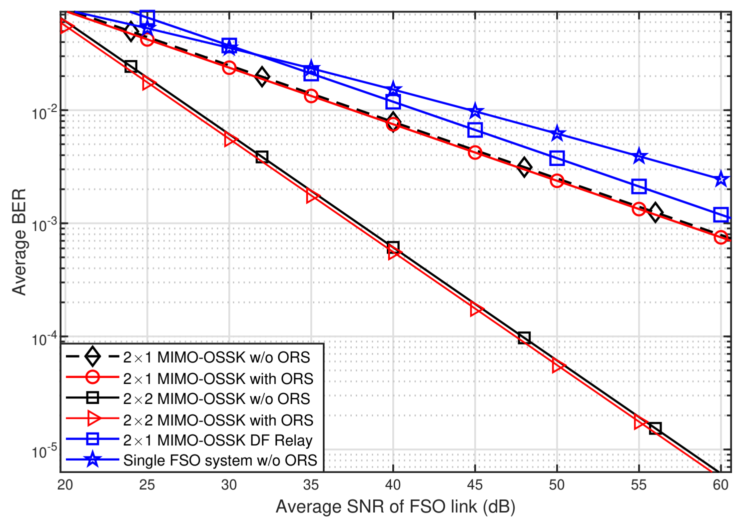

Fig. 6.7: Performance comparison of different FSO systems

the performance deteriorates more under foggy condition. It is clear from the plots that foggy condition requires 12 dBm of transmit power to attain an average BER value of 10^{-2}. However, clear air and rainy conditions require only 8 dBm and 9 dBm of transmit power values to attain the same BER, respectively.

Fig. 6.7 shows the performance comparison of the ORS-assisted OSSK-based MIMO-FSO system in terms of average BER with the following conventional FSO systems: (a) Single-link FSO system without ORS, (b) OSSK-based MIMO-FSO system without ORS and (c) OSSK-based dual-hop (DH) DF relaying system. The parameter values are assumed as $\alpha = 2.95$ and $\beta = 3$. It can be clearly seen that the proposed system achieves almost similar or slightly better performance than the OSSK system without ORS. As expected, the performance of a conventional single-link FSO system without ORS is the worst among all the FSO-based systems and the proposed ORS-assisted FSO system achieves an SNR gain of 7 dB at a BER of 10^{-2}. In addition, the OSSK-based DF relaying system performs better than the single-link FSO system. However, the OSSK-based DF relaying system performs inferior compared to the proposed system, with an SNR loss of 5 dB to attain the BER of 10^{-2}. This is mainly due to the fact that the impact of decoding errors in a relaying system is far more severe than the impact of cascaded channel turbulence in the ORS-based FSO system. It is also to be noted that the OSSK-based FSO system without ORS requires the presence of a direct LOS link for message transmission. Therefore, it is inferred that in the absence of a direct link, the proposed ORS-assisted system can create a virtual direct LOS link with equal or slightly better BER performance than the existing OSSK-based MIMO system without ORS [132].

Fig. 6.8 shows the ergodic capacity performance under different turbulence and pointing error conditions. It can be observed that the performance of the proposed system declines as the turbulence severity increases. However, the difference in the performance after reaching 90% of the maximum achievable capacity $C_{D(\max)}^{avg}$ is very less. Similarly, as the pointing error severity increases (i.e. value of ζ decreases), the performance of the system degrades and there is around 5 dB SNR improvement from $\zeta = 0.98$ to $\zeta = 12.8$ under the strong turbulence condition to attain 90% of $C_{D(\max)}^{avg}$ value.

In Fig. 6.9, the ergodic capacity is given for different number of transmitting apertures $N_t = 2$, 4, 8, and 16. The plots show that the proposed system performs much better with an increase in N_t as expected. It is also confirmed from the plots that the maximum capacity for different N_t is obtained as $C_{D(\max)}^{avg} = \log_2 N_t$, which validates the derived expression for $C_{D(\max)}^{avg}$ in (6.26). Further, from Fig. 6.10, it is observed that there is a significant improvement in the capacity performance with an increase in N_r. It can also be noticed that there is a 7 dB SNR gain when $N_t = 4$ for $N_r = 2$ over $N_r = 1$ to achieve 90% of $C_{D(\max)}^{avg}$. Similarly, around 10 dB SNR gain is noticed by increasing N_r for the case when $N_t = 16$. From Fig.

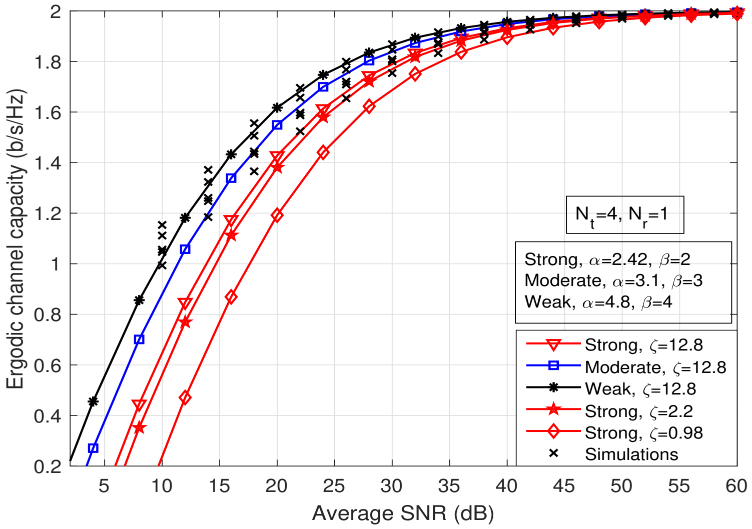

Fig. 6.8: Capacity performance for different turbulence and pointing errors conditions

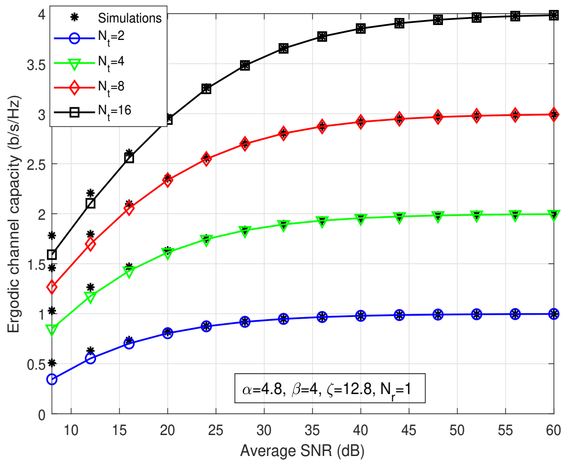

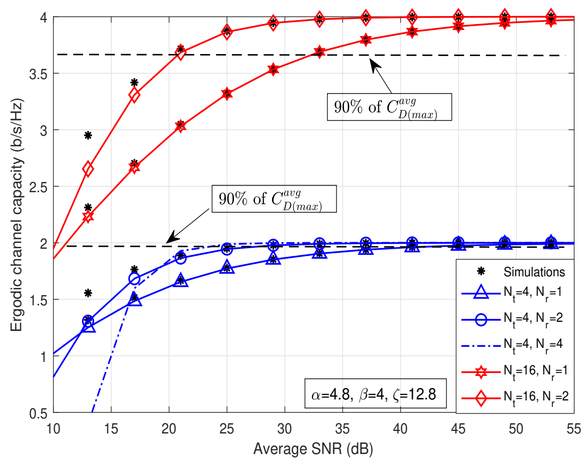

Fig. 6.9: Capacity performance for different N_t Fig. 6.10: Capacity performance for different N_r

6.10, it is clear that the SNR values required to achieve the maximum capacity is reduced by increasing N_r, as mentioned in Section 6.4.3 after (6.34). Furthermore, in Fig. 6.8, 6.9, and 6.10, Monte-Carlo simulations are closely matching with the theoretical lower bound results as evident from the figure, especially after the system achieves 90% of $C^{avg}_{D(\max)}$, which establishes the correctness of our derived lower bound expressions.

In Fig. 6.11, the proposed ORS-based OSSK system is compared with the OSSK-based MIMO-FSO system without ORS [132] and DF relaying-based OSSK system in terms of ergodic capacity. It can be clearly observed from the plots that the proposed ORS system achieves similar capacity performance equivalent to the OSSK system without ORS. However, as already mentioned, the ORS-assisted OSSK sys-

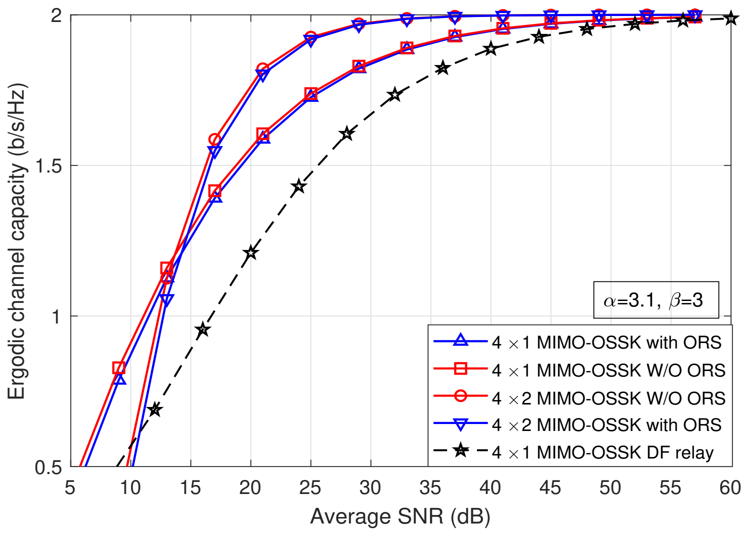

Fig. 6.11: Capacity performance comparison of various MIMO systems

tem does not require the presence of LOS link compared to the OSSK system without ORS. Thus, similar to BER performance in Fig. 6.7, it is inferred that a virtual LOS path is created using ORS without any significant degradation in the capacity performance. Further, the DF relaying-based system performs inferior compared to OSSK-based systems with ORS due to the fact that the impact of the worst channel among S to R (relay) and R to D links in a relaying system is far more severe than the effect of cascaded channel gain in the ORS-assisted system.

In summary, six significant technical findings or insights in this chapter are given as follows:

- For the proposed ORS-assisted OSSK-based FSO system, statistical functions of absolute difference between two cascaded FSO channels and instantaneous SNR are obtained. Further, from the statistical functions, closed-form expressions for two different performance metrics are derived for analysing the end-to-end system performance.

- The proposed ORS-assisted FSO system is highly beneficial, in case if a direct LOS path is not available between the source and the destination. This is because, it performs almost similar or slightly better than the FSO system without ORS, which alleviates the requirement of LOS path in FSO communication.

- Asymptotic analysis shows that the diversity gain of the proposed system is equal to $N_r/2$. Thus, the performance of the system improves with increasing number of receiving apertures N_r.

- Since the diversity gain does not depend on the channel parameters, high diversity gain shall be retained even under strong turbulence and high pointing error severity conditions.

- In addition, when turbulence fluctuates among weak, moderate, and strong turbulence conditions, the average BER of ORS-assisted OSSK-based MIMO-FSO is not changing significantly unlike conventional FSO systems.

- The proposed system performs better than a DF relaying-based OSSK system in terms of average BER and ergodic capacity without any additional signal processing or energy requirements. Hence, ORS-assisted FSO system can be proposed as an alternative to DF-relaying-based FSO system.

6.6 Chapter Summary

In this chapter, an ORS-assisted OSSK-based MIMO-FSO system was proposed with an aim of mitigating the blockage in OSSK-based MIMO FSO systems. Specifically, the closed-form expressions for PDF of the absolute difference between two cascaded FSO channels, PDF of instantaneous SNR, and MGF of the instantaneous SNR were derived. Further, with the help of the aforementioned expressions, the average PEP, the upper bound on average BER, and lower bound on ergodic capacity were evaluated over Malaga distributed turbulence along with pointing errors. Further, asymptotic expressions for average BER and ergodic capacity were derived and diversity gain of the proposed system was also obtained. The numerical results showed that the average BER and ergodic capacity performances were significantly improved as N_r increases and the maximum capacity achieved was $\log_2 N_t$. It was also confirmed from the analytical results that the effect of turbulence and pointing errors on the performance of the proposed system was not very significant, unlike the conventional FSO system, due to the usage of the OSSK scheme.

Chapter 7

Performance Analysis of Multiple Optical Reflecting Surfaces Assisted FSO Communication

7.1 Introduction

In the earlier works, the FSO systems were studied over a single optical IRS and cascaded multiple IRS without employing any selection schemes [27], [50], and [52]. In [50], the FSO communication link was aided by a IRS module to relax the LOS requirement, which helped to provide the coverage in remote areas and skip zones. Furthermore, in [27], a complete performance of an FSO system empowered by single IRS was presented over different FSO turbulence models. Acquiring precise channel state information (CSI) in practical scenarios is challenging due to the presence of channel estimation errors [203]. Obtaining perfect CSI directly is nearly impossible because the wireless channel experiences rapid variations caused by fading and atmospheric attenuation [56]. Therefore, it is crucial to study the impact of channel estimation errors on the performance of the system. In [109], performance analysis of the FSO system was carried out by including the impact of imperfect CSI over the Fisher-Snedecor ($\mathcal{F}$) turbulence channel model. Further, the authors in [111] investigated the FSO system empowered by a single IRS by assuming imperfect CSI over the $\mathcal{F}$-distribution model.

To improve the performance of a FSO system assisted by a single ORS necessitates the inclusion of multiple ORSs in a backhaul network scenario along the path between the source and destination. However, the performance of optical reflecting surfaces (ORSs)-assisted FSO communication system comprising multiple ORSs in parallel has not been investigated in the existing works. Further, the effect of imperfect CSI on multiple ORSs-assisted FSO system has not been studied in the previous works.

In this chapter, a multiple ORSs-assisted FSO communication is proposed considering parallel data transmission between source and destination nodes. In addition, the ORS selection scheme is implemented in which the best ORS is selected from the multiple available ORSs to improve the performance of the existing single optical IRS-based FSO system. The closed-form expression for the end-to-end PDF of the maximum instantaneous SNR among multiple ORSs-aided FSO links is derived by including turbulence, pointing errors, and imperfect CSI. With the aid of the above PDF expression, the exact outage probability and average SER expressions are obtained for the proposed system with perfect CSI and imperfect CSI conditions. Further, simpler asymptotic expressions are also derived, which give more useful insights into the multiple ORSs system, along with performing diversity gain analysis.

7.2 Organization of the Chapter

The remainder of this chapter is structured as follows: Section 7.3 presents the system and channel models for multiple ORSs-assisted FSO system with end-to-end channel PDF and SNR statistics for perfect and imperfect CSI conditions. In Section 7.4, the outage probability and average SER of the proposed system are investigated for both perfect and imperfect CSI cases. Section 7.5 presents the asymptotic analysis with diversity gain of the multiple ORSs-assisted FSO system. Further, the numerical results with related inferences and technical insights are provided in section 7.6. Finally, the chapter is concluded in Section 7.7.

7.3 System and Channel Models

7.3.1 System Model

We consider a multiple ORSs-assisted FSO communication between a single source with multiple aperture arrays and a receiving aperture as shown in Fig. 7.1. The source has multiple laser transmitters which are oriented towards the respective ORSs and these ORS redirects the incoming optical beam towards a single receiving aperture. In this case, the ORS is assumed as a perfect mirror without any amplitude gain or phase errors. In addition, the source communicates with the receiver through the best possible ORS, which is selected among M available parallel ORSs to improve the performance of the system. Further, ORS-assisted FSO link which is having the maximum end-to-end instantaneous SNR will be selected as the best ORS to communicate with the receiver. It is assumed that there is no direct path between the source S and the destination D. Thus, the signal is transmitted from S to D through the best ORS to achieve performance gain. Furthermore, the input-output relationship of the system can be expressed as

$$y_k = \mathcal{R} P_t h_k x_k + n_k, \tag{7.1}$$

where $\mathcal{R}$ is the responsivity of the photo-detector, P_t denotes the peak transmit power, h_k is the cascaded channel coefficient between k^{th} transmitting aperture and receiver assisted by k^{th} ORS, y_k denotes the output signal, x_k is input signal, and n_k denotes the AWGN corresponding to the k^{th} ORS-assisted FSO channel with zero-mean and variance σ_n^2.

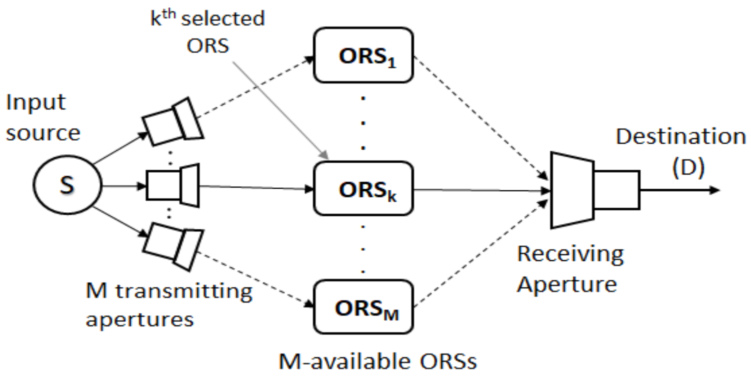

Fig. 7.1: The selection-based multiple ORSs-assisted FSO system model

7.3.2 Channel Model

The cascaded FSO channel from S to D, which includes both atmospheric turbulence and pointing errors, can be written as

$$h_k = h_{a_{1k}} h_{a_{2k}} h_{pk} h_{\ell k}, \tag{7.2}$$

where $h_{a_{1k}}$ and $h_{a_{2k}}$ represent the atmospheric turbulence from k^{th} transmitting aperture of S to k^{th} ORS and k^{th} ORS to D, respectively, h_{pk} represents the end-to-end pointing errors of the k^{th} ORS-based FSO link, and $h_{\ell k}$ is the end-to-end atmospheric attenuation.

7.3.2.1 Atmospheric Turbulence Model

We assume the Gamma-Gamma distributed FSO turbulence for $h_{a_{1k}}$ and $h_{a_{2k}}$, which incorporates moderate to strong turbulence regimes. Further, the PDF of Gamma-Gamma distribution is given by [50, eq. (13)] and by using [187, eq. (07.34.03.0605.01)], the unified PDF for $h_{a_{1k}}$ and $h_{a_{2k}}$ can be expressed as

$$f_{h_{a_{ik}}}(h) = \frac{h^{-1}}{\Gamma(\alpha_{ik})\Gamma(\beta_{ik})} G_{0\,2}^{2\,0}\left(\alpha_{ik}\beta_{ik}h \,\middle|\, \begin{matrix} - \\ \alpha_{ik}, \beta_{ik} \end{matrix}\right), \tag{7.3}$$

where $i = \{1, 2\}$, α_{ik} is the large-scale scattering coefficient, β_{ik} represents the small-scale scattering coefficient of the FSO link [190, eq. (60)], and $G^{m\ n}_{p\ q}(\cdot)$ denotes the Meijer G-function [186, 9.301]. In addition, the atmospheric attenuation of the FSO link in (7.1) is given by Beers-Lambert law and is expressed as $h_{\ell k} = \exp(-\Omega_l L_k)$, where Ω_l is the weather dependent parameter and $L_k = L_{1k} + L_{2k}$, L_{1k} and L_{2k} are the distances between S to k^{th} ORS and k^{th} ORS to D, respectively,.

7.3.2.2 Pointing Errors Model

The pointing error model for the ORS-assisted FSO system has already been discussed in Chapter 6, Section 6.3.2.1. From (6.6), the PDF of the pointing error coefficient h_{pk} can be written as

$$f_{h_{pk}}(h) = \frac{\xi_k}{A_k^{\xi_k}} h^{\xi_k - 1}, \quad 0 \le h \le A_k, \tag{7.4}$$

where $\xi_k = \frac{W^2_{z_{eq}^{(k)}}}{(2L_k\sigma_{\theta_k})^2 + (4L_{2k}\sigma_{\varphi_k})^2}$ is the pointing error parameter, $W^2_{z_{eq}^{(k)}}$, $\sigma^2_{\theta_k}$, and $\sigma^2_{\varphi_k}$ are given in Chapter 6, Section 6.3.2.1.

7.3.2.3 PDF of End-to-End FSO Channel

The PDF of end-to-end turbulence of the FSO channel, i.e. $h_{ak}^{eq} = h_{a_{1k}} h_{a_{2k}}$, can be expressed as

$$f_{h_{ak}^{eq}}(t) = \int_0^\infty \frac{1}{x} f_{h_{a_{1k}}}(x) f_{h_{a_{2k}}}\left(\frac{t}{x}\right) dx. \tag{7.5}$$

Replacing $f_{h_{a_{1k}}}(\cdot)$ and $f_{h_{a_{2k}}}(\cdot)$ by (7.3) and utilizing [187, eq. (07.34.21.0013.01)], $f_{h_{ak}^{eq}}(t)$ is written as

$$f_{h_{ak}^{eq}}(t) = \frac{t^{-1}}{\Gamma(\alpha_{1k})\Gamma(\beta_{1k})\Gamma(\alpha_{2k})\Gamma(\beta_{2k})} G^{4\ 0}_{0\ 4}\left(\alpha_{1k}\beta_{1k}\alpha_{2k}\beta_{2k} t \,\middle|\, \begin{matrix} - \\ \mathcal{C}_{1k} \end{matrix}\right), \tag{7.6}$$

where $\mathcal{C}_{1k} = [\alpha_{2k}, \beta_{2k}, \alpha_{1k}, \beta_{1k}]$. Similarly, the product of end-to-end turbulence and pointing errors, i.e. $h_k = h_{ak}^{eq} h_{pk} h_{\ell k}$, results in the overall channel coefficient and using [187, eq. (07.34.21.0085.01)], the PDF of h_k is given by

$$f_{h_k}(t) = B_k t^{-1} G_{1\,5}^{5\,0}\left(D_k t \middle| \begin{matrix} \xi_k + 1 \\ \mathcal{C}_{2k} \end{matrix} \right), \tag{7.7}$$

where B_k, D_k, and $\mathcal{C}_{2k}$ are given in Table 7.1.

7.3.2.4 PDF of Imperfect Channel

In practical scenarios, the perfect estimation of the FSO channel gain is not possible, as there are errors associated with the channel estimation. Further, the output signal of the proposed system with imperfect CSI can be expressed as [203, eq. (3)]

$$\tilde{y_k} = \mathcal{R} P_t \tilde{h_k} x_k + n_k, \tag{7.8}$$

where $\tilde{h_k}$ is the imperfect channel gain of the FSO link and it is given as [109, eq. (10)]

$$\tilde{h_k} = \delta h_k + \sqrt{1 - \delta^2}\epsilon\,, \tag{7.9}$$

where $\delta \in [0, 1]$ represents the correlation coefficient and ϵ denotes the channel estimation errors. Here, $\delta = 1$ represents no errors in the channel estimation. Moreover, ϵ is a random variable, which is independent of h_k, following zero-mean Gaussian distribution with variance equal to σ_e^2. Note that the above channel modeling of the imperfect CSI in (7.9) is well established in the literature [56, 57, 109, 111, 203].

Theorem 7.1. *The PDF of ORS-assisted FSO channel with imperfect CSI over Gamma-Gamma turbulence distribution and pointing errors is given by*

Table 7.1: List of notations

$D_k = \frac{\alpha_{1k}\beta_{1k}\alpha_{2k}\beta_{2k}}{h_{\ell k}A_k}$	$B_k = \frac{\xi_k}{\Gamma(\alpha_{1k})\Gamma(\beta_{1k})\Gamma(\alpha_{2k})\Gamma(\beta_{2k})}$	$P_1 = n + \alpha_{1k} + \alpha_{2k} + \beta_{1k} + \beta_{2k} - 5$
$\mathcal{C}_{2k} = [\xi_k, \alpha_{2k}, \beta_{2k}, \alpha_{1k}, \beta_{1k}]$	$G_{1k} = G_{10\ 3}^{1\ 10}\left(\frac{2^8 K_2 \delta^2}{D_k}\middle\vert\begin{matrix}\mathcal{X}_{1k}\\ \mathcal{X}_{2k}\end{matrix}\right)$	$P_2 = \alpha_{1k} + \alpha_{2k} + \beta_{1k} + \beta_{2k} - 5$
$\mathcal{X}_{2k} = \left[\frac{n}{2}, \frac{-\xi_k}{2}, \frac{1-\alpha_{2k}}{2}\right]$	$\mathcal{X}_{1k} = \left[\frac{1-\xi_k}{2}, \frac{2-\xi_k}{2}, \frac{1-\alpha_{2k}}{2}, \frac{2-\alpha_{2k}}{2}, \frac{1-\beta_{2k}}{2}, \frac{2-\beta_{2k}}{2}, \frac{1-\alpha_{1k}}{2}, \frac{2-\alpha_{1k}}{2}, \frac{1-\beta_{1k}}{2}, \frac{2-\beta_{1k}}{2}\right]$	
$\mathcal{C}_{3i} = [(\xi_i + 1, 1)]$	$\mathcal{C}_{4i} = [(\xi_i, 1), (\alpha_{2i}, 1), (\beta_{2i}, 1), (\alpha_{1i}, 1), (\beta_{1i}, 1)]$	
$\mathcal{C}_{5j} = [(1, 1), (\xi_i + 1, 1)]$	$\mathcal{C}_{6j} = [(\xi_j, 1), (\alpha_{2j}, 1), (\beta_{2j}, 1), (\alpha_{1j}, 1), (\beta_{1j}, 1), (0, 1)]$	

$$f_{\tilde{h}_k}(t) = \begin{cases} \frac{B_k K_1}{\pi^2} \exp\left(-K_2 t^2\right) \sum\limits_{n=0}^{\infty} \frac{2^{P_1} K_2^{\frac{n}{2}}}{n!} G_{1k} t^n, & t > 0 \\ 1 - I_0^{(k)}, & t = 0. \end{cases} \tag{7.10}$$

where

$$I_0^{(k)} = \frac{B_k K_1}{2\pi^2} \sum_{n=0}^{\infty} \frac{2^{P_1} K_2^{-\frac{1}{2}}}{n!} G_{1k} \Gamma\left(\frac{n+1}{2}\right) \tag{7.11}$$

Note that P_1 and G_{1k} are listed in Table 7.1.

Proof. Please see Appendix D. □

7.3.3 SNR Statistics

The instantaneous SNR with PDF and CDF expressions for both perfect and imperfect CSI cases are presented in this section.

7.3.3.1 With Perfect CSI

The instantaneous SNR of the k^{th} ORS-based FSO link is defined as $\gamma_k = |h_k|^r \overline{\gamma}$, where $\overline{\gamma} = P_t/\sigma_n^2$ is the average SNR of the ORS-assisted FSO link, $r = 1$ and $r = 2$ represent HD and IM/DD techniques, respectively. Now, by applying the transformation of random variable on (7.7), the unified PDF of γ_k can be calculated as

$$f_{\gamma_k}(\gamma)=\frac{B_k}{r}\gamma^{-1}G_{1\,5}^{5\,0}\left(D_k\left(\frac{\gamma}{\overline{\gamma}}\right)^{\frac{1}{r}}\middle|\begin{matrix}\xi_k+1\\ \mathcal{C}_{2k}\end{matrix}\right). \tag{7.12}$$

Further, by integrating the above PDF using [187, eq. (07.34.21.0084.01)], the CDF of the instantaneous SNR γ_k is given by

$$F_{\gamma_k}(\gamma)=B_k G_{2\,6}^{5\,1}\left(D_k\left(\frac{\gamma}{\overline{\gamma}}\right)^{\frac{1}{r}}\middle|\begin{matrix}1,\xi_k+1\\ \mathcal{C}_{2k},0\end{matrix}\right). \tag{7.13}$$

7.3.3.2 With Imperfect CSI

The unified instantaneous SNR of the end-to-end k^{th} FSO link with imperfect CSI is given by $\tilde{\gamma}_k = |\tilde{h_k}|^r\overline{\gamma}$.

Using the power transformations of random variable in (7.10), the PDF of γ_k is expressed as

$$f_{\tilde{\gamma}_k}(x)=\begin{cases}\frac{B_k K_1}{r\pi^2}e^{-\frac{K_2 x^{2/r}}{\overline{\gamma}^{2/r}}}\sum\limits_{n=0}^{\infty}\frac{2^{P_1}K_2^{\frac{n}{2}}}{n!}G_{1k}\frac{x^{\left(\frac{n-r+1}{r}\right)}}{\overline{\gamma}^{\frac{n+1}{r}}}, & x>0\\ 1-I_0^{(k)}, & x=0.\end{cases} \tag{7.14}$$

Now the CDF of $\tilde{\gamma}_k$ can be evaluated as $F_{\tilde{\gamma}_k}(x) = \int\limits_0^x f_{\tilde{\gamma}_k}(t)dt$. By employing [187, 07.34.03.0228.01] and [187, 07.34.21.0084.01], the final expression for the CDF is given by

$$F_{\tilde{\gamma}_k}(x) = \frac{B_k K_1}{r\pi^2}\sum_{n=0}^{\infty}\frac{2^{P_1}K_2^{-\frac{1}{2}}}{n!}G_{1k}G_{1\,2}^{1\,1}\left(\frac{K_2 x^{\frac{2}{r}}}{\overline{\gamma}^{\frac{2}{r}}}\middle|\begin{matrix}1\\ \frac{n+1}{2},0\end{matrix}\right)+1-I_0^{(k)} \tag{7.15}$$

7.4 Performance Analysis

In this section, the expressions for the outage probability and average SER of the proposed multiple ORSs-assisted FSO system are derived.

7.4.1 Outage Probability

In the proposed system model, if the instantaneous SNR of the best ORS-based FSO link, which offers the highest instantaneous SNR, falls below a particular value of threshold SNR γ_T, then outage will be declared. Further, the instantaneous SNR of the best ORS link is given as $\gamma_{\max} = \max(\gamma_1, \gamma_2, ..., \gamma_M)$. The outage probability of the selection-based multiple ORSs-assisted FSO system is given by

$$P_{out} = \Pr(\gamma_{\max} < \gamma_T) = \Pr(\gamma_1 < \gamma_T, ..., \gamma_M < \gamma_T) \tag{7.16}$$

7.4.1.1 Outage Probability for Perfect CSI

Since each of the ORS-based FSO link is assumed to be independent of each other, the outage expression for the considered system with perfect CSI can be simplified as

$$P_{out} = F_{\gamma_{max}}(\gamma_T) = \prod_{k=1}^{M} F_{\gamma_k}(\gamma_T), \tag{7.17}$$

where $F_{\gamma_k}(\gamma_T)$ is the CDF of γ_k given by (7.13). By putting $\gamma = \gamma_T$ in (7.13) and by substituting its value in 7.17, the final expression for outage probability is given by

$$P_{out} = \prod_{k=1}^{M} B_k G_{2\,6}^{5\,1} \left(D_k \left(\frac{\gamma_T}{\overline{\gamma}} \right)^{\frac{1}{r}} \middle| \begin{matrix} 1, \xi_k + 1 \\ \mathcal{C}_{2k}, 0 \end{matrix} \right), \tag{7.18}$$

7.4.1.2 Outage Probability for Imperfect CSI

Similar to perfect CSI case, the outage probability for the proposed system with imperfect CSI is given by

$$P_{out}^{(I)} = F_{\tilde{\gamma}_{max}}(\gamma_T) = \prod_{k=1}^{M} F_{\tilde{\gamma}_k}(\gamma_T) \tag{7.19}$$

By replacing x with γ_T in (7.15), the final expression for outage probability in closed-form is given by

$$P_{out}^{(I)} = \prod_{k=1}^{M} \left[\frac{B_k K_1}{r\pi^2} \sum_{n=0}^{\infty} \frac{2^{P_1} K_2^{-\frac{1}{2}}}{n!} G_{1k} G_{1\,2}^{1\,1} \left(\frac{K_2 \gamma_T^{\frac{2}{r}}}{\overline{\gamma}^{\frac{2}{r}}} \middle| \begin{matrix} 1 \\ \frac{n+1}{2}, 0 \end{matrix} \right) + 1 - I_0^{(k)} \right] \tag{7.20}$$

7.4.2 Average Symbol Error Rate

In this section, the average SER performance is presented for the proposed system with perfect CSI and Imperfect CSI.

7.4.2.1 Average Symbol Error Rate for Perfect CSI

The expression for evaluating the average SER of the multiple ORSs-assisted FSO system is given by

$$\overline{P}_e = \int_0^{\infty} p(e|\gamma) f_{\gamma_{\max}}(\gamma) d\gamma, \tag{7.21}$$

where $p(e|\gamma)$ represents the conditional SER of $\mathcal{M}-$ary phase-shift-keying (MPSK) signalling conditioned on the given instantaneous SNR γ and it is expressed as [190, eq. (25)] $p(e|\gamma) = \frac{P}{2}\text{erfc}(Q\sqrt{\gamma})$, where $P = 1$ for modulation order $\mathcal{M} = 2$, $P = 2$ for $\mathcal{M} > 2$, $Q = \sin(\pi/\mathcal{M})$, and $\text{erfc}(\cdot)$ is the complementary error function [186, eq. (8.250.4)]. Using [187, 07.34.26.0008.01], $p(e|\gamma)$ can be rewritten in terms of Fox's

$$\overline{P}_e = \frac{P}{2r\sqrt{\pi}} \prod_{k=1}^{M} B_k \Bigg\{ H^{0,2:\ 5,0:\ 5,1:\cdots:\ 5,1}_{2,1:\ 1,5:\ 2,6:\cdots:\ 2,6} \left(\frac{D_1}{(Q^2\overline{\gamma})^{\frac{1}{r}}},\cdots,\frac{D_M}{(Q^2\overline{\gamma})^{\frac{1}{r}}} \middle| \begin{matrix} \left(1;\{\frac{1}{r}\}_1^M\right),\left(0.5;\{\frac{1}{r}\}_1^M\right);\mathcal{C}_{31};\mathcal{C}_{52};\cdots;\mathcal{C}_{5M} \\ \left(0;\{\frac{1}{r}\}_1^M\right);\mathcal{C}_{41};\mathcal{C}_{62};\cdots;\mathcal{C}_{6M} \end{matrix} \right)$$
$$+ H^{0,2:\ 5,1:\ 5,0:\cdots:\ 5,1}_{2,1:\ 2,6:\ 1,5:\cdots:\ 2,6} \left(\frac{D_1}{(Q^2\overline{\gamma})^{\frac{1}{r}}},\cdots,\frac{D_M}{(Q^2\overline{\gamma})^{\frac{1}{r}}} \middle| \begin{matrix} \left(1;\{\frac{1}{r}\}_1^M\right),\left(0.5;\{\frac{1}{r}\}_1^M\right);\mathcal{C}_{51};\mathcal{C}_{32};\cdots;\mathcal{C}_{5M} \\ \left(0;\{\frac{1}{r}\}_1^M\right);\mathcal{C}_{61};\mathcal{C}_{42};\cdots;\mathcal{C}_{6M} \end{matrix} \right) + \cdots$$
$$\cdots + H^{0,2:\ 5,1:\ 5,1:\cdots,:\ 5,0}_{2,1:\ 2,6:\ 2,6:\cdots:\ 1,5} \left(\frac{D_1}{(Q^2\overline{\gamma})^{\frac{1}{r}}},\cdots,\frac{D_M}{(Q^2\overline{\gamma})^{\frac{1}{r}}} \middle| \begin{matrix} \left(1;\{\frac{1}{r}\}_1^M\right),\left(0.5;\{\frac{1}{r}\}_1^M\right);\mathcal{C}_{51};\mathcal{C}_{52};\cdots;\mathcal{C}_{3M} \\ \left(0;\{\frac{1}{r}\}_1^M\right);\mathcal{C}_{61};\mathcal{C}_{62};\cdots;\mathcal{C}_{4M} \end{matrix} \right) \Bigg\} \tag{7.25}$$

H-function as

$$p(e|\gamma) = \frac{P}{2\sqrt{\pi}} H^{2\ 0}_{1\ 2} \left(Q^2\gamma \middle| \begin{matrix} (1,1) \\ (0,1),(0.5,1) \end{matrix} \right). \tag{7.22}$$

Furthermore, in (7.21), $f_{\gamma_{\max}}(\gamma)$ is the PDF of $\gamma_{\max}$ and by differentiating (7.17), it is calculated as

$$f_{\gamma_{\max}}(\gamma) = \sum_{i=1}^{M} \prod_{k=1,k\neq i}^{M} f_{\gamma_i}(\gamma) F_{\gamma_k}(\gamma), \tag{7.23}$$

where $f_{\gamma_i}(\gamma)$ and $F_{\gamma_k}(\gamma)$ are given by (7.12) and (7.13), respectively. Further, (7.12) and (7.13) can be expressed in terms of Fox's H-function using [187, 07.34.26.0008.01] and by substituting these expressions in (7.21), the average SER integral can be rewritten as

$$\overline{P}_e = \frac{P}{2r\sqrt{\pi}} \prod_{k=1}^{M} B_k \sum_{i=1}^{M} \int_0^\infty \gamma^{-1} H^{2\ 0}_{1\ 2} \left(Q^2\gamma \middle| \begin{matrix} (1,1) \\ (0,1),(0.5,1) \end{matrix} \right) H^{5\ 0}_{1\ 5} \left(D_i \left(\frac{\gamma}{\overline{\gamma}}\right)^{\frac{1}{r}} \middle| \begin{matrix} \mathcal{C}_{3i} \\ \mathcal{C}_{4i} \end{matrix} \right)$$
$$\times \prod_{\substack{j=1 \\ j\neq i}}^{M} H^{5\ 1}_{2\ 6} \left(D_j \left(\frac{\gamma}{\overline{\gamma}}\right)^{\frac{1}{r}} \middle| \begin{matrix} \mathcal{C}_{5j} \\ \mathcal{C}_{6j} \end{matrix} \right) d\gamma, \tag{7.24}$$

where $\mathcal{C}_{3i}$, $\mathcal{C}_{4i}$, $\mathcal{C}_{5j}$, and $\mathcal{C}_{6j}$ are given in Table 7.1. By applying the Mellin convolution theorem [204, eq. (1.29)] and after employing the definition of multivariate Fox's H-function [189, eq. (A.1)], we obtain the average SER, which is given by (7.25). Note that there are total M terms in (7.25) and $\{a_l\}_1^M$ denotes $a_1, a_2, \cdots, a_M$.

7.4.2.2 Average Symbol Error Rate for Imperfect CSI

The average SER of the proposed system with imperfect CSI for MPSK signaling is obtained by utilizing the derived CDF $F_{\tilde{\gamma}_{max}}(x)$ and is given by [175]

$$\overline{P}_e^{(I)} = \frac{\mathcal{A}\sqrt{\mathcal{D}}}{2\sqrt{2\pi}} \int_0^\infty x^{-1/2} F_{\tilde{\gamma}_{max}}(x) e^{-\frac{\mathcal{D}x}{2}} dx, \tag{7.26}$$

where $\mathcal{A} = 1$, $\mathcal{D} = 2$ for $\mathcal{M}$=2 and $\mathcal{A} = 2$, $\mathcal{D} = 2\sin^2\left(\frac{\pi}{\mathcal{M}}\right)$ for $\mathcal{M}$ >2. Since the evaluation of the above integral is complicated, we have used a Gauss-Laguerre quadrature approximation [205] to evaluate and the final average SER expression is given by

$$\overline{P}_e^{(I)} = \frac{\mathcal{A}\sqrt{\mathcal{D}}}{2\sqrt{2\pi}} \sum_{j=1}^{m} W_j \prod_{k=1}^{M} F_{\tilde{\gamma}_k}(\omega_j) \tag{7.27}$$

where W_j denotes the weight coefficient and is expressed as

$$W_j = \frac{\omega_j \Gamma(m+0.5)}{m!(m+1)^2 (L_{m+1}^{-1/2}(\omega_j))^2} \tag{7.28}$$

In (7.27), ω_j is the j^{th} zero of the Laguerre polynomial $L_m^{-1/2}(\cdot)$, which is given as [186, eq. (8.970.1)]

$$L_m^{-1/2}(y) = \sum_{l=0}^{m} \binom{m-\frac{1}{2}}{m-l} \frac{(-y)^l}{l!} \tag{7.29}$$

7.5 Asymptotic Analysis and Diversity Gain

In this section, more tractable asymptotic expressions for both outage and average SER, which are calculated at a high average SNR regime, are derived to deduce valuable insights and to determine the diversity gain.

7.5.1 Asymptotic Outage Probability

7.5.1.1 Asymptotic Outage Probability for Perfect CSI

The expression for the asymptotic outage probability is evaluated by assuming $\overline{\gamma} \to \infty$. Further, by using [187, eq. (07.34.06.0040.01)], the Meijer G-function in (7.13) is asymptotically expanded at $(1/\overline{\gamma}) \to 0$ and after substituting its values in (7.18), the asymptotic outage probability for the proposed system with perfect CSI is given by

$$P_{out}^{\infty} = \prod_{k=1}^{M} B_k \sum_{l=1}^{5} \frac{\prod\limits_{\substack{m=1\\m\neq l}}^{5} \Gamma(\mathcal{C}_{2k,m} - \mathcal{C}_{2k,l})}{\mathcal{C}_{2k,l}\Gamma(\xi_k + 1 - \mathcal{C}_{2k,l})} D_k^{\mathcal{C}_{2k,l}} \left(\frac{\gamma_T}{\overline{\gamma}}\right)^{\mathcal{C}_{2k,l}/r}, \tag{7.30}$$

where $\mathcal{C}_{2k,i}$ is the i^{th} term of $\mathcal{C}_{2k}$.

7.5.1.2 Asymptotic Outage Probability for Imperfect CSI

In order to calculate the asymptotic outage probability for imperfect CSI case, we assume $\overline{\gamma} \to \infty$ in (7.20) and by using [187, eq. (07.34.06.0040.01)], we obtain the asymptotic outage probability as

$$P_{out}^{(I)\infty} = \prod_{k=1}^{M} \left[\frac{B_k K_1}{\pi^2} \sum_{n=0}^{\infty} \frac{2^{P_1} K_2^n}{(n+1)!} G_{1k} \left(\frac{\gamma_T^{\frac{n+1}{r}}}{\overline{\gamma}^{\frac{n+1}{r}}} \right) + 1 - I_0^{(k)} \right]. \tag{7.31}$$

By assuming $n = 0$, which is the dominant term in (7.31), a more simplified expression is obtained and is given by

$$P_{out}^{(I)\infty} = \prod_{k=1}^{M} \Bigg[\underbrace{\frac{B_k K_1}{\pi^2} 2^{P_1} G_{1k} \left(\frac{\gamma_T^{\frac{1}{r}}}{\overline{\gamma}^{\frac{1}{r}}} \right)}_{T_1^P} + \underbrace{\left(1 - I_0^{(k)}\right)}_{T_2^P} \Bigg]. \tag{7.32}$$

It is important to note that (7.32) contains two terms, where the first term T_1^P depends on $\overline{\gamma}$ and the second term T_2^P is a constant independent of $\overline{\gamma}$. As a result,

$T_2^P \gg T_1^P$ in the high-SNR region and the outage probability will attain a floor value, which is given by

$$P_{out}^{(I)^{\text{fixed}}} = \prod_{k=1}^{M} \left(1 - I_0^{(k)}\right). \tag{7.33}$$

7.5.2 Asymptotic Average SER

7.5.2.1 For Perfect CSI

The asymptotic average SER can be obtained by calculating the residues of multiple Mellin-Barnes contour integrals of multivariate Fox's H-function at the dominant poles [27]. By assuming $\overline{\gamma} \to \infty$ in the average SER expression (7.25), the poles are determined as $P_k = \min\{\xi_k, \alpha_{2k}, \beta_{2k}, \alpha_{1k}, \beta_{1k}\}$, where $k = 1, 2, \cdots, M$. It is to be noted that there are M poles for each multivariate Fox's H-function term in (7.25). Therefore, by calculating the residues at the poles, we obtain asymptotic average SER as

$$\begin{aligned}\overline{P}_e^{\infty} = \frac{P}{2\sqrt{\pi}} \left(\frac{1}{Q^2\overline{\gamma}}\right)^{\frac{1}{r}\sum\limits_{s=1}^{M} P_s} \Bigg[\frac{\Gamma\left(\frac{1}{2} + \frac{1}{r}\sum\limits_{s=1}^{M} P_s\right)}{\sum_{s=1}^{M} P_s} \sum_{i=1}^{M} \frac{1}{\prod_{\substack{j=1 \\ j\neq i}}^{M} P_j} \\ \times \prod_{k=1}^{M} \frac{\prod\limits_{\substack{m=1 \\ \mathcal{C}_{2k,m}\neq P_k}}^{5} \Gamma(\mathcal{C}_{2k,m} - P_k)}{\Gamma(\xi_k + 1 - P_k)} B_k D_k^{P_k} \Bigg].\end{aligned} \tag{7.34}$$

Further, by comparing (7.34) with a general asymptotic SER form, which is given by $P_e^{\infty} \approx (G_c\overline{\gamma})^{-G_d}$, where G_c and G_d are coding gain and diversity gain of the system, it is clear that the diversity gain of the multiple ORSs-assisted FSO system is obtained as $G_d = \frac{1}{r}\sum\limits_{s=1}^{M} P_s$, where P_s are the poles that are already determined for (7.25).

7.5.2.2 For Imperfect CSI

Similar to outage, the asymptotic expression for average SER after employing [187, eq. (07.34.06.0040.01)] in (7.27) is given by

$$\overline{P}_e^{(I)\infty} = \frac{\mathcal{A}\sqrt{\mathcal{D}}}{2\sqrt{2\pi}} \sum_{j=1}^{m} W_j \prod_{k=1}^{M} \left\{ \frac{B_k K_1}{\pi^2} \sum_{n=0}^{\infty} \frac{2^{P_1} K_2^n}{(n+1)!} G_{1k} \frac{\omega_j^{\frac{n+1}{r}}}{\overline{\gamma}^{\frac{n+1}{r}}} + \left(1 - I_0^{(k)}\right) \right\} \tag{7.35}$$

Using the dominant term in (7.35) by substituting $n = 0$, a more simpler average SER expression is obtained, which is given by

$$\overline{P}_e^{(I)\infty} = \frac{\mathcal{A}\sqrt{\mathcal{D}}}{2\sqrt{2\pi}} \sum_{j=1}^{m} W_j \prod_{k=1}^{M} \Bigg\{ \underbrace{\frac{B_k K_1}{\pi^2} 2^{P_2} G_{1k} \left(\frac{\omega_j}{\overline{\gamma}}\right)^{\frac{1}{r}}}_{T_1^s} + \underbrace{\left(1 - I_0^{(k)}\right)}_{T_2^s} \Bigg\} \tag{7.36}$$

Similar to outage probability, the first term T_1^s in (7.36) depends on $\overline{\gamma}$ and the second term T_2^s is a constant. Since $T_2^s \gg T_1^s$ in the high-SNR region, average SER will also approach to a floor value, which is equal to

$$P_{e_{\text{fixed}}}^{(I)} = \frac{\mathcal{A}\sqrt{\mathcal{D}}}{2\sqrt{2\pi}} \sum_{j=1}^{m} W_j \prod_{k=1}^{M} \left(1 - I_0^{(k)}\right). \tag{7.37}$$

7.6 Numerical and Simulation Results

This section presents the simulation and analytical results for the outage probability and average SER of the proposed system. The multivariate Fox's H-function in (7.25) is evaluated by utilizing a Python code given in [206]. The system parameters assumed for perfect CSI condition are as follows: $\phi_{d_k} = 8$ mrad, $\lambda_F = 1550$ nm, $r_a = 0.1$ m, $\mathcal{M} = 2$, and $L_{1k} = L_{2k} = 250$ m. For imperfect CSI condition, the parameters assumed in the simulations are $\phi_{d_k} = 2$ mrad, $\delta = 0.9$, $\sigma_{\theta_k} = 0.0008$, $\sigma_{\varphi_k} = 0.0001$, and $\mathcal{M} = 2$. It is to be noted that we have assumed the same parameters for S to k^{th} ORS and k^{th} ORS to D links, i.e. $\xi_k = \xi$, $\alpha_{1k} = \alpha_{2k} = \alpha$, and $\beta_{1k} = \beta_{2k} = \beta$, unless and otherwise stated, for simplicity without loss of generality.

Table 7.2: Truncation accuracy for the infinite summation in (7.27)

$\overline{\gamma}$	Final values of average SER (7.27) for truncation limit n				Upper limit
	40	80	120	140	
20	0.022437	0.022430	0.022429	0.022429	$n=120$
30	0.015875	0.015869	0.015868	0.015868	$n=120$
40	0.014275	0.014270	0.014269	0.014269	$n=120$

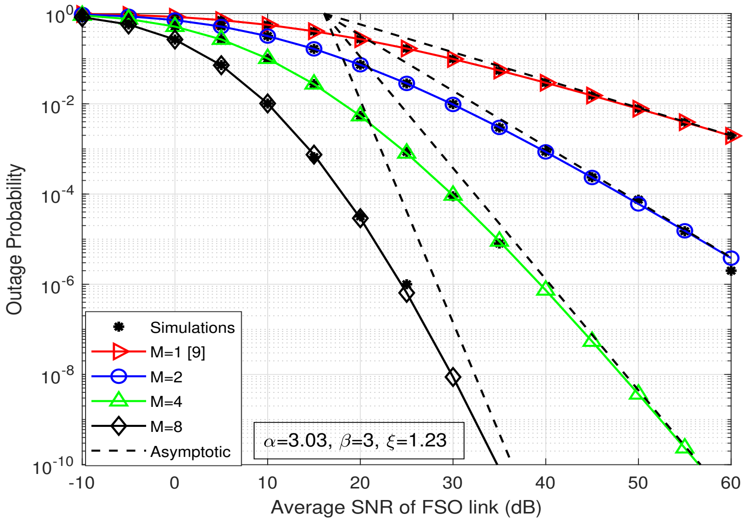

Fig. 7.2: Outage probability under perfect CSI for different number of ORSs

The number of bits to perform Monte-Carlo simulations are assumed as 10^6. The truncation accuracy for infinite summation used in (7.27) is listed in Table 7.2. If the values greater than the upper limits are applied, then it is inferred that the fifth decimal figure of final average SER values is not altered.

Fig. 7.2 shows the outage probability of the multiple ORSs-assisted FSO system with perfect CSI for different numbers of reflecting surfaces M. It is observed from the plots that the outage performance is significantly improved by increasing the reflecting surfaces from $M = 1$ to $M = 8$, as expected. In addition, the SNR gain achieved by $M = 2$ over $M = 1$ (i.e. single ORS-assisted FSO system [50]) is 18 dB to attain an outage probability of 10^{-2}. Similarly, the SNR gains achieved by $M = 4$ and $M = 8$ over $M = 2$ and $M = 4$ are 12 and 8 dB, respectively, for an outage value of 10^{-2}.

In Fig. 7.3, the average SER is plotted against the average SNR for different values of M. The SER performance trends observed from the plots corresponding to

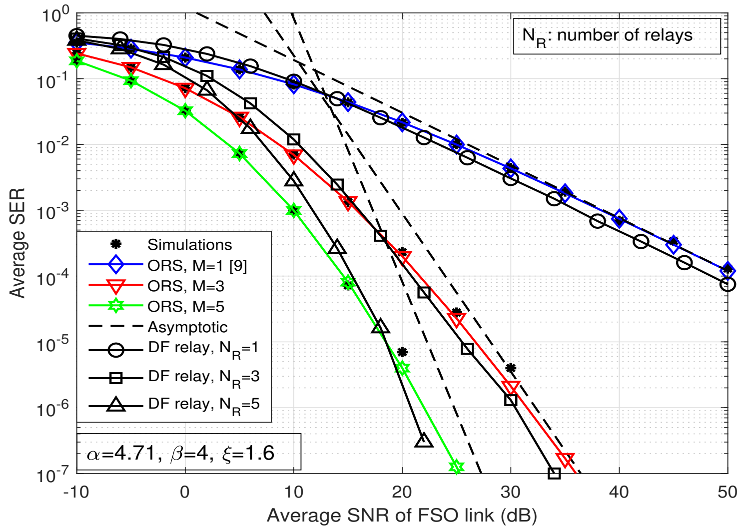

Fig. 7.3: Average SER performance under perfect CSI for different number of ORSs

$M = 1, 3, 5$ are similar to Fig. 7.2. Further, the performance of a multiple parallel relay FSO system with DF relaying protocol [135], which employs the opportunistic relay selection scheme to select the best relay, is compared with the proposed multiple ORS-assisted FSO system. Here, we plot the performance curves by varying the number of relays N_R in accordance with M. It is noticed that the ORS-assisted system is performing better than the DF relaying system, especially for the scenario when average SNR $\overline{\gamma} < 20$ dB for all three cases (i.e. $N_R = M = 1, 3,$ and 5) and the SNR gain to achieve an SER value of 10^{-2} increases with increasing value of M compared to increasing value of N_R. However, for $\overline{\gamma} > 20$ dB, the DF relaying system outperforms the ORS-assisted system with a small SNR gain. This is because, in the DF relaying system, the decoding errors are dominating in the SNR region less than 20 dB compared to the ORS-assisted system, which limits the system performance. Additionally, it can be seen from Fig. 7.2 and 7.3 that the simulation results closely coincide with the analytical results, which validates the accuracy of our derived outage and average SER expressions. Finally, the asymptotic results are closely matching with the theoretical results at the high SNR values, which also confirms the correctness of the asymptotic analysis as well as the obtained diversity gain.

In Fig. 7.4, the average SER is plotted for different modulation techniques, i.e. BPSK, QPSK, 8-PSK, and 16-PSK, by assuming $M = 3$. From the performance

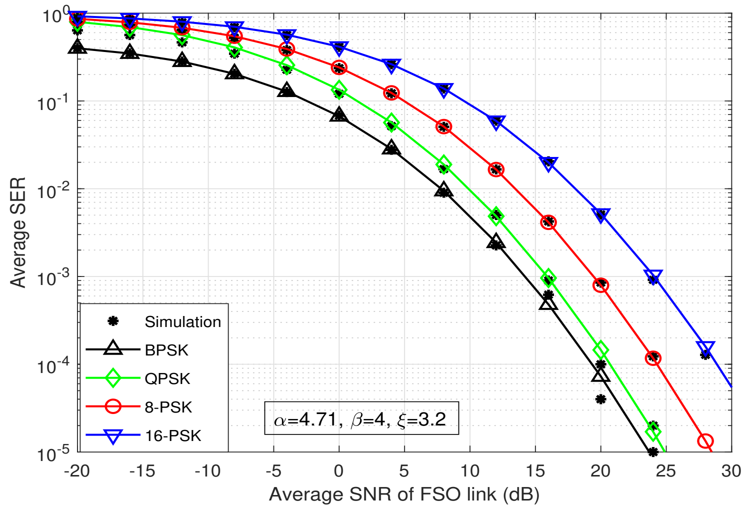

Fig. 7.4: Average SER performance under perfect CSI for different modulation techniques

plots, it is clear that the performance of the system degrades with the increasing value of modulation order $\mathcal{M}$, as expected. Additionally, for achieving the average SER value of 10^{-3}, BPSK requires an average SNR value of 14 dB. Similarly, QPSK, 8-PSK, and 16-PSK require average SNR values of 16 dB, 20 dB, and 24 dB, respectively.

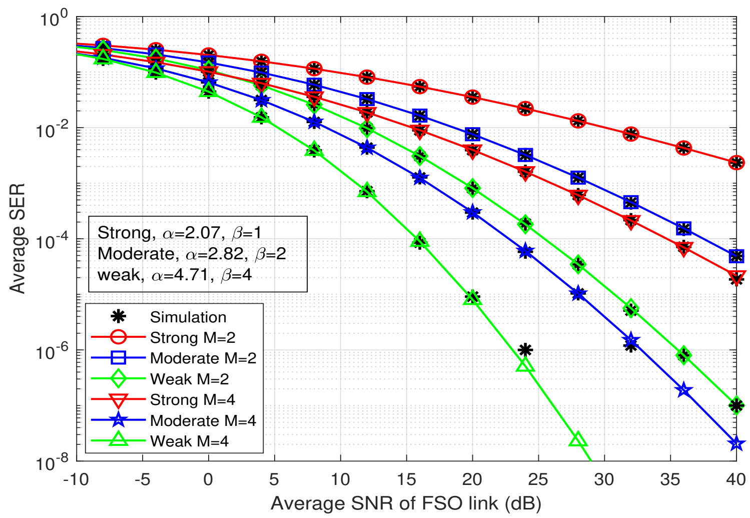

Fig. 7.5: Average SER performance under perfect CSI for various turbulence conditions

Fig. 7.5 presents the average SER performance of the proposed system with perfect CSI under various turbulence conditions. The average SER of the considered system under these turbulence conditions is also compared for both $M = 2$ and $M = 4$ cases. As expected, the performance under strong turbulence condition is poorer as compared to the moderate and weak turbulence conditions for both

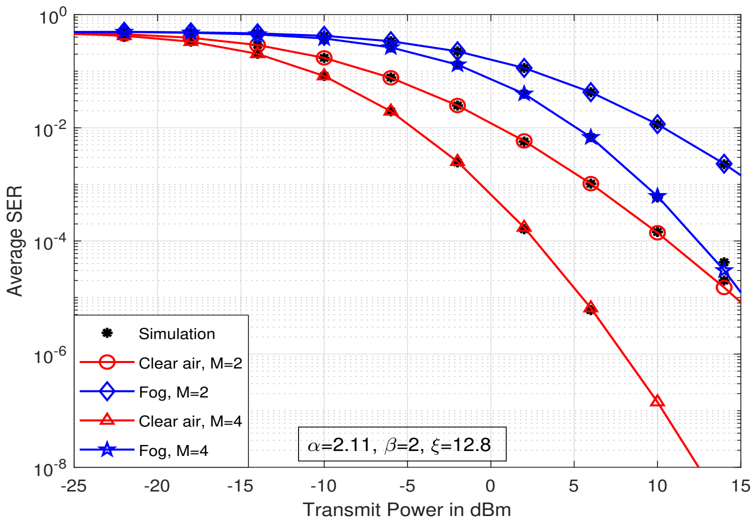

Fig. 7.6: Average SER for perfect CSI under clear air and foggy conditions

the cases. This is because, random fluctuations in the atmospheric channel under strong turbulence condition are more pronounced compared to the moderate and weak turbulence conditions. In addition, the SNR gain achieved to attain a SER of 10^{-2} by the multiple ORSs system with $M = 4$ over the system with $M = 2$ is approximately 15 dB under strong turbulence condition. Accordingly, the SNR gains obtained for $M = 4$ over $M = 2$ under moderate and weak turbulence conditions are 10 dB and 6 dB, respectively. Therefore, as M increases, it is evident from the plots that the SNR gains for strong turbulence condition are higher than the moderate and weak turbulence conditions.

Fig. 7.6 illustrates the performance of the multiple ORSs system for clear and foggy weather conditions. The average SER is plotted against the FSO transmit power in dBm. The values of the weather coefficient for clear air and fog are assumed as $\Omega_l = 0.43$ and $\Omega_l = 20$, respectively. It is noticed from the curves that the average SER of the ORS-assisted FSO system increases for foggy weather condition compared to clear air for both $M = 2$ and $M = 4$ cases. It is mainly because, the FSO channel is more susceptible to foggy conditions and as a result, the performance of the FSO system degrades in foggy conditions. Further, the SNR gain of 5 dB is noticed to attain the SER of 10^{-3} for $M = 4$ over $M = 2$ under both clear air and foggy conditions.

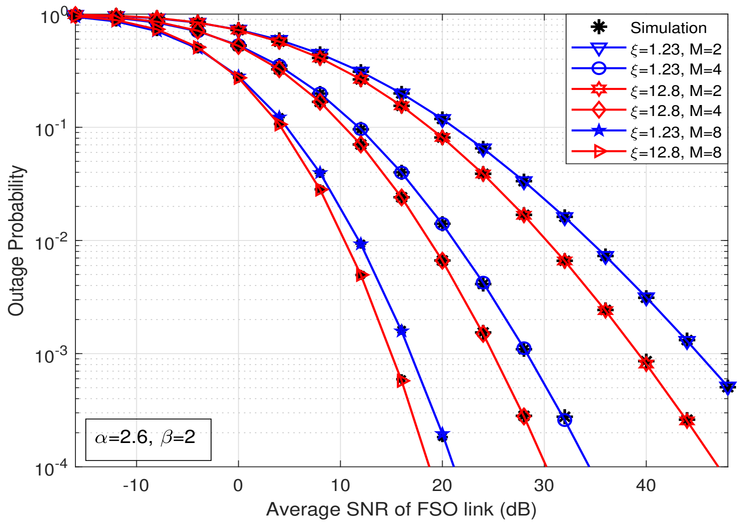

Fig. 7.7: Outage probability under perfect CSI for different pointing errors conditions

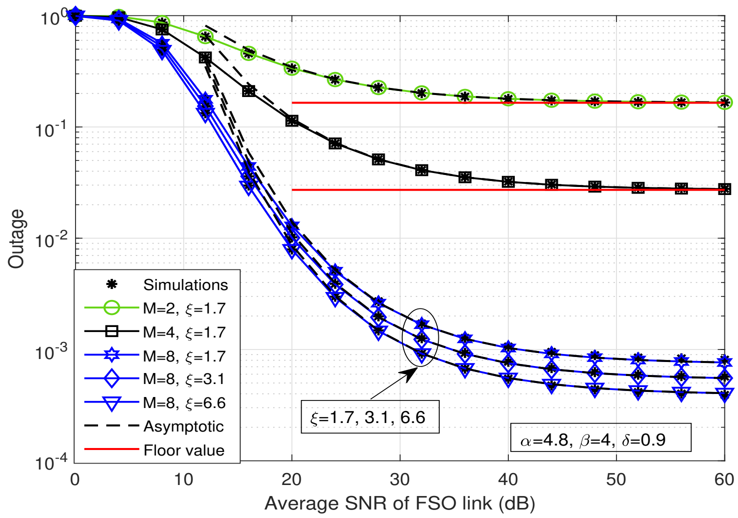

Fig. 7.8: Outage probability under imperfect CSI for various ORSs and different pointing errors

In Fig. 7.7, the outage probability of the proposed system with perfect CSI is depicted for different pointing errors scenarios by assuming $M = 2, 4$, and 8. The pointing errors parameters are assumed as $\sigma_{\theta_k} = 3$ mrad, $\sigma_{\varphi_k} = 2$ mrad, and $\xi = 1.23$ for high pointing errors case and $\sigma_{\theta_k} = 1$ mrad, $\sigma_{\varphi_k} = 0.5$ mrad, and $\xi = 12.8$ for low pointing errors case. In Fig. 7.7, as the value of ξ increases from $\xi = 1.23$ to $\xi = 12.8$, the performance of the multiple ORSs system improves in all three cases $M = 2, 4$, and 8. This is because, low values of ξ depict the higher severity of pointing errors, which deteriorate the system performance. Moreover, the SNR gains obtained by the multiple ORSs system for $\xi = 1.23$ and $\xi = 12.8$ are given in Table 7.3. It is clear from Table 7.3 that the SNR gains achieved for

Table 7.3: SNR gain comparison in Fig. 7.7

Outage Probability 10^{-2}	SNR gain	
	$\xi = 1.23$	$\xi = 12.8$
$M = 4$ over $M = 2$	14 dB	12 dB
$M = 8$ over $M = 4$	9 dB	8 dB

the high pointing errors case (i.e. $\xi = 1.23$) are higher than the low pointing errors case (i.e. $\xi = 12.8$). Similar outage performance trends are observed for imperfect CSI under different pointing error coefficients $\xi = 1.7, 3.1, \text{and } 6.6$ in Fig. 7.8. It is also observed from the plots that increasing M considerably improves the outage of the system, since the outage performance directly depends on M as given by (7.31). For instance in Fig. 7.8, at $\overline{\gamma} = 32$ dB, the outage probability value for $M = 2$ is 2.02×10^{-1}. Similarly, the outage values for $M = 4$ and 8 are 4.09×10^{-2} and 1.67×10^{-3}, respectively.

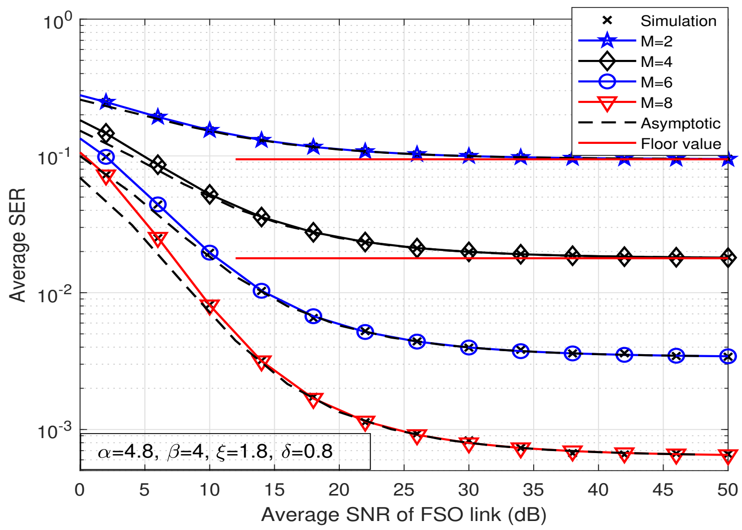

Fig. 7.9: Average SER performance under imperfect CSI for different number of ORSs

In Fig. 7.9, the average SER performance for imperfect CSI case is presented for $M = 2, 4, 6, \text{and } 8$. It is evident that by increasing M, average SER performance of the system also improves significantly. It is also noticed from the outage and average SER performances in Fig. 7.8 and 7.9 that the curves are saturated at high-SNR region and attain outage and average SER floor values equal to $P_{out}^{(I)\text{fixed}}$ and $P_{e_{\text{fixed}}}^{(I)}$ as given by (7.33) and (7.37), respectively. In addition, the asymptotic results are intently concur with the analytical results at the high-SNR region, which affirms the accuracy of the asymptotic analysis.

In Fig. 7.10, the average SER performance of the proposed system is shown for imperfect CSI case with correlation coefficient $\delta = 0.7, 0.8, 0.9$ and perfect channel case with $\delta = 1$. It is seen that the increasing values of correlation coefficient enhances the average SER performance. For example, at $\overline{\gamma} = 22$ dB, the average SER values for $\delta = 0.7, 0.8, 0.9$ are $8.6 \times 10^{-3}, 5.5 \times 10^{-3}, 2.3 \times 10^{-3}$, respectively. It is due to the fact that high value of δ implies less errors in channel estimation. Furthermore, it is evident from Fig. 7.8, 7.9, and 7.10 that the simulation results intently coincide with the analytical results, which approves our derived outage and average SER expressions for imperfect CSI case.

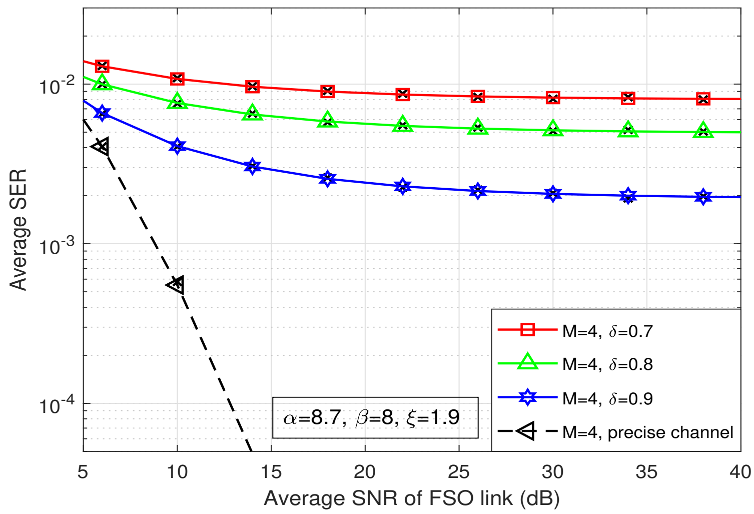

Fig. 7.10: Average SER performance under imperfect CSI for various correlation coefficients

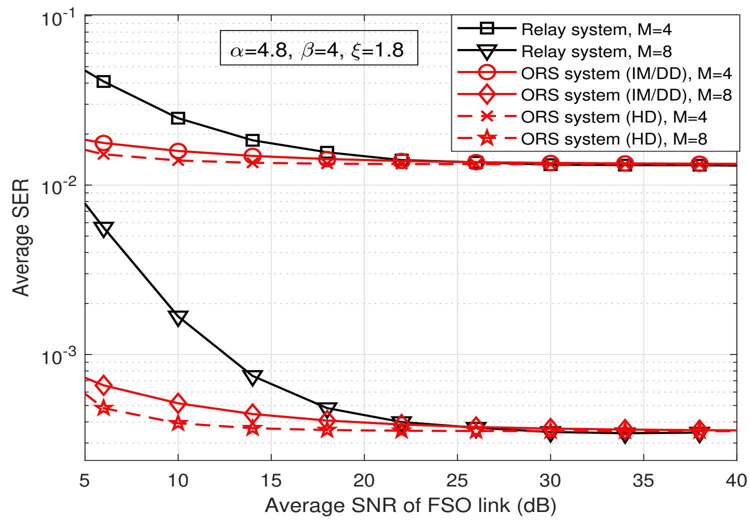

Fig. 7.11: Average SER performance under imperfect CSI for different detection techniques

In Fig. 7.11, it is observed that the multiple ORS-assisted FSO system performs better than the multiple parallel relay FSO system, which utilizes DF relaying protocol with maximum instantaneous SNR-based relay selection technique, especially in the SNR region $\overline{\gamma} < 22$ dB. Further, it can be seen that the relay-aided system achieves an average SER of 1.6×10^{-3} for $M = 8$ at $\overline{\gamma} = 10$ dB, whereas for the same SNR, the ORS-assisted system attains the average SER values of 5.1×10^{-4} and 3.9×10^{-4} under IM/DD and HD techniques, respectively. This is because, the decoding errors effect in the DF relaying system dominate compared to the cascaded channel effect in the ORS-assisted system, which is also observed in case of perfect CSI in Fig. 7.3. As a result, the performance of the system degrades.

7.7 Chapter Summary

In this chapter, the performance of a multiple ORSs-aided FSO system was examined considering a selection scheme, which selects the best ORS for transmission, assuming atmospheric turbulence, attenuation, pointing errors, and imperfect CSI conditions. Moreover, the closed-form expressions for outage probability and average SER were obtained from the derived statistical functions for both perfect and imperfect CSI cases. According to the analytical findings, it was inferred that the errors due to imperfect CSI significantly impacts the system performance and the performance of the proposed system improves with the usage of more number of reflecting surfaces. Finally, multiple ORSs-aided FSO system outperformed multiple DF-relaying based FSO system under both perfect and imperfect CSI scenarios.

Chapter 8

Conclusions and Future Work

8.1 Concluding Remarks

The purpose of this thesis is to investigate the techniques for improving the reliability and performance of FSO communication system. Several system models, including hard-switching-based hybrid FSO/RF system, MRC-based and adaptive combining-based hybrid FSO/RF systems, ORS-assisted OSSK-based MIMO-FSO system, and multiple ORSs-aided FSO systems were studied to demonstrate substantial performance enhancements over single-link FSO systems. The key concluding remarks of the thesis are outlined as follows.

- In Chapter 3, a comprehensive performance analysis of hybrid FSO/RF system was presented by assuming a single-threshold-based hard-switching scheme over the most generalized fading channel models, i.e. Malaga distribution for modeling FSO link and α-η-κ-μ distribution for modeling RF link. The asymptotic expressions, which are easily tractable, were derived for outage probability, average SER, and ergodic capacity and based on the asymptotic expressions, the diversity gain and coding gain were determined for different scenarios. In addition, the condition for obtaining full diversity gain from both the FSO and RF links was also discussed. The performance plots of other well-known FSO and RF distributions, which can be used in different applications/

scenarios, were obtained as special cases of these generalized distributions. We also obtained the optimum switching threshold SNR and beam waist values, which minimize the average SER and outage probability as well as maximize the ergodic capacity, using numerical optimization technique. Further, the impact of zenith angle and wind velocity on the performance of hybrid FSO/RF satellite communication system was also investigated. It is concluded that the hybrid FSO/RF system performs better than the FSO-based SSC and single-link FSO systems and better coding gain is obtained for the scenarios with high pointing errors, strong turbulence, longer link distance, high attenuation, high zenith angle, and high wind speed due to higher probability of usage of backup RF link.

- In Chapter 4, the novel closed-form expressions for the PDF and CDF of the MRC of FSO and RF links were derived over the generalized fading models, namely Malaga and α-η-κ-μ distributions, respectively. With the aid of the obtained statistical functions, the unified closed-form expressions for the performance metrics such as outage probability and average SER for MRC-based and adaptive-combining-based hybrid FSO/RF systems were derived considering non-zero boresight pointing errors. From the simpler asymptotic expressions, diversity gains of MRC-based and adaptive-combining-based hybrid systems were determined for various cases and the conditions to obtain full diversity gain from both the hybrid systems were also reported. We also obtained the optimal performance of adaptive combining scheme by determining optimum switching threshold SNR and beam waist values. Further, it was inferred that the average SER of adaptive-combining-based hybrid system operating at the optimum switching threshold SNR value γ_T^{opt} was equal to the average SER of the MRC-based hybrid system. From the numerical analysis, it was observed that the hybrid system with MRC and adaptive combining schemes perform better than the single-link FSO system and hybrid system with the single-threshold-based hard-switching scheme.

- In Chapter 5, the ergodic capacity performance of the hybrid FSO/RF system was analyzed by utilizing the adaptive-combining-based switching scheme over the generalized Malaga and κ–μ distributions. Specifically, the unified closed-form expression for the ergodic capacity was derived in terms of extended generalized bivariate Meijer G-function and bivariate Fox's H- function, which embraces various FSO and RF channel distributions as well as two types of FSO detection techniques (i.e. IM/DD and HD). Apart from modeling atmospheric turbulence using the generalized Malaga distribution, the non-zero boresight pointing errors and path loss have been taken into consideration for modeling the combined FSO channel. Moreover, the analytical expression for computing the optimum transmit beamwidth was derived and also validated using numerical optimization technique. Numerical results revealed that the adaptive-combining-based hybrid FSO/RF system performs better in terms of normalized ergodic capacity than the single-link FSO system under various channel conditions. In addition, it was also observed that the ergodic capacity performance (in terms of Gbps) of the adaptive-combining-based hybrid FSO/RF system is also better than the MRC-based and hard-switching-based hybrid FSO/RF systems. Finally, it can be concluded that the RF backup link in hybrid FSO/RF systems, i.e., hard-switching-based and adaptive-combining-based helps in improving the reliability of FSO communication to a larger extent by compromising on the ergodic capacity in the low-SNR region to a smaller extent.

- In Chapter 6, an ORS-assisted OSSK-based MIMO-FSO system was proposed with an aim of mitigating the blockage in OSSK-based MIMO FSO systems. Specifically, the average PEP, the upper bound on average BER, and lower bound on ergodic capacity were evaluated over Malaga distributed turbulence along with pointing errors. Further, the asymptotic expressions for average BER and ergodic capacity were derived and diversity gain of the proposed system was also obtained. The numerical results showed that the average

BER and ergodic capacity performances were significantly improved as N_r increases and the maximum capacity achieved was $\log_2 N_t$. It was also confirmed from the analytical results that the effect of turbulence and pointing errors on the performance of the proposed system was not very significant, unlike the conventional FSO system, due to the usage of the OSSK scheme. Since ORS is assumed to be equivalent to a reflecting mirror which redirects the incident optical signal to the destination receiver with non-reconfigurable surfaces, the performance is almost similar or slightly better than the system without ORS. This alleviates the requirement of LoS transmission for the OSSK-based MIMO-FSO system and the proposed system also emerged as a better alternative to the DF relaying system.

- In Chapter 7, the performance of a multiple ORSs-assisted FSO system, which is based on the selection of the best ORS from M number of available ORSs, was investigated. The main purpose of introducing the selection of ORS in the FSO system is to minimize the LOS blockage in the FSO channel as well as to improve the performance compared to the existing single ORS-assisted FSO system (i.e. $M = 1$). Firstly, the end-to-end channel statistics were obtained for both perfect and imperfect CSI cases by including the factors such as atmospheric turbulence, pointing errors, and atmospheric attenuation in the FSO channel model. With the aid of the above-derived statistics, the unified exact closed-form expressions for the outage probability and average SER were obtained for two cases, i.e. perfect CSI and imperfect CSI. Furthermore, an asymptotic analysis, which is mathematically more tractable, was presented and the diversity gain of the multiple ORSs-assisted FSO system was determined. From the analytical results, it was clear that the performance of the proposed system improves with increasing the number of reflecting surfaces M and higher SNR gains were obtained under unfavourable conditions such as strong turbulence, high pointing errors, and foggy weather.

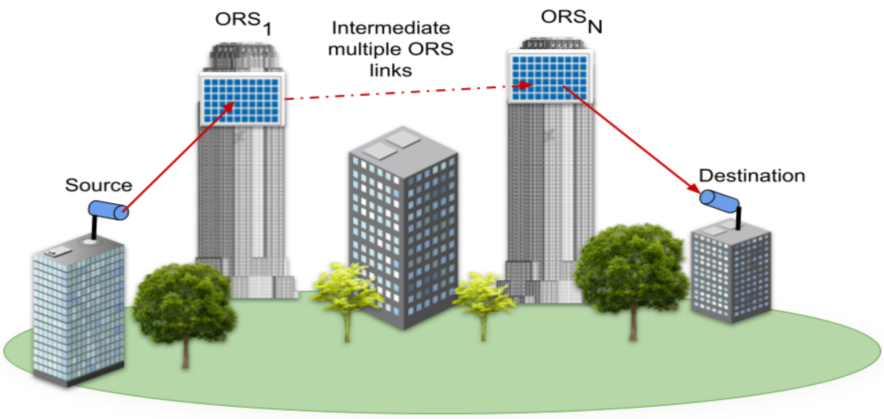

Fig. 8.1: Multiple ORSs-assisted FSO system model

8.2 Future Research Scope

There are several potential directions for expanding the scope of this thesis and improving the reliability, performance, and applicability of FSO communication systems. The following are some suggested avenues for further research on the FSO systems:

- In this thesis, the multiple ORSs-assisted FSO system was analyzed by considering a single reflecting element in each ORS. Further, to improve the SNR of the overall system, multiple elements can be included in each ORS. Therefore, as a part of our future work, a multiple ORSs-assisted FSO system model will be proposed with arbitrary number of reflecting elements in ORSs as depicted in Fig. 8.1. Further, its performance will be analyzed by incorporating the turbulence, pointing errors, and weather attenuation. In addition, the effects of imperfect CSI and imperfect phase compensation of ORS on the multiple ORSs-assisted FSO system will also be considered for more practical scenario.
- In prior works, the RIS-assisted hybrid FSO/RF system was studied based on hard-switching scheme only. In this regard, the RIS-assisted hybrid FSO/RF system can be explored with novel switching schemes such as SSC, SEC, and adaptive combining, which can provide better performance. The spatial modulation techniques such as OSSK and OSM, which provide higher spectral

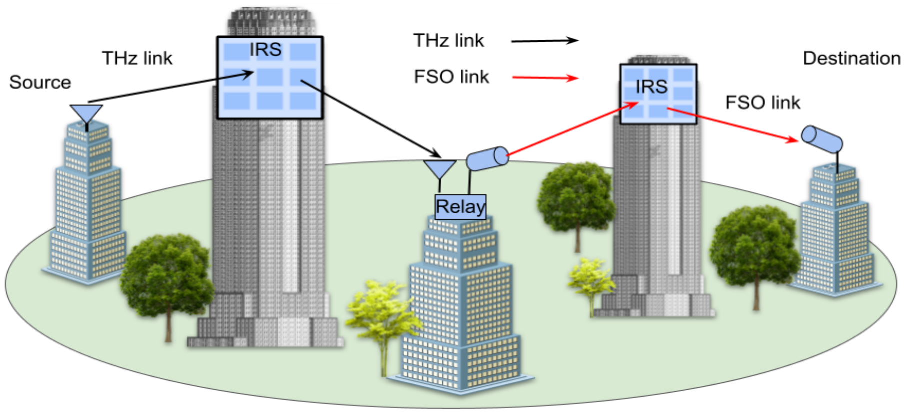

Fig. 8.2: RIS-assisted Mixed FSO/THz system

efficiency, can also be considered for the proposed RIS-assisted hybrid system. Moreover, the performance of the proposed RIS-assisted hybrid FSO/RF system can be investigated in terms of various performance metrics.

- The combination of RIS-assisted FSO and RIS-assisted RF subsystems can be further extended to various scenarios such as relay-based RIS-assisted mixed FSO/RF system, SC-based hybrid FSO/RF, and MRC-based hybrid FSO/RF. Additionally, different statistics based on the instantaneous SNRs of FSO and RF links can be obtained to analyze the performance of the proposed system models for the RIS-assisted FSO/RF system.

- The millimeter (mmWave) frequencies have been introduced in 5G communications with the aim of providing high data rates. However, the upcoming 6G technology will push the frequency band to the terahertz range, which is between 0.1 THz and 10 THz, aiming to meet higher demands for bandwidth and data rates. In this regard, Terahertz (THz) communication assisted by FSO will be the new frontier for meeting the demands of next-generation wireless communications. Therefore, a backhaul network enabled with hybrid FSO/THz communication will be considered assuming hard-switching and adaptive combining switching schemes and its system performance will be analyzed.

- Both FSO and THz communications experience significant interference when there are obstructions in the LOS path. In such situations, the use of RIS with the FSO and THz communication can provide an alternate path for its data transmission Therefore, a RIS-assisted mixed THz/FSO system as shown in Fig. 8.2 will also be proposed to enhance the coverage and reliability, while delivering high data rates and extensive bandwidth. In addition, the exact and asymptotic bounds of the performance metrics, including outage, average SER, and capacity, will be derived for the proposed mixed system.

Appendices

Appendix A

Expressions for α and β

The expressions for large scale and small scale turbulence parameters, α and β, in case of terrestrial communication are, respectively, given by [168, eq. (2)]

$$\alpha = \left[\exp\left(0.49\chi^2\left(1+0.56\chi^{12/5}\right)^{-7/6}\right)-1\right]^{-1},$$
$$\beta = \left[\exp\left(0.51\chi^2\left(1+0.69\chi^{12/5}\right)^{-5/6}\right)-1\right]^{-1}, \tag{A.1}$$

where $\chi^2 = 0.5C_n^2 k_n^{7/6} L^{11/6}$ is the Rytov variance for terrestrial communication. For satellite communication scenario, the parameters α and β depend on the satellite height 'H', which is above the ground level [76]. Additionally, the refractive index parameter $C_n^2(h)$ is defined in terms of altitude h and wind speed v_S as [76, eq. (9)]

$$C_n^2(h) = 0.00594(v_s/27)^2(10^{-5}h)^{10}\exp(-h/1000) + 2.7\times10^{-16}\exp(-h/1500)$$
$$+ 1.7\times10^{-14}\exp(-h/100). \tag{A.2}$$

It is to be noted that the modeling of turbulence parameters α and β are different for uplink and downlink scenarios. The large scale turbulence parameter α includes the beam-wander-induced pointing errors for uplink case, as the turbulent eddy size is larger than the transmitter beam size. The expressions for α and β for uplink case are, respectively, given by [76, eq. (7a, 7b)]

$$\alpha = \left[5.95(H-h_0)^2 \sec^2(\theta_Z) \left(\frac{2W_0}{r_0}\right)^{5/3} \left(\frac{\Delta_{pe}}{W_p}\right)^2 + \exp\left(\frac{0.49\sigma_{UL}^2}{\left(1+0.56\sigma_{UL}^{12/5}\right)^{-7/6}} \right) - 1 \right]^{-1},$$

$$\beta = \left[\exp\left(\frac{0.51\sigma_{UL}^2}{\left(1+0.69\sigma_{UL}^{12/5}\right)^{-5/6}} \right) - 1 \right]^{-1}, \qquad (A.3)$$

where W_0 is the laser beam size at the transmitter, h_0 is the ground station aperture height, θ_Z denotes the zenith angle, $W_p = W_0 \sqrt{\left(1 - \frac{L_s}{F_0}\right)^2 + \frac{4L_s^2}{k_n^2 W_0^4}}$ is the received laser beam size. Here, F_0 denotes the curvature radius of the phase front at the transmitter. Further, r_0 denotes the fried parameter and expression for the same is given by

$$r_0 = \left[0.42 \sec(\theta_Z) k_n^2 \int_{h_0}^{H} C_n^2(h) dh \right]^{-\frac{3}{5}}. \qquad (A.4)$$

In (A.3), $\Delta_{pe} = \sigma_{pe}/L_s$ represents the beam-wander-induced pointing errors parameter, σ_{pe}^2 denotes the variance of beam-wander-induced pointing errors, $L_s = \frac{H-h_0}{\cos(\theta_Z)}$ is the propagation distance between satellite and ground station in meters, and σ_{UL}^2 is the Rytov variance for uplink scenario. Moreover, the expressions for σ_{UL}^2 and σ_{pe}^2 are, respectively, given by

$$\sigma_{UL}^2 = 2.25\, k_n^{\frac{7}{6}} (H-h_0)^{\frac{5}{6}} \sec^{\frac{11}{6}}(\theta_Z) \int_{h_0}^{H} C_n^2(h) \left(1 - \frac{h-h_0}{H-h_0}\right)^{\frac{5}{6}} \left(\frac{h-h_0}{H-h_0}\right)^{\frac{5}{6}} dh, \qquad (A.5)$$

$$\sigma_{pe}^2 = 0.54(H-h_0)^2 \sec^2(\theta_Z) \left(\frac{\lambda_f}{2W_0}\right)^2 \left(\frac{2W_0}{r_0}\right)^{5/3} \left[1 - \left(\frac{4\pi^2 (W_0)^2/r_0^2}{1+4\pi^2 (W_0)^2/r_0^2} \right)^{\frac{1}{6}} \right]. \qquad (A.6)$$

The effect of beam-wander-induced pointing errors is neglected in case of downlink scenario, as the beam size when reaches the atmosphere is much larger than the turbulent eddy size. So the turbulence parameters, α and β, for downlink scenario are, respectively, expressed as [207, eq.(6, 7)]

$$\alpha = \left[\exp\left(0.49\sigma_{DL}^2\left(1+1.11\sigma_{DL}^{12/5}\right)^{-7/6}\right)-1\right]^{-1},$$
$$\beta = \left[\exp\left(0.51\sigma_{DL}^2\left(1+0.69\sigma_{DL}^{12/5}\right)^{-5/6}\right)-1\right]^{-1}, \tag{A.7}$$

where σ_{DL}^2 denotes the Rytov variance for downlink scenario and is defined as

$$\sigma_{DL}^2 = 2.25k_n^{\frac{7}{6}}\sec^{\frac{11}{6}}(\theta_Z)\int_{h_0}^{H} C_n^2(h)(h-h_0)^{\frac{5}{6}}dh. \tag{A.8}$$

Appendix B

B.1 Convergence Test for $f_{\gamma_{RF}}(\gamma)$

In this section, a Cauchy ratio test is performed on the infinite series given in (4.21), which is the PDF $f_{\gamma_{RF}}(\gamma)$, to test its convergence. According to the Cauchy ratio test, $\sum_{l=0}^{\infty} x_l$ is said to be absolutely convergent, if it satisfies the condition given below [186, eq. (0.222)]

$$\lim_{l\to\infty}\left|\frac{x_{l+1}}{x_l}\right| < 1, \tag{B.1}$$

For the infinite series given in (4.21), the power series coefficient is obtained in the form of a summation as

$$x_l = \sum_{m=0}^{l} \frac{c_l(-l)_m \gamma^{\tilde{\alpha}(\mu+m)-1} \exp\left(-\gamma^{\tilde{\alpha}}/2\overline{\gamma}_{RF}^{\tilde{\alpha}}\right)}{m!\Gamma(\mu+m)2^{\mu-m}\overline{\gamma}_{RF}^{\tilde{\alpha}(\mu+m)}}. \tag{B.2}$$

Now, the series coefficient can be further simplified by assuming $m = l$, which is the last term of the series, and is given by

$$\hat{x}_l = \frac{c_l(-1)^l \gamma^{\tilde{\alpha}(\mu+l)-1} \exp\left(-\frac{\gamma^{\tilde{\alpha}}}{2\overline{\gamma}_{RF}^{\tilde{\alpha}}}\right)}{\Gamma(\mu+l)2^{\mu-l}\overline{\gamma}_{RF}^{\tilde{\alpha}(\mu+l)}} \tag{B.3}$$

Further, by using (B.3) and (B.1), the ratio of series coefficients can be written as

$$\left|\frac{\hat{x}_{l+1}}{\hat{x}_l}\right| = \left|\frac{\frac{c_{l+1}(-1)^{l+1}\gamma^{\tilde{\alpha}(\mu+l+1)-1}\exp\left(-\frac{\gamma^{\tilde{\alpha}}}{2\overline{\gamma}_{RF}^{\tilde{\alpha}}}\right)}{\Gamma(\mu+l+1)2^{\mu-l-1}\overline{\gamma}_{RF}^{\tilde{\alpha}(\mu+l+1)}}}{\frac{c_l(-1)^l\gamma^{\tilde{\alpha}(\mu+l)-1}\exp\left(-\frac{\gamma^{\tilde{\alpha}}}{2\overline{\gamma}_{RF}^{\tilde{\alpha}}}\right)}{\Gamma(\mu+l)2^{\mu-l}\overline{\gamma}_{RF}^{\tilde{\alpha}(\mu+l)}}}\right| \tag{B.4}$$

$$\left|\frac{\hat{x}_{l+1}}{\hat{x}_l}\right| = \mathcal{A}_1\frac{2}{\mu+l}\left(\frac{\gamma}{\overline{\gamma}_{RF}}\right)^{\tilde{\alpha}} \tag{B.5}$$

where $\mathcal{A}_1 = \frac{c_{l+1}}{c_l}$ is a decreasing function with respect to l [165, eq. (15)], [165, eq. (31)] and it tends to zero for $l \to \infty$. It can be clearly seen that for a finite value of γ and $\overline{\gamma}_{RF}$, (B.5) will be tending to zero by applying the limit $l \to \infty$. This eventually shows that the condition given in (B.5) is satisfied. Therefore, it can be inferred that the PDF $f_{\gamma_{RF}}(\gamma)$, which is given by (4.21) with an infinite series is absolutely convergent.

B.2 Convergence Test for $f_{\gamma_{MRC}}(\gamma)$

The convergence test for $f_{\gamma_{MRC}}(\gamma)$ can be initiated similar to the Cauchy ratio test performed for $f_{\gamma_{RF}}(\gamma)$. From (4.25), the power series coefficient can be obtained as

$$\begin{aligned} y_{l,i} = {} & C_2\frac{(-1)^l c_l(-1)^i\Gamma(\tilde{\alpha}(\mu+l+i))}{l!\Gamma(\mu+l)2^{\mu-l+i}i!\overline{\gamma}_{RF}^{\tilde{\alpha}(\mu+l+i)}}\gamma^{\tilde{\alpha}(\mu+l+i)-1} \\ & \times\sum_{d=1}^{\beta} t_d G_{p+1\ 3p+1}^{3p\ \ \ 1}\left(B_2\gamma\left|\begin{matrix}1, \mathcal{K}_1 \\ \mathcal{K}_2, 1-\tilde{\alpha}(\mu+l+i)\end{matrix}\right.\right) \end{aligned} \tag{B.6}$$

Since there are two infinite power series in (4.25), the coefficient in (B.6) depends on two variables (i.e. l and i). The condition for the convergence of (4.25) is given by

$$\lim_{l\to\infty, i\to\infty} \left| \frac{y_{l+1,i+1}}{y_{l,i}} \right| < 1, \tag{B.7}$$

Further, the ratio of the series coefficients is given by

$$\left| \frac{\hat{y}_{l+1,i+1}}{\hat{y}_{l,i}} \right| = \left| \mathcal{A}_2 \left(\frac{\gamma}{\gamma_{RF}} \right)^{2\tilde{\alpha}} \left[\frac{\tilde{\alpha}+1}{l\,i} + \frac{1}{i} + \frac{1}{l} \right] \right| \tag{B.8}$$

where $\mathcal{A}_2 = \frac{c_{l+1} \sum_{d=1}^{\beta} t_d G\,{}^{3p\quad 1}_{p+1\ 3p+1}\left(B_2\gamma \middle| {}^{1,\mathcal{K}_1}_{\mathcal{K}_2, 1-\tilde{\alpha}(\mu+l+i+2)} \right)}{c_l \sum_{d=1}^{\beta} t_d G\,{}^{3p\quad 1}_{p+1\ 3p+1}\left(B_2\gamma \middle| {}^{1,\mathcal{K}_1}_{\mathcal{K}_2, 1-\tilde{\alpha}(\mu+l+i)} \right)}$ is a constant for all l and i. By applying the limits $l \to \infty$ and $i \to \infty$, the expression in (B.8) will be tending to zero, which satisfies the condition given in (B.7). Hence, it is clear that the PDF $f_{\gamma_{MRC}}(\gamma)$, which is given by (4.25), is also absolutely convergent.

Appendix C

C.1 Proof of Theorem 6.1

We assume $U_{kij} = |Z_{kij}|$, where $Z_{kij} = h_{ki} - h_{kj}$. Utilizing [132, eq. (9)], the PDF of Z_{kij} is given by

$$f_{Z_{kij}}(z) = \int_0^\infty f_{h_{ki}}(z+x) f_{h_{kj}}(x) dx. \tag{C.1}$$

Substituting $f_{h_{ki}}(\cdot)$ and $f_{h_{kj}}(\cdot)$ from (6.14) in (C.1) and employing [208, eq. (2.24.1.3)], we get the PDF $f_{Z_{kij}}(z)$ as

$$f_{Z_{kij}}(z) = \frac{(A_1 A_2 \zeta)^2 B_1 B_2}{16 A_0 h_\ell} \sum_{p=1}^{\beta_1} \sum_{q=1}^{\beta_2} \sum_{r=1}^{\beta_1} \sum_{s=1}^{\beta_2} b_p^{(1)} b_q^{(2)} b_r^{(1)} b_s^{(2)} \sum_{n=0}^{\infty} \left(\frac{-B_1 B_2}{A_0 h_\ell} \right)^n \frac{z^n}{n!} G_{7\,7}^{5\,6} \left(1 \middle| \begin{matrix} \mathcal{N}_3 \\ \mathcal{N}_4 \end{matrix} \right), \tag{C.2}$$

where $\mathcal{N}_3 = [0, n-\zeta+1, n-\alpha_2+1, n-q+1, n-\alpha_1+1, n-p+1, \zeta]$ and $\mathcal{N}_4 = [\zeta-1, \alpha_2-1, s-1, \alpha_1-1, r-1, n-\zeta, n]$. Therefore, the PDF of U_{kij} can be written as [132]

$$f_{U_{kij}}(u) = 2 f_{Z_{kij}}(u). \tag{C.3}$$

Further, by substituting (C.2) in (C.3), the final expression for $f_{U_{kij}}(u)$ is obtained as (6.17).

C.2 Proof of Theorem 6.2

The PDF of the instantaneous SNR of k^{th} FSO link $\gamma_{kij} = U_{kij}^2 \overline{\gamma}_{FSO}$ is written in terms of PDF of Z_{kij} as

$$f_{\gamma_{kij}}(\gamma) = \frac{1}{\sqrt{\gamma \overline{\gamma}_{FSO}}} f_{Z_{kij}} \left(\sqrt{\frac{\gamma}{\overline{\gamma}_{FSO}}} \right). \tag{C.4}$$

Substituting $f_{Z_{kij}}(\cdot)$ from (C.2) in (C.4), we get the PDF of γ_{kij} as

$$\begin{aligned} f_{\gamma_{kij}}(\gamma) = &\frac{(A_1 A_2 \zeta)^2 B_1 B_2}{16 A_0 h_\ell} \sum_{p=1}^{\beta_1} \sum_{q=1}^{\beta_2} \sum_{r=1}^{\beta_1} \sum_{s=1}^{\beta_2} b_p^{(1)} b_q^{(2)} b_r^{(1)} b_s^{(2)} \\ &\times \sum_{n=0}^{\infty} \left(\frac{-B_1 B_2}{A_0 h_\ell} \right)^n \frac{\gamma^{\frac{n-1}{2}}}{n! \overline{\gamma}_{FSO}^{\frac{n+1}{2}}} G_{7\,7}^{5\,6} \left(1 \middle| \begin{matrix} \mathcal{N}_3 \\ \mathcal{N}_4 \end{matrix} \right) \end{aligned} \tag{C.5}$$

Further, to calculate the PDF of overall instantaneous SNR, which is given as $\gamma_{ij} = \overline{\gamma}_{FSO} \sum_{k=1}^{N_r} U_{kij}^2 = \sum_{k=1}^{N_r} \gamma_{kij}$, we use MGF-based approach. The MGF of the γ_{ij} is given by

$$\Psi_{\gamma_{ij}}(-t) = \prod_{k=1}^{N_r} \Psi_{\gamma_{kij}}(-t), \tag{C.6}$$

where $\Psi_{\gamma_{kij}}(-t)$ is the MGF of γ_{kij} and is calculated as

$$\Psi_{\gamma_{kij}}(-t) = \sum_{n=0}^{\infty} C_n t^{-\frac{n+1}{2}}, \tag{C.7}$$

where

$$C_n = \frac{(A_1 A_2 \zeta)^2 B_1 B_2}{16 A_0 h_\ell} \sum_{p=1}^{\beta_1} \sum_{q=1}^{\beta_2} \sum_{r=1}^{\beta_1} \sum_{s=1}^{\beta_2} b_p^{(1)} b_q^{(2)} b_r^{(1)} b_s^{(2)} \left(\frac{-B_1 B_2}{A_0 h_\ell} \right)^n \frac{\Gamma\left(\frac{n+1}{2}\right)}{n! \overline{\gamma}_{FSO}^{\frac{n+1}{2}}} G_{7\,7}^{5\,6} \left(1 \middle| \begin{matrix} \mathcal{N}_3 \\ \mathcal{N}_4 \end{matrix} \right)$$

Substituting (C.7) in (C.6) and utilizing [186, eq. (0.314)], we can write $\Psi_{\gamma_{ij}}(-t)$ as

$$\Psi_{\gamma_{ij}}(-t) = \sum_{n=0}^{\infty} D_n t^{-\frac{n+N_r}{2}}, \tag{C.8}$$

where $D_0 = C_0^{N_r}$ and $D_u = \frac{1}{uC_0}\sum_{m=1}^{u}(mN_r - u + m)C_m D_{u-m}$. Further, by taking the inverse Laplace transform of $\Psi_{\gamma_{ij}}(-t)$, the PDF of γ_{ij} can be obtained as (6.18).

Appendix D

Proof of Theorem 7.1

From (7.9), let us assume $\tilde{h}_k = \rho_1 + \rho_2$ as the sum of two independent random variables, where $\rho_1 = \delta h_k$ and $\rho_2 = \sqrt{1-\delta^2}\epsilon$. Furthermore, the PDF of E is given by

$$f_{\rho_2}(y) = K_1 \exp\left(-K_2 y^2\right) \,, \tag{D.1}$$

where $K_1 = \frac{1}{\sqrt{2\pi(1-\delta^2)\sigma_e^2}}$ and $K_2 = \frac{1}{2(1-\delta^2)\sigma_e^2}$. Using the convolution theorem, we can write the PDF of $\tilde{I}_j$ as

$$f_{\tilde{h_k}}(t) = \int_0^\infty f_{\rho_1}(x) f_{\rho_2}(t-x) dx \,, \tag{D.2}$$

where $f_{\rho_1}(x) = \frac{1}{\delta} f_{h_k}\left(\frac{x}{\delta}\right)$. By substituting (D.1) in (D.2) and after writing the exponential function in (D.1) in terms of Meijer G-function using [187, 07.34.03.0228.01], we get the following integral

$$\begin{aligned} f_{\tilde{h_k}}(t) &= B_k K_1 \exp\left(-K_2 t^2\right) \sum_{n=0}^{\infty} \frac{(2K_2)^n}{n!} t^n \\ &\times \int_0^\infty x^{n-1} G^{5\,0}_{1\,5}\left(\frac{D_k}{\delta} x \,\middle|\, \begin{matrix} \rho_j + 1 \\ \mathcal{C}_{2k} \end{matrix} \right) G^{1\,0}_{0\,1}\left(K_2 x^2 \,\middle|\, \begin{matrix} - \\ 0 \end{matrix} \right) dx \end{aligned} \tag{D.3}$$

Finally, by utilizing [187, 07.34.21.0013.01], the above integral is evaluated as

$$f_{\tilde{h_k}}(t) = \frac{B_k K_1}{\pi^2} \exp\left(-K_2 t^2\right) \sum_{n=0}^{\infty} \frac{2^{P_1} K_2^{\frac{n}{2}}}{n!} G_{1k} t^n \tag{D.4}$$

It can be observed from (7.9) that $\epsilon \in \mathcal{R}$. However, in case of a practical channel, the channel gain values are positive. Therefore, by assuming the negative channel values as zero [109], the PDF $f_{\tilde{h_k}}(t)$ can be rewritten as (7.10), where $I_0^{(k)} = \int_0^\infty f_{\tilde{h_k}}(t)dt$. After substituting (D.4) in place of $f_{\tilde{h_k}}(t)$ and using [186, eq. (3.381.4)], we get $I_0^{(k)}$ as (7.11).

References

[1] D. Killinger. Free space optics for laser communication through the air. *Optics and Photonics News*, 13(10):36–42, 2002.

[2] D. K. Borah, A. C. Boucouvalas, C. C Davis, S. Hranilovic, and Konstantinos Yiannopoulos. A review of communication-oriented optical wireless systems. *EURASIP Journal on Wireless Communications and Networking*, 2012:1–28, 2012.

[3] S. A. Al-Gailani, M. F. Mohd Salleh, A. A. Salem, R. Q. Shaddad, U. U. Sheikh, N. A. Algeelani, and T. A. Almohamad. A survey of free space optics (FSO) communication systems, links, and networks. *IEEE Access*, 9:7353–7373, 2021.

[4] A. K. Majumdar and J. C. Ricklin. *Free-space laser communications: principles and advances*, volume 2. Springer Science & Business Media, 2010.

[5] H. E. Nistazakis, T. A. Tsiftsis, and G. S. Tombras. Performance analysis of free-space optical communication systems over atmospheric turbulence channels. *IET communications*, 3(8):1402–1409, 2009.

[6] I. Alimi, A. Shahpari, A. Sousa, R. Ferreira, P. Monteiro, and A. Teixeira. Challenges and opportunities of optical wireless communication technologies. *Optical Communication Technology*, 10, 2017.

[7] I. Takai, T. Harada, M. Andoh, K. Yasutomi, K.and Kagawa, and S. Kawahito.

Optical vehicle-to-vehicle communication system using led transmitter and camera receiver. *IEEE Photonics Journal*, 6(5):1–14, 2014.

[8] L. Grobe, A. Paraskevopoulos, J. Hilt, D. Schulz, F. Lassak, F.and Hartlieb, C. Kottke, V. Jungnickel, and K.-D. Langer. High-speed visible light communication systems. *IEEE Communications Magazine*, 51(12):60–66, 2013.

[9] D. Kedar and S. Arnon. Urban optical wireless communication networks: the main challenges and possible solutions. *IEEE Communications Magazine*, 42(5):S2–S7, 2004.

[10] S. Arnon, J. Barry, G. Karagiannidis, R. Schober, and M. Uysal. *Advanced optical wireless communication systems*. Cambridge University Press, 2012.

[11] M. Khalighi and M. Uysal. Survey on free space optical communication: A communication theory perspective. *IEEE Communications Surveys & Tutorials*, 16(4):2231–2258, 2014.

[12] T. Koonen. Indoor optical wireless systems: technology, trends, and applications. *Journal of Lightwave Technology*, 36(8):1459–1467, 2017.

[13] Z. Xu and B. M. Sadler. Ultraviolet communications: potential and state-of-the-art. *IEEE Communications Magazine*, 46(5):67–73, 2008.

[14] H. Kaushal and G. Kaddoum. Optical communication in space: Challenges and mitigation techniques. *IEEE Communications Surveys & Tutorials*, 19(1):57–96, 2017.

[15] H. Elgala, R. Mesleh, and H. Haas. Indoor optical wireless communication: potential and state-of-the-art. *IEEE Communications Magazine*, 49(9):56–62, 2011.

[16] T. S. Rappaport *et al.* . Wireless communications and applications above 100 GHz: Opportunities and challenges for 6G and beyond. *IEEE Access*, 7:78729–78757, 2019.

[17] A. S. Hamza, J. S. Deogun, and D. R. Alexander. Classification framework for free space optical communication links and systems. *IEEE Communications Surveys & Tutorials*, 21(2):1346–1382, 2019.

[18] S. Arnon. Effects of atmospheric turbulence and building sway on optical wireless-communication systems. *Optics Letters*, 28(2):129–131, 2003.

[19] F. Dios, J. A. Rubio, A. Rodríguez, and A. Comeron. Scintillation and beam-wander analysis in an optical ground station-satellite uplink. *Applied Optics*, 43(19):3866–3873, 2004.

[20] D. K. Borah and D. G. Voelz. Pointing error effects on free-space optical communication links in the presence of atmospheric turbulence. *Journal of Lightwave Technology*, 27(18):3965–3973, 2009.

[21] X. Liu. Free-space optics optimization models for building sway and atmospheric interference using variable wavelength. *IEEE Transactions on Communications*, 57(2):492–498, 2009.

[22] V. Palliyembil, J. Vellakudiyan, and P. Muthuchidambaranathan. Asymptotic bit error rate analysis of free space optical systems using spatial diversity. *Optics Communications*, 427:617–621, 2018.

[23] A. Das, B. Bag, C. Bose, and A. Chandra. Free space optical links over Málaga turbulence channels with transmit and receive diversity. *Optics Communications*, 456:124591, 2017.

[24] S. Enayati and H. Saeedi. Deployment of hybrid FSO/RF links in backhaul of relay-based rural area cellular networks: Advantages and performance analysis. *IEEE communications letters*, 20(9):1824–1827, 2016.

[25] M. Usman, H. Yang, and M. Alouini. Practical switching-based hybrid FSO/RF transmission and its performance analysis. *IEEE Photonics Journal*, 6(5):1–13, 2014.

[26] M. Najafi, B. Schmauss, and R. Schober. Intelligent reflecting surfaces for free space optical communication systems. *IEEE Transactions on Communications*, 69(9):6134–6151, 2021.

[27] V. K. Chapala and S. M. Zafaruddin. Unified performance analysis of reconfigurable intelligent surface empowered free-space optical communications. *IEEE Transactions on Communications*, 70(4):2575–2592, 2022.

[28] J. A. Anguita, M. A. Neifeld, and B. V. Vasic. Spatial correlation and irradiance statistics in a multiple-beam terrestrial free-space optical communication link. *Applied Optics*, 46(26):6561–6571, 2007.

[29] Z. Wang, W.-D. Zhong, S. Fu, and C. Lin. Performance comparison of different modulation formats over free-space optical (FSO) turbulence links with space diversity reception technique. *IEEE Photonics Journal*, 1(6):277–285, 2009.

[30] T. A. Tsiftsis, H. G. Sandalidis, G. K. Karagiannidis, and M. Uysal. Optical wireless links with spatial diversity over strong atmospheric turbulence channels. *IEEE Transactions on Wireless Communications*, 8(2):951–957, 2009.

[31] M. R. Bhatnagar and Z. Ghassemlooy. Performance analysis of Gamma–Gamma fading FSO MIMO links with pointing errors. *J. Lightwave Technol.*, 34:2158–2169, May 2016.

[32] N. Letzepis and A. G. I. Fabregas. Outage probability of the gaussian mimo free-space optical channel with ppm. *IEEE Transactions on Communications*, 57(12):3682–3690, 2009.

[33] R. Mesleh, H. Elgala, and H. Haas. Optical spatial modulation. *Journal of Optical Communications and Networking*, 3(3):234–244, Mar 2011.

[34] T. Özbilgin and M. Koca. Optical spatial modulation over atmospheric turbulence channels. *Journal of Lightwave Technology*, 33(11):2313–2323, 2015.

[35] G. K. Karagiannidis, T.A. Tsiftsis, and H.G. Sandalidis. Outage probability of relayed free space optical communication systems. *Electronics Letters*, 42(17):994–996, 2006.

[36] M. A. Kashani, M. Safari, and M. Uysal. Optimal relay placement and diversity analysis of relay-assisted free-space optical communication systems. *Journal of Optical Communications and Networking*, 5(1):37–47, 2013.

[37] E. Zedini, H. Soury, and M.-S. Alouini. Dual-hop FSO transmission systems over gamma–gamma turbulence with pointing errors. *IEEE Transactions on Wireless Communications*, 16(2):784–796, 2017.

[38] C. K. Datsikas, K. P. Peppas, N. C. Sagias, and G. S. Tombras. Serial free-space optical relaying communications over gamma-gamma atmospheric turbulence channels. *Journal of Optical Communications and Networking*, 2(8):576–586, 2010.

[39] A. Touati, A. Abdaoui, F. Touati, M. Uysal, and A. Bouallegue. On the effects of combined atmospheric fading and misalignment on the hybrid FSO/RF transmission. *Journal of Optical Communications and Networking*, 8(10):715–725, 2016.

[40] I. I. Kim and E. J. Korevaar. Availability of free-space optics (fso) and hybrid FSO/RF systems. In *Optical Wireless Communications IV*, volume 4530, pages 84–95. SPIE, 2001.

[41] B. He and R. Schober. Bit-interleaved coded modulation for hybrid RF/FSO systems. *IEEE Transactions on Communications*, 57(12):3753–3763, 2009.

[42] E. Basar and I. Yildirim. Reconfigurable intelligent surfaces for future wireless networks: A channel modeling perspective. *IEEE Wireless Communications*, 28(3):108–114, 2021.

[43] E. Basar, M. D. Renzo, J. De Rosny, M. Debbah, M.S. Alouini, and R. Zhang. Wireless communications through reconfigurable intelligent surfaces. *IEEE Access*, 7:116753–116773, 2019.

[44] J. Xu, C. Yuen, C. Huang, N. U. Hassan, G. C. Alexandropoulos, M. D. Renzo, and M. Debbah. Reconfiguring wireless environments via intelligent surfaces for 6G: reflection, modulation, and security. *SCIENCE CHINA Information Sciences*, 66(3):130304–, 2023.

[45] Q. Wu, S. Zhang, B. Zheng, C. You, and R. Zhang. Intelligent reflecting surface-aided wireless communications: A tutorial. *IEEE Transactions on Communications*, 69(5):3313–3351, 2021.

[46] M. D. Renzo, A.O. Zappone, M. Debbah, M.S. Alouini, C. Yuen, J. D. Rosny, and S. Tretyakov. Smart radio environments empowered by reconfigurable intelligent surfaces: How it works, state of research, and the road ahead. *IEEE Journal on Selected Areas in Communications*, 38(11):2450–2525, 2020.

[47] C. Liaskos, S. Nie, A. Tsioliaridou, A. Pitsillides, S. Ioannidis, and I. Akyildiz. A new wireless communication paradigm through software-controlled metasurfaces. *IEEE Communications Magazine*, 56(9):162–169, 2018.

[48] N. D. Chatzidiamantis, G. K. Karagiannidis, E. E. Kriezis, and M. Matthaiou. Diversity combining in hybrid RF/FSO systems with PSK modulation. In *proceedings IEEE International Conference on Communications (ICC)*, pages 1–6, 2011.

[49] L. Huang, S. Liu, P. Dai, M. Li, G. K. Chang, Y. Shi, and X. Chen. Unified performance analysis of hybrid FSO/RF system with diversity combining. *Journal of Lightwave Technology*, 38(24):6788–6800, 2020.

[50] A. R. Ndjiongue, Telex. M. N. Ngatched, O. A. Dobre, A. G. Armada, and H. Haas. Analysis of RIS-based terrestrial-FSO link over G-G turbulence with

distance and jitter ratios. *Journal of Lightwave Technology*, 39(21):6746–6758, 2021.

[51] D. Tyrovolas, S. A. Tegos, E. C. Dimitriadou-Panidou, P. D. Diamantoulakis, C. K. Liaskos, and G. K. Karagiannidis. Performance analysis of cascaded reconfigurable intelligent surface networks. *IEEE Wireless Communications Letters*, 11(9):1855–1859, 2022.

[52] H. Wang, Z. Zhang, B. Zhu, J. Dang, L. Wu, L. Wang, K. Zhang, and Y. Zhang. Performance of wireless optical communication with reconfigurable intelligent surfaces and random obstacles. `https://arxiv.org/abs/2001.05715`.

[53] A. Jaiswal, M. R. Bhatnagar, and V. K. Jain. Performance of optical space shift keying over gamma–gamma fading with pointing error. *IEEE Photonics Journal*, 9(2):1–16, 2017.

[54] M. Abaza, R. Mesleh, A. Mansour, and M. Hadi. The performance of space shift keying for free-space optical communications over turbulent channels. In *Proceedings of SPIE - The International Society for Optical Engineering*, volume 9387, 02 2015.

[55] A. Jaiswal, M. R. Bhatnagar, and V. K. Jain. Performance evaluation of space shift keying in free-space optical communication. *Journal of Optical Communications and Networking*, 9(2):149–160, 2017.

[56] H. Lei, H. Luo, K.-H. Park, Z. Ren, G. Pan, and M.S. Alouini. Secrecy outage analysis of mixed RF-FSO systems with channel imperfection. *IEEE Photonics Journal*, 10(3):1–13, 2018.

[57] A. I. Abdulgani, Ö. A. Serdar, E. Eylem, and D.-A. Lütfiye. Performance analysis of free space optical communication systems over imprecise malaga fading channels. *Optics Communications*, 457:124694, 2020.

[58] M. Z. Chowdhury, Md. Shahjalal, S. Ahmed, and Y. M. Jang. 6G wireless communication systems: Applications, requirements, technologies, challenges, and research directions. *IEEE Open Journal of the Communications Society*, 1:957–975, 2020.

[59] D. Serghiou, M. Khalily, T. W. C. Brown, and R. Tafazolli. Terahertz channel propagation phenomena, measurement techniques and modeling for 6G wireless communication applications: A survey, open challenges and future research directions. *IEEE Communications Surveys & Tutorials*, 24(4):1957–1996, 2022.

[60] C. -X. Wang *et al.* On the road to 6G: Visions, requirements, key technologies, and testbeds. *IEEE Communications Surveys & Tutorials*, 25(2):905–974, 2023.

[61] W. Jiang, B. Han, M. A. Habibi, and H. D. Schotten. The road towards 6G: A comprehensive survey. *IEEE Open Journal of the Communications Society*, 2:334–366, 2021.

[62] N. -N. Dao *et al.* Survey on aerial radio access networks: Toward a comprehensive 6G access infrastructure. *IEEE Communications Surveys & Tutorials*, 23(2):1193–1225, 2021.

[63] Z. Ghassemlooy, S. Arnon, M. Uysal, Z. Xu, and J. Cheng. Emerging optical wireless communications-advances and challenges. *IEEE Journal on Selected Areas in Communications*, 33(9):1738–1749, 2015.

[64] M. Z. Chowdhury, M. T. Hossan, A. Islam, and Y. M. Jang. A comparative survey of optical wireless technologies: Architectures and applications. *IEEE Access*, 6:9819–9840, 2018.

[65] A. Jahid, M. H. Alsharif, and T. J. Hall. A contemporary survey on free space optical communication: Potentials, technical challenges, recent ad-

vances and research direction. *Journal of Network and Computer Applications*, 200:103311, 2022.

[66] V. W. S. Chan. Free-space optical communications. *Journal of Lightwave Technology*, 24(12):4750–4762, 2006.

[67] E. Ciaramella, Y. Arimoto, G. Contestabile, M. Presi, A. D'errico, V. Guarino, and M. Matsumoto. 1.28-tb/s (32× 40 gb/s) free-space optical WDM transmission system. *IEEE Photonics Technology Letters*, 21(16):1121–1123, 2009.

[68] K. Su, L. Moeller, R. B. Barat, and J. F. Federici. Experimental comparison of performance degradation from terahertz and infrared wireless links in fog. *JOSA A*, 29(2):179–184, 2012.

[69] S. Zhang, S. Watson, J. J. McKendry, A. Massoubre, D.and Cogman, E. Gu, R. K. Henderson, A. E. Kelly, and M. D. Dawson. 1.5 gbit/s multi-channel visible light communications using CMOS-controlled GaN-based LEDs. *Journal of Lightwave Technology*, 31(8):1211–1216, 2013.

[70] M. Z. Chowdhury, M. K. Hasan, M. Shahjalal, M. T. Hossan, and Y. M. Jang. Optical wireless hybrid networks: Trends, opportunities, challenges, and research directions. *IEEE Communications Surveys & Tutorials*, 22(2):930–966, 2020.

[71] M. Alzenad, M. Z. Shakir, H. Yanikomeroglu, and M.S. Alouini. FSO-based vertical backhaul/fronthaul framework for 5G+ wireless networks. *IEEE Communications Magazine*, 56(1):218–224, 2018.

[72] A. Douik, Ha. Dahrouj, T. Y. Al-Naffouri, and M.S. Alouini. Hybrid radio/free-space optical design for next generation backhaul systems. *IEEE Transactions on Communications*, 64(6):2563–2577, 2016.

[73] H. Hemmati. *Near-Earth Laser Communications*. CRC Press, Boca Raton, 2020.

[74] H. T. Yura and W. G. McKinley. Optical scintillation statistics for IR ground-to-space laser communication systems. *Applied Optics*, 22(21):3353–3358, 1983.

[75] V. Sharma and N. Kumar. Improved analysis of 2.5 Gbps-inter-satellite link (ISL) in inter-satellite optical-wireless communication (IsOWC) system. *Optics Communications*, 286:99–102, 2013.

[76] A. Viswanath, V. K. Jain, and S. Kar. Analysis of earth-to-satellite free-space optical link performance in the presence of turbulence, beam-wander induced pointing error and weather conditions for different intensity modulation schemes. *IET Communications*, 9(18):2253–2258, 2015.

[77] J. B. Carruthers and J. M. Kahn. Multiple-subcarrier modulation for non-directed wireless infrared communication. In *proceedings IEEE GLOBECOM. Communications: The Global Bridge*, volume 2, pages 1055–1059. IEEE, 1994.

[78] T. Ohtsuki. Multiple-subcarrier modulation in optical wireless communications. *IEEE Communications Magazine*, 41(3):74–79, 2003.

[79] K. P. Peppas and C. K. Datsikas. Average symbol error probability of general-order rectangular quadrature amplitude modulation of optical wireless communication systems over atmospheric turbulence channels. *Journal of Optical Communications and Networking*, 2(2):102–110, 2010.

[80] H. Kaushal, V. K. Jain, and S. Kar. *Free Space Optical Communication*. Springer, India, 2017.

[81] N. Perlot. Turbulence-induced fading probability in coherent optical communication through the atmosphere. *Applied Optics*, 46(29):7218–7226, 2007.

[82] H. G. Sandalidis, T. A. Tsiftsis, and G. K. Karagiannidis. Optical wireless communications with heterodyne detection over turbulence channels with pointing errors. *Journal of Lightwave Technology*, 27(20):4440–4445, 2009.

[83] S. B. Alexander. *Optical communication receiver design*, volume 37. SPIE Press, 1997.

[84] J. C. Ricklin and F. M. Davidson. Atmospheric turbulence effects on a partially coherent gaussian beam: implications for free-space laser communication. *Journal of the Optical Society of America A*, 19(9):1794–1802, 2002.

[85] H. G. Sandalidis, T. A. Tsiftsis, G. K. Karagiannidis, and M. Uysal. BER performance of FSO links over strong atmospheric turbulence channels with pointing errors. *IEEE Communications Letters*, 12(1):44–46, 2008.

[86] L. C. Andrews, R. L. Phillips, C. Y. Hopen, and M. A. Al-Habash. Theory of optical scintillation. *JOSA A*, 16(6):1417–1429, 1999.

[87] L. C. Andrews, R. L. Phillips, and C. Y. Hopen. *Laser beam scintillation with applications*, volume 99. SPIE press, 2001.

[88] L. Andrews and R. Phillips. *Laser Beam Propagation Through Random Media*. SPIE Publications, 2nd edition, 2005.

[89] D. L. Hutt. Modeling and measurement of atmospheric optical turbulence over land. *Optical Engineering*, 38(8):1288–1295, 1999.

[90] X. Zhu and J. M. Kahn. Free-space optical communication through atmospheric turbulence channels. *IEEE Transactions on Communications*, 50(8):1293–1300, 2002.

[91] M. A. Al-Habash, L. C. Andrews, and R. L. Phillips. Mathematical model for the irradiance probability density function of a laser beam propagating through turbulent media. *Optical Engineering*, 40(8):1554–1562, 2001.

[92] J. Cang and X. Liu. Average capacity of free-space optical systems for a partially coherent beam propagating through non-kolmogorov turbulence. *Optics Letters*, 36(17):3335–3337, 2011.

[93] C. Liu, Y. Yao, Y. Sun, and X. Zhao. Average capacity for heterodyne FSO communication systems over gamma-gamma turbulence channels with pointing errors. *Electronics Letters*, 46(12):851–853, 2010.

[94] A. Farid and S. Hranilovic. Outage capacity optimization for free-space optical links with pointing errors. *IEEE/OSA Journal of Lightwave Technology*, 25(7):1702–1710, 2007.

[95] A. J. Navas, J. M. G. Balsells, J. F. Paris, and A. P. Notario. A unifying statistical model for atmospheric optical scintillation. In Jan Awrejcewicz, editor, *Numerical Simulations of Physical and Engineering Processes*, chapter 8. IntechOpen, Rijeka, 2011.

[96] I. S. Ansari, F. Yilmaz, and M. Alouini. Performance analysis of free-space optical links over Málaga ($\mathcal{M}$) turbulence channels with pointing errors. *IEEE Transactions on Wireless Communications*, 15(1):91–102, 2016.

[97] D. Kedar and S. Arnon. Optical wireless communication through fog in the presence of pointing errors. *Applied Optics*, 42(24):4946–4954, 2003.

[98] Y. Ren, A. Dang, B. Luo, and H. Guo. Capacities for long-distance free-space optical links under beam wander effects. *IEEE Photonics Technology Letters*, 22(14):1069–1071, 2010.

[99] A. A. Farid and S. Hranilovic. Outage capacity for MISO intensity-modulated free-space optical links with misalignment. *Journal of Optical Communications and Networking*, 3(10):780–789, 2011.

[100] A. J. Navas, J. M. G. Balsells, J. F. Paris, M. C. Vazquez, and A. P. Notario. Impact of pointing errors on the performance of generalized atmospheric optical channels. *Optics Express*, 20(11):12 550–12 562, 2012.

[101] S. S. Muhammad, B. Flecker, E. Leitgeb, and M. Gebhart. Characterization of fog attenuation in terrestrial free space optical links. *Optical Engineering*, 46(6):066001–066001, 2007.

[102] Z. Ghassemlooy, W. Popoola, and Su. Rajbhandari. *Optical wireless communications: system and channel modelling with Matlab®*. CRC press, 2019.

[103] U. Ketprom, S. Jaruwatanadilok, Y. Kuga, A. Ishimaru, and J. Ritcey. Channel modeling for optical wireless communication through dense fog. *Journal of Optical Networking*, 4(6):291–299, 2005.

[104] I. I. Kim, B. McArthur, and E. J. Korevaar. Comparison of laser beam propagation at 785 nm and 1550 nm in fog and haze for optical wireless communications. In *Optical Wireless Communications III*, volume 4214, pages 26–37. Spie, 2001.

[105] M. Aharonovich and S. Arnon. Performance improvement of optical wireless communication through fog with a decision feedback equalizer. *Journal of the Optical Society of America A*, 22(8):1646–1654, Aug 2005.

[106] M. Grabner and V. Kvicera. The wavelength dependent model of extinction in fog and haze for free space optical communication. *Optics Express*, 19(4):3379–3386, 2011.

[107] X. Chen and C. Yuen. On interference alignment with imperfect CSI: Characterizations of outage probability, ergodic rate and SER. *IEEE Transactions on Vehicular Technology*, 65(1):47–58, 2015.

[108] J. Feng and X. Zhao. Performance analysis of OOK-based FSO systems in Gamma–Gamma turbulence with imprecise channel models. *Optics Communications*, 402:340–348, 2017.

[109] L. Han, X. Liu, Y. Wang, and B. Li. Joint impact of channel estimation errors and pointing errors on fso communication systems over $\mathcal{F}$ turbulence channel. *Journal of Lightwave Technology*, 40(14):4555–4561, 2022.

[110] M. Petkovic, G. T. Djordjevic, and I. B. Djordjevic. Analysis of mixed RF/FSO system with imperfect CSI estimation. In *proceedings 19th Inter-*

national Conference on Transparent Optical Networks (ICTON), pages 1–7. IEEE, 2017.

[111] L. Han, X. Liu, Y. Wang, and X. Hao. Analysis of RIS-assisted FSO systems over $\mathcal{F}$ turbulence channel with pointing errors and imperfect CSI. *IEEE Wireless Communications Letters*, 11(9):1940–1944, 2022.

[112] P. Polynkin, A. Peleg, L. Klein, T. Rhoadarmer, and J. Moloney. Optimized multiemitter beams for free-space optical communications through turbulent atmosphere. *Optics Letters*, 32(8):885–887, 2007.

[113] M. Razavi and J. H Shapiro. Wireless optical communications via diversity reception and optical preamplification. *IEEE Transactions on wireless Communications*, 4(3):975–983, 2005.

[114] D. C. O'Brien, S. Quasem, S. Zikic, and G. E. Faulkner. Multiple input multiple output systems for optical wireless: challenges and possibilities. *Free-Space Laser Communications VI*, 6304:289–295, 2006.

[115] N. Cvijetic, S. G. Wilson, and M. Brandt-Pearce. Performance bounds for free-space optical MIMO systems with APD receivers in atmospheric turbulence. *IEEE Journal on Selected Areas in Communications*, 26(3):3–12, 2008.

[116] M. A Kashani, M. Uysal, and M. Kavehrad. On the performance of MIMO FSO communications over double generalized gamma fading channels. In *proceedings IEEE International Conference on Communications (ICC)*, pages 5144–5149. IEEE, 2015.

[117] A. G.-Zambrana, C. C.-Vázquez, B. C.-Vázquez, and A. H.-Gómez. Selection transmit diversity for FSO links over strong atmospheric turbulence channels. *IEEE Photonics Technology Letters*, 21(14):1017–1019, 2009.

[118] M. A. Khalighi, N. Aitamer, N. Schwartz, and S. Bourennane. Turbulence mitigation by aperture averaging in wireless optical systems. In *proceedings*

10th International Conference on Telecommunications, pages 59–66. IEEE, 2009.

[119] H. Yuksel, S. Milner, and C. Davis. Aperture averaging for optimizing receiver design and system performance on free-space optical communication links. *Journal of Optical Networking*, 4(8):462–475, 2005.

[120] F. S. Vetelino, C. Young, L. Andrews, and J. Recolons. Aperture averaging effects on the probability density of irradiance fluctuations in moderate-to-strong turbulence. *Applied Optics*, 46(11):2099–2108, 2007.

[121] A. Viswanath, P. Gopal, V. K. Jain, and S. Kar. Performance enhancement by aperture averaging in terrestrial and satellite free space optical links. *IET Optoelectronics*, 10(3):111–117, 2016.

[122] H. Kazemi and M. Uysal. Performance analysis of MIMO free-space optical communication systems with selection combining. In *2013 21st Signal Processing and Communications Applications Conference (SIU)*, pages 1–4, 2013.

[123] S. M. Navidpour, M. Uysal, and M. Kavehrad. Ber performance of free-space optical transmission with spatial diversity. *IEEE Transactions on wireless communications*, 6(8):2813–2819, 2007.

[124] E. Bayaki, R. Schober, and R. K. Mallik. Performance analysis of mimo free-space optical systems in gamma-gamma fading. *IEEE Transactions on Communications*, 57(11):3415–3424, 2009.

[125] S. Malik and P. K. Sahu. M-ary phase-shift keying-based single-input-multiple-output free space optical communication system with pointing errors over a Gamma–Gamma fading channel. *Applied Optics*, 59(1):59–67, Jan 2020.

[126] N. D. Milosevic, M. I. Petkovic, and G. T. Djordjevic. Average BER of SIM-DPSK FSO system with multiple receivers over $\mathcal{M}$-distributed atmospheric channel with pointing errors. *IEEE Photonics Journal*, 9(4):1–10, 2017.

[127] H. Moradi, H.H. Refai, and P.G. LoPresti. Switch-and-stay and switch-and-examine dual diversity for high-speed free-space optics links. *IET Optoelectronics*, 6:34–42(8), February 2012.

[128] S. Yu, C. Geng, J. Zhong, and D. Kang. Performance analysis of optical spatial modulation over a correlated Gamma–Gamma turbulence channel. *Applied Optics*, 61(8):2025–2035, Mar 2022.

[129] T. Fath and H. Haas. Optical spatial modulation using colour LEDs. In *proceedings IEEE International Conference on Communications (ICC)*, pages 3938–3942, 2013.

[130] I. Chauhan, P. Paul, M. R. Bhatnagar, and J. Nebhen. Performance of optical space shift keying under jamming. *Applied Optics*, 60(7):1856–1863, Mar 2021.

[131] A. Jaiswal, M. R. Bhatnagar, and Virander K. Jain. On the ergodic capacity of optical space shift keying based FSO-MIMO system under atmospheric turbulence. In *proceedings IEEE International Conference on Communications (ICC)*, pages 1–7, 2017.

[132] A. Jaiswal, M. Abaza, M. R. Bhatnagar, and V. K. Jain. An investigation of performance and diversity property of optical space shift keying-based FSO-MIMO system. *IEEE Transactions on Communications*, 66(9):4028–4042, 2018.

[133] M. R. Bhatnagar. Performance analysis of decode-and-forward relaying in Gamma-Gamma fading channels. *IEEE Photonics Technology Letters*, 24(7):545–547, 2012.

[134] E. Zedini and M.S. Alouini. On the performance of multihop heterodyne FSO systems with pointing errors. *IEEE Photonics Journal*, 7(2):1–10, 2015.

[135] M. Safari and M. Uysal. Relay-assisted free-space optical communication. *IEEE Transactions on Wireless Communications*, 7(12):5441–5449, 2008.

[136] A. Nosratinia, T. E. Hunter, and A. Hedayat. Cooperative communication in wireless networks. *IEEE communications Magazine*, 42(10):74–80, 2004.

[137] M. Karimi and M. N.-Kenari. Ber analysis of cooperative systems in free-space optical networks. *Journal of Lightwave Technology*, 27(24):5639–5647, 2009.

[138] M. Karimi and M. N.-Kenari. Free space optical communications via optical amplify-and-forward relaying. *Journal of Lightwave Technology*, 29(2):242–248, 2011.

[139] O. M. S. Al-Ebraheemy, A. M. Salhab, A. Chaaban, S. A. Zummo, and M. Alouini. Precise performance analysis of dual-hop mixed RF/unified-FSO DF relaying with heterodyne detection and two IM-DD channel models. *IEEE Photonics Journal*, 11(1):1–22, 2019.

[140] P. V. Trinh, T. Cong Thang, and A. T. Pham. Mixed mmwave RF/FSO relaying systems over generalized fading channels with pointing errors. *IEEE Photonics Journal*, 9(1):1–14, 2017.

[141] E. Zedini, I. S. Ansari, and M. Alouini. Performance analysis of mixed Nakagami-m and Gamma–Gamma dual-hop FSO transmission systems. *IEEE Photonics Journal*, 7(1):1–20, 2015.

[142] S. Anees and M. R. Bhatnagar. Performance evaluation of decode-and-forward dual-hop asymmetric radio frequency-free space optical communication system. *IET Optoelectronics*, 9(5):232–240, 2015.

[143] E. S.-Nasab and M. Uysal. Generalized performance analysis of mixed RF/FSO cooperative systems. *IEEE Transactions on Wireless Communications*, 15(1):714–727, 2016.

[144] B. Ashrafzadeh, E. S.-Nasab, M. Kamandar, and M. Uysal. A framework on the performance analysis of dual-hop mixed FSO-RF cooperative systems. *IEEE Transactions on Communications*, 67(7):4939–4954, 2019.

[145] C. Yan, J. Fu, L.and Zhang, and J. Wang. A comprehensive survey on UAV communication channel modeling. *IEEE Access*, 7:107769–107792, 2019.

[146] M. Q. Vu, N. T.T. Nguyen, H. T.T. Pham, and N. T. Dang. Performance enhancement of LEO-to-ground FSO systems using All-optical HAP-based relaying. *Physical Communication*, 31:218–229, 2018.

[147] M. K. Simon and M. S. Alouini. *Digital Communications Over Fading Channels: A Unified Approach to Performance Analysis.* Wiley-Interscience, 2nd ed. New York, NY, USA, 2005.

[148] S. Sharma, A. S. Madhukumar, and Swaminathan R. MIMO hybrid FSO/RF system over generalized fading channels. *IEEE Transactions on Vehicular Technology*, 70(11):11565–11581, 2021.

[149] A. Touati, F. Touati, A. Abdaoui, A. Khandakar, S. J. Hussain, and A. Bouallegue. An experimental performance evaluation of the hybrid FSO/RF. In Hamid Hemmati and Don M. Boroson, editors, *Free-Space Laser Communication and Atmospheric Propagation XXIX*, volume 10096, pages 409 – 415. International Society for Optics and Photonics, SPIE, 2017.

[150] W. Zhang, S. Hranilovic, and C. Shi. Soft-switching hybrid FSO/RF links using short-length raptor codes: Design and implementation. *IEEE Journal on Selected Areas in Communications*, 27(9):1698–1708, 2009.

[151] H. Liang, C. Gao, Y. Li, M. Miao, and X. Li. Analysis of selection combining scheme for hybrid FSO/RF transmission considering misalignment. *Optics Communications*, 435:399–404, 2019.

[152] K. O. Odeyemi and P. A. Owolawi. Selection combining hybrid FSO/RF systems over generalized induced-fading channels. *Optics Communications*, 433(8):159–167, 2019.

[153] O. S. Badarneh and R. Mesleh. Diversity analysis of simultaneous mmwave and free-space-optical transmission over $\mathcal{F}$-distribution channel models. *Journal of Optical Communications and Networking*, 12(11):324–334, Nov 2020.

[154] H. Liang, Y. Li, M. Miao, C. Gao, and X. Li. Analysis of selection combining hybrid FSO/RF systems considering physical layer security and interference. *Optics Communications*, 497:127146, 2021.

[155] T. Rakia, H. Yang, M. Alouini, and F. Gebali. Outage analysis of practical FSO/RF hybrid system with adaptive combining. *IEEE Communications Letters*, 19(8):1366–1369, 2015.

[156] M. Siddharth, S. Shah, N.Vishwakarma, and Swaminathan R. Performance analysis of adaptive combining based hybrid FSO/RF terrestrial communication. *IET Communications*, 14:4057–4068(11), Dec. 2020.

[157] T. Rakia, H. Yang, F. Gebali, and M. Alouini. Power adaptation based on truncated channel inversion for hybrid FSO/RF transmission with adaptive combining. *IEEE Photonics Journal*, 7(4):1–12, 2015.

[158] M. Siddharth, S. Shah, and Swaminathan R. Outage analysis of adaptive combining scheme for hybrid FSO/RF communication. In *proceedings National Conference on Communications (NCC)*, pages 1–6, 2020.

[159] S. Shah, M. Siddharth, N. Vishwakarma, R. Swaminathan, and A. S. Madhukumar. Adaptive-combining-based hybrid FSO/RF satellite communication with and without HAPS. *IEEE Access*, 9:81492–81511, 2021.

[160] M. D. Yacoub. The κ-μ distribution and the η-μ distribution. *IEEE Antennas and Propagation Magazine*, 49(1):68–81, 2007.

[161] J. M. Moualeu, D. B. da Costa, W. Hamouda, U. S. Dias, and R. A. A. de Souza. Performance analysis of digital communication systems over α-κ-μ fading channels. *IEEE Communications Letters*, 23(1):192–195, 2019.

[162] J. F. Paris. Outage probability in η-μ/η-μ and κ-μ/η-μ interference-limited scenarios. *IEEE Transactions on Communications*, 61(1):335–343, 2013.

[163] K. P. Peppas. Sum of nonidentical squared κ-μ variates and applications in the performance analysis of diversity receivers. *IEEE Transactions on Vehicular Technology*, 61(1):413–419, 2012.

[164] M.K. Arti. Beamforming and combining based scheme over κ-μ shadowed fading satellite channels. *IET Communications*, 10(15), 2016.

[165] M. D. Yacoub. The α-η-κ-μ fading model. *IEEE Transactions on Antennas and Propagation*, 64(8):3597–3610, 2016.

[166] J. M. Moualeu, D. B. da Costa, F. J. Lopez-Martinez, and R. A. A. d. Souza. On the performance of α-η-κ-μ fading channels. *IEEE Communications Letters*, 23(6):967–970, 2019.

[167] X. Li, X. Chen, J. Zhang, Y. Liang, and Y. Liu. Capacity analysis of α-η-κ-μ fading channels. *IEEE Communications Letters*, 21(6):1449–1452, 2017.

[168] S. Sharma, A.S. Madhukumar, and Swaminathan R. Effect of pointing errors on the performance of hybrid FSO/RF networks. *IEEE Access*, 7:131418–131434, 2019.

[169] B. Bag, A. Das, C. Bose, and A. Chandra. Improving the performance of a DF relay-aided FSO system with an additional source–relay mmwave RF backup. *Journal of Optical Communications and Networking*, 12(12):390–402, 2020.

[170] S. Sharma, A. S. Madhukumar, and Swaminathan R. Switching-based cooperative decode-and-forward relaying for hybrid FSO/RF networks. *Journal of Optical Communications and Networking*, 11(6):267–281, 2019.

[171] W. A. Alathwary and E. S. Altubaishi. On the performance analysis of decode-and-forward multi-hop hybrid FSO/RF systems with hard-switching configuration. *IEEE Photonics Journal*, 11(6):1–12, 2019.

[172] Thang V. Nguyen, Hoang D. Le, Ngoc T. Dang, and Anh T. Pham. On the design of rate adaptation for relay-assisted satellite hybrid FSO/RF systems. *IEEE Photonics Journal*, 14(1):1–11, 2022.

[173] Swaminathan R., S. Sharma, N. Vishwakarma, and A. S. Madhukumar. HAPS-based relaying for integrated space–air–ground networks with hybrid FSO/RF communication: A performance analysis. *IEEE Transactions on Aerospace and Electronic Systems*, 57(3):1581–1599, 2021.

[174] N. Vishwakarma and Swaminathan R. On the performance of hybrid FSO/RF system over generalized fading channels. In *proceedings IEEE International Conference on Advanced Networks and Telecommunications Systems (ANTS)*, pages 1–6, 2020.

[175] V. D. Phan *et al.* Performance of cooperative communication system with multiple reconfigurable intelligent surfaces over Nakagami-m fading channels. *IEEE Access*, 10:9806–9816, 2022.

[176] L. Yang, F. Meng, Q. Wu, Da. B. da Costa, and M.S. Alouini. Accurate closed-form approximations to channel distributions of RIS-aided wireless systems. *IEEE Wireless Communications Letters*, 9(11):1985–1989, 2020.

[177] A. M. Salhab and M. H. Samuh. Accurate performance analysis of reconfigurable intelligent surfaces over Rician fading channels. *IEEE Wireless Communications Letters*, 10(5):1051–1055, 2021.

[178] S. P. Dash, R. K. Mallik, and N. Pandey. Performance analysis of an index modulation-based receive diversity RIS-assisted wireless communication system. *IEEE Communications Letters*, 26(4):768–772, 2022.

[179] J. Yao, J. Xu, W. Xu, C. Yuen, and X. You. A universal framework of superimposed RIS-phase modulation for MISO communication. *IEEE Transactions on Vehicular Technology*, 72(4):5413–5418, 2023.

[180] M. Di Renzo *et al.* Reconfigurable intelligent surfaces vs. relaying: Differences, similarities, and performance comparison. *IEEE Open Journal of the Communications Society*, 1:798–807, 2020.

[181] L. Yang, W. Guo, D. B. da Costa, and M.S. Alouini. Free-space optical communication with reconfigurable intelligent surfaces. https://arxiv.org/abs/2012.00547.

[182] A. M. Salhab and L. Yang. Mixed RF/FSO relay networks: RIS-equipped RF source vs RIS-aided RF source. *IEEE Wireless Communications Letters*, 10(8):1712–1716, 2021.

[183] S. Sharma, N. Vishwakarma, and Swaminathan, R. Performance analysis of IRS-assisted hybrid FSO/RF communication system. In *proceedings National Conference on Communications (NCC)*, pages 268–273, 2022.

[184] S. Malik, P. Saxena, and Y. H. Chung. Performance analysis of a UAV-based IRS-assisted hybrid RF/FSO link with pointing and phase shift errors. *Journal of Optical Communications and Networking*, 14(4):303–315, Apr 2022.

[185] Thang V. Nguyen, Hoang D. Le, and Anh T. Pham. On the design of RIS–UAV relay-assisted hybrid FSO/RF satellite–aerial–ground integrated network. *IEEE Transactions on Aerospace and Electronic Systems*, 59(2):757–771, 2023.

[186] I. S. Gradshteyn and I. M. Ryzhik. *Table of Integrals, Series, and Products.* Academic, 7th ed., 2007.

[187] Wolfram Research Inc. Mathematica edition: Version 8. https://functions.wolfram.com/HypergeometricFunctions/MeijerG/, 2010.

[188] Log expansions. http://www.math.com/tables/expansion/log.htm, 2001.

[189] A. M. Mathai, R.K. Saxena, and H.J. Haubold. *The H-Function Theory and Applications*. Springer, New York, 2010.

[190] N. Vishwakarma and Swaminathan R. Performance analysis of hybrid FSO/RF communication over generalized fading models. *Optics Communications*, 487:126796, 2021.

[191] M. Khalighi, F. Xu, Y. Jaafar, and S. Bourennane. Double-laser differential signaling for reducing the effect of background radiation in free-space optical systems. *Journal of Optical Communications and Networking*, 3(2):145–154, 2011.

[192] P. Adhikari. Understanding millimeter wave wireless communication, 2008.

[193] F. Yang, J. Cheng, and T. A. Tsiftsis. Free-space optical communication with nonzero boresight pointing errors. *IEEE Transactions on Communications*, 62(2):713–725, 2014.

[194] Z. Rahman, S. M. Zafaruddin, and V. K. Chaubey. Performance of opportunistic receiver beam selection in multiaperture OWC systems over foggy channels. *IEEE Systems Journal*, 14(3):4036–4046, 2020.

[195] M. R. Bhatnagar and Z. Ghassemlooy. Performance analysis of Gamma–Gamma fading FSO MIMO links with pointing errors. *Journal of Lightwave Technology*, 34(9):2158–2169, 2016.

[196] M. D. Yacoub. The $\kappa - \mu$ distribution and the $\eta - \mu$ distribution. *IEEE Antennas and Propagation Magazine*, 49(1):68–81, 2007.

[197] A. Lapidoth, S. M. Moser, and Michele A. Wigger. On the capacity of free-space optical intensity channels. *IEEE Transactions on Information Theory*, 55(10):4449–4461, 2009.

[198] N. T. Hai and S. B. Yakubovich. *The Double Mellin-Barnes Type Integrals and Their Application to Convolution Theory.* Singapore: World Scientific, 6 edition, 1992.

[199] P. K. Mittal and K. C. Gupta. An integral involving generalized function of two variables. *Proceedings of the Indian Academy of Sciences - Section A*, 75:117–123, 1972.

[200] A. Kilbas and M. Saigo. *H-Transforms: Theory and Applications (Analytical Method and Special Function)*. Boca Raton, FL, USA: CRC Press, 1st edition, 2004.

[201] W. N. Edward and M. Geller. *A table of integrals of the error functions.* J. Res. Nat. Bur. Stand., 1968.

[202] N. Vishwakarma and Swaminathan R. On the maximal-ratio combining of FSO and RF links over generalized distributions and its applications in hybrid FSO/RF systems. *Optics Communications*, 520:128542, 2022.

[203] Zihan Zhang, Qiang Sun, Miguel López-Benítez, Xiaomin Chen, and Jiayi Zhang. Performance analysis of dual-hop RF/FSO relaying systems with imperfect CSI. *IEEE Transactions on Vehicular Technology*, 71(5):4965–4976, 2022.

[204] R. J. Sasiela. *Electromagnetic Wave Propagation in Turbulence.* Springer Science & Business Media, 12 2012.

[205] P. Concus, D. Cassatt, G. Jaehnig, and E. Melby. Tables for the evaluation of $\int_0^\infty x^\beta e^{-x} f(x)dx$ by gauss-laguerre quadrature. *Mathematics of Computation*, 17(83):245–256, 1963.

[206] H. R. Alhennawi, M. M. H. El Ayadi, M. H. Ismail, and H.-A. M. Mourad. Closed-form exact and asymptotic expressions for the symbol error rate and capacity of the h-function fading channel. *IEEE Transactions on Vehicular Technology*, 65(4):1957–1974, 2016.

[207] M. Vu, N. Nguyen, H. Pham, and N. Dang. Performance enhancement of LEO-to-ground FSO systems using All-optical HAP-based relaying. *Physical Communication*, 31:218–229, 2018.

[208] A. P. Prudnikov, Y. A. Brychkov, and O. I. Marichev. *Integrals and Series.* Gordon and Breach, 1968.